Mechanical Excitation of Trapped Ions Coupled to a Nanomechanical Oscillator

Inauguraldissertation

zur

Erlangung der Würde eines Doktors der Philosophie

vorgelegt der

Philosophisch-Naturwissenschaftlichen Fakultät

der Universität Basel

von

Moritz Weegen

2024

Genehmigt von der Philosophisch-Naturwissenschaftlichen Fakultät
auf Antrag von

Erstbetreuer: Prof. Dr. Stefan Willitsch
Zweitbetreuer: Prof. Dr. Martino Poggio
Externe Expertin: Prof. Dr. Martina Knoop

Basel, den 25.06.2024

Prof. Dr. Marcel Mayor
Dekan

Abstract

Laser-cooled ions confined in radiofrequency traps count among the best controllable quantum systems with applications in fields such as spectroscopy, ultracold chemistry and quantum technologies. They offer a variety of well-established techniques for the manipulation and readout of their internal and external quantum states and exhibit excellent coherence properties. Nanomechanical oscillators are solid-state objects on the nanometer scale. Their small sizes make them excellent candidates for the study of the interface between classical and quantum physics and the cooling and manipulation of their motion on the single-phonon level has recently been achieved. Nanomechanical oscillators are highly sensitive transducers, making them excellent sensors for small forces with famous applications such as atomic force microscopy. The combination of different types of physical systems into a single hybrid system has been of increasing interest in recent years. The goal is to exploit the individual advantages of the constituents in order to develop new applications and techniques that the individual systems alone could not provide. Hybrid systems coupling trapped ions to a charged nanomechanical oscillator may offer novel techniques for the bidirectional manipulation and readout of the quantum states of motion of both constituents. The subsystems are coupled by the electrostatic interaction of their charges and act as coupled harmonic oscillators. By resonantly driving the ions with driven vibrations of the nanomechanical oscillator, strong coupling can be achieved and the motional state of the ions can be manipulated. Here, we present the successful coupling of trapped $^{40}Ca^{+}$ ions to a charged Ag_2Ga nanowire in an ion-nanowire hybrid system in the classical regime. We present a theoretical description for the classical dynamics of the resonantly driven ion motion and support the results with numerical simulations. We simulate and experimentally investigate the static effects of the charged nanowire on the trapping potential. We present experimental results for the resonant excitation of the ion motion with the mechanically driven nanowire and show the effects on the coupling strength for the variation of different coupling parameters.

Contents

1 Introduction

The development of the theory of quantum mechanics in the 20^{th} century has laid the foundation for modern physics as we know it and has opened up a variety of new fields of study over the years. Not only did quantum mechanics reshape our understanding and theoretical description of fundamental physics at the atomic level, its practical applications may arguably have led to the biggest and fastest leap in technology. Quantum physics is directly tied to the development of now indispensable devices and technologies for the scientific community and for everyday life, such as lasers and semiconductors used in all modern computers. In early experiments, quantum-mechanical phenomena and properties, such as the photoelectric effect, electronic and nuclear spins, the wave-particle duality and quantum tunneling have been observed on ensembles of quantum systems. As the understanding and study of these systems progressed, exceptional control even over *single* quantum systems, such as individual atoms, has been achieved.

This progress gave rise to the development and study of *quantum technologies* [1], which harness the control over quantum systems and quantum-mechanical phenomena for the realization of new technological devices and applications. These include quantum information processing [2] for quantum communication [3] and quantum cryptography [4], the realization of quantum processors for quantum simulations [5, 6] and applications involving integrated quantum photonics [7]. The development of devices fundamentally working on the quantum level requires evermore sensitive measurements for the realization of control systems like feedback and error correction [1], leading to the study of quantum metrology [8] and quantum sensing [9]. One of the most prominent applications of single quantum systems incorporating the aforementioned features is the realization of a general-purpose *quantum computer*. Originally proposed in the early 1980s [10], quantum computers offer the capability to complement the use cases of classical computers and reach unprecedented computational power for certain applications. For example, quantum computers are predicted to efficiently factorize prime numbers with Shor's algorithm [11] and allow for the development of quantum algorithms for computations regarding, e. g., quantum (many-body) dynamics and open quantum systems [12], quantum chemistry [13] and quantum materials science [14]. The enormous potential of quantum computers has not only piqued the interest of academic researchers, but also of international companies and startups. In fact, IBM and Google are currently at the forefront of the development of a large-scale quantum computer and offer platforms with more than 50 qubits, which have been made available by online cloud services [15, 16]. Although impressive progress has been made in recent years, quantum computing is still largely in its infancy, and the development of a viable large-scale quantum computer is an ongoing effort in the early 21^{st} century.

The counterpart of a bit in a classical computer is the *qubit* (quantum bit) in a quantum computer. While a classical bit can only be set to one of two states (0 or 1), qubits can be prepared in any superposition of two quantum states $|0\rangle$ and $|1\rangle$. Fundamentally, any two-level

quantum system can be seen as a qubit. However, in order to be viable for practical applications, the qubit system needs to be well controllable, offer excellent coherence properties and allow for quantum error correction and high fidelity. Furthermore, the choice of qubit needs to offer scalability for the practical implementation within a single device. A variety of qubit candidates and approaches for the realization of a large-scale quantum computer have been proposed over the years. On the one hand, solutions with solid-state systems, such as superconducting qubits [17], quantum dots [18] and nitrogen-vacancy centers in diamonds [19], are considered promising candidates. On the other hand, atomic systems such as trapped ions [20, 21] or neutral atoms [22] offer alternative approaches. Trapped atoms and ions are fundamental quantum systems by nature and offer a variety of possible qubit states. Long-lived two-level states of trapped ions, such as spin states or dipole-forbidden electronic transitions, are famous candidates for the realization of ion-based qubits in quantum computers with high fidelity [21, 23]. Their excellent coherence times [24] make them prime candidates for quantum memory [25, 26] and quantum simulation [27–29] applications. Additionally, the Hilbert space spanned by the motional states of trapped ions offers ways of qubit encoding and error correction within a single quantum system [30, 31].

Besides the possibility of ion-based quantum computers, the development and improvement of ion trapping [32, 33] and laser cooling techniques [34–36] has led to great advances in applications for the modern physical sciences. Single trapped ions, as well as Coulomb crystals [37] consisting of many ions, offer applications in precision spectroscopy [38], as frequency standards in atomic and molecular clocks [39, 40] and for quantum technologies [28, 41]. Trapped ions can be cooled to their motional ground state and are used for the sympathetic cooling of molecular ions in ultracold chemistry experiments [42–45], as well as in hybrid experiments with neutral atoms [46–48]. They are near-perfectly isolated quantum harmonic oscillators with long coherence times and a variety of well-established techniques for quantum state engineering and control [49–52]. Recently, applications of trapped ions as ultrasensitive force sensors [53, 54] and thermal probes [55] have been proposed.

In order to further push the boundaries of quantum technologies and applications with trapped ions, adequate ion trap architectures need to be designed and implemented. The realization of a viable quantum processor requires the scalability to large numbers of qubits, making miniaturized chip-like devices and nanomechanical objects natural choices [56–59]. The research on solid-state physics and mechanical oscillators on the nanometer scale has seen great advances with many innovative [60] and famous applications, such as the development of atomic force microscopy [61]. Cryogenic cooling of nanomechanical oscillators in combination with other cooling techniques has enabled the leap from the classical to the quantum regime by reducing their temperature close to their motional ground state [62–66]. Nanowires are ultrahigh-sensitivity transducers capable of coupling to other physical systems via a variety of mechanisms such as small magnetic, optical or electric forces [67–69]. Their small sizes on the nanometer scale and

high sensitivity are evident advantages and enable the direct integration within miniaturized and scalable quantum devices [70, 71]. Recent advances in the designs of miniaturized radiofrequency traps have demonstrated the direct integration of nanomechanical oscillators as well as integrated optical and electrical components for the control of trapped ions [71–75].

The aforementioned advances of the exceptional control over single quantum systems and nanomechanical oscillators has lead to the theoretical study and the development of *quantum hybrid systems* [26, 76–79]. These hybrid systems aim to combine and couple different physical systems and offer a promising way of exploring the interface between quantum physics and solid-state physics [80]. The aim is to combine the individual advantages of the constituents and to interface them by a variety of possible coupling mechanisms. Quantum hybrid systems may offer novel approaches for the study of quantum effects in solid-state objects [76] and new applications in quantum technologies [81]. The individual control over the coupled subsystems offers possibilities of bidirectional sympathetic cooling [65, 66] as well as the manipulation and readout of motional quantum states and high-precision sensing of forces [53, 54, 82, 83]. In a recent theoretical study, the possibility of generating a variety of motional state distributions of a single trapped ion with the mechanical drive of a nanooscillator has been proposed [84].

A variety of hybrid systems and coupling mechanisms have been proposed in recent years, some of which have been realized experimentally, e. g., with Bose-Einstein condensates and neutral atoms [85, 86]. Among the most promising candidates for the quantum systems are quantum dots [87], defect centers [88], superconductors [89, 90], spins [91, 92] as well as neutral atoms or charged particles such as trapped ions or electrons [26, 93, 94]. The manufacturing and control over nanoscopic objects like nanomechanical oscillators [61, 95] and nanoparticles [83, 96] has seen great advances in recent years. Their properties make them excellent candidates for the realization of ion-oscillator hybrid systems, as they are objects on the border between classical and quantum physics. The available variety of materials and types of nanomechanical oscillators [95] offers a variety of approaches for the coupling to quantum systems. The possible combinations of the available candidates for hybrid systems yield coupling mechanisms such as electrostatic coupling [50, 84, 93, 97, 98], magnetic coupling [99, 100] and optical coupling in free space or optical cavities [101–104].

Trapped neutral atoms and ions are especially interesting for the realization of a hybrid system. On the one hand, they offer a large variety of well-established techniques for the control and manipulation of their quantum states with excellent coherence properties [105–107]. On the other hand, their confinement forces them onto oscillatory motions, described by the states of a quantum harmonic oscillator. Due to this, trapped neutral atoms and ions can be considered as mechanical oscillators themselves [78] and thus offer the possibility to *mechanically* couple to other oscillators, such as nanomembranes, nanowires, nanocantilevers or vibrating mirrors [78]. This enables the possibility for hybrid systems consisting of two coupled mechanical os-

cillators [94, 108–110]. This mechanical coupling can be mediated by a distance-dependent interaction, such as the electrostatic interaction of trapped ions to a charged nanomechanical oscillator or coupling to an oscillator mediated by optical forces in cavity-QED systems [94]. The latter approach may be of interest for experiments with trapped ions as it avoids the introduction of perturbations to the electric trapping potential.

Ion-nanooscillator hybrid systems have been theoretically proposed [26, 93, 94, 97] and one was recently designed, manufactured and experimentally implemented by Panagiotis Fountas at the University of Basel [80, 84]. It was designed to couple trapped $^{40}Ca^{+}$ ions to a charged Ag_2Ga nanocantilever whose tip can be freely positioned inside of the trap with the use of nanopositioners. In contrast, the direct integration of doubly-clamped nanowires to the geometry of an ion trap offers alternative approaches. These nanowires could either directly act as the trapping electrodes [93] or be equipped with small localized electrodes [97] to couple to trapped ions via an applied static voltage. This direct integration as part of the trap design may reduce perturbations to the trapping potential introduced by the nanomechanical oscillator. Moreover, other types of oscillators such as quartz bulk acoustic resonators and electrical resonators have been proposed for hybrid systems with charged particles such as trapped ions or electrons [26].

The realization of a hybrid system coupling trapped ions to a charged cantilever may offer some unique advantages. The charge on the nanocantilever may be used for additional control over the trapping potential and allow the controlled generation of anharmonicities and double-well potentials [84]. By placing the cantilever on nanopositioners, the coupling strength between the systems can be dynamically adjusted by changing experimental parameters, such as the charge of the nanocantilever and the ion-nanowire distance. Furthermore, nanomechanical oscillators generally exhibit large quality factors, a requirement for the coherent exchange of quantum states between the subsystems [26]. By mechanically driving vibrations of the nanocantilever on resonance with the motion of the trapped ions, strong mechanical coupling can be achieved. According to theoretical studies of the system with a semi-classical approach, this allows the mechanical generation of coherent states of the ions with large amplitudes, as well as the generation of purely non-classical states of motion in combination with anharmonicities of the trapping potential [84]. An additional possibility may be to use the ions as ultrasensitive sensors to measure the motion of the cantilever [97]. However, ion-nanooscillator systems coupled by their electrostatic interaction also introduce challenges that need to be taken into consideration. The addition of a charged nanomechanical oscillator leads to perturbations of the electric potential experienced by the trapped ions and results in changes of the equilibrium position and oscillation frequencies of the ion [94]. Thus, matching of the frequencies of the ion and the oscillator needs to be dynamically adjusted when experimental parameters change. Furthermore, the fundamental strength of the mechanical coupling between an ion of mass m_{ion} and a nanomechanical oscillator of mass m_{osc} is directly proportional to $1/\sqrt{m_{\mathrm{ion}} m_{\mathrm{osc}}}$ [26, 84]. It is thus favorable to use nanomechanical oscillators with very low masses, such as carbon

nanotubes [111], or couple to charged particles of lower masses, such as electrons [26]. Another limiting factor for the coupling strength is the dissipation of the nanomechanical oscillator due to thermal coupling to the environment. In order to observe coherent exchange of quantum states between the systems and enter the *strong-coupling regime* [26], the nanocantilever should be cryogenically cooled to very low temperatures [26, 84].

The objective of the work presented in this thesis was the experimental realization, demonstration and characterization of the coupling between trapped ions and a nanomechanical oscillator. We aimed to demonstrate the coupling by exciting the motion of trapped $^{40}Ca^{+}$ ions with the *mechanically* driven motion of a Ag_2Ga nanocantilever in order to provide a proof-of-principle for the feasibility of such a hybrid system with possible applications for quantum technologies [81]. Ultimately, the goal is to achieve strong coupling [26] and a bidirectional transfer of motional states between the two systems on the quantum level [80, 84]. Applications of such a hybrid system include the sympathetic cooling as well as the bidirectional quantum state engineering, sensing and readout of its constituents [84, 97].

In this thesis, we present new studies and results obtained with the ion-nanowire hybrid system designed by Panagiotis Fountas [80]. We discuss an extended and more generalized theoretical description of the classical coupled dynamics of the system and report theoretical predictions for the coupling strength under consideration of a relative ion-nanowire position in three dimensions. For the first time, a hybrid system coupling trapped ions to a charged nanocantilever was successfully demonstrated in the classical regime. The static effects of the charged nanomechanical oscillator on the trapping potential experienced by the ions were experimentally investigated and compared to the theory. The trapped $^{40}Ca^{+}$ ions were successfully coupled to and their motion resonantly excited by the mechanically driven Ag_2Ga nanocantilever. The strength of the coupling was experimentally studied in the classical regime for the variation of different coupling parameters and compared to the theoretical predictions.

The experimental results reported in this thesis were limited to the study of the ion-nanowire hybrid system in the classical regime. No quantum dynamics of this new system were yet experimentally investigated. However, the results provide a proof-of-principle for the mechanical manipulation of trapped ions by a nanomechanical oscillator and lay the foundation for future experiments. By eventually bringing the hybrid system into the quantum regime, we aim to contribute to the development of new techniques for the manipulation of quantum systems and possible applications for quantum technologies. With this in mind, this novel system provides a playground for the study of a variety of applications in future research, e. g., the direct mechanical manipulation of single ions, the manipulation of internal modes of ion strings and Coulomb crystals, or the bidirectional transmission of quantum information.

1.1 Outline of the Thesis

In the following chapters 2 to 5, we introduce the theoretical background and formulas describing the physical concepts, phenomena and experimental applications mentioned throughout the remainder of the thesis. The topics covered are the theory of ion trapping, interaction of light with a two-level system, laser cooling and nanomechanics.

The theoretical background is followed by an overview of the experimental setup and the applied experimental techniques in chapters 6 and 7. These chapters aim to provide a detailed overview of the individual parts of the experimental setup and describe the crucial experimental techniques used to obtain the experimental results presented in this thesis, such as the optomechanical readout of the resonances of the nanomechanical oscillator and the photon-correlation method.

Chapter 8 shows simulations of the electric potentials generated by the ion trap. The simulations were performed with the finite-element method in Comsol Multiphysics [112]. The chapter describes the use of potential basis functions for the simulations and provides an overview of the generated potentials for different trap geometries and different configurations of the applied voltages. It further shows the effects and contributions of the nanowire to the total potential.

We provide a detailed description of the ion-nanowire interaction model in the classical regime, as well as supporting results obtained from numerical simulations in chapters 9 and 10. The model describing the electrostatic interaction between the ion and the nanowire [80] was extended and generalized for arbitrary positions of the nanowire as well as the possibility of coupled motion of trapped ions along different directions of oscillation. This extension yielded additional insights into the coupling strength of the resonantly driven ions. The findings were supported and confirmed by numerical simulations of molecular dynamics.

The central experimental results of this thesis are presented in chapter 11. We discuss and present measurements of the excess micromotion of trapped ions obtained with the photon-correlation method. We show the electrostatic effect of the nanowire on the trapping potential by measuring the shift of the axial frequency of the ions for different nanowire positions and applied static voltages and find good agreement to the theoretical model. We experimentally demonstrate the resonant drive of trapped ions by the vibrating nanowire. We show the mechanical nature of the interaction by correlation of the resulting velocity amplitudes of the ions to the mechanical spectrum of the nanowire. We further show the changes of the coupling strength and resonantly driven ion motion for the variation of different coupling parameters, such as the oscillation amplitude of the nanowire, the ion-nanowire distance and the applied static voltage.

Lastly, we conclude the thesis in chapter 12. Here, we summarize the central results of the

work presented in this thesis and give an outlook on future prospects. We discuss limitations of the experimental setup as well as the progress made over the course of this project and provide suggestions for additional improvements, future applications and experiments.

2 Theory of Ion Trapping

2.1 Earnshaw's Theorem

The trapping of positively charged particles with purely electric fields requires the simultaneous generation of effective potential minima along all directions x, y, z in a single point. Earnshaw's theorem, however, states that such fields cannot be generated with *static* electric fields alone [33].

An instructive example is the desired generation of a three-dimensional harmonic trapping potential $\Phi(x,y,z) = \frac{\Phi_0}{2d^2}(Ax^2 + By^2 + Cz^2) + \Phi_{\text{offset}}$ with real coefficients $A, B, C \in \mathbb{R}$. Φ_0 is the potential difference between electrodes in a given geometry with some characteristic distance d. Φ_{offset} is a constant offset to the potential that might be required to accurately represent the applied voltages. In the following discussions, we will omit Φ_{offset} for clarity as it has no influence on the dynamics of the system.

Any electric potential in charge-free space needs to satisfy Laplace's equation $\Delta\Phi = 0$, which directly follows from Maxwell's equations [113], thus:

$$\begin{aligned} \Delta\Phi &= 0, \\ \Leftrightarrow \frac{\partial^2}{\partial x^2}\Phi + \frac{\partial^2}{\partial y^2}\Phi + \frac{\partial^2}{\partial z^2}\Phi &= 0, \\ \Leftrightarrow A + B + C &= 0. \end{aligned} \tag{2.1}$$

The parameters A, B and C describe the curvature of the electric potential they represent. For simplicity and relevance with regard to the theory of ion trapping in radiofrequency traps, it is useful to consider the following two sets of parameters satisfying equation 2.1:

$$\begin{aligned} A = B &= -\frac{1}{2}C, \\ C &\neq 0, \\ \Rightarrow \Phi(x,y,z) &= \frac{\Phi_0}{2d^2}(2z^2 - y^2 - x^2) \\ &= \frac{\Phi_0}{2d^2}(2z^2 - r^2). \end{aligned} \tag{2.2}$$

$$\begin{aligned} A &= -B, \\ C &= 0, \\ \Rightarrow \Phi(x,y) &= \frac{\Phi_0}{2r_0^2}(x^2 - y^2). \end{aligned} \tag{2.3}$$

Equation 2.2 corresponds to an electric potential with cylindrical symmetry around the z-axis. Due to this, it can be expressed in terms of a radial coordinate $r^2 = x^2 + y^2$. It exhibits a

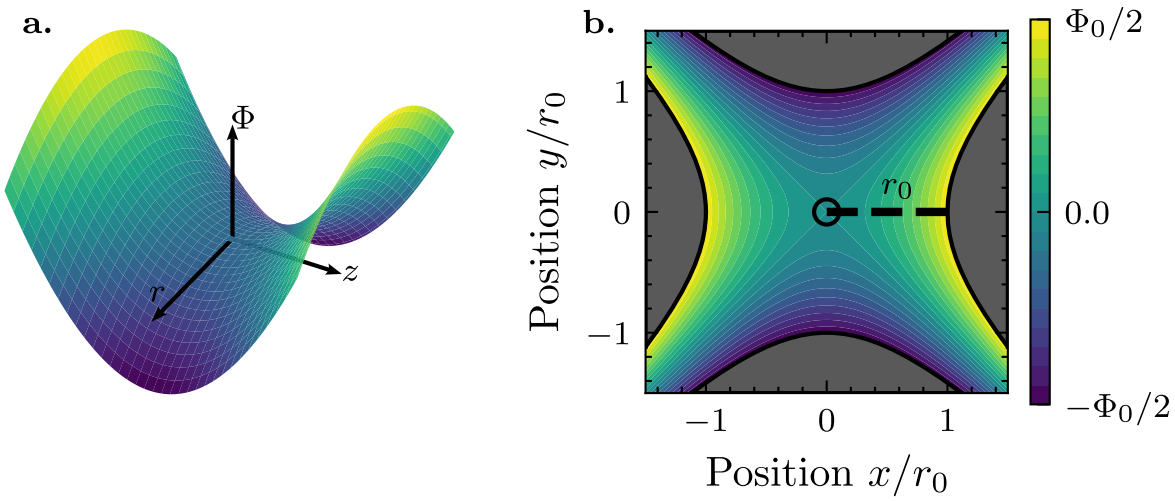

Figure 2.1: Generation of cylindrically symmetric and quadrupolar trapping potentials. **a**, Potential $\Phi = \frac{\Phi_0}{2d^2}(2z^2 - r^2)$ with $r^2 = x^2 + y^2$. The potential is cylindrically symmetric around the z-axis and exhibits a saddle point at the origin. **b**, Radial plane of a quadrupolar potential $\Phi = \frac{\Phi_0}{2r_0^2}(x^2 - y^2)$. The potential is generated with four hyperbolically shaped electrodes (dark gray) set to $\pm\Phi_0/2$. r_0 is the characteristic center-to-electrode distance of the geometry.

three-dimensional saddle point at the origin $\vec{x} = (0, 0, 0)$ as shown in figure 2.1a. Equation 2.3 corresponds to a quadrupolar electric potential without a gradient along the z-direction ($\frac{\partial}{\partial z}\Phi = 0$). Figure 2.1b shows the radial plane of the quadrupolar potential with its characteristic distance r_0.

In accordance with Earnshaw's theorem, stable trapping of charged particles is impossible in either of the static electric potentials described by equations 2.2 and 2.3, as the parameters A, B and C cannot have the same sign simultaneously.

As will become clear in the following chapters, however, the addition of *dynamic*, time-dependent electric potentials can enable the effective trapping and tight spatial confinement of charged particles [33].

2.2 The Ideal Paul Trap

The ideal Paul Trap generates a cylindrically symmetric trapping potential in its center. The total electric potential $\Phi(\vec{x}, t)$ is comprised of a static potential $\Phi_{\mathrm{DC}}(\vec{x})$ and a periodically time-dependent potential $\Phi_{\mathrm{RF}}(\vec{x}, t)$. Both terms of $\Phi(\vec{x}, t)$ are described by equation 2.2 to ensure full cylindrical symmetry around the z-axis:

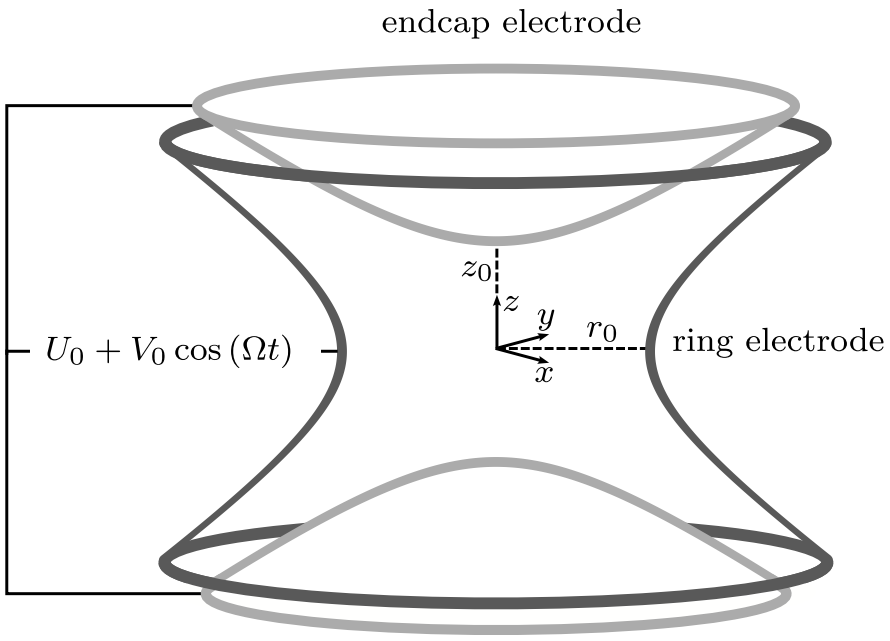

Figure 2.2: Design of the ideal Paul trap. The original design consists of a *ring electrode* (dark gray) and two *endcap electrodes* (light gray) with applied static and time-dependent voltages $U_0 + V_0 \cos(\Omega t)$. The electrodes exhibit a hyperbolic shape to ensure the generation of the desired potential in the center of the trap. The center-to-electrode distances are typically related via $r_0 = \sqrt{2} z_0$.

$$\begin{aligned}\Phi(\vec{x}, t) &= \Phi_{\mathrm{DC}}(\vec{x}) + \Phi_{\mathrm{RF}}(\vec{x}, t) \\ &= \frac{QU_0}{2d^2}(2z^2 - y^2 - x^2) + \frac{QV_0 \cos(\Omega t)}{2d^2}(2z^2 - y^2 - x^2) \\ &= \frac{Q}{2d^2}(U_0 + V_0 \cos(\Omega t))(2z^2 - y^2 - x^2).\end{aligned} \tag{2.4}$$

$U_0 + V_0 \cos(\Omega t)$ is the time-dependent voltage difference applied to the trap electrodes. The radiofrequency (RF) potential oscillates at the angular frequency Ω. $d = \sqrt{\frac{1}{2} r_0^2 + z_0^2}$ is a characteristic distance of the trap geometry, defined by the radial and axial center-to-electrode distances r_0 and z_0. Figure 2.2 shows the design of an ideal Paul trap with hyperbolically shaped electrodes.

In order for Laplace's equation $\Delta\Phi = 0$ to hold true at all times t, it needs to be satisfied by Φ_{DC} and Φ_{RF} in equation 2.4 individually [32].

2.2.1 The Mathieu Equations

Following classical Newtonian mechanics, the equations of motion described by the ideal Paul trap potential $\Phi(\vec{x}, t)$ given in equation 2.4 result in equations of the Mathieu type [114, 115].

For a single particle of mass m, $\frac{\mathrm{d}^2 x_i}{\mathrm{d}t^2} = -\frac{1}{m}\frac{\partial \Phi}{\partial x_i}$ yields three independent equations of mo-

tion:

$$\begin{aligned}
\frac{\mathrm{d}^2x}{\mathrm{d}t^2} &= \frac{Q}{md^2}(U_0 + V_0\cos(\Omega t))x, \\
\frac{\mathrm{d}^2y}{\mathrm{d}t^2} &= \frac{Q}{md^2}(U_0 + V_0\cos(\Omega t))y, \\
\frac{\mathrm{d}^2z}{\mathrm{d}t^2} &= -\frac{2Q}{md^2}(U_0 + V_0\cos(\Omega t))z.
\end{aligned} \tag{2.5}$$

Substituting $t \to \frac{2}{\Omega}\tau$ ($\mathrm{d}t \to \frac{2}{\Omega}\mathrm{d}\tau$) and rearranging equation 2.5 leads to:

$$\begin{aligned}
\frac{\mathrm{d}^2x}{\mathrm{d}\tau^2} &= \left(\frac{4QU_0}{md^2\Omega^2} + 2\frac{2QV_0}{md^2\Omega^2}\cos(2\tau)\right)x, \\
\frac{\mathrm{d}^2y}{\mathrm{d}\tau^2} &= \left(\frac{4QU_0}{md^2\Omega^2} + 2\frac{2QV_0}{md^2\Omega^2}\cos(2\tau)\right)y, \\
\frac{\mathrm{d}^2z}{\mathrm{d}\tau^2} &= -\left(\frac{8QU_0}{md^2\Omega^2} + 2\frac{4QV_0}{md^2\Omega^2}\cos(2\tau)\right)z.
\end{aligned} \tag{2.6}$$

By introducing the dimensionless parameters

$$\begin{aligned}
a_x &= -\frac{4QU_0}{md^2\Omega^2}, \\
a_y &= -\frac{4QU_0}{md^2\Omega^2}, \\
a_z &= \frac{8QU_0}{md^2\Omega^2}, \\
q_x &= \frac{2QV_0}{md^2\Omega^2}, \\
q_y &= \frac{2QV_0}{md^2\Omega^2}, \\
q_z &= -\frac{4QV_0}{md^2\Omega^2},
\end{aligned} \tag{2.7}$$

the equations of motion 2.6 for each direction x_i can be identified as Mathieu equations [114]:

$$\frac{\mathrm{d}^2x_i}{\mathrm{d}\tau^2} + (a_i - 2q_i\cos(2\tau))x_i = 0. \tag{2.8}$$

Note how the a_i and q_i parameters describe the static and dynamic parts of the total trapping potential $\Phi(\vec{x}, t)$ given by equation 2.4, respectively. They individually satisfy Laplace's equation 2.1 such that $a_x + a_y + a_z = 0$ and $q_x + q_y + q_z = 0$ [32].

2.3 The Adiabatic Approximation

The Mathieu equations 2.8 can be solved analytically by an infinite sum exhibiting recursive coefficients in a continued fraction expression [32, 115, 116]. However, for all practical purposes in ion trapping experiments presented in this thesis, the motion of trapped ions will be described by the *adiabatic approximation* in which the continued fraction is truncated early on due to quickly decreasing coefficients [32, 33].

In the adiabatic approximation, it is assumed that the spatial amplitude of the inhomogeneous oscillating electric field $\vec{E}(\vec{x},t)$ of $\Phi(\vec{x},t)$ is nearly constant over the extension of the ion micromotion [33]. This approximation is valid for strongly cooled ions with low oscillation amplitudes and requires low a_i and q_i parameters satisfying $|q_i| \lesssim 0.4$ and $|a_i| \ll |q_i|$ [117].

The *stability parameters* β_i for each direction are given by [118]:

$$\beta_i = \sqrt{a_i + \frac{q_i^2}{2}}. \tag{2.9}$$

The solutions to the Mathieu equations 2.8 of trapped ions in the adiabatic approximation are found to be two superimposed oscillations [118]:

$$x_i(t) = x_{0,i} \cos(\omega_i t) \left(1 - \frac{q_i}{2} \cos(\Omega t)\right). \tag{2.10}$$

The total motion in one direction consists of slower oscillations at angular frequency $\omega_i = \frac{\beta_i}{2}\Omega$ called *secular motion* or *macromotion* and a superimposed, faster *micromotion* at the applied radiofrequency $\Omega \gg \omega_i$. The secular motion and micromotion amplitudes are given by $x_{0,i}$ and $x_{0,i}\frac{q_i}{2}$, respectively. A possible phase φ_i has been omitted for clarity. Fig. 2.3 shows example trajectories of equation 2.10 for different parameter pairs (a_i, q_i).

The micromotion of trapped ions is inherently *driven* motion [119] induced by the oscillating radiofrequency potential Φ_{RF}. It can be minimized [120], but is unavoidable in a direction of motion x_i if a radiofrequency component $q_i \neq 0$ exists. However, in the case of $q_i = 0$ the ion trajectory 2.10 as well as the respective equation of motion 2.8 are reduced to a simple harmonic oscillator [121] without any superimposed micromotion.

2.4 Linear Radiofrequency Traps

Linear radiofrequency traps or *linear Paul traps* are cylindrically symmetric ion traps designed to generate quadrupolar radiofrequency potentials $\Phi_{\mathrm{RF}}(\vec{x},t) = \frac{\Phi_0}{2r_0^2}(x^2 - y^2)\cos(\Omega t)$ with vanishing gradient $\frac{\partial}{\partial z}\Phi_{\mathrm{RF}} = 0$ along the axial z-direction. The advantage of this type of potential

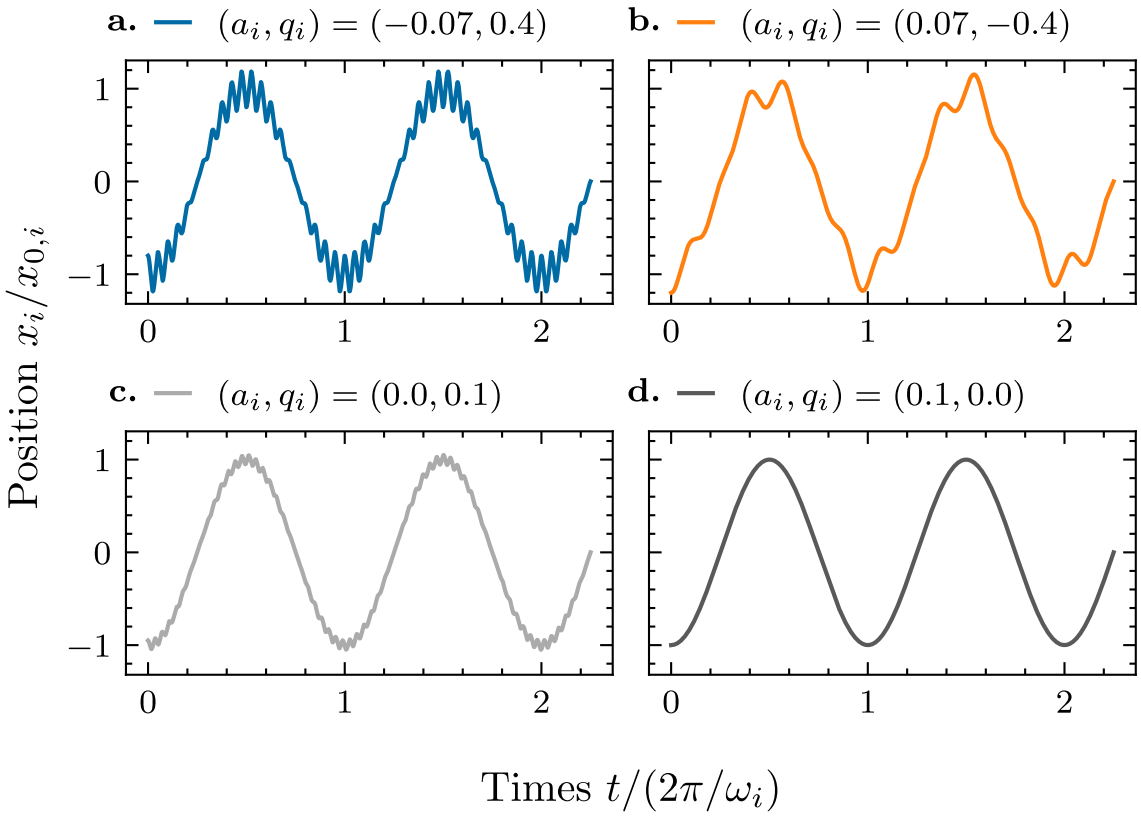

Figure 2.3: Trapped ion trajectories for different pairs of (a_i, q_i) parameters. **a**, High $|q_i|$ parameters correspond to high amplitudes of micromotion superimposed on the slower secular motion. **b**, Some pairs (a_i, q_i) lead to high frequencies of secular motion $\omega_i/\Omega = (\sqrt{a_i + q_i^2/2})/2$ compared to the driven radiofrequency. In the shown trajectory, a single oscillation of secular motion encompasses only five full RF oscillations. **c**, Stable trapping in one direction can be achieved without any static potential component ($a_i = 0$). Low $|q_i|$ parameters translate to low oscillation amplitudes of micromotion. **d**, $q_i = 0$ reduces the motion to a simple harmonic oscillation at the secular-motion frequency ω_i.

is the absence of a radiofrequency component along a whole *RF null line* [42, 48] instead of only in a single point. This is particularly useful for the simultaneous trapping of several ions as they will inevitably occupy an extended trap volume due to their mutual Coulomb repulsion [42, 122].

The generation of a quadrupolar potential is approximately well achieved close to the trap center with RF electrodes of lengths l significantly larger than the radial dimension r_0 of the trap as shown in figure 2.4, i. e., $l \gg r_0$.

The total electric potential $\Phi(\vec{x}, t)$ of a linear radiofrequency trap is given by:

$$\begin{aligned}\Phi(\vec{x}, t) &= \Phi_{\mathrm{DC}}(\vec{x}) + \Phi_{\mathrm{RF}}(\vec{x}, t) \\ &= \kappa_a \frac{QU_0}{2z_0^2}(2z^2 - y^2 - x^2) + \kappa_q \frac{QV_0 \cos(\Omega t)}{2r_0^2}(x^2 - y^2).\end{aligned} \tag{2.11}$$

Here, κ_a and κ_q are geometric correction factors accounting for the deviation of the potential from the ideal case generated with hyperbolic electrodes [126–128]. The description of the mo-

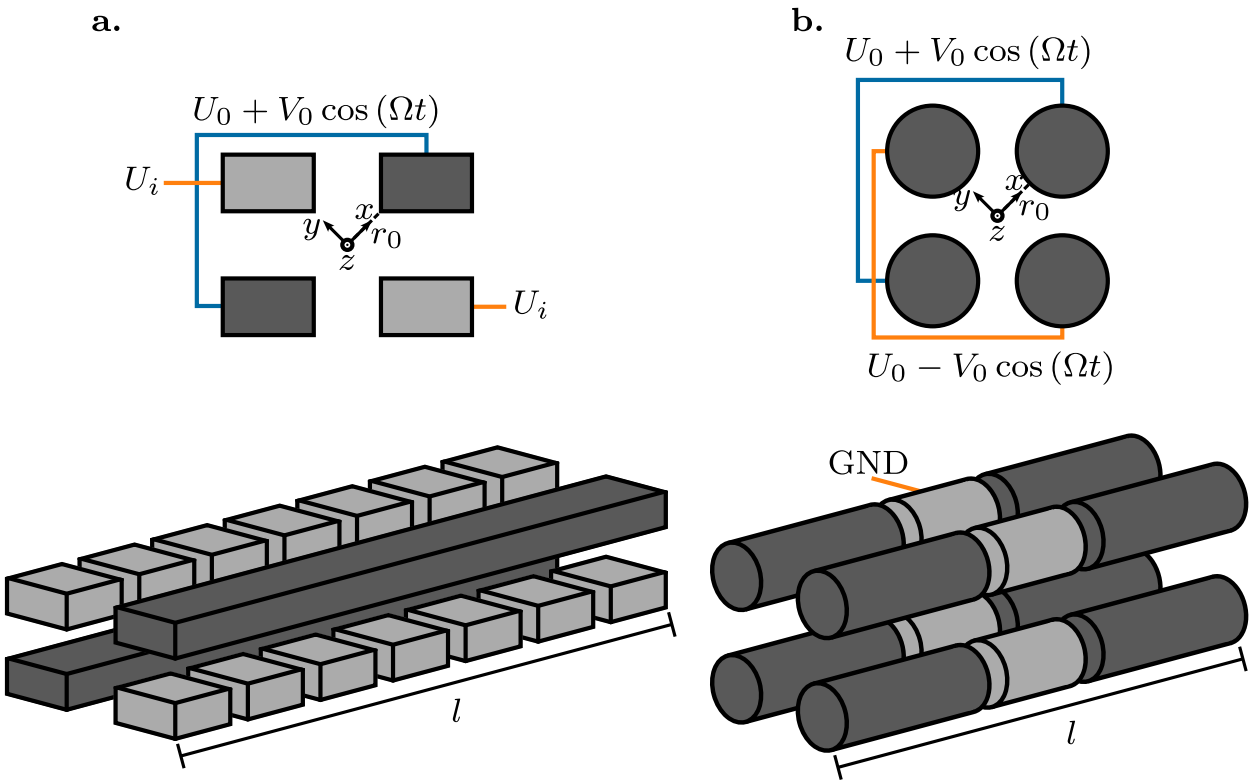

Figure 2.4: Examples of linear radiofrequency trap designs. **a**, Linear ion trap with electrodes of rectangular cross section. The two RF electrodes (dark gray) are operated with a single-phase RF voltage $V_0 \cos(\Omega t)$. Multiple DC electrodes (light gray) of static voltages U_i enable the trapping and shuttling of ions in multiple regions of the trap [123, 124]. The shown geometry corresponds to the trap used for the work presented in this thesis (see also chapter 6.1). **b**, Linear ion trap with cylindrical rod-electrode design. The RF electrode segments (dark gray) are operated with opposite-phase RF voltages $\pm V_0 \cos(\Omega t)$ and simultaneously act as the endcaps for static axial confinement by addition of a bias voltage U_0. The central DC electrodes (light gray) are typically grounded (GND). The common feature of all linear radiofrequency traps is the generation of quadrupolar radiofrequency potentials with high-aspect-ratio RF electrodes of lengths $l \gg r_0$. A variety of further linear trap designs and electric configurations exists [125].

tion of ions confined in linear radiofrequency traps is very similar to the ideal Paul trap shown in chapter 2.2 and will briefly be discussed in the following chapter 2.5. It is relevant to the work presented in this thesis as the trap used for the presented experimental and theoretical results was of a linear radiofrequency trap design.

2.5 The Mathieu Equations of Linear Radiofrequency Traps

Identifying the Mathieu equations of motion for the case of a linear radiofrequency trap is conceptually identical to chapter 2.2.1. The main difference lies in the generation of a *quadrupolar* time-dependent potential without gradient in the z-direction, given by equation 2.3. This leads to $q_x = -q_y$ and $q_z = 0$, satisfying Laplace's equation 2.1.

Following chapter 2.2.1, the a_i and q_i parameters for a linear ion trap are found to be:

$$
\begin{aligned}
a_x &= -\kappa_a \frac{4QU_0}{mz_0^2\Omega^2}, \\
a_y &= -\kappa_a \frac{4QU_0}{mz_0^2\Omega^2}, \\
a_z &= \kappa_a \frac{8QU_0}{mz_0^2\Omega^2}, \\
q_x &= -\kappa_q \frac{2QV_0}{mr_0^2\Omega^2}, \\
q_y &= \kappa_q \frac{2QV_0}{mr_0^2\Omega^2}, \\
q_z &= 0.
\end{aligned}
\tag{2.12}
$$

The equations of motion can be rewritten in the form of Mathieu equations [114]:

$$
\frac{\mathrm{d}^2 x_i}{\mathrm{d}\tau^2} + (a_i - 2q_i \cos(2\tau))x_i = 0. \tag{2.13}
$$

The solutions to equation 2.13 in the adiabatic approximation are identical to equation 2.10 [118]:

$$
x_i(t) = x_{0,i} \cos(\omega_i t) \left(1 - \frac{q_i}{2} \cos(\Omega t)\right). \tag{2.14}
$$

However, the specific definitions of the a_i and q_i parameters in equation 2.12 lead to different ion trajectories compared to the ideal Paul trap parameters given in equation 2.7. Notably, $q_z = 0$ reduces the equation of motion in z-direction to a simple harmonic oscillator [121] without superimposed micromotion:

$$
\begin{aligned}
&\frac{\mathrm{d}^2 z}{\mathrm{d}\tau^2} + a_z z = 0, \\
\Leftrightarrow &\frac{\mathrm{d}^2 z}{\mathrm{d}t^2} + \frac{\Omega^2}{4} a_z z = 0.
\end{aligned}
\tag{2.15}
$$

The respective trajectory is shown in figure 2.3d. By resubstitution of $\mathrm{d}\tau \rightarrow \frac{\Omega}{2}\mathrm{d}t$ in the second line of equation 2.15, we can identify the motion of a particle along the symmetry axis z as a harmonic oscillator of angular frequency ω_z given by:

$$
\omega_z = \sqrt{\frac{\Omega^2}{4} a_z} = \sqrt{\kappa_a \frac{2QU_0}{mz_0^2}}. \tag{2.16}
$$

The absence of a radiofrequency component q_z along the axial z-direction makes linear radiofrequency traps the typical choice for a variety of modern ion trapping experiments and applications [33, 125]. Several ions can be trapped and individually addressed in *ion strings* or *ion chains* along the micromotion-free z-axis for a variety of applications [21, 122, 129].

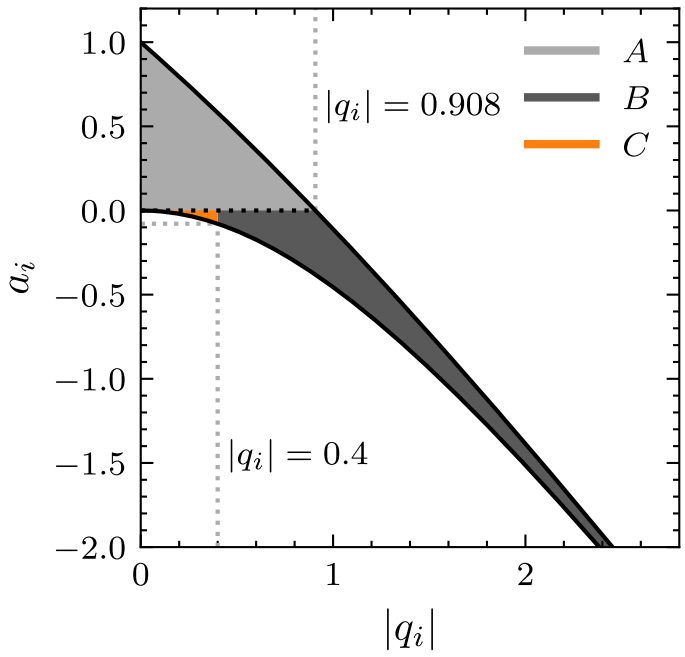

Figure 2.5: Fundamental stability region in the a_iq_i-plane for a single ion confined in a radiofrequency trap. Regions of bound and unbound solutions of the Mathieu equations 2.13 for any individual direction $i \in \{x, y, z\}$ are separated by the black curves [130]. Stable solutions are given by points (a_i, q_i) within the colored domains A, B, C. However, stable trapping along the z-axis in *linear traps* with $q_z = 0$ requires $a_z > 0$ and thus $a_r < 0$ ($r \in \{x, y\}$) to satisfy Laplace's equation. This limits the solutions of simultaneous *three-dimensional* confinement for the radial parameters a_r and q_r to the domains B and C. Solutions satisfying the adiabatic approximation are further limited to domain C with $|q_r| < 0.4$ and $0 > a_r \gtrsim -0.078$.

2.6 The Stability Diagram of a Radiofrequency Trap

Stable trapping of ions in radiofrequency traps is not a given for arbitrary values of the a_i and q_i parameters. There are distinct *stability regions* in the a_iq_i-plane in which ions remain confined due to bound solutions of the Mathieu equations 2.13 [115, 130]. For any other pairs (a_i, q_i) the ions follow unbound trajectories and are eventually emitted from the trap. Figure 2.5 shows the *fundamental stability region* [131] in the a_iq_i-plane for a single ion confined in a radiofrequency trap [132]. Typically, ion trapping is performed within this stability region which also includes the conditions for the adiabatic approximation [33] (see chapter 2.3).

2.7 The Pseudopotential Approximation

The trapping potential experienced by ions in the adiabatic approximation can be simplified by an effective harmonic *pseudopotential* given by [33]:

$$\Phi_{\text{pseudo}} = \frac{1}{2} m(\omega_x^2 x^2 + \omega_y^2 y^2 + \omega_z^2 z^2). \tag{2.17}$$

While equation 2.17 does not satisfy Laplace's equation $\Delta\Phi = 0$, it approximates the oscillations of trapped ions entirely by their secular motion at angular frequencies ω_i. This *pseudopotential*

approximation offers a picture of the ion dynamics in which the small superimposed micromotion oscillations are averaged out and the ion follows a corresponding secular motion trajectory $\vec{x}_0(t)$ smoothly. The secular motion angular frequencies are given by [118]:

$$\omega_i = \frac{\beta_i}{2}\Omega = \sqrt{a_i + \frac{q_i^2}{2}}\frac{\Omega}{2}. \tag{2.18}$$

In the following, we will demonstrate the validity of equation 2.17 [133].

Consider the electric field $\vec{E}_{\mathrm{RF}}(\vec{x},t)$ of a radiofrequency potential $\Phi_{\mathrm{RF}}(\vec{x},t)$ oscillating at angular frequency Ω:

$$\vec{E}_{\mathrm{RF}}(\vec{x},t) = \vec{E}_0(\vec{x})\cos(\Omega t) = -\frac{1}{Q}\vec{\nabla}\Phi_{\mathrm{RF}}. \tag{2.19}$$

$\vec{E}_0(\vec{x})$ is the position-dependent amplitude of the electric field, assumed to be nearly constant over the extension of the ion oscillations. Taylor expanding equation 2.19 to first order around the secular-motion position $\vec{x}_0$ yields:

$$\vec{E}_0(\vec{x})\cos(\Omega t) = \vec{E}_0\cos(\Omega t) + (\delta\vec{x}\vec{\nabla})[\vec{E}_0]\cos(\Omega t). \tag{2.20}$$

Here, $\delta\vec{x} = \vec{x} - \vec{x}_0$ and $\vec{E}_0$ is used to denote the electric field and its derivatives evaluated at $\vec{x} = \vec{x}_0$ specifically. This notation will be kept for the remainder of this chapter to allow better legibility.

In the adiabatic approximation we can assume the total ion trajectory $\vec{x}(t)$ to be well described by the superposition of two independent oscillations [133, 134]:

$$\vec{x}(t) = \vec{x}_0(t) + \delta\vec{x}(t) = \vec{x}_0(t) - \frac{Q\vec{E}_0}{m\Omega^2}\cos(\Omega t). \tag{2.21}$$

Equation 2.21 corresponds to the superposition of the secular motion $\vec{x}_0(t)$ and an added perturbation from the micromotion $\delta\vec{x}(t)$. The expression for $\delta\vec{x}(t)$ in equation 2.21 corresponds to the solution for an ion in a perfectly homogeneous oscillating electric field $\vec{E}_0\cos(\Omega t)$ with $\vec{E}_0 = \text{constant}$ [135].

Inserting $\delta\vec{x}(t)$ from equation 2.21 into equation 2.20 and time-averaging over one radiofrequency period $T_{\mathrm{RF}} = 2\pi/\Omega$ yields the time-averaged electric field $\langle\vec{E}_0\rangle$ experienced by the ion at position $\vec{x}_0$:

$$\begin{aligned}\langle \vec{E}_0 \rangle &= \langle \vec{E}_0 \cos(\Omega t) - \left(\frac{Q\vec{E}_0}{m\Omega^2} \vec{\nabla} \right) [\vec{E}_0] \cos^2(\Omega t) \rangle \\ &= -\frac{Q}{2m\Omega^2} (\vec{E}_0 \vec{\nabla})[\vec{E}_0].\end{aligned} \tag{2.22}$$

The *momentary* position $\vec{x}_0$ of the secular motion at any time t is assumed to remain nearly unchanged ($\vec{x}_0(t) = \vec{x}_0(t + T_{\mathrm{RF}}) = \text{constant}$) over the course of one RF period T_{RF} due to the significantly faster dynamics of the micromotion $\Omega \gg \omega_i$. The equation of motion for the secular motion $\vec{x}_0(t)$ is then governed entirely by the time-averaged force exerted from the electric field [133]:

$$m\ddot{\vec{x}}_0 = Q\langle \vec{E}_0 \rangle. \tag{2.23}$$

Considering $\vec{E} = -\frac{1}{Q}\vec{\nabla}\Phi$ and $\frac{\partial}{\partial x_i}[E^2(\vec{x})] = 2E(\vec{x})\frac{\partial}{\partial x_i}[E(\vec{x})]$, the time-averaged electric potential $\langle \Phi \rangle$ corresponding to equation 2.22 is found to be [133]:

$$\langle \Phi \rangle = \frac{Q^2}{4m\Omega^2} \vec{E}_0^2 = \frac{|\vec{\nabla}\Phi_{\mathrm{RF}}|^2}{4m\Omega^2}. \tag{2.24}$$

Note that the potential given by equation 2.24 is equivalent to the time-averaged kinetic energy $\langle E_{\mathrm{kin}} \rangle$ stored in the driven micromotion $\delta\vec{x}(t)$ of an ion [33, 42]:

$$\langle E_{\mathrm{kin}} \rangle = \frac{1}{2} m \langle \delta\dot{\vec{x}}^2 \rangle = \frac{1}{2} m \langle \left(\frac{Q\vec{E}_0}{m\Omega} \right)^2 \sin^2(\Omega t) \rangle = \frac{Q^2}{4m\Omega^2} \vec{E}_0^2. \tag{2.25}$$

Equation 2.24 allows the computation of a time-averaged effective pseudopotential $\langle \Phi \rangle$ for a given radiofrequency potential Φ_{RF}. It is particularly useful for the conversion of a numerically simulated RF potential to an effective static potential [80, 136] for the design of trap geometries and the analysis of trapping potentials [56, 137, 138]. Note that the charge Q of the trapped ion is already absorbed in the definition of the potential gradient $|\vec{\nabla}\Phi_{\mathrm{RF}}|^2 = Q^2\vec{E}_0^2$ in equation 2.24.

For a radiofrequency potential $\Phi_{\mathrm{RF}}(\vec{x}, t) = \frac{QV_0 \cos(\Omega t)}{2d^2}(2z^2 - y^2 - x^2)$ as in an ideal Paul trap (see equation 2.4), the resulting time-averaged pseudopotential following equation 2.24 is given by:

$$\Phi_{\mathrm{pseudo}} = \langle \Phi \rangle = \frac{Q^2 V_0^2}{4m\Omega^2 d^4}(4z^2 + y^2 + x^2). \tag{2.26}$$

Adding a static potential $\Phi_{\mathrm{DC}}(\vec{x}, t)$ as in equation 2.4, the total potential $\Phi = \Phi_{\mathrm{DC}} + \Phi_{\mathrm{RF}}$ in the pseudopotential approximation can be expressed as:

$$\Phi = \frac{QU_0}{2d^2}(2z^2 - y^2 - x^2) + \frac{Q^2V_0^2}{4m\Omega^2 d^4}(4z^2 + y^2 + x^2). \tag{2.27}$$

Following the definitions of the a_i and q_i parameters given in equation 2.7, equation 2.27 can be rewritten to:

$$\begin{aligned}\Phi &= \frac{1}{2}m\left(\left(a_x + \frac{q_x^2}{2}\right)\frac{\Omega^2}{4}x^2 + \left(a_y + \frac{q_y^2}{2}\right)\frac{\Omega^2}{4}y^2 + \left(a_z + \frac{q_z^2}{2}\right)\frac{\Omega^2}{4}z^2\right) \\ &= \frac{1}{2}m(\omega_x^2 x^2 + \omega_y^2 y^2 + \omega_z^2 z^2).\end{aligned} \tag{2.28}$$

The total pseudopotential in equation 2.28 derived directly from the time-averaged equation 2.24 is thus shown to be equivalent to the three-dimensional harmonic potential 2.17 with the definitions of ω_i given by equation 2.18. It is just as valid for linear radiofrequency traps with the definitions of the a_i and q_i parameters given in equation 2.12.

3 Light-Matter Interaction in a Two-Level System

The free evolution of a two-level state $\Psi(\vec{x},t)$ for an unperturbed Hamiltonian $\hat{H}_0 = \frac{\hat{p}^2}{2m}$ is given by:

$$\Psi(\vec{x},t) = c_\mathrm{g}(t)|\mathrm{g}\rangle e^{-i\omega_\mathrm{g}t} + c_\mathrm{e}(t)|\mathrm{e}\rangle e^{-i\omega_\mathrm{e}t}. \tag{3.1}$$

Without external forces, the two electronic states $|n\rangle$ remain decoupled and the populations $\rho_{nn}(t) = |c_n(t)|^2$ stay constant.

Using a semiclassical description for the interaction of light with a two-level system, the electromagnetic radiation of a laser can be described by a monochromatic oscillating electric field:

$$\vec{E}(\vec{x},t) = \vec{E}_0 \cos(\omega t). \tag{3.2}$$

The interaction of the two-level system with the oscillating electric field given by equation 3.2 is described by an interaction term $\hat{H}_\mathrm{IA}$ in the total Hamiltonian $\hat{H} = \hat{H}_0 + \hat{H}_\mathrm{IA}$ of the system. $\hat{H}_\mathrm{IA}$ corresponds to the energy of an electric dipole with charge e in the electric field given by [139]:

$$\hat{H}_\mathrm{IA} = e\hat{r}\vec{E}_0 \cos(\omega t). \tag{3.3}$$

Here, $\hat{r}$ is the electron position operator relative to the center of mass of the atomic two-level system [139]. The corresponding Schrödinger equation is given by:

$$i\hbar\frac{\partial}{\partial t}\Psi(\vec{x},t) = (\hat{H}_0 + \hat{H}_\mathrm{IA})\Psi(\vec{x},t). \tag{3.4}$$

Inserting equation 3.1 into the Schrödinger equation 3.4 yields two differential equations for $c_\mathrm{g}(t)$ and $c_\mathrm{e}(t)$ in the rotating-wave approximation [139]. The rotating-wave approximation neglects fast oscillating terms at $\omega+\omega_0 \approx 2\omega_0$. For details on the complete mathematics, see [139].:

$$\begin{aligned} i\dot{c}_\mathrm{g} &= c_\mathrm{e} e^{i(\omega-\omega_0)t\frac{\Omega_\mathrm{R}}{2}}, \\ i\dot{c}_\mathrm{e} &= c_\mathrm{g} e^{-i(\omega-\omega_0)t\frac{\Omega_\mathrm{R}}{2}}, \\ \Rightarrow \frac{\mathrm{d}^2 c_\mathrm{e}}{\mathrm{d}t^2} &= -i(\omega-\omega_0)\frac{\mathrm{d}c_\mathrm{e}}{\mathrm{d}t} - \left|\frac{\Omega_\mathrm{R}}{2}\right|^2 c_\mathrm{e}. \end{aligned} \tag{3.5}$$

Here, $\omega_0 = (E_\mathrm{e} - E_\mathrm{g})/\hbar$ is the angular frequency of the transition $|\mathrm{g}\rangle \leftrightarrow |\mathrm{e}\rangle$. ω is the angular frequency of the monochromatic light and Ω_R is the *Rabi frequency*. With a known solution for $|c_\mathrm{e}(t)|^2$, the population $|c_\mathrm{g}(t)|^2$ can be directly computed from the condition $|c_\mathrm{g}(t)|^2 = 1 - |c_\mathrm{e}(t)|^2$.

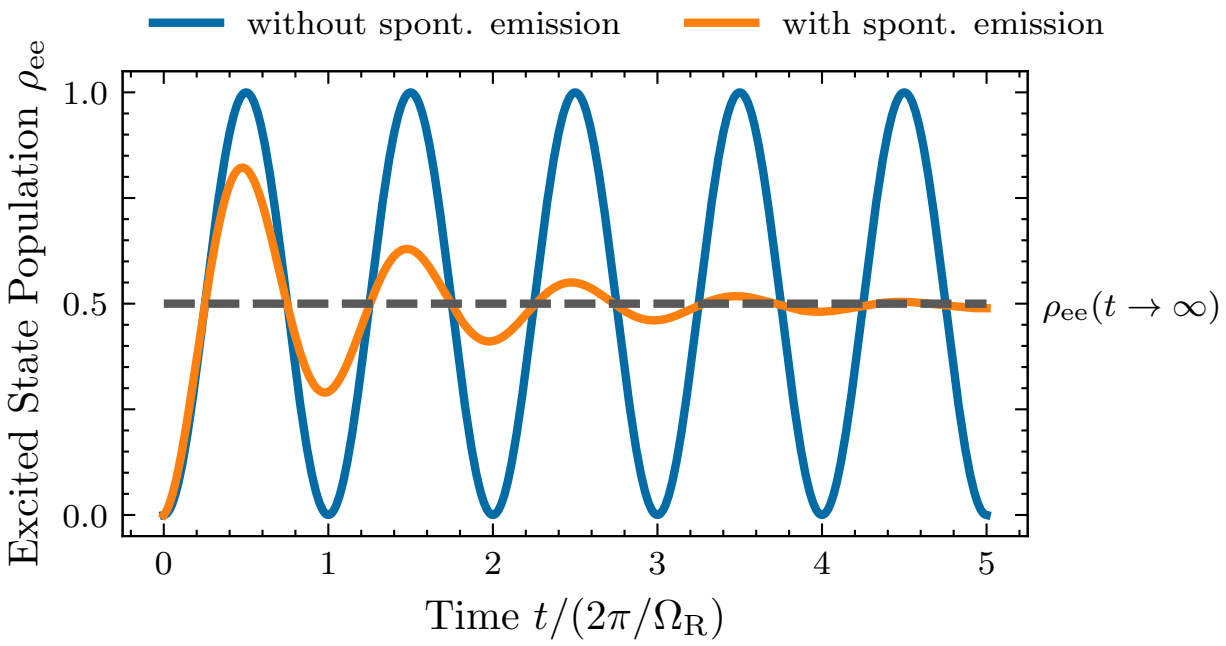

Figure 3.1: Dynamics of a two-level system under the influence of monochromatic radiation of energy $E = \hbar\omega_0$. The intensity of the light in the shown curves is $I = 100 I_{sat}$ at detuning $\delta_0 = 0$. Neglecting spontaneous emission, the state populations ρ_{nn} are periodically exchanged at the angular Rabi frequency Ω_R (blue curve). Including spontaneous emission at lifte time $\tau = 1/\Gamma$ yields damped oscillations reaching a steady-state population $\rho_{ee}(t \to \infty)$ (orange curve). For light of intensity $I \gg I_{sat}$, the limit of the steady-state population is $\rho_{ee} \to \frac{1}{2}$ (dashed gray line).

The solution to equation 3.5 for the excited state population $\rho_{ee}(t) = |c_e(t)|^2$ with initial conditions $\rho_{gg}(0) = 1$ and $\rho_{ee}(0) = 0$ is given by [139]:

$$\rho_{ee}(t) = \frac{\Omega_R^2}{\Omega_R^2 + \delta_0^2} \sin^2\left(\frac{\sqrt{\Omega_R^2 + \delta_0^2}\, t}{2}\right). \tag{3.6}$$

$\delta_0 = \omega - \omega_0$ is the detuning of the monochromatic light from the resonance of the transition at ω_0. For a detuning $\delta_0 = 0$, equation 3.6 simplifies to:

$$\rho_{ee}(t) = \sin^2\left(\frac{\Omega_R t}{2}\right). \tag{3.7}$$

Equation 3.7 shows that the populations ρ_{nn} of a two-level system can be periodically exchanged under the influence of near monochromatic light such as laser beams. The exchange rate between the two levels is given by the Rabi frequency Ω_R as shown in figure 3.1. Ω_R depends on properties of the electronic transition as well as the intensity I of the driving light:

$$\Omega_R^2 = \frac{1}{2}\frac{I}{I_{sat}}\Gamma^2. \tag{3.8}$$

I_{sat} is the *saturation intensity* of the electronic transition given by:

$$I_{\mathrm{sat}} = \frac{\hbar\omega_0^3}{12\pi c^2}\Gamma. \tag{3.9}$$

It is convenient to define the relative intensity parameter $s_0 = I/I_{\mathrm{sat}}$.

Note that the light-matter interaction described in this chapter does not yet include the mechanism of spontaneous emission. Spontaneous emission can be included as exponential decay at life time $\tau = 1/\Gamma$ in the differential equation for the excited state population ρ_{ee}:

$$\dot{\rho}_{\mathrm{ee}}(t) \to \dot{\rho}_{\mathrm{ee}}(t) - \Gamma\rho_{\mathrm{ee}}(t). \tag{3.10}$$

Equation 3.10 leads to steady-state solutions of the populations $\rho_{nn}(t)$ for $t \to \infty$ as shown in figure 3.1. This means that a two-level system interacting with monochromatic radiation will eventually reach a superposition state $|\Psi\rangle = c_{\mathrm{g}}|\mathrm{g}\rangle + c_{\mathrm{e}}|\mathrm{e}\rangle$ with constant populations ρ_{nn}.

The steady-state solution for the excited state at a detuning δ_0 is found to be [139]:

$$\begin{aligned}\rho_{\mathrm{ee}} &= \frac{1}{4}\frac{\Omega_{\mathrm{R}}^2}{\delta_0^2 + (\Omega_{\mathrm{R}}^2/2) + (\Gamma^2/4)} \\ &= \frac{1}{2}\frac{s_0}{1 + s_0 + 4\left(\frac{\delta_0}{\Gamma}\right)^2}.\end{aligned} \tag{3.11}$$

The steady-state population for a laser intensity of $I = I_{\mathrm{sat}}$ ($s_0 = 1$) is $\rho_{\mathrm{ee}} = \frac{1}{4}$. It reaches $\rho_{\mathrm{ee}} = \frac{1}{2}$ in the limit $I \to \infty$.

Ions laser-cooled on an electronic two-level transition of natural linewidth Γ quickly reach the steady-state distribution. The rate of spontaneously emitted photons R_{s} of laser-cooled ions is then directly proportional to the steady-state population of the excited state. It is given by [140]:

$$R_{\mathrm{s}} = \Gamma\rho_{\mathrm{ee}}. \tag{3.12}$$

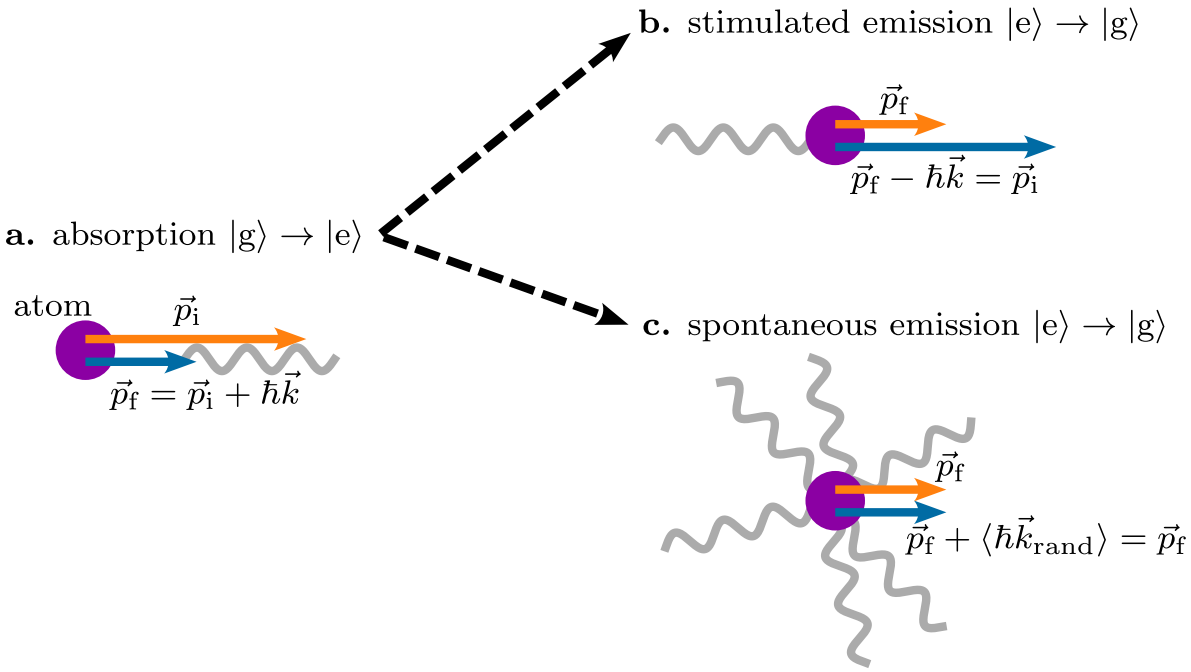

Figure 4.1: Photon absorption and emission processes used in laser cooling techniques. An atom at initial momentum $\vec{p}_\mathrm{i}$ interacts with an incoming laser field (light gray) with wave vector $\vec{k}$. **a**, The absorption of a single laser photon leads to a complete momentum transfer to the atom, leaving it with a changed momentum $\vec{p}_\mathrm{f} = \vec{p}_\mathrm{i} + \hbar\vec{k}$. After absorption, the atom can undergo two distinct emission events: **b**, The photon emitted from a stimulated emission event is coherent with the interacting laser field. The momentum of the atom is then completely recovered to $\vec{p}_\mathrm{i} = \vec{p}_\mathrm{f} - \hbar\vec{k}$. **c**, Spontaneously emitted photons are isotropically emitted in random directions. On average, the change of momentum over many cycles is $\langle\hbar\vec{k}_\mathrm{rand}\rangle = 0$ and the atom remains at $\vec{p}_\mathrm{f}$. If $\vec{k}\vec{v} < 0$, this process leads to a net cooling of the atom.

4 Laser Cooling Techniques

Laser cooling of atoms relies on the transfer of momentum during absorption and emission of photons of a laser beam [34]. The momentum carried by a single photon moving in direction of the wave vector $\vec{k}$ of the laser is given by:

$$\vec{p}_\mathrm{photon} = \hbar\vec{k}. \tag{4.1}$$

The absorption of a single photon on an electronic transition $|\mathrm{g}\rangle \rightarrow |\mathrm{e}\rangle$ leads to a complete transfer of $\vec{p}_\mathrm{photon}$ to the momentum of the particle as shown in figure 4.1. Denoting the initial and final momenta of the particle as $\vec{p}_\mathrm{i}$ and $\vec{p}_\mathrm{f}$, the momentum transfer is given by:

$$\vec{p}_\mathrm{i} \rightarrow \vec{p}_\mathrm{i} + \hbar\vec{k} = \vec{p}_\mathrm{f}. \tag{4.2}$$

Equation 4.2 corresponds to a decrease of the velocity $|\vec{v}|$ of the particle if it counter-propagates with respect to the laser beam ($\vec{k}\vec{v} < 0$). This corresponds to cooling of the particle by reducing its kinetic energy (and thus temperature) $E_\mathrm{kin} = \frac{1}{2}m|\vec{v}|^2 = \frac{3}{2}k_\mathrm{B}T$. Vice versa, absorption of a photon satisfying $\vec{k}\vec{v} > 0$ results in heating of the particle.

Subsequent photons of a continuous laser beam interacting with the now excited particle may lead to stimulated emission. The wave vector $\vec{k}$ of the emitted photon is identical to the incoming laser photons [35], restoring the particle back to its ground state $|\mathrm{e}\rangle \rightarrow |\mathrm{g}\rangle$ with its initial momentum:

$$\vec{p}_\mathrm{f} \rightarrow \vec{p}_\mathrm{f} - \hbar\vec{k} = \vec{p}_\mathrm{i}. \tag{4.3}$$

The repeated cycle of absorption and stimulated emission described by equations 4.2 and 4.3 does *not* lead to any net change in the momentum or kinetic energy of the particle. However, *spontaneous* emission may occur instead of stimulated emission. It results in the excited particle decaying back into its ground state $|\mathrm{e}\rangle \rightarrow |\mathrm{g}\rangle$ while emitting a photon in a random direction $\vec{k}_\mathrm{rand}$ [35]:

$$\vec{p}_\mathrm{f} \rightarrow \vec{p}_\mathrm{f} + \hbar\vec{k}_\mathrm{rand} \neq \vec{p}_\mathrm{i}. \tag{4.4}$$

Over many cycles of absorption followed by spontaneous emission, the random momentum transfers isotropically average out to zero, i. e., $\langle\hbar\vec{k}_\mathrm{rand}\rangle = \vec{0}$ [141, 142]. This leaves the particle with a net change of its momentum $\vec{p}_\mathrm{f} \neq \vec{p}_\mathrm{i}$, corresponding to an effective cooling of the particle if $|\vec{p}_\mathrm{f}| < |\vec{p}_\mathrm{i}|$.

The effective change of momentum per spontaneous emission event is $\Delta\vec{p} = \hbar\vec{k}$. Given a scattering rate R_s of spontaneously emitted photons, the radiation pressure force $\vec{F}_\mathrm{s}$ experienced by the particle is then given by [142]:

$$\vec{F}_s = R_s\hbar\vec{k}. \tag{4.5}$$

4.1 Doppler Cooling

Consider an ion moving at velocity $\vec{v}$ interacting with a laser beam of angular frequency ω_ℓ. The detuning δ_0 of the laser with respect to a two-level cooling transiton $|\mathrm{g}\rangle \leftrightarrow |\mathrm{e}\rangle$ at angular frequency ω_0 is given by $\delta_0 = \omega_\ell - \omega_0$. As shown in figure 4.2, the first-order Doppler shift leads to a velocity-dependent detuning $\delta(\vec{v})$ in the frame of reference of the ion [34]:

$$\delta(\vec{v}) = \delta_0 - \vec{k}\vec{v}. \tag{4.6}$$

The absorption of photons is maximized on resonance, i. e., at $\delta(\vec{v}) = 0$. In order to ensure

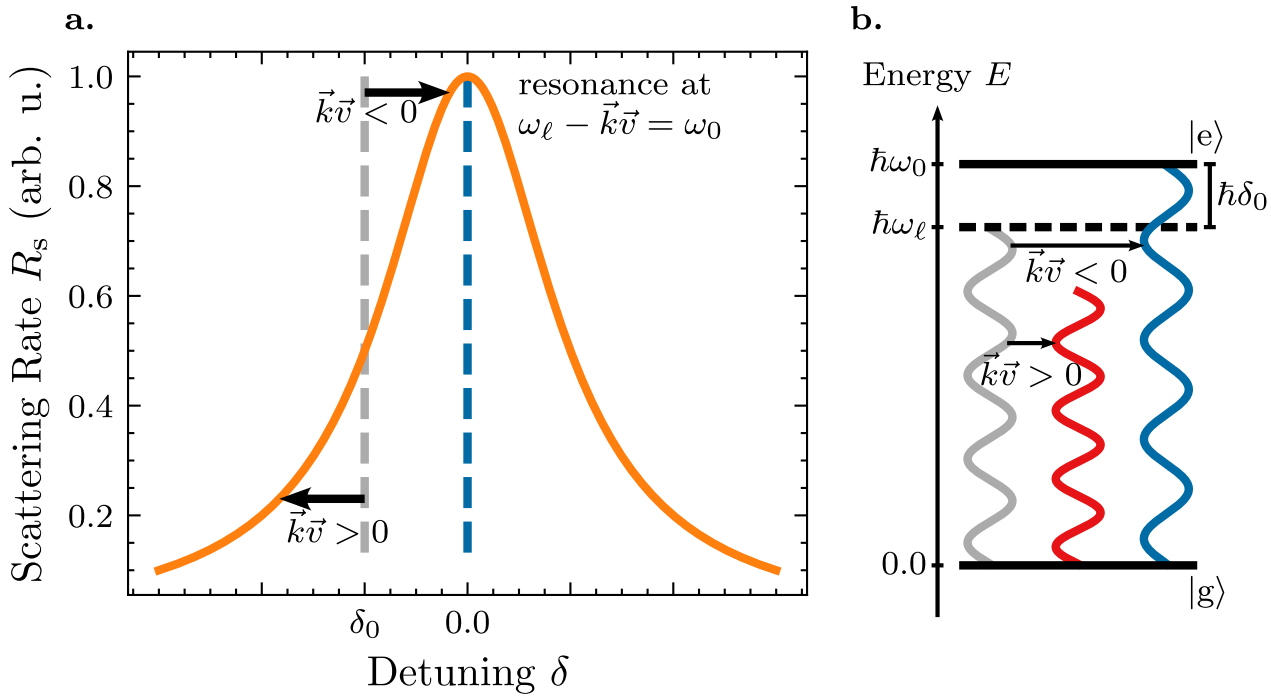

Figure 4.2: Doppler-shifted laser frequencies for the implementation of Doppler cooling. a, The detuning of a laser to an electronic transition frequency ω_0 in the laboratory frame is given by $\delta_0 = \omega_\ell - \omega_0$ (light gray line). The first order Doppler effect yields a velocity-dependent detuning $\delta(\vec{v}) = \delta_0 - \vec{k}\vec{v}$ experienced by an atom. Depending on the direction $\vec{v}$, the atom is shifted closer to or further away from resonance (blue line). The choice $\delta_0 < 0$ enhances the rate of scattered photons for $\vec{k}\vec{v} < 0$ and suppresses it for $\vec{k}\vec{v} > 0$, leading to effective cooling of the atom. **b**, In the frame of reference of the atom, a laser photon of energy $\hbar\omega_\ell$ (light gray) is red-shifted or blue-shifted according to the first order Doppler shift $\omega_\ell - \vec{k}\vec{v}$. Resonance to the transition $|g\rangle \leftrightarrow |e\rangle$ is obtained when $\vec{k}\vec{v} = \delta_0$.

cooling of the ion by the mechanism discussed in chapter 4, resonance should be obtained when $\vec{k}\vec{v} < 0$, i. e., when $\vec{k}$ and $\vec{v}$ are counter-propagating. This is achieved by choosing $\delta_0 < 0$, equivalent to red-detuning of the laser frequency with respect to the cooling transition [141], i. e., $\omega_\ell < \omega_0$. This technique is called *Doppler cooling*. As an additional consequence of $\delta_0 < 0$, an ion moving along the laser beam ($\vec{k}\vec{v} > 0$) shifts the total detuning $\delta(\vec{v})$ even further away from resonance, conveniently decreasing the probability of heating from the laser field.

The lowest temperature reachable by Doppler cooling of a particular transition $|g\rangle \leftrightarrow |e\rangle$ is given by the Doppler limit T_D [139, 141]:

$$T_D = \frac{\hbar\Gamma}{2k_B}, \tag{4.7}$$

where Γ is the natural linewidth of the transition. For the 397 nm cooling transition of $^{40}Ca^+$ used in the work presented in this thesis ($\Gamma = 132$ MHz [140]), the limit is:

$$T_D \approx 0.5 \text{ mK}. \tag{4.8}$$

Two counter-propagating cooling lasers with $\vec{k}_1 = -\vec{k}_2$ may be used along a given axis in order to ensure the particle experiences cooling from the interaction with either of the lasers [139, 143], i. e., $\vec{k}_1\vec{v} < 0$ or $\vec{k}_2\vec{v} < 0$ at all times. This is typically implemented for the Doppler cooling of neutral atoms [33, 143, 144]. However, in the case of ions confined in the harmonic potential of a radiofrequency trap, a single cooling laser is sufficient. This is due to the restoring force of the trapping potential, forcing ions to periodically counter-propagate with respect to the laser on their oscillatory motion [144, 145].

Ideally, cooling transitions are described by a two-level system $|\mathrm{g}\rangle \leftrightarrow |\mathrm{e}\rangle$. In reality, excited ions can often decay into some intermediate state $|\mathrm{i}\rangle$ at a certain branching ratio $\mathcal{B}$, as is the case for $^{40}Ca^+$ (see chapter 6.3). In order to reintroduce the ions back to the main cooling transition $|\mathrm{g}\rangle \leftrightarrow |\mathrm{e}\rangle$, a *repumper* laser is added to drive the $|\mathrm{i}\rangle \leftrightarrow |\mathrm{e}\rangle$ transition [141, 142, 146].

The cooling of *molecular* ions is particularly challenging due to the abundance of available transitions [42, 147]. It is often realized by indirect means such as sympathetic cooling in conjunction with trapped atomic ions [148, 149] or by direct cooling schemes of diatomic [150–152] and polyatomic [153, 154] molecular ions.

4.1.1 Doppler Cooling as a Continuous Friction Force

The cooling rate of a continuously laser-cooled particle is equal to its rate of spontaneously emitted photons. The particle will quickly reach the steady state population ρ_{ee} of the excited state $|\mathrm{e}\rangle$ given by equation 3.11. The resulting scattering rate R_{s} is given by [139]:

$$R_{\mathrm{s}}(\vec{v}) = \Gamma\rho_{\mathrm{ee}} = \frac{\Gamma}{2}\frac{s_0}{1 + s_0 + 4\left(\frac{\delta(\vec{v})}{\Gamma}\right)^2}. \tag{4.9}$$

Γ is the respective natural linewidth of the transition, $s_0 = I/I_{\mathrm{sat}}$ is the ratio of the laser intensity to the saturation intensity and $\delta(\vec{v}) = \omega_\ell - \omega_0 - \vec{k}\vec{v}$ is the total detuning experienced by the particle in a laser field of angular frequency ω_ℓ with the first-order Doppler shift given by $-\vec{k}\vec{v}$. The wave vector $\vec{k}$ has an absolute value of $|\vec{k}| = \frac{2\pi}{\lambda_0}$ with λ_0 being the wavelength of the laser. Note that a more general description of equation 4.9 includes the Zeeman shift in the presence of a magnetic field [140]. However, there is no relevant magnetic field present for the study of driven ion motion in this work.

For small particle velocities, as expected for laser cooled ions, equation 4.9 can be Taylor expanded around $\vec{v} = \vec{0}$ to first order to obtain [35, 80]:

$$
\begin{aligned}
R_{\mathrm{s}}(\vec{v}) &\approx R_{\mathrm{s}}(\vec{v}=\vec{0}) + \vec{\nabla} R_{\mathrm{s}}(\vec{v}=\vec{0})\vec{v} + ... \\
&= R_{\mathrm{s}}(\vec{v}=\vec{0}) + \frac{4\delta_0}{\Gamma} \frac{s_0}{\left(1 + s_0 + 4\left(\frac{\delta_0}{\Gamma}\right)^2\right)^2} \vec{k}\vec{v} \\
&= R_0 - \beta \vec{k}\vec{v}.
\end{aligned}
\tag{4.10}
$$

Note that $\delta(\vec{v})$ in equation 4.10 is evaluated at $\vec{v} = \vec{0}$, so $\delta_0 = \omega_\ell - \omega_0$. Considering $\delta_0 < 0$ to achieve Doppler cooling, equation 4.10 exhibits a constant scattering rate of $R_0 = R_{\mathrm{s}}(\vec{v} = \vec{0})$ and a linearly velocity-dependent scattering rate $-\beta\vec{k}\vec{v} = \frac{4\delta_0}{\Gamma_{12}} \frac{s_0}{(1+s_0+4(\frac{\delta_0}{\Gamma_{12}})^2)^2} \vec{k}\vec{v}$.

The resulting force on the particle is then computed from the exchanged momentum per scattered photon $\Delta\vec{p} = \hbar\vec{k}$:

$$
\vec{F}_s = \hbar\vec{k} R_0 - \beta\hbar\vec{k}(\vec{k}\vec{v}). \tag{4.11}
$$

Equation 4.11 consists of a constant radiation pressure force in direction $\vec{k}$ of the incoming laser beam as well as a velocity-dependent friction force. Note the order of operation in the second term of equation 4.11 as $(\vec{k}\vec{k})\vec{v} \neq \vec{k}(\vec{k}\vec{v})$. Often, a one-dimensional description is applicable in which $\vec{k}\vec{v} = k_i v_i$ in direction x_i. We can identify the damping factor γ due to the friction force as [35]:

$$
\gamma = \beta\hbar\vec{k}^2/m. \tag{4.12}
$$

Equation 4.11 offers a continuous, non-probabilistic model of Doppler cooling for molecular dynamics simulations described by cooling rates [140]. Its application in numerical simulations performed with the velocity Verlet algorithm is demonstrated in chapter 10.

4.1.2 Probabilistic State-to-State Doppler Cooling in a Two-Level System

The treatment of Doppler cooling in chapter 4.1.1 was concerned with the *average* ion dynamics described by continuous cooling rates. Here, we describe Doppler cooling by tracking individual photon absorption, emission and scattering events for each time step Δt of a numerical simulation [155]. These quantum processes are fundamentally probabilistic and the description presented here is useful for simulations in which the state-to-state behavior of cooled ions is of interest [140, 156].

In the case of a non-degenerate two level system such as the 397 nm cooling transition of $^{40}Ca^+$, the rate of absorption and stimulated emission in a continuous laser field is given by [140, 157]:

$$\gamma = \frac{\Gamma \Omega_{\mathrm{R}}^2}{4\delta(\vec{v})^2 + \Gamma^2}, \tag{4.13}$$

where $\delta(\vec{v}) = \omega_\ell - \omega_0 - \vec{k}\vec{v}$ is the total detuning including the first-order Doppler shift and Ω_{R} is the Rabi frequency given by equation 3.8.

Absorption and emission events cannot occur unconditionally, but only for particles in their ground state $|\mathrm{g}\rangle$ or excited state $|\mathrm{e}\rangle$, respectively. Considering sufficiently small time steps Δt satisfying $\gamma \Delta t \ll 1$ and $\Gamma \Delta t \ll 1$, probabilities for electronic transitions $|\mathrm{g}\rangle \leftrightarrow |\mathrm{e}\rangle$ per time step are sufficiently low to be evaluated at every time step individually [156, 157]. This allows to keep track of the electronic state of a Doppler-cooled particle.

For a particle in its ground state $|\mathrm{g}\rangle$, only absorption can occur. The probability of absorption per time step Δt is given by:

$$P(|\mathrm{g}\rangle \to |\mathrm{e}\rangle) = \gamma \Delta t. \tag{4.14}$$

For the implementation in numerical simulations, a random number $r \in [0, 1]$ needs to be generated for each time step Δt. The absorption event then occurs if $r \leq \gamma \Delta t$ [155]. In the event of occurrence, the particle changes its electronic state and gains the momentum of a single photon:

$$\begin{aligned} &|\mathrm{g}\rangle \to |\mathrm{e}\rangle, \\ &\vec{p} \to \vec{p} + \hbar\vec{k}. \end{aligned} \tag{4.15}$$

If $r > \gamma \Delta t$, the state and momentum of the particle remain unchanged.

For a particle in its excited state $|\mathrm{e}\rangle$, both stimulated emission and spontaneous emission can occur. The total probability of either of these events to happen in one time step Δt is given by their sum:

$$P(|\mathrm{e}\rangle \to |\mathrm{g}\rangle) = (\Gamma + \gamma)\Delta t. \tag{4.16}$$

Since equation 4.16 includes *both* possibilities of spontaneous and stimulated emission, it is necessary to distinguish them. In the case of an emission event, their relative probabilities are given by:

$$\begin{aligned} P_{\mathrm{spont}} &= \frac{\Gamma}{\Gamma + \gamma}, \\ P_{\mathrm{stim}} &= \frac{\gamma}{\Gamma + \gamma}. \end{aligned} \tag{4.17}$$

Note that $P_{\text{spont}} + P_{\text{stim}} = 1$. In addition to updating the state of the particle to its ground state $|\text{e}\rangle \rightarrow |\text{g}\rangle$, the particle experiences a change in momentum. For stimulated emission, this corresponds to a momentum change in the opposite direction of the incoming laser beam:

$$\vec{p} \rightarrow \vec{p} - \hbar\vec{k}. \tag{4.18}$$

For spontaneous emission, the momentum change occurs along a vector with random direction [155] and with amplitude $|\vec{k}_{\text{rand}}| = \frac{2\pi}{\lambda_0}$:

$$\vec{p} \rightarrow \vec{p} + \hbar\vec{k}_{\text{rand}}. \tag{4.19}$$

Generating a random vector $\vec{k}_{\text{rand}}$ in numerical simulations can be implemented by the generation of two random variables $u, v \in [0, 1]$. From those, the spherical coordinate angles $\phi \in [0, 2\pi]$ and $\theta \in [0, \pi]$ satisfying a uniform distribution on a sphere of radius $\frac{2\pi}{\lambda_0}$ can be computed via [155]:

$$\begin{aligned} & u, v \in [0, 1], \\ \Rightarrow & \phi = 2\pi u, \\ & \theta = \arccos(1 - 2v), \\ \Rightarrow \vec{k}_{\text{rand}} = & \frac{2\pi}{\lambda_0} \begin{pmatrix} \sin(\theta)\cos(\phi) \\ \sin(\theta)\sin(\phi) \\ \cos(\theta) \end{pmatrix}. \end{aligned} \tag{4.20}$$

4.2 The Lamb-Dicke Regime

The dynamics of the motional quantum states of a single trapped ion can be described by the Hamiltonian of a quantum harmonic oscillator (see appendix A.2). The extension z_n of the wave function of a motional state $|n\rangle$ in z-direction is given by [158]:

$$\begin{aligned} z_n &= \sqrt{\langle n|\hat{z}^2|n\rangle} \\ &= z_0\sqrt{2n+1} \\ &= \sqrt{\frac{\hbar}{2m\omega_z}(2n+1)}, \end{aligned} \tag{4.21}$$

where ω_z is the angular trapping frequency along z and $z_0 = \sqrt{\langle 0|\hat{z}^2|0\rangle} = \sqrt{\frac{\hbar}{2m\omega_z}}$ is the extension of the motional ground state $|0\rangle$. Here, we only consider the motion along z.

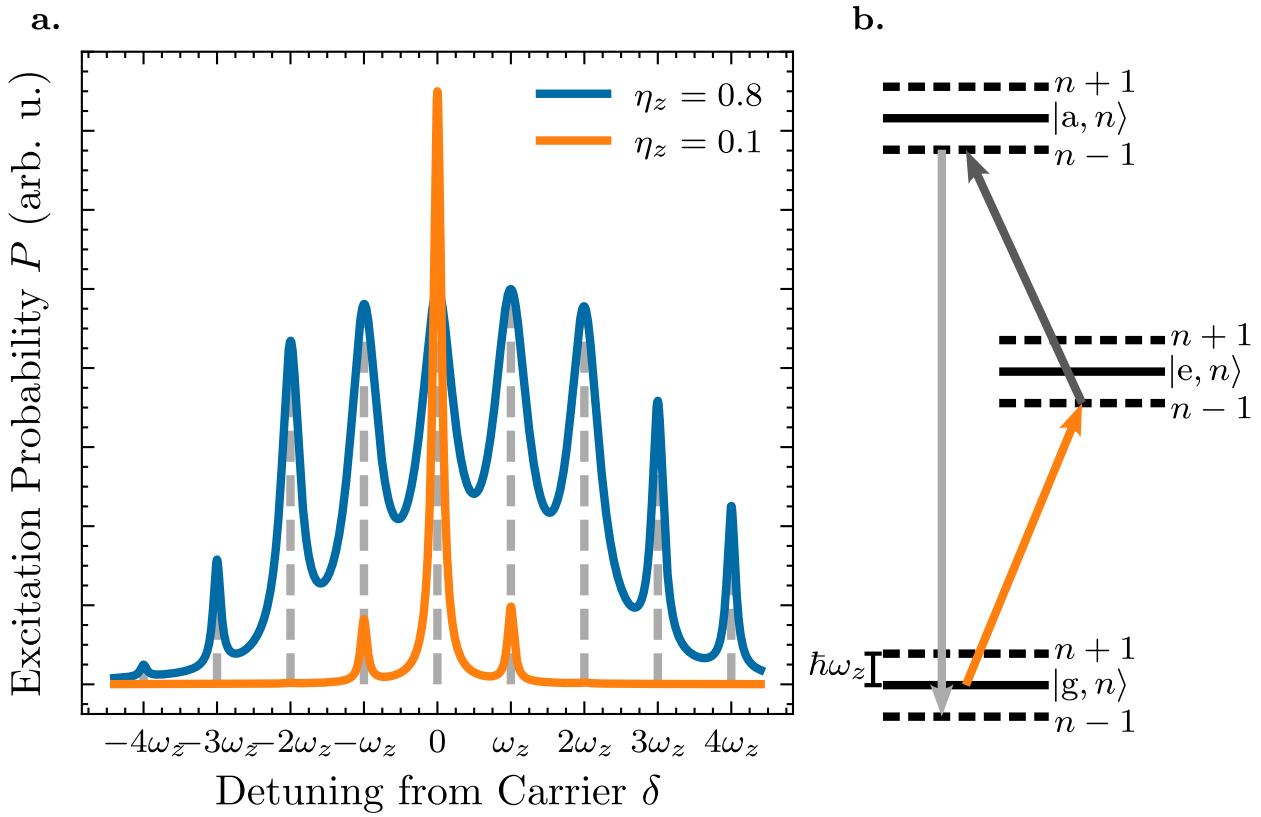

Figure 4.3: Resolved sideband transitions $|\mathrm{g}, n\rangle \leftrightarrow |\mathrm{e}, n \pm \Delta n\rangle$. **a**, The linewidth of the electronic transition yielding the shown excitation probabilities is $\Gamma = \omega_z/10$ at a motional state number $n = 5$. The Lamb-Dicke parameter $\eta_z < 1$ gives rise to resolved sidebands in the spectrum of the electronic transition. The sidebands occur at equally spaced frequencies $\omega_0 \pm k\omega_z$ ($k \in \mathbb{N}$, light gray lines) around the carrier frequency ω_0 at detuning $\delta = 0$ and can be addressed with a narrow laser. For $\eta_z = 0.8$ (blue), several broad sidebands are visible. For $\eta_z = 0.1$ (orange), the system approaches the Lamb-Dicke regime $\eta_z\sqrt{2n+1} \ll 1$ and only the first sidebands $|n\rangle \leftrightarrow |n \pm 1\rangle$ show a significant contribution. Furthermore, the carrier transition at ω_0 dominates the spectrum. **b**, Resolved sideband cooling is realized by addressing the $|\mathrm{g}, n\rangle \rightarrow |\mathrm{e}, n-1\rangle$ transition (orange) to lower the motional state number of a trapped ion. Subsequently pumping $|\mathrm{e}, n-1\rangle$ to a short-lived auxiliary state $|\mathrm{a}, n-1\rangle$ (dark gray) increases the efficiency of the cooling cycle. The ion eventually decays back into its ground state $|\mathrm{g}, n-1\rangle$ with a reduced motional quantum number (light gray).

For laser-cooled ions, the motional quantum state can be reduced to very low values of n. For an ion interacting with a monochromatic laser of wavelength λ, the *Lamb-Dicke parameter* η_z along z is defined as [33]:

$$\eta_z = k_z z_0 = k_z \sqrt{\frac{\hbar}{2m\omega_z}}, \tag{4.22}$$

where k_z is the projection of the wave vector $\vec{k}$ of the laser along z. Considering $k_z \propto \frac{2\pi}{\lambda}$, η_z can be interpreted as the oscillation amplitude of a trapped ion in its ground state relative to the wavelength of the interacting light.

$\eta_z < 1$ is a necessary condition to suppress Doppler broadening [159] and instead resolve motional sidebands on an electronic transition $|\mathrm{g}\rangle \leftrightarrow |\mathrm{e}\rangle$ driven by the interaction laser [117] as shown in figure 4.3a. However, η_z is only defined by the motional ground state $|0\rangle$. Taking into

account a general motional state $|n\rangle$ with extension z_n, a stricter condition is given by [32, 50]:

$$\begin{aligned} k_z z_n &\ll 1, \\ \Rightarrow \eta_z \sqrt{2n+1} &\ll 1. \end{aligned} \tag{4.23}$$

Equation 4.23 defines the *Lamb-Dicke regime* [32] in which sideband transitions $|n\rangle \rightarrow |n \pm \Delta n\rangle$ with $\Delta n > 1$ are strongly suppressed [33, 142] as can be seen in figure 4.3a. The following chapter 4.3 offers more details in the context of the experimental application of resolved sideband cooling [160].

4.3 Resolved Sideband Cooling

The total quantum state of a single trapped ion is described both by its *internal* electronic state and *external* motional state. The total state $|\Psi\rangle$ of an ion is then given by:

$$|\Psi\rangle = \sum_{n=0}^{\infty} c_{\mathrm{g},n}|\mathrm{g}, n\rangle + c_{\mathrm{e},n}|\mathrm{e}, n\rangle, \tag{4.24}$$

where $|c_{\mathrm{g},n}|^2$ and $|c_{\mathrm{e},n}|^2$ are the populations of the states $|\mathrm{g}, n\rangle$ and $|\mathrm{e}, n\rangle$, respectively.

It is possible to couple the electronic and motional states of an ion in order to reduce its average motional state number n and achieve sub-Doppler cooling temperatures with *resolved sideband cooling* [160]. Consider a single ion trapped in a radiofrequency trap potential of angular frequency ω_z with motional energy levels $(n + \frac{1}{2})\hbar\omega_z$. The energy difference $\hbar\omega_z$ between subsequent levels leads to motional sidebands on electronic transitions as shown in figure 4.3. For an electronic transition $|\mathrm{g}\rangle \leftrightarrow |\mathrm{e}\rangle$ at angular frequenycy ω_0, the sidebands appear at $\omega_0 \pm k\omega_z$, where $k \in \mathbb{N}$. The central transition at ω_0 is called the *carrier frequency*.

In order to resolve and thus be able to efficiently address the sidebands within the spectrum of the electronic transition, its natural linewidth Γ needs to be smaller than the frequency spacing of neighboring sidebands:

$$\Gamma \ll \omega_z, \tag{4.25}$$

called the *strong binding condition* [33]. This condition is typically not sufficiently met for electronic dipole transitions, as they exhibit short life times τ and broad natural linewidths Γ. In the case of $^{40}\mathrm{Ca}^+$, the 729 nm $4^2\mathrm{S}_{1/2} \leftrightarrow 3^2\mathrm{D}_{5/2}$ quadrupole transition with linewidth $\Gamma \approx 0.856$ Hz [146] is commonly used [161]. For comparison, typical secular trapping frequencies ω_z are on the order of several 100 kHz to a few MHz [162]. Furthermore, the linewidth of the interacting laser Γ_ℓ has to be smaller than the frequency separation in order to address

individual sidebands, i. e., $\Gamma_\ell \ll \omega_z$.

Ions need to be pre-cooled to sufficiently low motional numbers n in order to enter the Lamb-Dicke regime in which only the first sidebands can be efficiently addressed, given by the condition:

$$\eta_z \sqrt{2n+1} \ll 1, \tag{4.26}$$

where η_z is the Lamb-Dicke parameter defined in equation 4.22.

As shown in figure 4.3b, driving an electronic transition at one of the first sidebands leads to a change of n upon excitation:

$$|\mathrm{g}, n\rangle \rightarrow |\mathrm{e}, n \pm 1\rangle. \tag{4.27}$$

Given a Rabi frequency Ω_R of the carrier transition at ω_0, the Rabi frequencies of the first sideband transitions in the Lamb-Dicke regime are given by [33]:

$$\begin{aligned} &\Omega_{n,n\pm\Delta n} = \left\langle n \left| e^{i\eta(\hat{a}^\dagger + \hat{a})} \right| n \pm \Delta n \right\rangle, \\ \Rightarrow &\Omega_{n,n} = \Omega_\mathrm{R} \left(1 - \frac{1}{2}\eta^2(2n-1) \right) \approx \Omega_\mathrm{R}, \\ &\Omega_{n,n+1} = \Omega_\mathrm{R}\eta\sqrt{n+1}, \\ &\Omega_{n,n-1} = \Omega_\mathrm{R}\eta\sqrt{n}, \end{aligned} \tag{4.28}$$

where the subscripts $n, n \pm \Delta n$ denote the addressed motional transition $|n\rangle \rightarrow |n \pm \Delta n\rangle$.

In the Lamb-Dicke regime, the excited state $|\mathrm{e}, n \pm 1\rangle$ is most likely to spontaneously decay at the carrier frequency ω_0 [33] such that:

$$|\mathrm{e}, n \pm 1\rangle \rightarrow |\mathrm{g}, n \pm 1\rangle. \tag{4.29}$$

Equations 4.27 and 4.29 show how repeated cycling of a transition at one of its sidebands leads to a net increase or decrease in n. The $|n\rangle \rightarrow |n+1\rangle$ transitions at $\omega_0 + \omega_z$ are called *blue sideband* transitions, while transitions $|n\rangle \rightarrow |n-1\rangle$ at $\omega_0 - \omega_z$ are called *red sideband* transitions.

Resolved sideband cooling is experimentally realized by repeated excitation of a red sideband transition $|n\rangle \rightarrow |n-1\rangle$ at $\omega_0 - \omega_z$. It can reduce the ion motion almost entirely to its motional ground state $|0\rangle$ [163]. Due to the relatively long life times of the narrow electronic transitions used for resolved sideband cooling, the excited state $|\mathrm{e}, n-1\rangle$ is typically driven to a short-

lived auxiliary state $|\mathrm{a}, n-1\rangle$ as shown in figure 4.3b. The cooled ion then decays back into its ground state $|\mathrm{g}, n-1\rangle$ with the reduced motional quantum number, increasing the efficiency of the cooling by reintroducing the ion to the sideband cooling cycle at an accelerated rate [142].

Since the ground state $|0\rangle$ is a lower limit for the motional state distribution, the excitation probability $P_{n,n-1}$ for the red sideband transition $|\mathrm{g}, n\rangle \rightarrow |\mathrm{e}, n-1\rangle$ decreases for lower n, eventually reaching $P_{n,n-1} = 0$ for $n = 0$ [160].

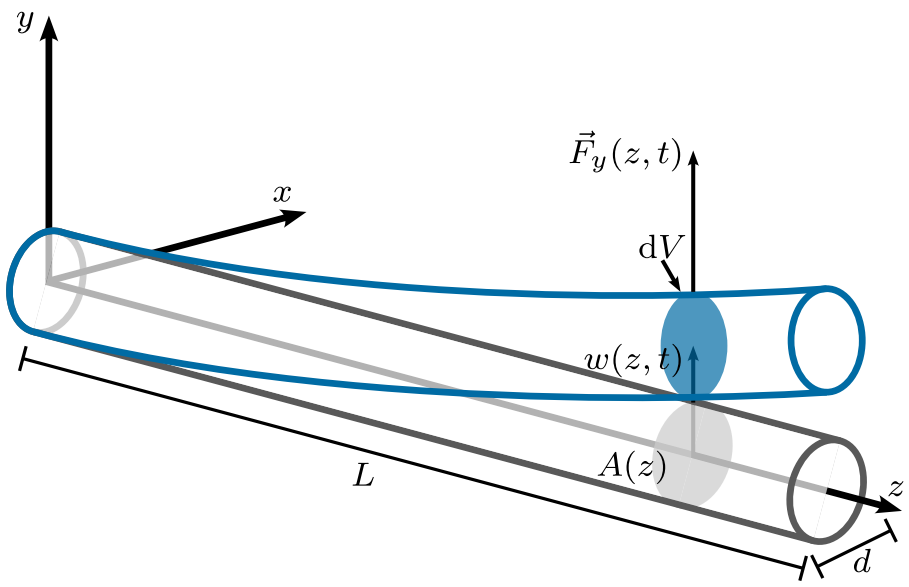

Figure 5.1: Deformation of a singly clamped cylindrical beam of cross section $A(z)$ under a force $\vec{F}_y(z,t)$. The displacement from the neutral position (dark gray cylinder) occurs purely in the y-direction and the shape of its deformation along z (blue cylinder) is described by $w(z,t)$. Geometric and material properties dictate the response of the beam to $\vec{F}_y(z,t)$.

5 Nanomechanics

5.1 Euler-Bernoulli Beam Theory

The dynamics and eigenfrequencies of a nanowire can be described by the *Euler-Bernoulli beam theory*. This theory is valid for shear-rigid thin beams [164] with high aspect ratios, i. e., of length L much larger than their largest cross-sectional extension d. It allows the determination of the eigenfrequencies and mode shapes of a beam and describes its deformations under applied loads [165–167]. In the following, we will only consider *flexural modes* of nanomechanical oscillators, i. e., transverse bending perpendicular to L.

Consider a cylindrical beam of length L with circular cross section $A(z) = \pi \left(\frac{d}{2}\right)^2$ as shown in figure 5.1. The origin of the coordinate system $\vec{x} = (0,0,0)$ is positioned at the centroid of one of the bases of the cylinder. Its orientation is chosen such that the z-axis is parallel to the length L of the beam and thus corresponds to its neutral axis. The beam position is fixed at its base at $z = 0$. Applying a position- and time-dependent force $\vec{F}_y(z,t)$ to the beam in y-direction will result in a transverse displacement $w(z,t)$ describing the deformation of the beam along the z-axis. The amplitude of $w(z,t)$ depends on geometric and material properties of the beam as well as on the applied force. The given choice of coordinate system reduces the problem to a one-dimensional description [168].

For a beam with high aspect ratio $L \gg d$ experiencing small deflections $w(z,t) \ll L$ the

equation of motion is given by [165, 168]:

$$\rho A(z)\frac{\partial^2 w(z,t)}{\partial t^2} + \frac{\partial^2}{\partial z^2}\left[E_{\mathrm{Y}} I_x(z)\frac{\partial^2 w(z,t)}{\partial z^2}\right] = f_y(z,t). \tag{5.1}$$

Here, ρ and E_{Y} are the density and Young's modulus of the beam material, respectively. $f_y(z,t)$ is the load applied on the system. I_x and I_y are the cross-sectional *area moments of inertia* or *second moments of area* [164] of the beam with respect to the x- and y-axis given by:

$$\begin{aligned} I_x &= \int_A y^2 \mathrm{d}A, \\ I_y &= \int_A x^2 \mathrm{d}A. \end{aligned} \tag{5.2}$$

In the case of a circular cross section as shown in figure 5.1, $I_x = I_y$ and is found to be:

$$I_x = \frac{\pi}{64} d^4. \tag{5.3}$$

The assumed perfect cylindrical symmetry $I_x = I_y$ leads to eigenmodes n of oscillations with identical sets of angular frequencies ω_n along orthogonal axes x and y. In reality, geometric imperfections (i. e., $I_x \neq I_y$) result in the frequency splitting of modes along orthogonal directions with eigenfrequencies $\omega_{n,x} \neq \omega_{n,y}$ [67, 69].

In the following, we will discuss the dynamics of a nanomechanical resonator purely oscillating along the defined y-axis as given by equation 5.1 and visualized in figure 5.1. However, the descriptions are valid along both orthogonal axes and can be treated independently by considering the corresponding area moment of inertia I.

5.2 Eigenfrequencies and Mode Shapes

The eigenfrequencies and mode shapes of a beam correspond to the free vibrations of the beam without external load, i. e., the solutions to equation 5.1 with $f_y(z,t) = 0$. Assuming a constant shape of the cross section over the length of the beam, we obtain $A(z) \to A$ and $I_x(z) \to I_x$. The equation of motion for a freely oscillating beam then reduces to:

$$\rho A\frac{\partial^2 w(z,t)}{\partial t^2} + E_{\mathrm{Y}} I_x \frac{\partial^4 w(z,t)}{\partial z^4} = 0. \tag{5.4}$$

The solutions $w(z,t)$ to equation 5.4 can be found by separation of variables $w(z,t) \to u(z)r(t)$. This ansatz of a Fourier decomposition [168] leads to infinite solutions to equation 5.4 with eigenfrequencies ω_n given by:

$$w(z,t) = \sum_{n=0}^{\infty} \mathbb{R}[u_n(z) r_n e^{-i\omega_n t}]. \tag{5.5}$$

Here, $\mathbb{R}[w_n(z,t)]$ denotes the real part of a given solution $w_n(z,t) = u_n(z)r_n(t)$. The time-independent term $u_n(z)$ in equation 5.5 corresponds to the shape of a given mode n and describes the deformation of a beam during free oscillations $r_n(t) = r_n e^{-i\omega_n t}$ at its angular eigenfrequencies $\omega_n = 2\pi f_n$. It is important to note that in the definition given by equation 5.5, $u_n(z)$ are dimensionless and only describe the shape of a mode. The amplitude information of the vibrations is given by r_n in the time evolution parts $r_n(t) = r_n e^{-i\omega_n t}$.

We introduce the dimensionless parameter β_n given by:

$$\beta_n = \left(\omega_n^2 \frac{\rho A}{E_\mathrm{Y} I_x}\right)^{\frac{1}{4}} L. \tag{5.6}$$

Inserting the ansatz given by equation 5.5 into equation 5.4 yields the equations of motion for a single oscillating mode shape $u_n(z)$:

$$\frac{\partial^4 u_n(z)}{\partial z^4} - \frac{\beta_n^4}{L^4} u_n(z) = 0. \tag{5.7}$$

The general solution to equation 5.7 is given by [165, 166]:

$$\begin{aligned} u_n(z) =& A_n \cos\left(\beta_n \frac{z}{L}\right) + B_n \cosh\left(\beta_n \frac{z}{L}\right) \\ &+ C_n \sin\left(\beta_n \frac{z}{L}\right) + D_n \sinh\left(\beta_n \frac{z}{L}\right). \end{aligned} \tag{5.8}$$

5.3 Cantilever Eigenfrequencies and Mode Shapes

The exact solutions of the mode shapes $u_n(z)$ to equation 5.7 and the values of β_n depend on the boundary conditions of the system. In the case of a singly clamped beam with one free end as shown in figure 5.1 (also called a *cantilever*) the boundary conditions are given by:

$$\begin{aligned} &u_n(0) = 0, \\ &\frac{\partial}{\partial z}[u_n(z)]_{z=0} = 0, \\ &E_\mathrm{Y} I_x \frac{\partial^2}{\partial z^2}[u_n(z)]_{z=L} = 0, \\ &E_\mathrm{Y} I_x \frac{\partial^3}{\partial z^3}[u_n(z)]_{z=L} = 0. \end{aligned} \tag{5.9}$$

Mode n	β_n	ω_n/ω_0
0	1.875	1.0
1	4.694	6.267
2	7.855	17.547
3	10.996	34.386
≥ 3	$(n+\frac{1}{2})\pi$	$((n+\frac{1}{2})\pi/\beta_0)^2$

Table 5.1: Values of β_n for cantilevers. The given β_n and frequency ratios ω_n/ω_0 are characteristic for singly clamped beams. The respective angular eigenfrequencies ω_n depend on geometric and material properties of the beam given by equation 5.11.

The first two lines in equation 5.9 demand that the position and slope of the beam be fixed at $z = 0$. The last two lines correspond to the conditions that the torque and transverse force at the free end $z = L$ must be 0, respectively [165].

Applying the conditions given by equation 5.9 to equation 5.8 yields the following characteristic equation for β_n for singly clamped beams [165, 166]:

$$\cos(\beta_n)\cosh(\beta_n) + 1 = 0. \tag{5.10}$$

The solutions of β_n to equation 5.10 are visualized in figure 5.2 and given in table 5.1 with the corresponding relative angular eigenfrequencies ω_n/ω_0. The relationship between ω_n and β_n is found by rearrangement of equation 5.6:

$$\omega_n = \frac{\beta_n^2}{L^2}\sqrt{\frac{E_Y I_x}{\rho A}}. \tag{5.11}$$

The mode shape solutions $u_n(z)$ to equation 5.7 for a singly clamped beam are given by [67, 166]:

$$\begin{aligned} u_n(z) = \frac{1}{\kappa_n}((\cos(\beta_n) + \cosh(\beta_n))(\sin\left(\beta_n\frac{z}{L}\right) - \sinh\left(\beta_n\frac{z}{L}\right)) \\ -(\sin(\beta_n) + \sinh(\beta_n))(\cos\left(\beta_n\frac{z}{L}\right) - \cosh\left(\beta_n\frac{z}{L}\right))). \end{aligned} \tag{5.12}$$

Figure 5.3 shows the mode shapes for $n = 0$ to $n = 4$ normalized to $u_n(L) = 1$, obtained by choosing $\kappa_n = 2(\sin(\beta_n)\cosh(\beta_n) - \cos(\beta_n)\sinh(\beta_n))$.

It can be shown that the eigenmodes $u_n(z)$ form an orthogonal basis for the description of the cantilever motion, such that equation 5.5 is the general solution of the oscillation shape as an infinite sum of orthogonal eigenmodes. The orthogonality can be expressed in terms of a scalar product for continuous functions over $z \in [0, L]$ [168]:

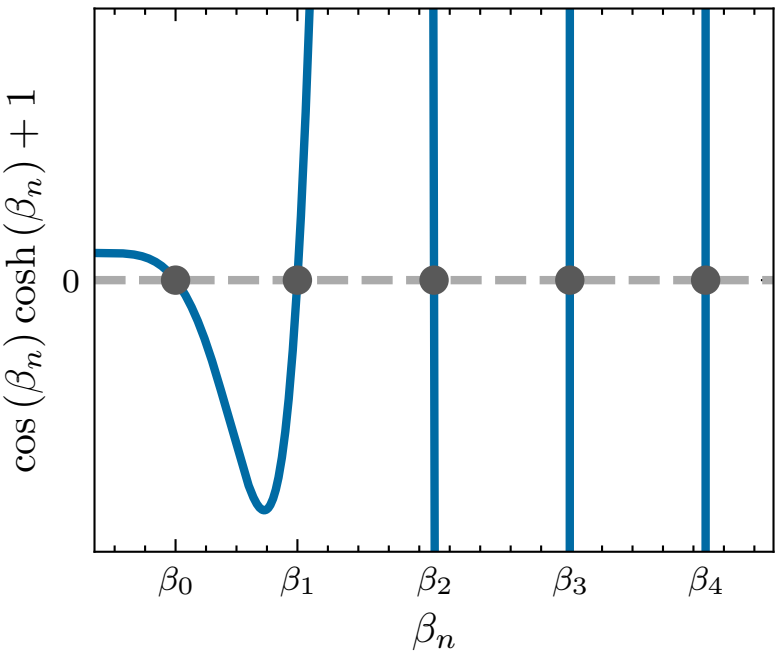

Figure 5.2: β_n parameters for the eigenmodes of a cantilever. The β_n satisfy the condition $\cos(\beta_n)\cosh(\beta_n) + 1 = 0$ (dark gray dots). The values of β_n and the corresponding angular eigenfrequencies ω_n/ω_0 are given in table 5.1.

$$\langle u_n, u_k \rangle = \int_0^L \rho A(z) u_n(z) u_k(z) \mathrm{d}z = M_n \delta_{nk}. \tag{5.13}$$

Here, M_n is the *modal mass* or *effective mass* [167] of the beam and δ_{nk} is the Kronecker delta. More details on M_n are given in chapter 5.4.

5.4 Effective Mass

Each volume element $\mathrm{d}V$ along z of a singly clamped beam as shown in figure 5.1 exhibits a different displacement for a given transversal load $f_y(z)$. This can be understood as a position-dependent effective inertia or local mass [67] of the volume elements of the beam along z.

Each eigenmode n can be assigned an effective mass M_n as introduced in equation 5.13. Denoting the total mass of the clamped beam as M and remembering the normalization $|u_n(L)| = 1$ in equation 5.12 the effective mass is found to be:

$$M_n = \frac{M}{L} \int_0^L |u_n(z)|^2 \mathrm{d}z = \frac{1}{4} M. \tag{5.14}$$

Equation 5.14 shows that the effective mass M_n of a singly clamped beam is identical for each mode and given by $M_n = \frac{1}{4} M$ [167].

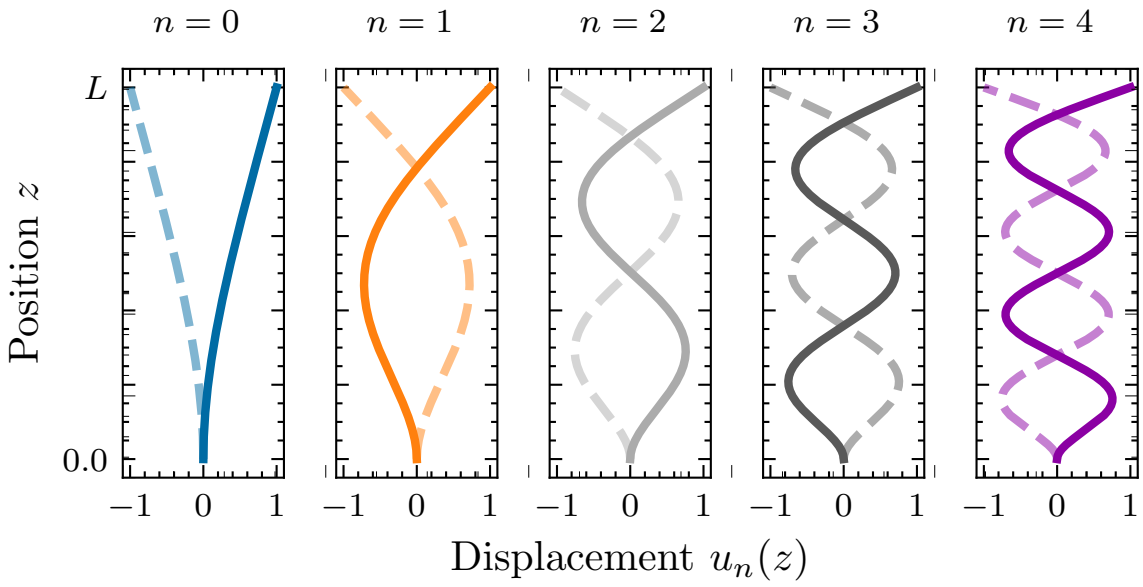

Figure 5.3: Mode shapes of a singly clamped beam for $n = 0$ to $n = 4$. The shapes are normalized to $u_n(L) = 1$ and fixed to $u_n(0) = 0$. The displacement of a free oscillating cantilever periodically alters between the solid and dashed lines at angular eigenfrequencies ω_n.

5.5 Mechanical Dissipation

The time evolutions $r_n e^{-i\omega_n t}$ of the mode shapes given in equation 5.5 correspond to free oscillations described by the equations of motion of undamped harmonic oscillators. In reality, nanomechanical oscillators exhibit mechanical energy dissipation described by the internal damping of viscoelastic materials [169] in which Young's modulus E_Y is given by a complex parameter [167]:

$$E_\mathrm{Y}(\omega) = E_{\mathrm{Y,eff}}(1 + i\phi(\omega)). \tag{5.15}$$

Here, $\phi(\omega)$ is the *loss angle* [168] defined by the energy fraction $(\Delta E_\mathrm{loss}/E_\mathrm{tot})$ lost per oscillation cycle:

$$\phi(\omega) = \frac{\Delta E_\mathrm{loss}}{2\pi E_\mathrm{tot}} = \frac{\mathbb{I}[E_\mathrm{Y}(\omega)]}{\mathbb{R}[E_\mathrm{Y}(\omega)]}. \tag{5.16}$$

In general, each eigenmode n of a nanomechanical oscillator has a unique damping factor γ_n given by:

$$\gamma_n = \frac{\omega_n}{Q_n}. \tag{5.17}$$

Here, we introduced the quality factor Q_n of the oscillator eigenmode n. Q_n is a measure for the conserved energy per oscillation cycle and directly defined as the inverse of equation 5.16:

$$Q_n = \phi^{-1}(\omega_n). \tag{5.18}$$

Nanomechanical oscillators typically have very high quality factors $Q \gg 1$ (i. e., $\phi(\omega) \ll 1$) [95] resulting in slow losses of stored energy over many oscillation cycles. The respectively low damping factors γ_n preserve the mode shapes $u_n(z)$ given by equation 5.12, but change the description of the time evolution part $r_n(t)$ of a mode to that of a damped harmonic oscillator:

$$M_n \ddot{r}_n(t) + M_n \gamma_n \dot{r}_n(t) + M_n \omega_n^2 r_n(t) = F_n(t). \tag{5.19}$$

Here, M_n is the effective mass of the nanomechanical oscillator (see chapter 5.4) and $F_n(t)$ was added to the right hand side of equation 5.19 for a generalized description of the equations of motion under the influence of a force. $M_n \gamma_n = \Gamma_n$ is the *mechanical dissipation* of the resonator [168].

The general solution for the damped oscillations of a singly clamped beam without any external forces $F_n(t)$ is then given by:

$$w(z,t) = \sum_{n=0}^{\infty} \mathbb{R}[u_n(z) r_n e^{-i\omega_n t}] e^{-(\gamma_n/2)t}. \tag{5.20}$$

The low damping factors $\gamma_n/\omega_n \ll 1$ make nanomechanical oscillators strongly underdamped systems. Figure 5.4 shows the exponentially decreasing oscillation amplitudes of an underdamped harmonic oscillator.

In general, the addition of damping shifts the oscillation frequency $\omega_n \rightarrow \omega_{n,\gamma}$ compared to the undamped case. However, this effect is typically negligible for nanomechanical resonators exhibiting $\gamma_n/\omega_n \ll 1$ [167, 169]:

$$\omega_{n,\gamma} = \omega_n \sqrt{1 - \left(\frac{\gamma_n}{2\omega_n}\right)^2} \approx \omega_n. \tag{5.21}$$

5.6 Nanomechanical Oscillator Spectrum

The equation of motion describing the oscillation amplitude $r(t)$ of a damped harmonic oscillator is given by equation 5.19. It is suitable for the description of nanomechanical oscillators

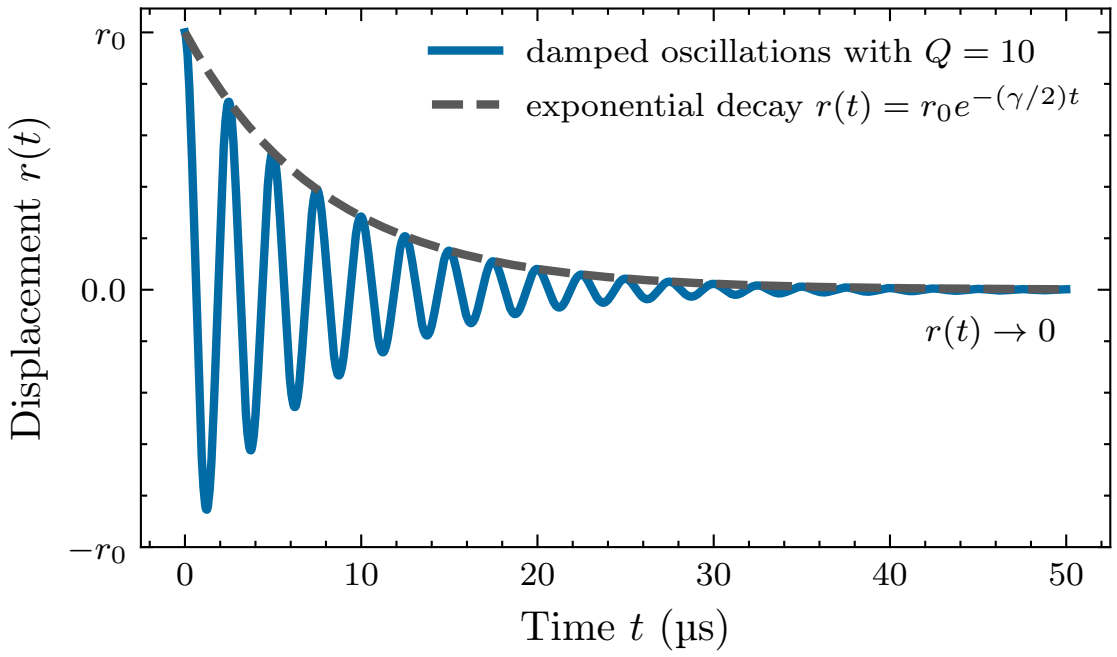

Figure 5.4: Oscillations of a damped harmonic oscillator. Starting at an initial deflection r_0, the oscillations exponentially decay to $r(t) \to 0$. The amplitude decay is a result of dissipation of energy stored in the motion of the oscillator. The shown trajectory $r(t)$ (blue curve) corresponds to an oscillator of natural angular frequency $\omega_0 = 2\pi \times 400$ kHz with a quality factor of $Q = 10$, i. e., damping factor $\gamma = 0.1\omega_0$. Nanomechanical oscillators can exhibit much larger quality factors than shown, corresponding to significantly slower decays and thus less dissipation of stored energy per oscillation.

with high quality factors Q. Without any external force $F(t)$, the damped oscillations converge to $r(t) \to 0$ for $t \to \infty$ (see figure 5.4).

Applying an external force $F(t)$ to a nanooscillator leads to a response of its displacement amplitude $r(t)$ according to equation 5.19. The applied force may be constant $F(t) = F_0$ or time-dependent, e. g. a periodic drive $F(t) = F_0 \cos(\omega t)$. It is instructive to study the response by performing a Fourier analysis on the system such that:

$$\begin{aligned} r(t) \to \hat{r}(\omega) &= \int_{-\infty}^{\infty} r(t) e^{i\omega t} \mathrm{d}t, \\ F(t) \to \hat{F}(\omega) &= \int_{-\infty}^{\infty} F(t) e^{i\omega t} \mathrm{d}t. \end{aligned} \tag{5.22}$$

The relation between $\hat{r}(\omega)$ and $\hat{F}(\omega)$ (displacement per applied force) is given by the *mechanical susceptibility* or *transfer function* $\chi(\omega)$ [67, 167, 168]:

$$\chi(\omega) = \frac{\hat{r}(\omega)}{\hat{F}(\omega)} = \frac{1}{M} \frac{1}{(\omega_0^2 - \omega^2) + i\omega\gamma}. \tag{5.23}$$

Here, ω_0 is the undamped *natural angular frequency* of the oscillator.

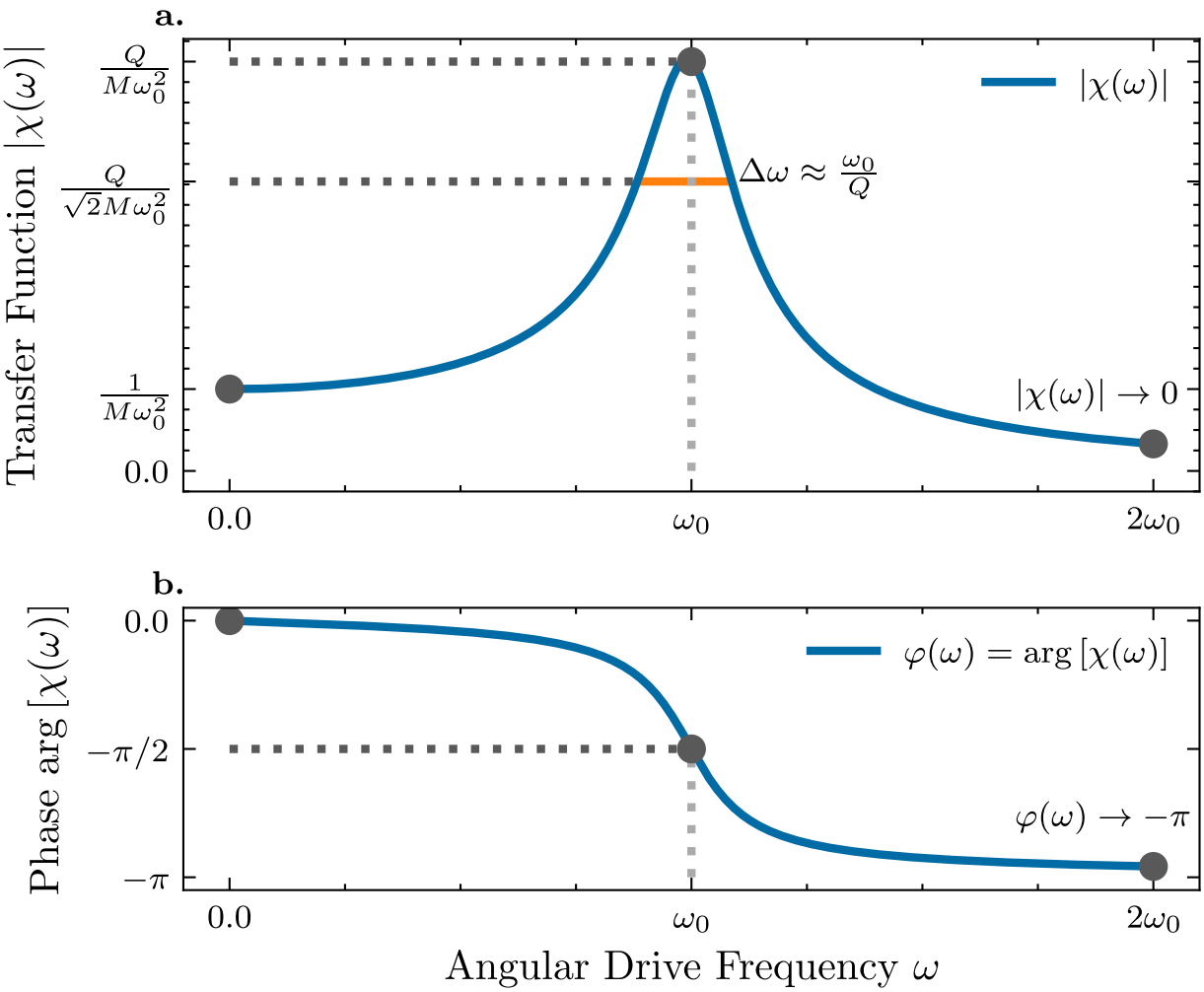

Figure 5.5: Amplitude and phase response of a damped harmonic oscillator of quality factor $Q = 5$. The amplitude of a periodically driven harmonic oscillator is directly proportional to the transfer function $|\chi(\omega)|$ (**a**) with a phase response $\varphi = \arg[\chi(\omega)]$ (**b**). For nanomechanical oscillators with very high $Q \gg 1$, resonant drive at the natural angular frequency ω_0 leads to the strongest amplitude response with a phase $\varphi = -\pi/2$. The quality factor of a nanooscillator can be determined from the frequency width $\Delta\omega$ of the spectrum at height $|\chi(\omega_0)|/\sqrt{2}$ (orange line). A constant force F_0 (i. e., $\omega = 0$) leads to a constant displacement $F_0/(M\omega_0^2)$ without phase lag, i. e., $\varphi = 0$. In the limit $\omega \to \infty$, the transfer function $|\chi(\omega)| \to 0$ vanishes with a phase response $\varphi \to -\pi$.

Equation 5.23 yields information on the amplitude and phase response of a driven harmonic oscillator. Consider a periodic drive force at angular frequency ω:

$$F(t) = F_0 \cos(\omega t). \tag{5.24}$$

The resulting amplitude response for an applied force is directly proportional to $|\chi(\omega)|$, also called the *motional spectrum*. The phase response φ of the harmonic oscillator relative to the periodic drive force is given by $\arg[\chi(\omega)]$. $|\chi(\omega)|$ and $\arg[\chi(\omega)]$ are shown in figure 5.5 as a function of the drive frequency ω. Their expressions are given by [121, 168]:

$$
\begin{aligned}
|\chi(\omega)| &= \frac{1}{M\sqrt{(\omega_0^2-\omega^2)^2+\omega^2\gamma^2}}, \\
\varphi = \arg\left[\chi(\omega)\right] &= \arctan\left(\frac{\omega\gamma}{\omega^2-\omega_0^2}\right).
\end{aligned}
\tag{5.25}
$$

The periodic drive $F(t) = F_0 \cos(\omega t)$ leads to steady state solutions $r(t)$ of the equation of motion 5.19 for $t \to \infty$ [121, 167]. The harmonic oscillator will be forced on oscillating trajectories at the drive frequency ω given by:

$$
r(t) = F_0|\chi(\omega)| \cos(\omega t + \varphi). \tag{5.26}
$$

As can be seen from figure 5.5 and equation 5.26, resonant drive at $\omega = \omega_0$ (valid for $\gamma/\omega_0 \ll 1$) leads to strongly increased oscillation amplitudes $F_0|\chi(\omega_0)|$ with a phase lag of $\varphi = -\pi/2$. In the edge case of high drive frequencies $\omega \to \infty$ the harmonic oscillator becomes increasingly unresponsive ($r(t) \to 0$) in opposite phase $\varphi \to -\pi$ to the driving force. The opposite limit $\omega = 0$ corresponds to a constant force $F(t) = F_0$ acting on the harmonic oscillator. This leads to a shifted equilibrium position at $r(t \to \infty) = F_0/(M\omega_0^2)$. In terms of nanomechanical oscillators, this corresponds to a static transversal bending. It occurs at a zero-lag phase response of $\varphi = 0$.

As shown in figure 5.5, the quality factor Q_n of a mode with low damping factor $\gamma_n/\omega_n \ll 1$ can be approximately determined from the width $\Delta\omega_n$ of the spectrum at $|\chi(\omega_0)|/\sqrt{2}$ [167, 169]:

$$
Q_n \approx \frac{\omega_n}{\Delta\omega_n}. \tag{5.27}
$$

$^{40}Ca^{+}$ Property	Value
Mass m	6.6×10^{-26} kg ≈ 40 u
Charge q	1.602×10^{-19} As $= 1e$
Electron Spin S	1/2
Nuclear Spin I	0
Ground State	$(4s)^2S_{1/2}$

Table 6.1: Physical properties of $^{40}Ca^{+}$.

6 Experimental Setup

6.1 Linear Radiofrequency Wafer Chip Trap

At the core of the experiment was a miniaturized linear radiofrequency ion trap for the trapping of laser-cooled $^{40}Ca^{+}$ ions. The trap consisted of layered aluminum-oxide wafers stacked on top of a printed circuit board (PCB) as shown in figure 6.1a. The wafers were separated by spacers and a skimmer plate was added to prevent contamination of the electrodes with excess calcium. The electrode wafers were sputtered with gold in order to ensure electrical conductivity. An additional compensation electrode was positioned above the trap (see figure 6.1b) in order to obtain an additional degree of freedom for the compensation of the DC potential of the trap. The trap was specifically designed and manufactured by Panagiotis Fountas for the realization of the ion-nanowire hybrid system presented in this thesis [80].

The geometry of the trap featured two pairs of diagonally opposing radiofrequency (RF) and direct current (DC) electrode wafers with rectangular cross sections for the generation of a quadrupolar RF potential (see figure 6.1c). The DC electrode wafers were split into seven individually addressable segments of length $l_{\mathrm{DC}} = 400$ µm and width $w_{\mathrm{DC}} = 200$ µm as shown in figure 6.1d. The length of the gaps between neighboring DC electrode segments was $l_{\mathrm{gap}} = 20$ µm. This design offered several degrees of freedom for the shaping of the trapping potential by adjusting the applied DC voltages as well as multiple possible trapping regions along the symmetry axis of the trap that could be used for ion shuttling [123]. The length of the RF electrode wafers was $l_{\mathrm{RF}} = 2.92$ mm to span the same length as the seven DC electrodes including the gaps. The width of the RF electrodes was $w_{\mathrm{RF}} = 200$ µm. The radial plane of the trap geometry had a square cross section with an electrode-to-electrode distance of $d_{\mathrm{ee}} = 400$ µm as shown in figure 6.1c.

6.1.1 $^{40}Ca^{+}$ Ion Properties

The trapped ion species used in this work was $^{40}Ca^{+}$, featuring a single valence electron in its outer shell. The electronic ground state configuration of $^{40}Ca^{+}$ is given by the $(4s)^2S_{1/2}$ spin doublet. Table 6.1 gives an overview of important physical properties of $^{40}Ca^{+}$ and figure 6.2 shows the electronic energy levels of $^{40}Ca^{+}$ relevant to the work presented in this thesis.

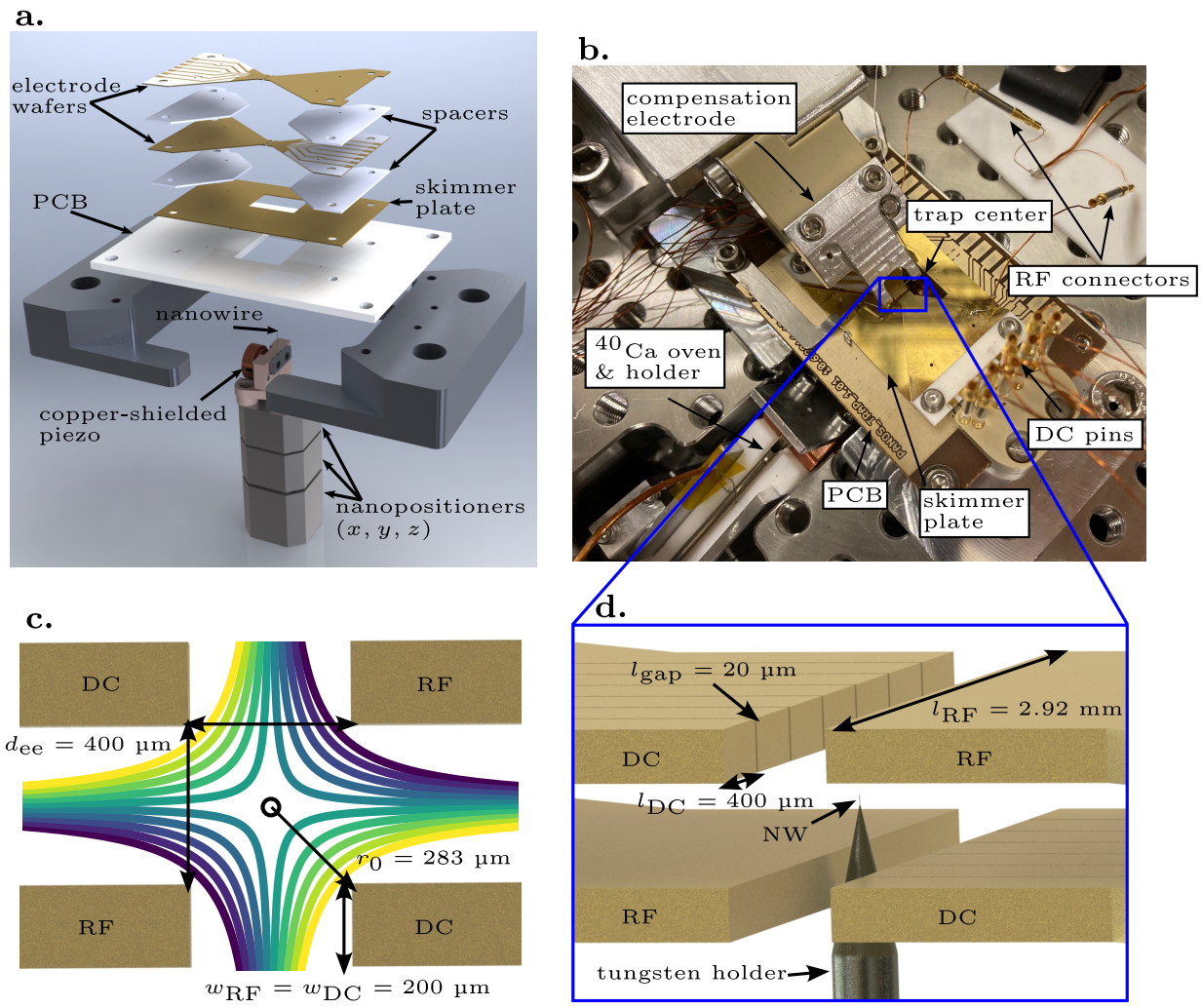

Figure 6.1: Miniaturized linear radiofrequency trap for the realization of an ion-nanowire hybrid system. **a**, The trap consisted of stacked aluminum-oxide wafers. They were layered on top of a PCB and the electrodes were sputtered with gold. The nanowire was mounted below the trap and mechanically driven by a copper-shielded piezo actuator. The nanowire was positioned with three nanopositioners. **b**, Photograph of the assembled trap inside of the vacuum chamber. **c**, View of the radial plane of the trap with electrodes of rectangular cross sections. The generated quadrupolar RF potential is indicated by the equipotential lines. **d**, The charged nanowire was positioned inside the trapping region to achieve strong coupling to the trapped $^{40}Ca^{+}$ ions. The DC electrode wafers were segmented into 7 individually addressable electrodes.

6.1.2 Calcium Source and Ionization

Neutral ^{40}Ca atoms were evaporated into the trapping region by resistive heating of a cylindrical *calcium oven* (AlfaVakuo AS-Ca25-2C-020) fixed to a holder as shown in figure 6.3. The holder was positioned such that the opening of the oven was pointed directly at the center of the trap (see figure 6.1b).

The holder consisted of a central MACOR piece and copper pieces on either of its ends. The calcium oven was clamped between the copper pieces and connected to wires for the supply of high currents ($I_{\text{oven}} \approx 4$ A). A 1 mm skimmer hole in front of the opening was designed to

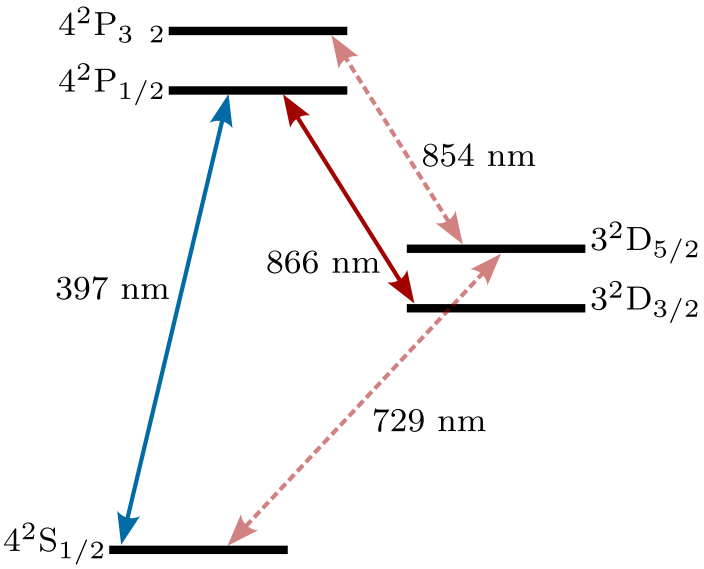

Figure 6.2: Electronic energy levels of $^{40}Ca^+$. A closed Doppler cooling cycle was achieved by driving the $4^2S_{1/2} \leftrightarrow 4^2P_{1/2}$ and $3^2D_{3/2} \leftrightarrow 4^2P_{1/2}$ transitions with an 397 nm and 866 nm laser, respectively. Other transitions (dashed arrows) are available for a variety of further applications and techniques such as resolved side-band cooling and motional state detection [33]. Those transitions were not addressed in the work presented in this thesis.

prevent contamination of the trap electrodes with calcium. The temperature of the oven was monitored with an attached thermocouple. The oven was typically operated at temperatures around 300 °C to 400 °C in order to obtain sufficiently fast ion loading rates.

Ionization of the neutral ^{40}Ca atoms was achieved with two overlapping laser beams at wavelengths 423 nm and 375 nm. The 423 nm laser excited the $(4s^2)^1S_0 \rightarrow (4s4p)^1P_1$ transition [170] of the neutral calcium atoms from which the 375 nm laser then ionized the atoms [171, 172] as shown in figure 6.4a. The ionized $^{40}Ca^+$ was subsequently confined in the center of the trap. To confirm the presence of neutral ^{40}Ca in the trap, the fluorescence on the 423 nm transition was observed using an EMCCD camera as shown in figure 6.4b.

6.2 Nanowire Assembly and Mechanical Piezo Drive

The ion trap was combined with an electrically conductive Ag_2Ga nanowire [173] as shown in figure 6.1a and 6.1d in order to realize an ion-nanowire hybrid system [80]. Over the course of this project, some of the mounted nanowires were accidentally broken and subsequently replaced. In the following, all reported properties refer to the last implemented nanowire that was ultimately used for the experimental demonstration of the ion-nanowire interaction shown in chapter 11.

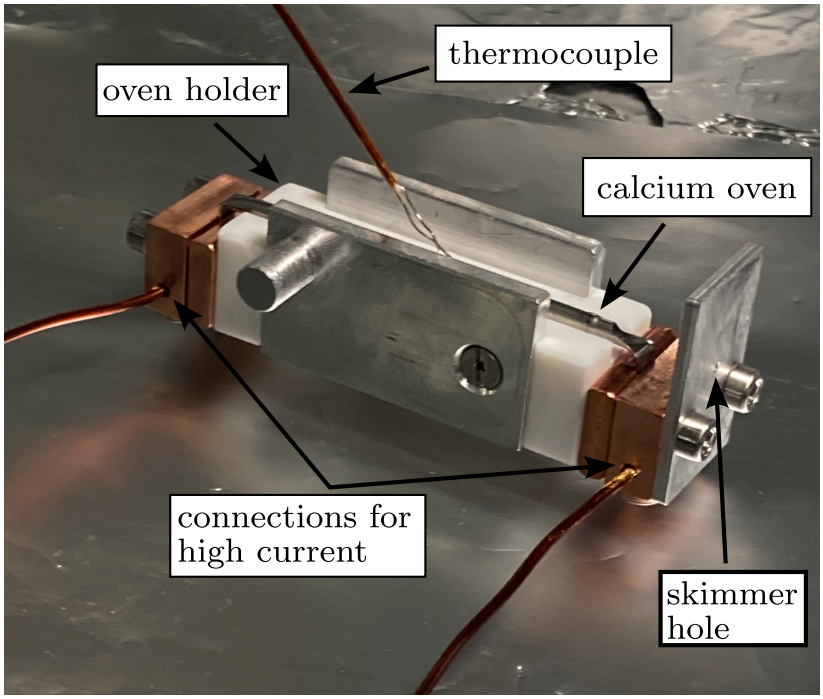

Figure 6.3: Calcium source for the loading of $^{40}Ca^{+}$ ions. Neutral ^{40}Ca atoms were evaporated by resistive heating of the calcium oven. The oven was positioned on a holder and pointed at the center of the radiofrequency ion trap. The calcium oven was clamped between the copper pieces on either end of the oven holder and a high current of $I_{\text{oven}} \approx 4$ A was applied. Neutral calcium atoms reaching the trap center were subsequently ionized by two photoionization lasers with wavelengths of 423 nm and 375 nm.

The length of the nanowire $l_{\text{nw}} = 16$ µm was determined with a microscope using a 20× magnification as shown in figure 6.5a. The diameter of the nanowire $d_{\text{nw}} = 150$ nm was reported by the manufacturer (NaugaNeedles). The nanowire was attached to the tip of a cylindrical tungsten holder with a conical end as shown in figure 6.1d and 6.5a. The total length of the holder was $l_{\text{holder}} \approx 4.8$ mm (including its conical tip) and a diameter of $d_{\text{holder}} = 250$ µm of its cylindrical part. The length of the conical end of the holder was $l_{\text{cone}} = 715$ µm. As can be seen in figure 6.5b, the surface of this particular tungsten holder was not very smooth.

The nanowire setup was mounted on a stack of three nanopositioners (attocube) in order to be able to place it at a desired position within the linear radiofrequency trap. Figure 6.1a shows the nanowire positioning setup located below the center of the ion trap. It consisted of one attocube ANPz51 nanopositioner for placement along the vertical y-direction and two attocube ANPx51 nanopositioners for placement along the horizontal x- and z-directions. The nanopositioners were controlled with the attocube ANC300 motion controller.

The tungsten holder was clamped to the side of a PEEK piece positioned on top of the attocube positioners. The assembly was mechanically driven with a piezo disk actuator of diameter $d_{\text{piezo}} = 5$ mm and thickness $h_{\text{piezo}} = 2$ mm clamped to the opposite side of the PEEK piece with firm mechanical contact (see figure 6.1a). Applying a sinusoidal AC voltage at drive frequency f_{drive} to the piezo actuator mechanically transferred its oscillatory motion along the axial z-direction to the tungsten holder and the nanowire on its tip. Significant responses of

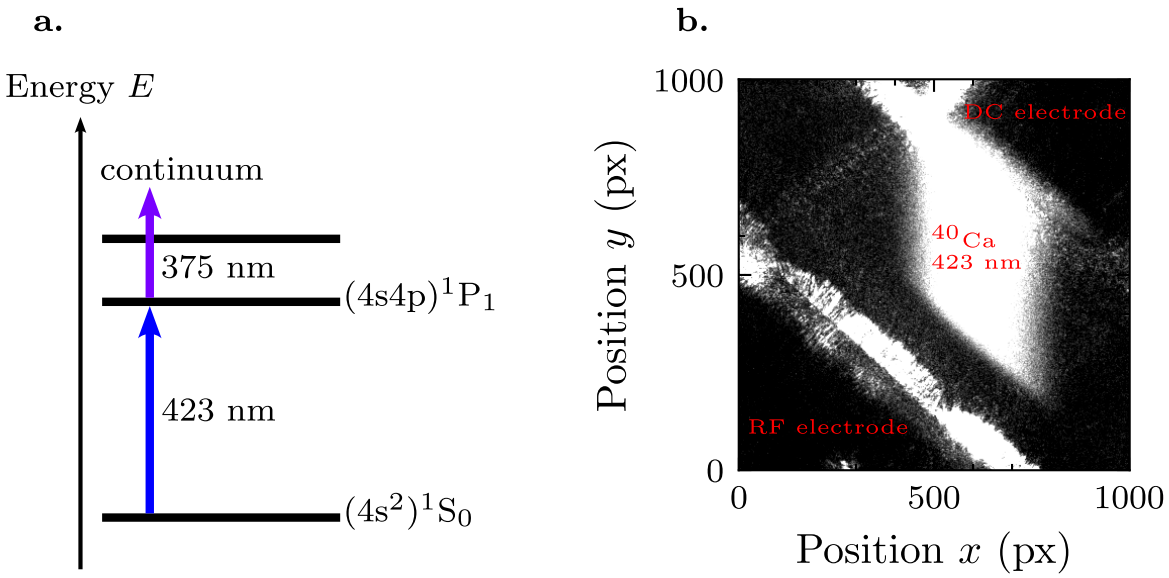

Figure 6.4: Two-step photoionization of neutral ^{40}Ca atoms. **a**, Relevant energy levels of neutral ^{40}Ca. A 423 nm laser excited the neutral atoms on the $(4s^2)^1S_0 \rightarrow (4s4p)^1P_1$ transition. The excited atoms were subsequently ionized ($^{40}Ca \rightarrow ^{40}Ca^+$) with a 375 nm laser. **b**, The presence of neutral calcium atoms in the center of the trap was confirmed by observing the fluorescence on the 423 nm $(4s^2)^1S_0 \leftrightarrow (4s4p)^1P_1$ transition with an EMCCD camera. The image shows the trapping region viewed from the top. The 423 nm laser beam (inducing the bright atom fluorescence) and the edges of a single DC electrode and RF electrode are visible.

Material Property	Ag_2Ga	Tungsten
Young's Modulus E_Y	84.4 GPa [173]	411 GPa
Material Density ρ	8960 kg/m^3 [173]	19250 kg/m^3

Table 6.2: Young's modulus E_Y and density ρ of Ag_2Ga and tungsten. The values for tungsten were taken from the material database offered by Comsol Multiphysics [112].

the oscillation amplitude of the nanowire were only achieved at drive frequencies f_{drive} close to the resonance frequencies f_n of the assembly (see also chapter 5.3). The piezo actuator was encased in a grounded copper shield to prevent electrical leakage of the applied AC voltage to the trapping region which could result in undesired *electrical* excitation of the trapped ions.

6.2.1 Ag_2Ga Nanowire Properties

The nanomechanical oscillator used for the realization of the ion-nanowire hybrid system presented in this thesis was an Ag_2Ga nanocantilever attached to the tip of a tungsten holder. Table 6.2 gives an overview of the densities ρ and Young's moduli E_Y of Ag_2Ga and tungsten. These material properties as well as the geometry of the nanomechanical oscillator assembly determined the resonance frequencies as discussed in chapter 5.

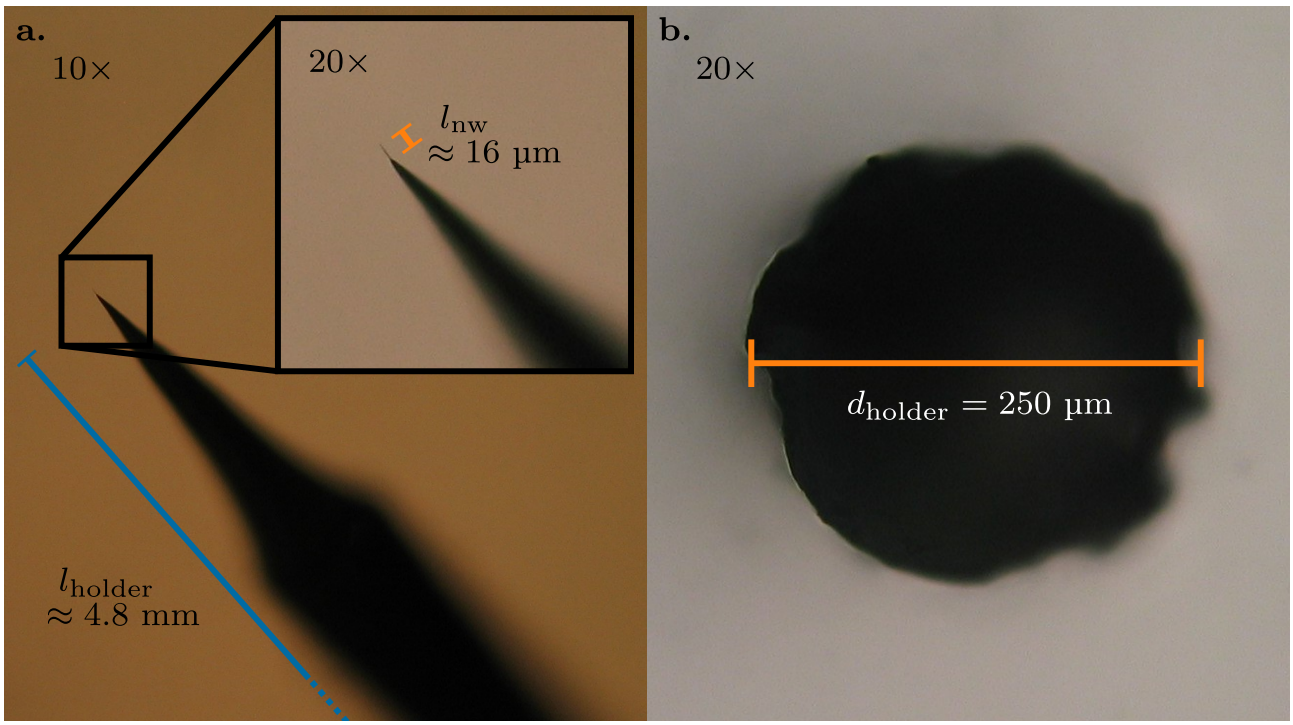

Figure 6.5: Microscope images of the nanowire used for the experimental demonstration of the ion-nanowire coupling. a, Microscope images of the nanowire and the tungsten holder viewed from the side at magnifications of 10× and 20×. The total length of the tungsten holder (including the conical tip) was $l_{\mathrm{holder}} \approx 4.8$ mm. The length of the nanowire at the tip was $l_{\mathrm{nw}} \approx 16$ µm and the diameter of the nanowire was $d_{\mathrm{nw}} = 150$ nm (reported by the manufacturer). **b**, Microscope image of the cross section of the tungsten holder at a magnification of 20×. The diameter of the holder reported by the manufacturer and confirmed with the microscope was $d_{\mathrm{holder}} = 250$ µm.

6.2.2 Eigenfrequencies and Mode Shapes of the Nanowire Assembly

The discussion of the eigenfrequencies f_n and mode shapes of a nanomechanical oscillator in chapter 5 assumed a cylindrical beam and a constant material density ρ. However, the complete assembly of the mechanical oscillator driven by the piezo actuator in the experiments consisted of two materials (Ag_2Ga and tungsten) and featured a conical geometry at the tip of the holder.

The mode shapes and eigenfrequencies of the combined nanowire-holder assembly were determined using the finite element method with the *structural mechanics* module of Comsol Multiphysics [112]. The geometry of the assembly is shown in figure 6.6a. The holder consisted of a cylinder of length $l_{\mathrm{cylinder}} = 4.145$ mm and diameter $d_{\mathrm{cylinder}} = 250$ µm and a cone with base diameter $d_{\mathrm{cone}} = 250$ µm and length $l_{\mathrm{cone}} = 715$ µm, resulting in a total holder length of $l_{\mathrm{holder}} = 4.86$ mm. The materials of the elements of the holder were tungsten with the parameters given in table 6.2. The tip of the cone had a diameter of $d_{\mathrm{nw}} = 150$ nm and a cylindrical nanowire of the same diameter $d_{\mathrm{nw}} = 150$ nm and length $l_{\mathrm{nw}} = 16$ µm was added to the tip. The material of the nanowire was Ag_2Ga with the parameters given in table 6.2. In the simulations performed with Comsol, the position of the assembly was fixed at the base of the holder.

Figure 6.6b shows the *flexural* mode shapes and corresponding eigenfrequencies f_n of the nanowire-holder assembly determined with Comsol Multiphyiscs [112] for $n \leq 4$. As will be

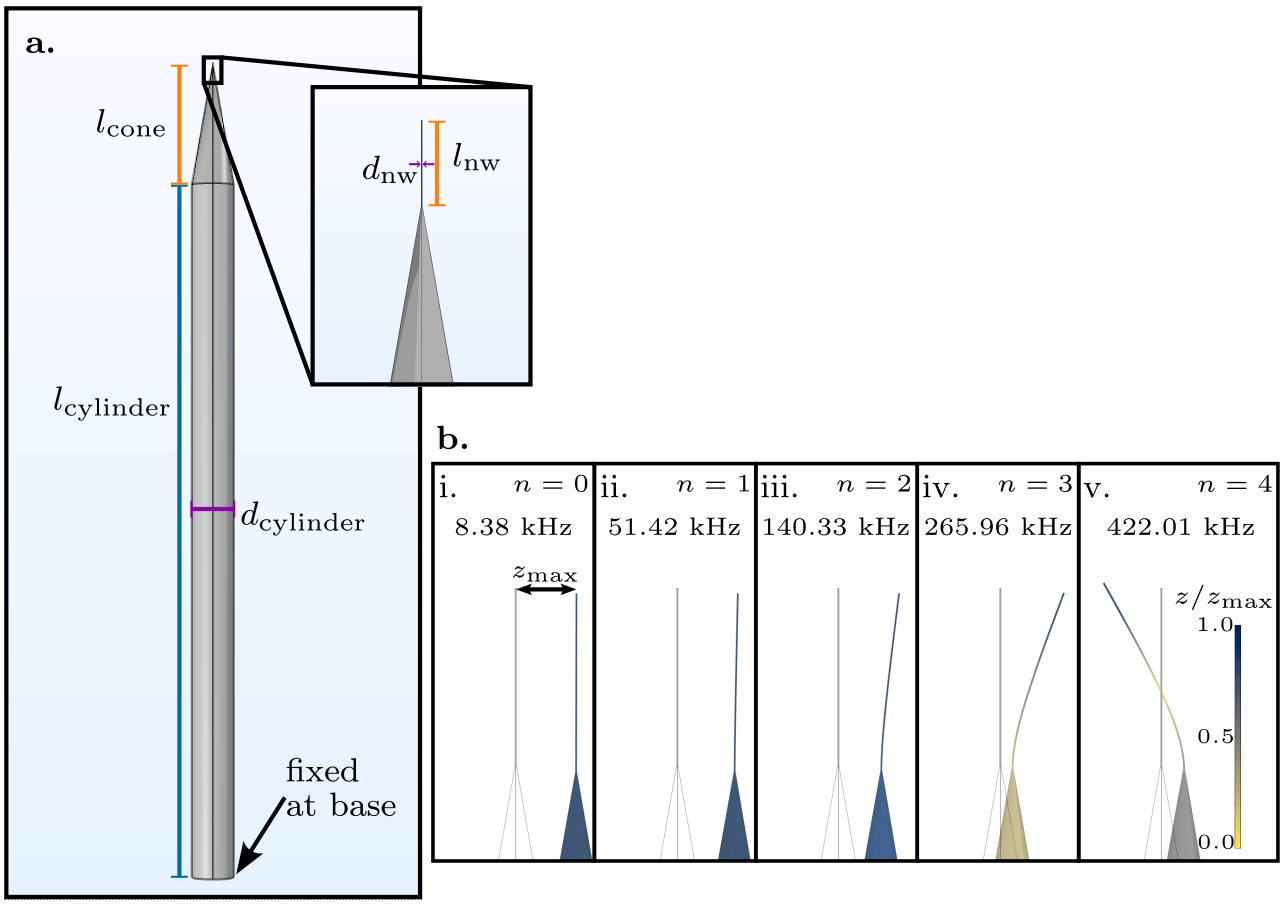

Figure 6.6: Determination of the mode shapes and eigenfrequencies of the nanowire assembly with Comsol Multiphysics. **a**, The geometry of the nanowire assembly used for the simulations. The tungsten holder consisted of a cylinder with diameter $d_{\mathrm{cylinder}} = 250$ µm and length $l_{\mathrm{cylinder}} = 4.145$ mm and a conical tip of length $l_{\mathrm{cone}} = 715$ µm. The Ag_2Ga nanowire was attached to the tip and had a diameter of $d_{\mathrm{nw}} = 150$ nm and a length of $l_{\mathrm{nw}} = 16$ µm. The position of the assembly was fixed at its base. **b**, Flexural mode shapes and corresponding eigenfrequencies f_n obtained from the Comsol simulations for $n \leq 4$. The mode shapes were normalized to an arbitrary maximum displacement z_{max}. All oscillations of the modes shown here feature contributions from the nanowire as well as from the tungsten holder.

shown in chapter 7.1, the simulated frequencies fit well to the experimental observations.

6.3 Laser Cooling of $^{40}Ca^{+}$

The laser cooling of $^{40}Ca^{+}$ ions was achieved with a combination of a 397 nm cooling laser and an 866 nm repumper laser [146]. The $4^2S_{1/2} \leftrightarrow 4^2P_{1/2}$ dipole transition was used as the main cooling transition driven by the 397 nm laser. Ions excited to the $4P_{1/2}$ state could spontaneously decay into the $3^2D_{3/2}$ level at a branching ratio of 6.43% [174]. The 866 nm laser driving the $3^2D_{3/2} \leftrightarrow 4^2P_{1/2}$ transition was used to reintroduce those ions back into the main cooling transition and obtain a closed cooling cycle. Details on the physical properties of the cooling transitions are given in table 6.3. The lifetime of the $4^2P_{1/2}$ state is $\tau \approx 7.1$ ns [174].

The cooling lasers entered the trapping region under an angle ($\approx 45°$) with respect to all three principal axes of the trap. This enabled the cooling of trapped ions in all spatial directions

Parameter	$4^2S_{1/2} \leftrightarrow 4^2P_{1/2}$	$3^2D_{3/2} \leftrightarrow 4^2P_{1/2}$
Wavelength λ	397 nm	866 nm
Frequency f	755222.765896 GHz[38]	346000.234867 GHz[175]
Linewidth Γ	132 MHz [140]	9.3 MHz [176]
Branching Ratio $\mathcal{B}$	93.57% [174]	6.43% [174]
Sat. Intensity I_{sat}	438.84 W/m^2	2.98 W/m^2

Table 6.3: Physical properties of the $4^2S_{1/2} \leftrightarrow 4^2P_{1/2}$ and $3^2D_{3/2} \leftrightarrow 4^2P_{1/2}$ cooling transitions of $^{40}Ca^+$. The saturation intensities I_{sat} were determined from equation 3.9.

with a single cooling axis simultaneously.

6.4 Experimental Chamber and Laser Setup

A top-view schematic of the experiment including the optical laser setup is shown in figure 6.7. It consisted of one main ultrahigh-vacuum chamber (Kimball Physics) with eight CF40 flange openings on the side and one CF200 flange with a viewport on the top. Flanges 2, 4, 6 and 8 were used for feedthroughs for electrical connections to the trap electrodes, the attocube nanopositioners, the calcium oven and the piezo actuator. The remaining four flanges featured viewports for optical access to the trap.

A total of four lasers were used in the experimental setup. The two-step photoionization of neutral ^{40}Ca atoms was achieved with two continuous-wave (cw) lasers with wavelengths of 423 nm and 375 nm [171]. Both ionization lasers exited optical fibers on the experimental table and were guided to the center of the trap through flange 1 with a series of mirrors. A dichroic mirror combined both lasers before entering the chamber.

Laser cooling of the $^{40}Ca^+$ ions was achieved with two cw lasers with wavelengths of 397 nm for the main cooling laser and 866 nm for the repumper laser. The lasers excited optical fibers on the experimental table and were guided to the center of the trap through flange 5. The 397 nm and 866 nm lasers were combined and overlapped with a dichroic mirror before entering the chamber. The path of the 866 nm laser was split by a polarizing beam splitter (PBS) in order to enter the experimental chamber additionally through flange 3. This additional beam path was mainly used for the optomechanical readout of the resonance frequencies f_n of the nanowire discussed in chapter 7.1. It further acted as a second axis of the 866 nm laser for increased cooling efficiency.

All lasers were focused to the center of the trap with convex lenses of focal lengths $f = 200$ mm placed in front of the respective flanges. With the exception of the 423 nm laser, all other lasers passed telescopes consisting of pairs of convex and concave lenses in order to obtain the desired beam diameters. The 375 nm and 397 nm lasers were directly placed on the experimental table.

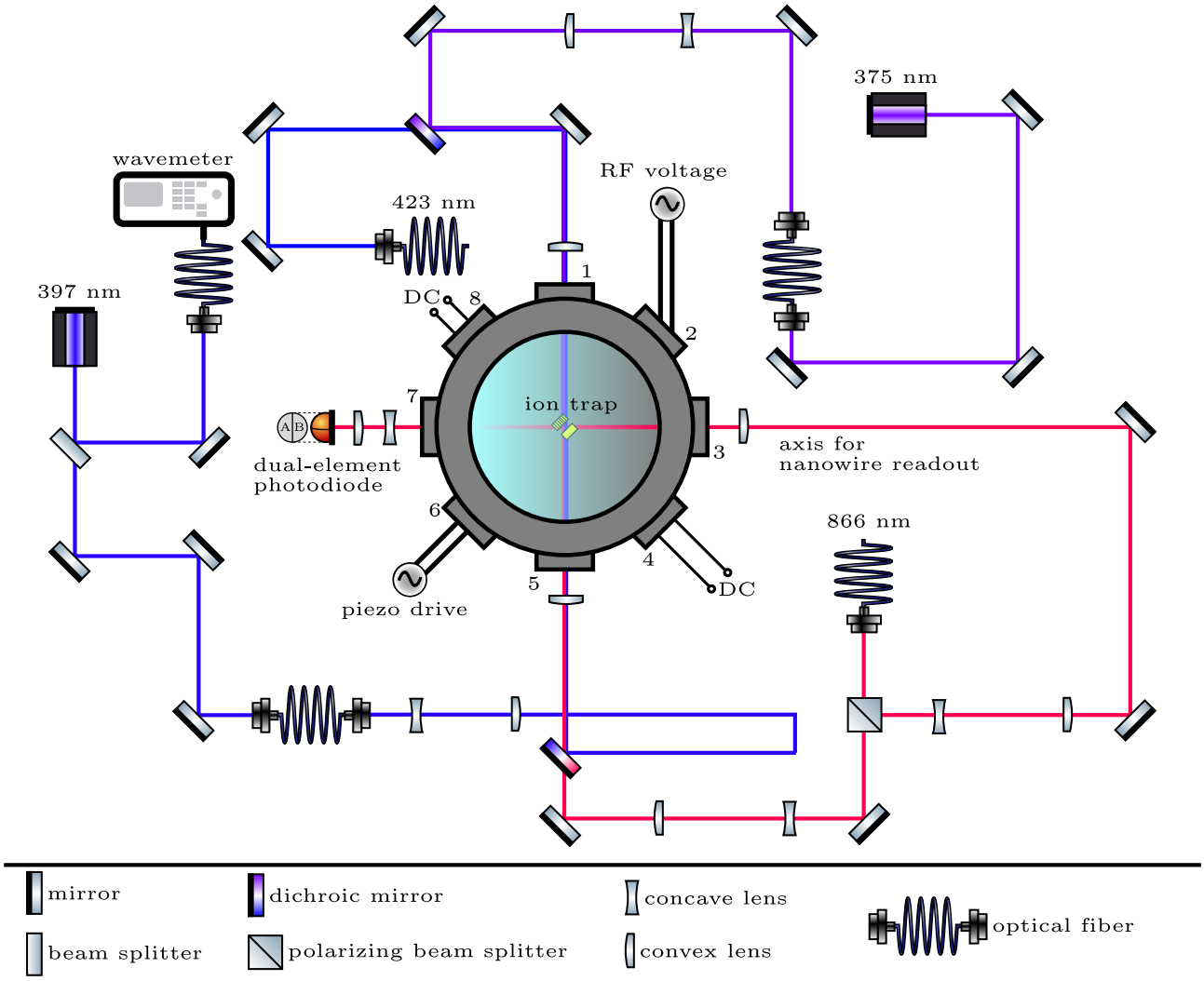

Figure 6.7: Schematic top-down view of the experimental chamber and the laser setup. A 423 nm and a 375 nm continuous-wave (cw) laser were used for the two-step photoionization of neutral calcium atoms. A 397 nm and an 866 nm cw laser were used to drive the cooling transitions $(4s)\ ^2S_{1/2} \leftrightarrow (4p)\ ^2P_{1/2} \leftrightarrow (3d)\ ^2D_{3/2}$ of $^{40}Ca^+$. The 397 nm and 375 nm laser diodes were placed on the experimental table, while the 866 nm and 423 nm laser diodes were placed on a separate optical table for common use throughout the laboratory. All wavelengths were monitored with a wavemeter. The resonance frequencies f_n of the nanowire were determined with an optomechanical readout performed with a dual-element photodiode measuring the incident light from a second axis of the 866 nm laser (see also chapter 7.1). The optical elements were provided by [177].

The 423 nm and 866 nm diode lasers were placed on a separate optical table and shared for common use in the laboratory.

The wavelengths of the 423 nm, 397 nm and 866 nm lasers were monitored with a wavemeter (HighFinesse WS-U) on a separate experimental table. A LabView program [178, 179] allowed the locking of the wavelengths to desired values by dynamically adjusting the piezo-controlled gratings inside the cw lasers with a PID feedback loop. The wavemeter was regularly calibrated. The wavelength of the 375 nm laser was not monitored, as it simply required to exceed the ionization energy (see figure 6.4a).

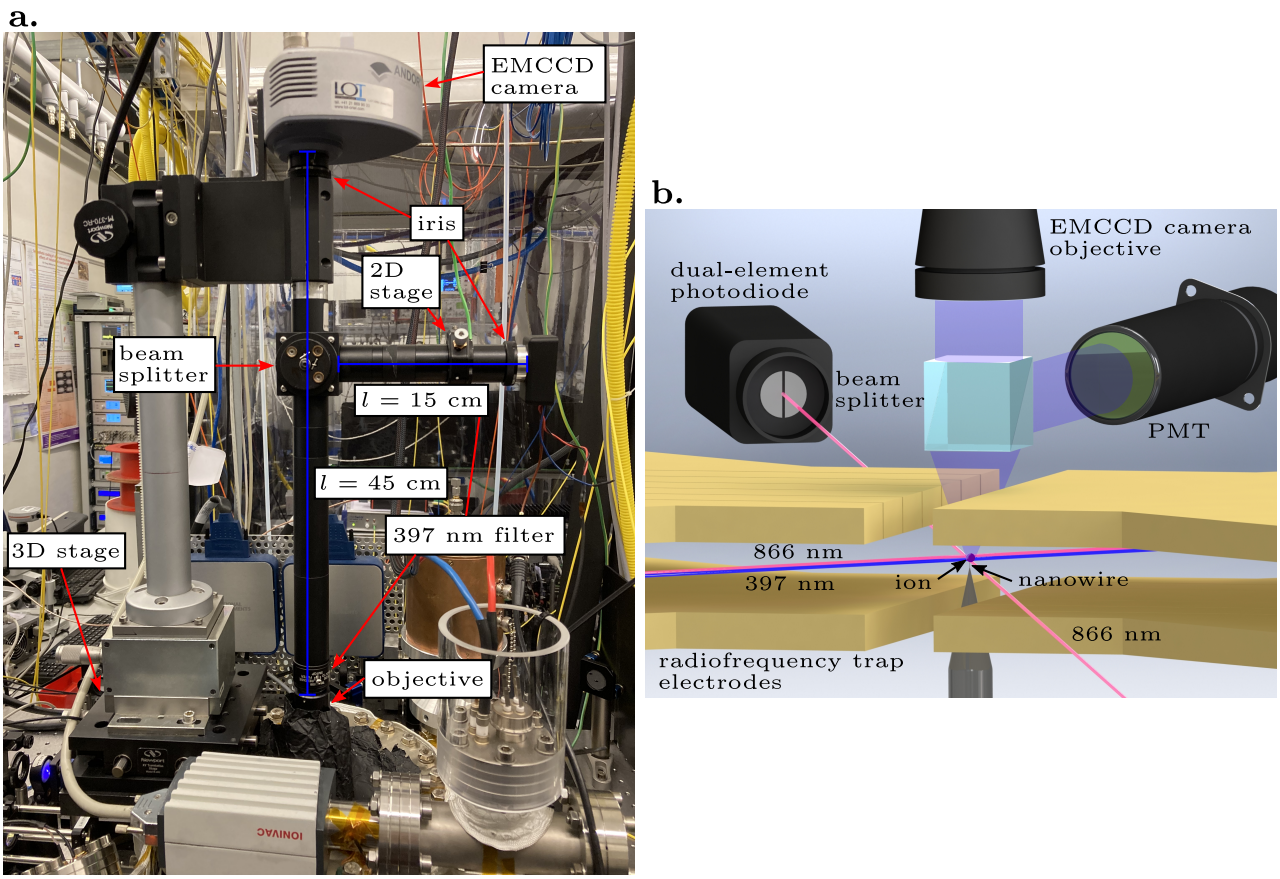

Figure 6.8: Optical setup for the imaging of trapped ions and the nanowire. **a**, Photograph of the ion imaging and detection system. An EMCCD camera was positioned above the experimental chamber for the resolved imaging of trapped ions as well as for the control of the horizontal position of the nanowire inside the trap. A 50:50 beams splitter guided half of the light onto a PMT positioned perpendicular to the camera. The PMT was used for the detection of ion fluorescence rates and the determination of driven ion motion. **b**, Schematic of the setup shown in **a**. The EMCCD camera and the PMT were used for the resolved imaging and detection of the emitted 397 nm light from trapped $^{40}Ca^{+}$ ions. The dual-element photodiode was used for the optomechanical readout of the eigenfrequencies of the nanowire (see chapter 7.1).

6.5 Ion Imaging and Detection Systems

Figure 6.8 shows a photograph and a schematic of the components used for the imaging and detection of the 397 nm fluorescence emitted by the laser-cooled $^{40}Ca^{+}$ ions. The setup consisted of an EMCCD camera for the spatially resolved imaging of trapped ions and a photon-multiplier tube (PMT) for the detection of fluorescence rates and single photons emitted by the trapped ions. The 397 nm photons scattered by spontaneous emission of the ions were separated with a 50:50 beam splitter to reach the camera and the PMT equally.

6.5.1 EMCCD Camera

An EMCCD camera (Andor Luca) with 1004 × 1002 pixels (pixel size = 8 µm × 8 µm) was positioned on top of the main vacuum chamber. It enabled the resolved imaging of trapped ions in the horizontal plane by collecting the scattered photons of the laser-cooled 397 nm $4S_{1/2} \leftrightarrow 4P_{1/2}$ transition. Figure 6.9 shows an EMCCD image of an ion string consisting of two

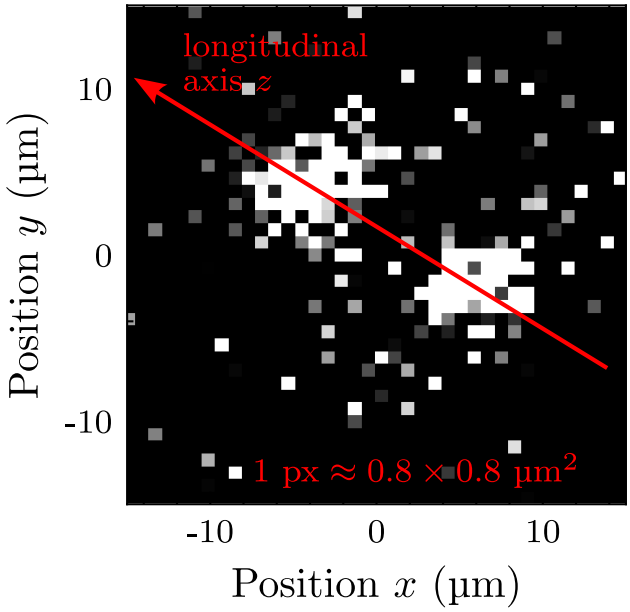

Figure 6.9: EMCCD image of a string of two trapped ions. The ion string extended along the symmetry axis z of the trap (red arrow). The positions x, y correspond to the position of the image on the CCD chip of the camera. The camera was rotated by $\approx 45°$ with respect to the symmetry axis of the trap. One pixel on the EMCCD camera corresponded to an area of 0.8×0.8 µm^2 in the image.

trapped $^{40}Ca^+$ ions.

The camera featured a Nikon 5X-A objective attached to a tube of diameter $d = 2.54$ cm (one inch) and length $l = 45$ cm, resulting in a magnification of ≈ 10 (see figure 6.9). The camera was positioned on a two-dimensional translation stage (Newport M-406) for horizontal positioning and a one-dimensional vertical linear stage (Newport M-MVN80) for vertical positioning. The height of the camera was chosen such that it was focused on the horizontal plane of the trapped ions. During operation of ion trapping experiments, a 397 nm filter was placed inside the camera tube in order to suppress the detection of scattered light from the 866 nm repumper laser and other background sources. The filter was removed if other procedures, such as laser alignment, positioning of the nanowire or the detection of neutral atoms, were performed.

In order to suppress background from scattered 397 nm light, an iris was positioned directly in front of the EMCCD chip of the camera. The iris was closed until only the scattered light from the ions was visible on the camera, significantly increasing the signal-to-background ratio.

Additionally, background light from the laboratory was suppressed by covering all viewports of the main vacuum chamber with blackout material.

The camera was controlled with a custom made graphical user interface (GUI) [180]. Dur-

ing experiments with trapped ions, the exposure time of a single frame of the camera was set to $T_{\text{exp}} = 0.1$ s and the gain of the camera was set to $G = 1000$. The image shown by the GUI was set to a running average of the last five frames captured by the camera. This increased the signal-to-background ratio additionally by averaging out the random nature of the background noise.

6.5.2 Photon-Multiplier Tube

A photon-multiplier tube (PMT, Hamamatsu H12386-210) was used for the detection of single scattered 397 nm photons. This allowed the precise determination of fluorescence rates and was the crucial addition to the setup for the detection of driven ion motion with the photon-correlation method (more details in chapters 7.3.2 and 11).

The PMT was attached to the end of a one-inch tube perpendicular to the EMCCD camera (see figure 6.8). Half of the 397 nm photons scattered from trapped ions were guided onto the PMT with a 50:50 beam splitter. The model of the PMT was chosen for 397 nm light, specifically. However, a 397 nm filter was additionally added inside the tube to suppress the detection of other wavelengths further. As for the EMCCD camera, an iris was added directly in front of the PMT to suppress scattered 397 nm background light.

The length of the one-inch tube leading to the PMT was $l = 15$ cm. It was chosen such that the plane of the image on the EMCCD camera coincided with the plane of the image on the PMT. A two-dimensional linear stage element allowed the positioning of the center of the PMT on the light scattered from the ions. The PMT was positioned in such a way that the image shown on the EMCCD camera coincided closely to the image/photons detected by the PMT.

6.6 Electrical Setup

6.6.1 DC Voltage Supply

The static voltages for the DC electrodes of the trap, the nanowire and the compensation electrode were supplied with a digital-to-analog converter (DAC) card (NI PXIe-6739). The outputs of the DAC card were connected to the electrical feedthroughs featured in flanges 4 and 8 (see figure 6.7). All cables inside of the vacuum chamber were coated with Kapton. The outputs of the DAC card were controlled with a custom-made graphical user interface [180].

Figure 6.10a schematically shows the electrical circuit for the supply of the static voltages to the DC electrodes. For each DC electrode, an output voltage V_{DC} in the range $V_{\text{DC}} \in [-10\text{ V}, 10\text{ V}]$ was connected to a single channel on the printed circuit board (PCB) of the trap via spring-loaded pin connectors (see figure 6.1b). Each channel of the PCB was then connected to its

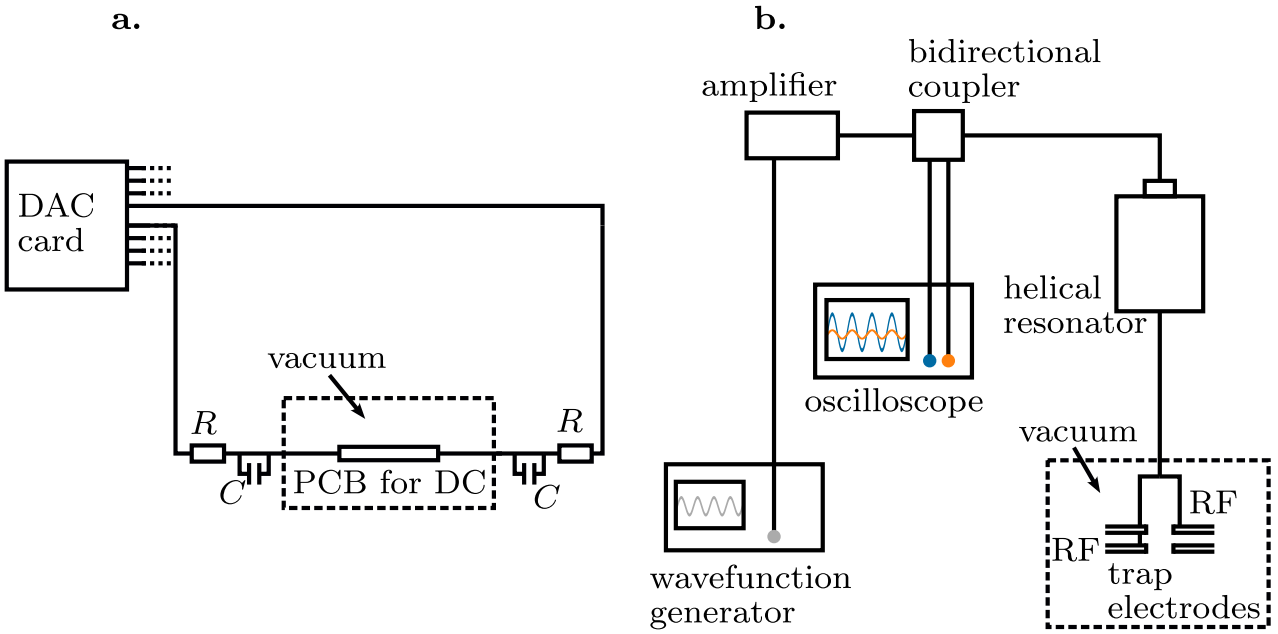

Figure 6.10: Schematics of the electrical circuits for the supply of DC and RF voltages. **a**, Static voltages were supplied to the DC electrodes, the nanowire and the compensation electrode with a digital-to-analog converter (DAC) card. Resistors ($R = 100$ kΩ) and capacitors ($C = 10$ µF) on the outside of the vacuum chamber acted as low-pass filters with a cut-off frequency of $\omega = 1$ Hz in order to suppress pickup from the RF electrodes. **b**, The sinusoidal RF voltage was generated with an arbitrary wavefunction generator. It was supplied to the RF electrodes after passing an amplifier, a bidirectional coupler and a helical resonator. The bidirectional coupler allowed the monitoring of the transmitted and reflected signal on an oscilloscope. The helical resonator enabled the impedance matching of the RF circuit to the trap. It further acted as a band-pass filter with resonance frequency $f_0 = 21.432$ MHz and quality factor $Q \approx 53$.

designated DC electrode segment by wire bonding with aluminum bonds. Each connection featured a resistor of $R = 100$ kΩ connected in series and a capacitor of $C = 10$ µF connected in parallel on the outside of the vacuum chamber. These elements acted as low-pass filters with a cut-off frequency of $\omega = 1$ Hz in order to suppress pickup from the RF electrodes. Additionally, small capacitors with $C = 1000$ pF were directly mounted on each channel of the PCB inside the vacuum chamber. However, those were parts of the original design of the trap [80] and their contribution to the RC low-pass filter was negligible due to the addition of the capacitors on the ouside of the vacuum chamber.

The static voltages for the nanowire and the compensation electrode were supplied by the same DAC card through flange 8. However, the voltages were not supplied via the PCB inside of the vacuum chamber. Instead, the voltages were directly supplied to the respective element via Kapton-coated wires inside of the chamber. As with the DC electrodes, the nanowire and the compensation electrode featured resistors ($R = 100$ kΩ) and capacitors ($C = 10$ µF) on the outside of the vacuum chamber to act as RC low-pass filters.

6.6.2 RF Voltage Supply

Figure 6.10b schematically shows the electrical circuit for the supply of the radiofrequency voltage to the RF electrodes. The sinusoidal radiofrequency voltage was generated with an arbitrary wavefunction generator (Tektronix AFG1062). It subsequently passed an RF amplifier (Mini Circuits ZHL-1-2W-S+, gain $G \approx 32$ dB) followed by a bidirectional coupler (Mini Circuits ZFBDC20-61HP+). The bidirectional coupler allowed the monitoring of the RF signal transmitted to and reflected from the trap. The transmitted and reflected signals were monitored on an oscilloscope.

A helical resonator [181] was added to the circuit. The helical resonator allowed impedance matching of the RF source to the trap [182] and acted as an additional frequency filter for the supply of the RF voltage [183]. More details on the helical resonator are given in chapter 6.6.3.

The radiofrequency voltage was supplied to the RF electrodes through electrical feedthroughs in flange 2 (see figure 6.7). On the inside of the vacuum chamber, a single Kapton-coated wire was connected to the RF electrodes via pin connectors that were directly soldered onto the electrodes, as can be seen in figure 6.1b.

6.6.3 Radiofrequency Helical Resonator

For the supply of the sinusoidal radiofrequency to the RF electrodes, a *helical resonator* [181] was added to the electrical circuit. Figure 6.11 shows a photograph and a schematic drawing of the helical resonator used for the work presented in this thesis. It consisted of a cylindrical copper case with two coils on the inside. The *main helix* was a coil with fixed position and directly connected to the RF electrodes on one end. The other end of the main helix was shorted to the copper case with a BNC cap. The *antenna coil* was a small coil connected to a copper lid and inserted on the opposite side of the helical resonator. The vertical position of the antenna coil could be adjusted and the lid could be fixed by a screw on the outside of the case. One end of the antenna coil was supplied with the incoming RF voltage, while the other end was shorted to the case.

Helical resonators are often used in ion trapping experiments [181, 182, 184] and allow impedance matching of the electrical radiofrequency circuit to the trap [184]. This suppresses the reflected signal from the incoming RF voltage and increases the efficiency of the applied RF voltage. Furthermore, the addition of a helical resonator to the circuit introduces a *resonance frequency* f_0 given by the resulting RLC circuit [184]. The resonator thus acts as a band-pass filter and suppresses noise from undesired frequency components [183, 184].

The helical resonator was optimized by adjusting the vertical position of the antenna coil and simultaneously monitoring the amplitude of the reflected signal from the bidirectional coupler

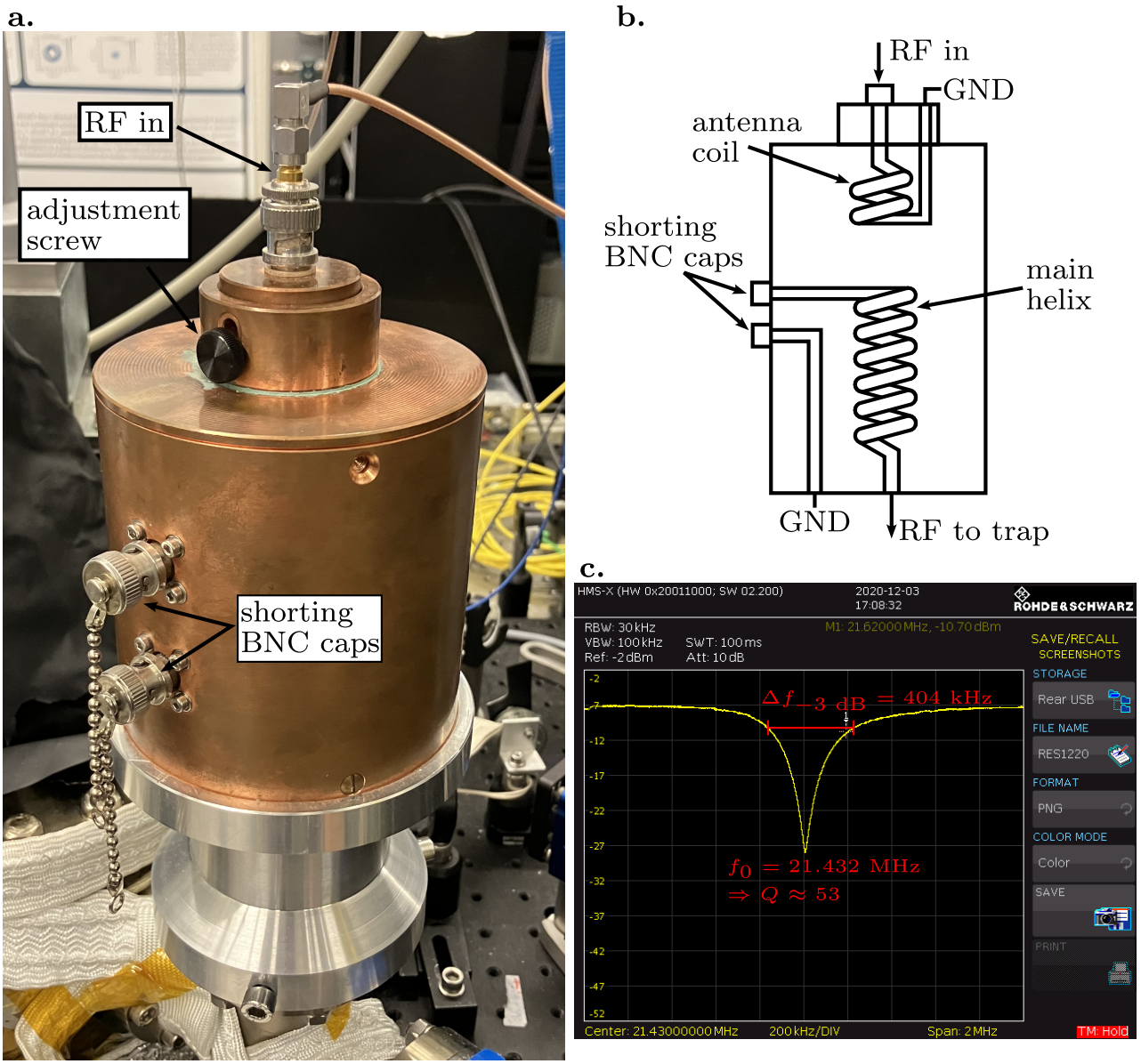

Figure 6.11: Helical resonator for the supply of the sinusoidal radiofrequency voltage. **a**, Photograph of the helical resonator used in the experiment. **b**, Schematic drawing of the helical resonator. **c**, Characterization of the helical resonator. The power of the reflected signal was measured with a spectrum analyzer while scanning the applied radiofrequency.

on an oscilloscope. The position was fixed where the reflected signal was minimized. Additionally, the resonance frequency was roughly determined in a first step by varying the frequency f_{RF} of the applied sinusoidal RF voltage and minimizing the reflected signal simultaneously.

In order to precisely determine the resonance frequency f_0 of the circuit, the power of the reflected signal was measured with a spectrum analyzer. As shown in figure 6.11c, the frequency of the applied radiofrequency voltage f_{RF} was scanned in the range $f_{\mathrm{RF}} \in [20.43\ \mathrm{MHz}, 22.43\ \mathrm{MHz}]$, resulting in the spectrum of the helical resonator with the resonance frequency at $f_0 = 21.432\ \mathrm{MHz}$. The width of the spectrum at -3 dB defines the quality factor Q of the helical resonator. It is given by [182]:

$$Q = \frac{f_0}{\Delta f_{-3\,\mathrm{dB}}}. \tag{6.1}$$

The quality factor Q is a measure for how well frequencies other than f_0 are suppressed by the helical resonator. For our resonator, we found:

$$Q \approx 53. \tag{6.2}$$

Over the course of this project, the resonance frequency of the circuit slightly shifted from $f_0 = 21.432$ MHz to $f_0 = 21.629$ MHz reported in the experimental results (see chapter 11). The shift came about due to small changes and replacements of electrical components. We further observed a gradual shift of the resonance frequency after turning on the radiofrequency supply. This shift occurred over a few minutes and eventually reached an equilibrium. Due to this, the radiofrequency supply was left running continuously to ensure constant operation at the resonance frequency f_0 at equilibrium.

6.7 Vacuum Components

The stable trapping of ions requires a low background pressure inside of the vacuum chamber in order to suppress collisions with background gas [42]. In order to achieve ultra-high-vacuum (UHV) pressures of $P < 10^{-8}$ mbar, two pumping units were included in the experimental setup.

In a first step, a modular pumping station [80] (Pfeiffer HiCube) with a small integrated turbomolecular pump reduced the pressure inside of the chamber to around $P \approx 10^{-8}$ mbar. In a second step, a larger turbomolecular pump (Oerlikon MAG W600) attached below the main vacuum chamber reduced the pressure to UHV at around $P \lesssim 10^{-10}$ mbar. The pressure inside of the main vacuum chamber was monitored with a hot-cathode gauge (Ionivac).

The pressure obtained from simple pumping of the vacuum chamber is typically limited due to residual gas consisting mainly of H_2O inside of the chamber. In order to reduce the pressure further and remove the remaining H_2O, the walls of the main vacuum chamber were heated with heating tapes to temperatures of $T \approx 200$ °C in a *bakeout* process. The final temperature of $T = 200$ °C was gradually applied to the chamber over the course of one to two days. The system was baked at the final temperature for one to two weeks. Furthermore, a titanium sublimation pump (Varian) was used for the gettering of other residual gases such as H_2, N_2 and O_2 [185].

Over the course of this project, we were typically able to reach pressures of $P < 5 \times 10^{-10}$ mbar (the limit of the hot-cathode gauge) with the use of the vacuum components and the bakeout

process described above. However, the chamber was reopened and reclosed several times during the project and we were only able to reach a pressure of $P \approx 2 \times 10^{-9}$ mbar after the last closing of the main vacuum chamber. We suspect the reason for this to be leaks in some of the CF40 flanges, possibly due to excessive tightening of the flanges. The trapping of single ions and Coulomb crystals was still possible and the ions typically remained trapped for around ten minutes.

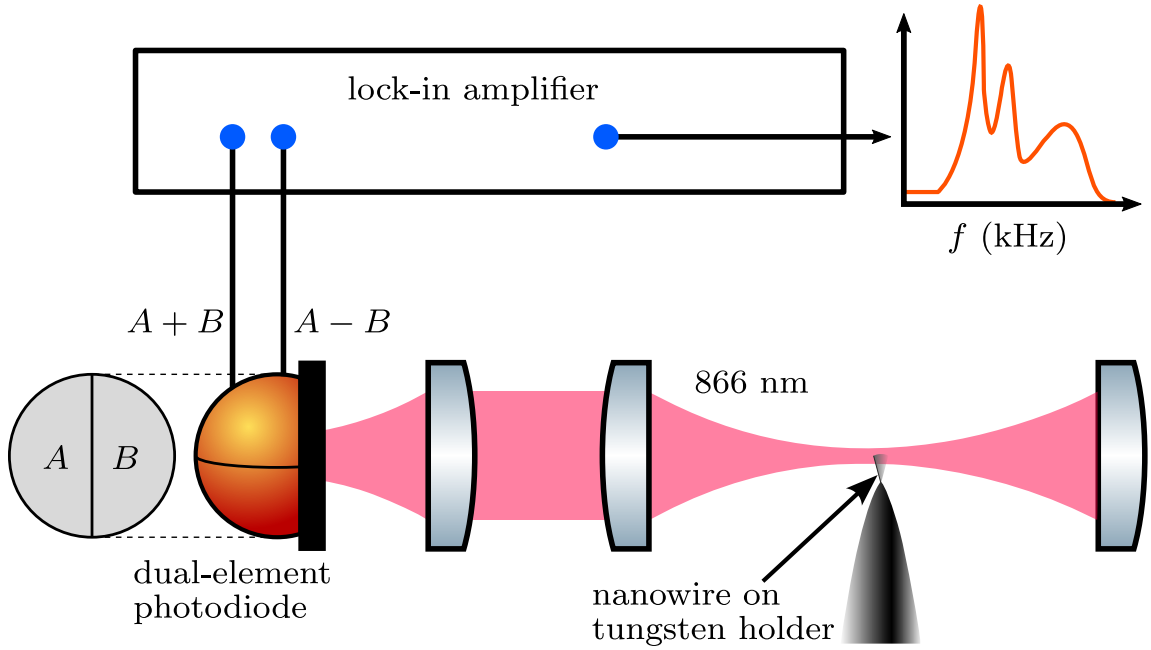

Figure 7.1: Optomechanical setup for the readout of the resonance frequencies of the mechanical oscillator. The tip of the nanowire assembly was positioned in the focus of an incoming 866 nm laser beam. The exiting light was collected on a dual-element photodiode on the opposite side of the experimental chamber. The signal measured on the photodiode was modulated by the oscillations of the mechanically driven nanowire. Demodulating the signal with a lock-in amplifier while scanning the drive frequency f_{drive} yielded the resonance spectrum of the mechanical oscillator. The drawings of the optical elements were provided by [177].

7 Experimental Techniques

7.1 Optomechanical Readout of the Nanowire Frequency Spectrum

The characterization of the vibrations and resonance frequencies of the nanowire assembly was performed inside the experimental chamber using an optomechanical readout [69, 186]. The setup used is schematically shown in figure 7.1.

The 866 nm laser entering the experimental chamber (see also figure 6.7) was focused onto the tip of the nanowire as shown in figure 7.1. A lens with focal length $f = 200$ mm placed outside of the experimental chamber focused the beam diameter down to $d_{\text{focus}} \approx 55$ µm. The light of the beam exiting the chamber on the opposite side was collected on a dual-element Si PIN photodiode (Hamamatsu S4204).

The photodiode transmitted a sum signal $A + B$ and a difference signal $A - B$ to a lock-in amplifier (Zurich Instruments HF2LI) as shown in figure 7.1. The mechanically driven nanowire was placed in the focus of the beam, leading to modulations of the signal measured by the photodiode. The magnitude of the modulations depended on the amplitude of the driven nanowire. Mechanically driving the nanowire and simultaneously demodulating the signal as a function of the drive frequency f_{drive} yielded the response spectrum of the oscillator with the resonance frequencies f_n shown in figure 7.2.

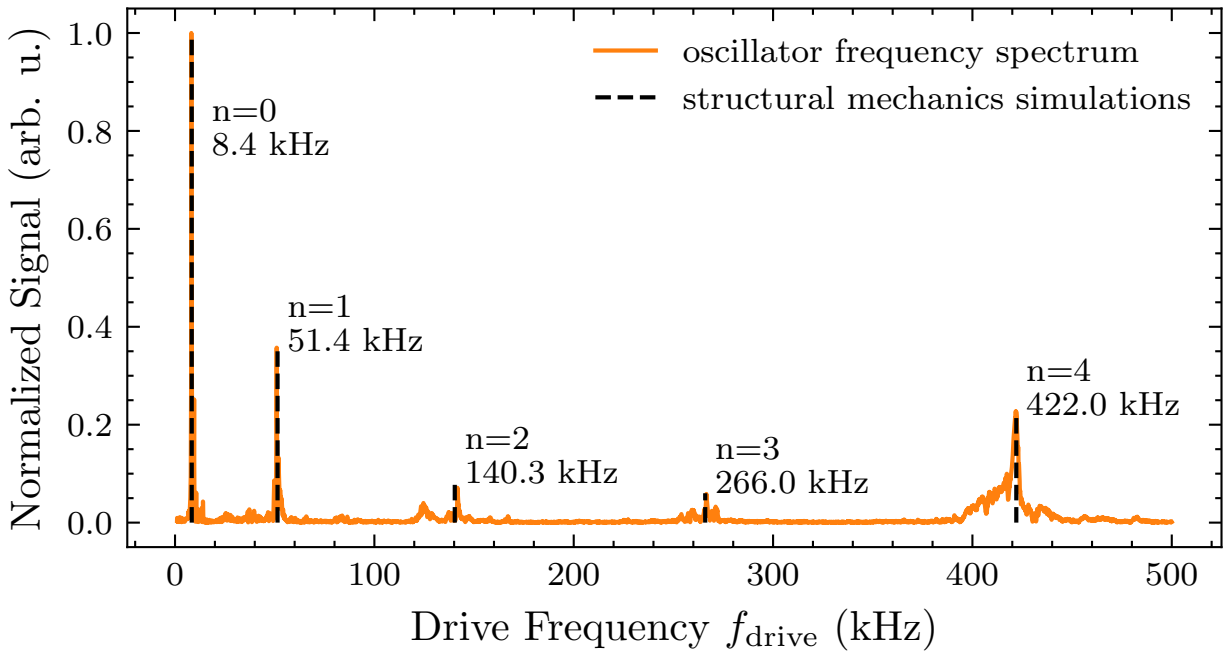

Figure 7.2: Resonance frequencies of the nanowire assembly. The frequency spectrum of the oscillator (orange) was determined by an optomechanical readout [69, 186]. The experimentally obtained resonance frequencies f_n follow the expected distribution derived from the Euler-Bernoulli beam theory in chapter 5. They are in good agreement with the values obtained from the structural mechanics simuations discussed in chapter 6.2.2 (dashed black lines).

Ideally, the diameter d_{focus} of the focus of the imaging laser should be smaller than the length of the nanowire l_{nw} for the optomechanical readout of the resonances f_n, i. e., $d_{\mathrm{focus}} < l_{\mathrm{nw}}$. This is best obtained with optics of low focal lengths f positioned in-vacuum and close to the tip of the nanowire. The lens used in the setup with focal length $f = 200$ mm restricted the obtainable size of the 866 nm focus to an upper limit of $d_{\mathrm{focus}} \approx 55\ \mu\mathrm{m} > l_{\mathrm{nw}}$. This made the detection of an isolated mode of the nanowire impossible. However, the optomechanical readout was still feasible to determine the relevant resonances of the *combined* geometry of the nanowire and the tungsten holder as discussed in chapter 6.2.2. The experimentally obtained resonance frequencies f_n shown in figure 7.2 were in good agreement to the frequencies obtained from the structural mechanics simulations shown in figure 6.6.

7.2 Determination of Trap Frequencies

The matching of the axial trap frequency $f_z = \frac{\omega_z}{2\pi}$ of trapped ions to a resonance f_{nw} of the nanowire assembly (see figure 7.2) was crucial for the efficient transfer of energy between the two systems. As discussed in chapter 9, variations of parameters such as the ion-nanowire distance d and the effective nanowire charge q_{nw} lead to shifts in the effective trapping frequency f_z due to the resulting changes in the interaction potential Φ_{IA}. This required the adjustment of the trapping potential Φ_{trap} with the voltages supplied to the DC electrodes in order to preserve

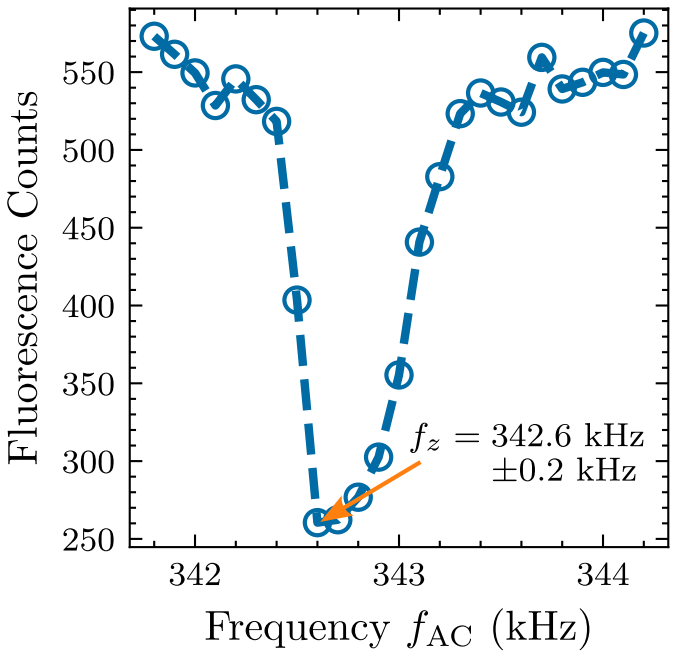

Figure 7.3: Measurement of the axial trap frequency f_z by parametric excitation. The fluorescence of photons scattered on the 397 nm $4^2S_{1/2} \leftrightarrow 4^2P_{1/2}$ transition of trapped $^{40}Ca^+$ ions was measured with the EMCCD camera. A sinusoidal voltage at frequency f_{AC} was applied to the compensation electrode. Scanning of f_{AC} in steps of $\Delta f_{\mathrm{AC}} = 0.1$ kHz yielded a response spectrum with strong excitation of the trapped ions on resonance ($f_{\mathrm{AC}} = f_z$). The resonant excitation lead to a noticeable decrease in the average fluorescence [187]. The axial trap frequency f_z was determined from the minimum of the resulting excitation spectrum (blue curve) with an assigned systematic uncertainty of $\Delta f_z = \pm 0.2$ kHz.

resonance, i. e., $f_z = f_{\mathrm{nw}}$.

The axial frequencies f_z of trapped ions were determined by parametric excitation [187] of the motion of trapped ions. For this, small strings of ions were trapped and an AC voltage component was added to the compensation electrode of the experiment. The frequency f_{AC} of the applied AC voltage was scanned over a desired range. The motion of the ions was resonantly excited when f_{AC} matched the axial trapping frequency f_z, leading to a decrease in the fluorescence of the ions [187] observed on the EMCCD camera as shown in figure 7.3. The frequencies were scanned with step sizes of $\Delta f_{\mathrm{AC}} = 0.1$ kHz and we assigned systematic uncertainties of $\Delta f_z = \pm 0.2$ kHz to the axial trap frequencies f_z obtained from the minima of the fluorescence responses. For each data point, the average of the fluorescence over five frames of the camera was taken. The amplitude of the AC voltage applied to the compensation electrode was chosen to yield clear responses of the fluorescence without ejecting any ions from the trap.

7.3 Photon-Correlation Measurements

7.3.1 Fluorescence of Driven Ion Motion

Doppler-cooled oscillating ions in radiofrequency traps exhibit periodic modulations of the fluorescence of photons scattered on the cooling transition due to their oscillatory motion. Their velocity $v(t) = v_{\max} \cos(\omega t - \varphi)$ leads to a detuning $\delta(t) = \delta_0 - k v_{\max} \cos(\omega t - \varphi)$ periodically Doppler-shifted with respect to the resonance of the electronic cooling transition. The resulting photon scattering rate $R(t)$ in the low intensity limit is given by[120][188]:

$$R(t) = R_0 \frac{(\Gamma/2)^2}{(\Gamma/2)^2 + (\delta_0 - k v_{max} \cos(\omega t - \varphi))^2}. \tag{7.1}$$

Here, R_0 is the scattering rate on resonance, Γ is the natural linewidth of the transition and k is the wave number of the laser.

Figure 7.4 visualizes the oscillations of driven ions along the transition spectrum as well as the corresponding periodic fluorescence distributions. The shapes of the distributions depend on the ion velocity amplitude $v_{\max}$ relative to the initial laser detuning δ_0. The most notable observation is the possible splitting of the fluorescence distributions into double peak structures. Three cases can be identified:

- $k v_{\max} < |\delta_0|$,
- $k v_{\max} = |\delta_0|$,
- $k v_{\max} > |\delta_0|$.

In the case of $k v_{\max} < |\delta_0|$, the ion oscillations remain at total detunings $\delta(t) < 0$ on the transition spectrum. This leads to periodic fluorescence distributions with single maxima after each oscillation period $T = \frac{2\pi}{\omega}$ (see figure 7.4a).

For $k v_{\max} = |\delta_0|$, the ions reach the resonance of the transition $\delta(t) = 0$ in a single point in time per oscillation period $T = \frac{2\pi}{\omega}$, leading to plateau-shaped maxima in the fluorescence distribution (see figure 7.4b).

In the case of $k v_{\max} > |\delta_0|$, the ions exceed the resonance of the transition and reach detunings $\delta(t) > 0$. The corresponding fluorescence distributions start exhibiting double peak structures (see figure 7.4c). This phenomenon occurs because the ions pass the resonance position $\delta(t) = 0$ twice per oscillation cycle. The time splitting of the double peaks is given by $\Delta T = 2 \arccos(\frac{\delta_0}{k v_{\max}})/\omega$ and tends to $\Delta T = \frac{T}{2} = \frac{\pi}{\omega}$ for $v_{\max} \to \infty$.

Another interesting observation lies in the shape of the fluorescence distributions for large initial detunings δ_0 combined with large velocity amplitudes $v_{\max}$ as shown in figure 7.5. In

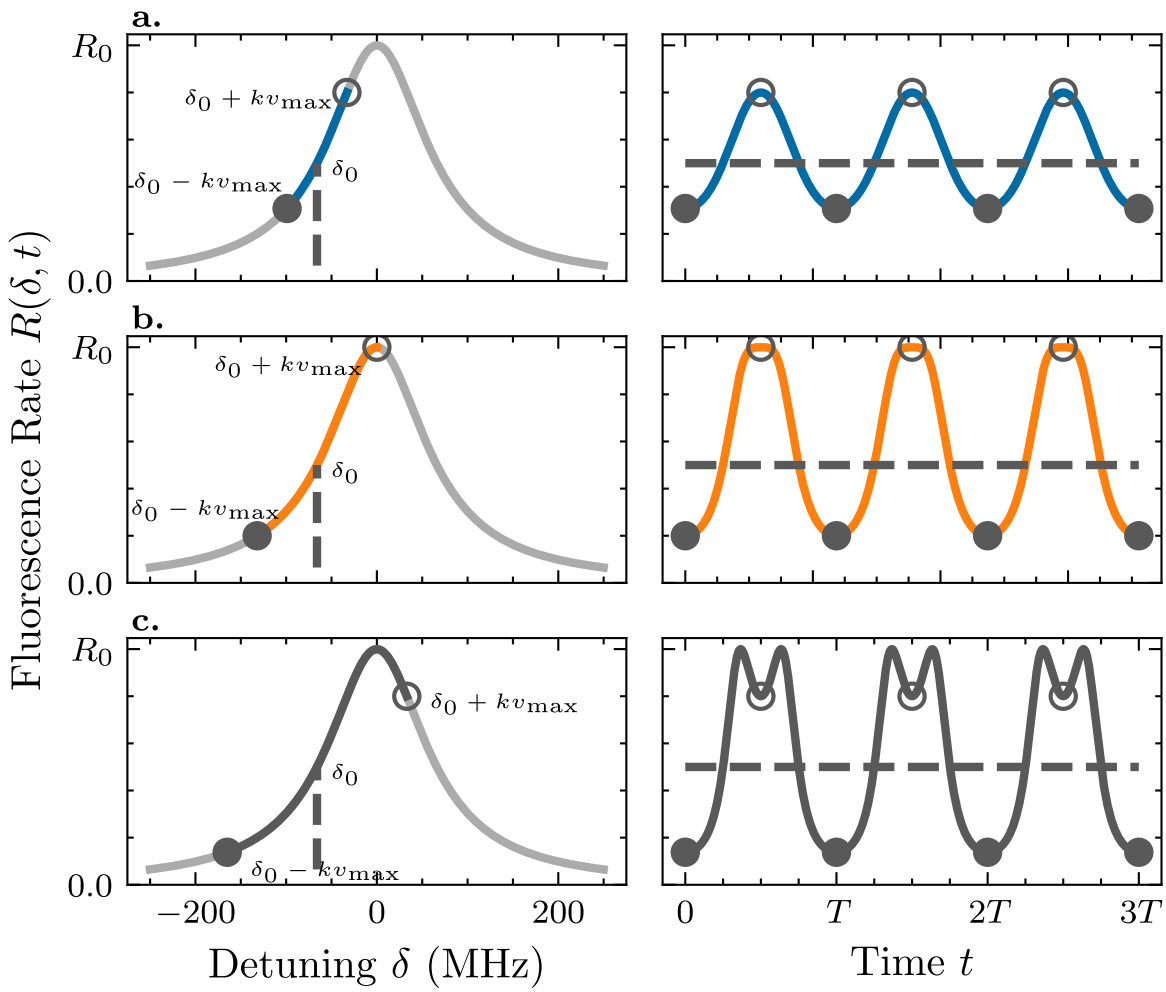

Figure 7.4: Transition spectrum and periodic fluorescence rates of a driven ion at different velocity amplitudes $v_{\max}$. The ion oscillates along the indicated parts of the transition spectrum (blue, orange, dark gray), resulting in the fluorescence rate distributions of the respective color. Points corresponding to δ_0 (dashed lines) as well as the maximum and minimum detunings $\delta_0 \pm kv_{\max}$ (dark gray markers) are indicated in the figures. The shapes depend on the ratio $kv_{\max}/\delta_0$ and exhibit double peak structures for $kv_{\max} > |\delta_0|$ (dark gray). For small $v_{\max}$, the fluorescence rate can be approximated by $R(t) = R_0 + \Delta R \cos(\omega t - \varphi)$ [120, 162].

those cases, the periodic fluorescence distributions can exhibit sharp peaks followed by shallow valleys (see figure 7.5b). This shape occurs because the oscillating ions experience significantly higher gradients of the transition spectrum in the region $\delta(t) > \delta_0$ than in the region $\delta(t) < \delta_0$.

For small velocity amplitudes $v_{\max}$, the scattering rate given by equation 7.1 can be Taylor expanded to first order and described by a (co-)sinusoidal behavior [120, 162]:

$$R(t) \approx R_0 + \Delta R \cos(\omega t - \varphi) \tag{7.2}$$

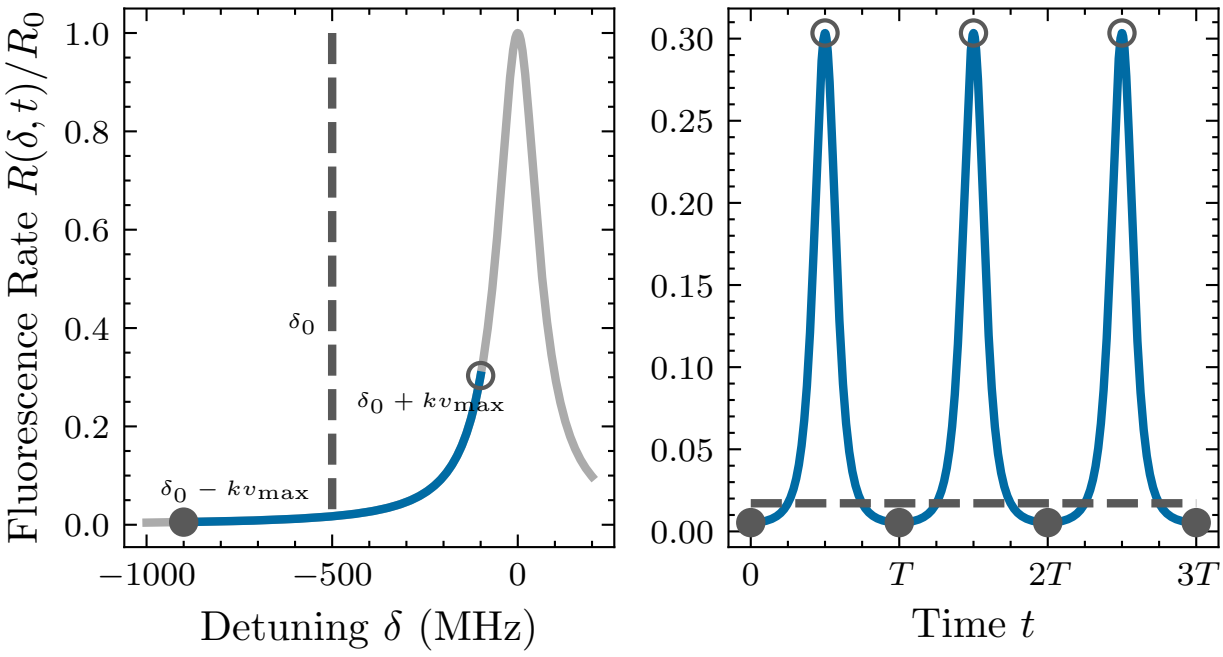

Figure 7.5: Transition spectrum and fluorescence rate of periodically driven ion motion at high laser detunings δ_0. The driven ion oscillates along the blue line in the transition spectrum at high velocity amplitudes $v_{\max}$. The high gradient of the spectrum in the region $\delta(t) > \delta_0$ leads to sharp peaks in the periodic fluorescene rate distribution. The low gradient region $\delta(t) < \delta_0$ corresponds to the shallow valleys of the fluorescence rate below the dashed gray line.

7.3.2 The Photon-Correlation Method

The periodic fluorescence rate of trapped ions given by equation 7.1 was experimentally resolved with the photon-correlation method [162]. The photon-correlation method is typically used for the determination and minimization of excess *micromotion* of trapped ions [120, 162], since micromotion is inherently *driven* motion at the angular radiofrequency Ω [53, 162, 188].

For this work, the photon-correlation method was extended to measure the *secular* motion of trapped ions mechanically driven by the nanowire. Its implementation proved crucial for the observation and quantification of the ion-nanowire coupling in the classical regime.

The underlying principle is the correlation of the periodic scattering rate $R(t)$ given by equation 7.1 to a periodic reference signal with angular frequency $\omega_{\text{ref}} = 2\pi f_{\text{ref}}$. As shown in figure 7.6, a photon multiplier tube (PMT) detecting single fluorescence photons scattered on the 397 nm cooling transition of $^{40}Ca^{+}$ initialized time measurements at t_{start} by sending a pulse to a universal time interval counter (Stanford Research Systems SR620). The time measurements were stopped at t_{stop} when the reference signal at ω_{ref} reached the next zero crossing with a negative slope.

By design, the stop signal was triggered periodically after each time step $T_{\text{ref}} = \frac{2\pi}{\omega_{\text{ref}}}$. Photon detection events triggering the start signals, however, followed a probability distribution

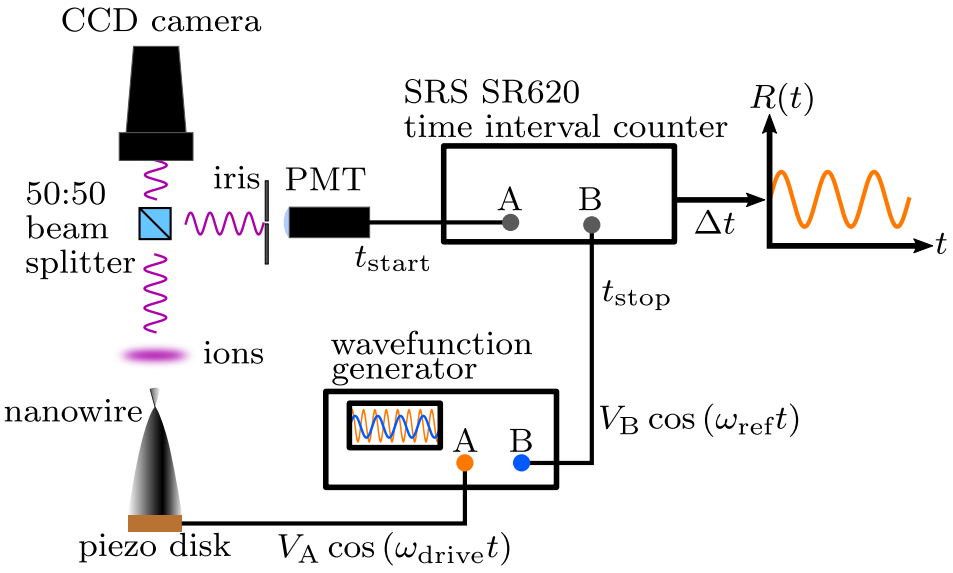

Figure 7.6: Experimental setup for the photon-correlation method. Trapped ions were mechanically driven by the nanowire at the angular drive frequency ω_{drive}. Single photons of the driven ion fluorescence detected by a PMT started a time measurement at t_{start}. The time measurement was stopped at t_{stop} when a sinusoidal reference signal at frequency f_{ref} reached a zero-crossing with negative slope. The distribution of the time intervals $\Delta t = t_{\text{stop}} - t_{\text{start}}$ over several measurements (typically $N = 10^5$) corresponded to the periodic fluorescence rate of the driven ions. The velocity amplitude v_{max} of the driven ion motion was determined by fitting of equation 7.1 to the distribution. The drive frequency and the reference frequency were perfectly phase-coherent with $\omega_{\text{ref}} = \frac{1}{3}\omega_{\text{drive}}$.

proportional to the periodic photon scattering rate $R(t)$ of driven ions given by equation 7.1. Start signals were thus more likely to be triggered at periodic times t at which the ions were closer to the resonance of the transition due to the periodically Doppler-shifted detuning $\delta(t)$.

The time differences $\Delta t = t_{\text{stop}} - t_{\text{start}}$ obtained from samples containing several time measurements were binned and presented in histograms as shown in figure 7.7. In order to be able to detect the periodic fluorescence of ions driven at ω_{drive}, the reference frequency ω_{ref} needed to be perfectly phase-coherent with the driven motion. This was ensured by applying the drive and reference from two outputs of a single device and choosing an integer-multiple relation between the applied frequencies. By choosing $\omega_{\text{ref}} = \frac{1}{3}\omega_{\text{drive}}$, three periods of the driven motion were resolved. Any motion not exactly coherent with ω_{ref} was averaged out and showed no correlation (see figure 7.7a).

7.3.3 Experimental Implementation

A universal time interval counter (Stanford Research Systems SR620) was used for the time measurements for the photon-correlation method performed in our experiments. A PMT (Hamamatsu H12386-210) was used for the detection of the ion fluorescence. This PMT model was pre-optimized by the manufacturer and directly generated rectangular output pulses at a height

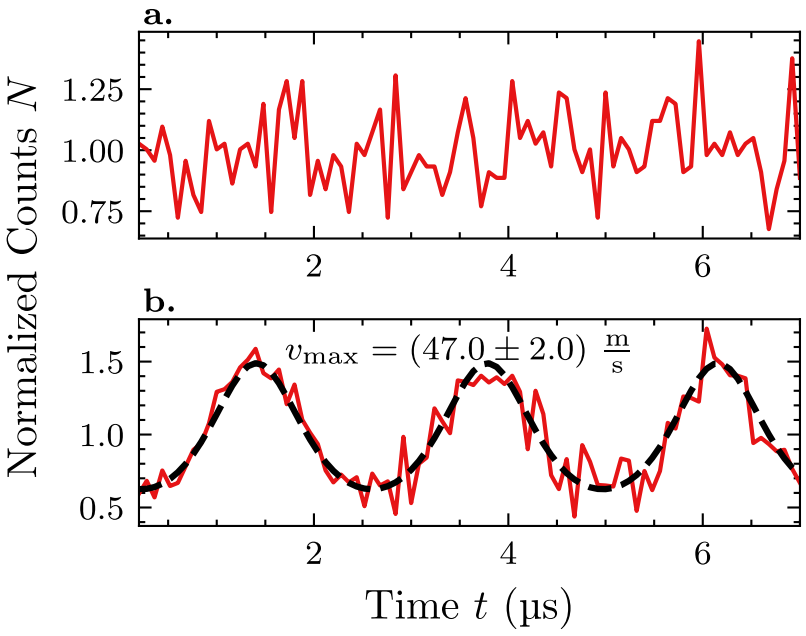

Figure 7.7: Histograms of fluorescence rates $R(t)$ obtained with the photon-correlation method. **a**, Measurement of the background fluorescence without any trapped ions. The scattered 397 nm light of the background was entirely uncorrelated to the reference signal at frequency f_{ref}. This is evident by the random distribution of the fluorescence. **b**, Measurement of the fluorescence of a two-ion string mechanically driven by the nanowire at $f_{\mathrm{drive}} = 422$ kHz. The distribution of the fluorescence shows a clear periodic behavior. It is perfectly correlated to the reference signal at frequency $f_{\mathrm{ref}} = \frac{1}{3} f_{\mathrm{drive}}$ and three periods are resolved. The velocity amplitude obtained from a fit of equation 7.1 was $v_{\max} = (47.0 \pm 0.2)\ \frac{\mathrm{m}}{\mathrm{s}}$. The sample size of both histograms was $N = 10^5$. The histograms were normalized as discussed in chapter 7.3.4.

of 2 V and with a length of 10 ns for each photon detection event. A time measurement `START` signal at t_{start} was triggered by the time interval counter on the positive slope at 1 V of a PMT pulse.

The periodic reference signal at angular frequency $\omega_{\mathrm{ref}} = 2\pi f_{\mathrm{ref}}$ was given by a sinusoidal voltage of amplitude $V_{\mathrm{ref}} = 10$ V generated from one of two outputs of a lock-in amplifier (Zurich Instruments HF2LI). The time measurement `STOP` signal at t_{stop} was triggered whenever the reference signal reached 0 V at a negative slope. The thresholds for the triggering of the `START` and `STOP` signals were chosen to minimize the trigger error in time.

Once a time measurement was triggered, no new measurements could be started by additional photon detection events until the active measurement was finished. However, this typically did not occur since the photon detection rate on the PMT was much lower (≈ 1 kHz) than the reference frequency (typically $f_{\mathrm{ref}} \approx 140$ kHz).

The time interval counter continuously performed time measurements until a selected sample size N was reached. The data was directly binned into a 250-bin histogram of chosen bin size. The data was read out via a serial RS-232 connection to a computer. In the experiments presented in this thesis, the selected sample size was typically $N = 10^5$. The time to obtain a

full sample was ≈ 2 minutes. The sample size $N = 10^5$ was chosen due to the limited life time of the trapped ions of a few minutes.

The nanowire was mechanically driven by a sinusoidal voltage at angular frequency ω_{drive} applied to the attached piezo disk actuator (see chapter 6.2). The drive voltage was generated from a second output of the lock-in amplifier. By choosing $\omega_{\text{ref}} = \frac{1}{3}\omega_{\text{drive}}$, the signals were guaranteed to be phase-coherent and the resulting histograms showed three periods of the ion fluorescence distributions (see figure 7.7b).

The frequency of the drive was typically set to the resonance of the mechanical oscillator at $f_{\text{drive}} = 422$ kHz (see figure 7.2), except when the off-resonant drive was studied. With a corresponding period of $T \approx 2.4$ µs, the bin size of the histograms was set to 80 ns in order to well resolve the resulting periodic fluorescence rates.

7.3.4 Measurement Protocol & Data Analysis

Prior to each measurement, the background-to-signal ratio B/S was determined in order to perform background corrections to the obtained fluorescence distributions. The signal S was determined by measuring the average fluorescence rate of 397 nm photons detected by the PMT in the presence of trapped ions mechanically driven by the nanowire. The background B was determined by measuring the fluorescence rate of 397 nm photons detected by the PMT *without* any trapped ions, all other conditions kept equal. The ratio for strings of two trapped ions was typically $B/S \approx 80\%$. The SR620 universal time interval counter had a built-in count function to measure the number of detected photons per second on the PMT.

Next, a photon-correlation measurement with mechanically driven trapped ions was started. After the acquisition of a full sample of time measurements (typically $N = 10^5$), the first two and last two bins of the resulting histogram were omitted, because the edge regions systematically showed faulty artifacts.

The histogram was then corrected according to the determined background-to-signal ratio B/S. Since the background light from scattered 397 nm photons was completely uncorrelated to the reference signal at frequency f_{ref} (see figure 7.7a), counts originating from the background were on average evenly distributed and the background was thus uniformly subtracted from the signal. For example, in a histogram consiting of 100 bins and $N = 1000$ total counts at $B/S = 80\%$, a total of 800 background counts would be subtracted. In order to ensure uniform subtraction over all 100 bins, 8 counts would be subtracted from every individual bin.

Lastly, the histogram was normalized by dividing the counts in each individual bin N_{bin} by the average counts $\langle N_{\text{bin}} \rangle$ of the entire histogram. The normalization was performed for better

comparison of different acquisitions at equal conditions and had no influence on the driven velocity amplitude $v_{\max}$ extracted from fitting of equation 7.1. The detuning δ_0 for the fit was determined with a wavemeter (see also chapter 6).

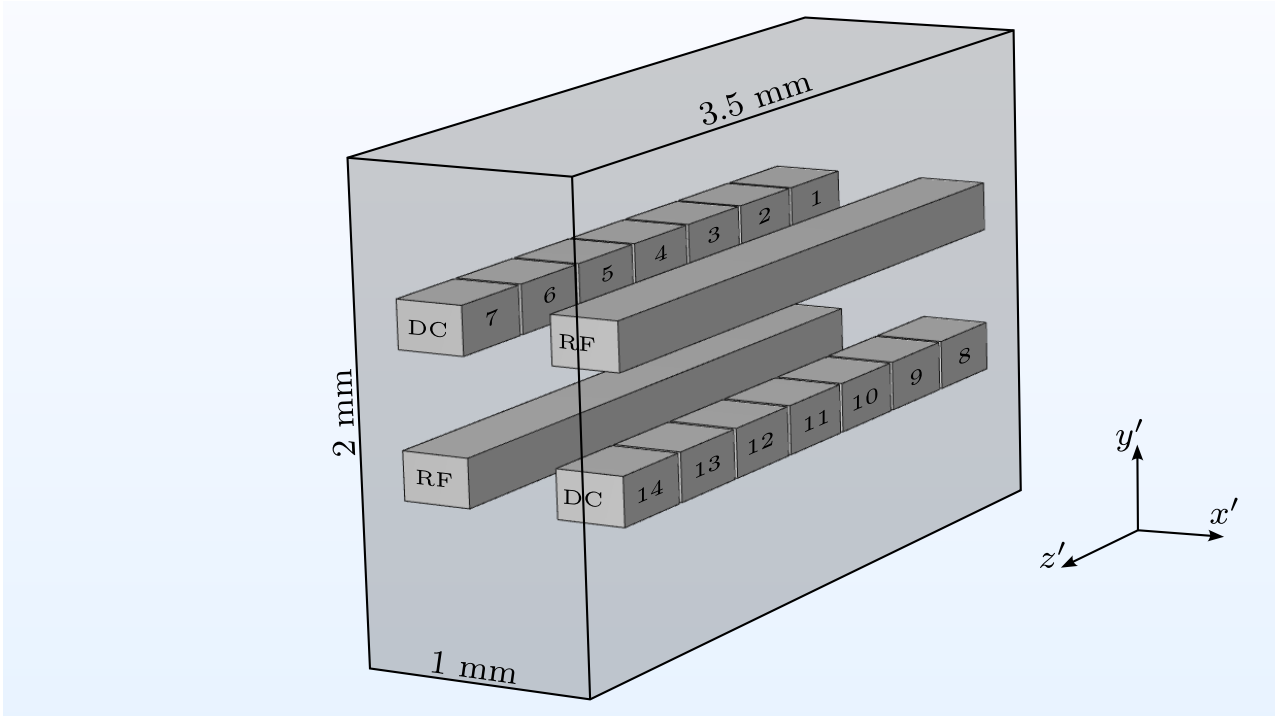

Figure 8.1: Trap geometry for the simulation of trapping potentials with the finite element method. The simulations were performed with Comsol Multiphysics [112]. The geometry consisted of the central parts of the trap located within the region of interest (ROI) of size 1 mm × 2 mm × 3.5 mm (gray box). It consisted of fourteen DC electrodes and two RF electrodes (see also figure 6.1). The potential basis functions Θ_i were simulated for each electrode individually and the total potential Φ_{tot} was given by the sum of the basis functions (see equation 8.1). The borders of the ROI were set to *infinite element domains* within Comsol, ensuring $\Phi \to 0$ for $|\vec{r}| \to \infty$. For simulations of the modified trap, DC11 was entirely removed from the shown geometry. x', y' and z' define the coordinate system in the laboratory frame.

8 Trapping Potential Simulations

The total potential Φ_{tot} generated by the linear ion trap used for the work presented in this thesis was simulated with the finite element method (FEM) in Comsol Multiphysics [112]. The simulations were performed with the ideal trap geometry and dimensions discussed in chapter 6.1 and shown in figure 6.1c and 6.1d. The geometry of the nanowire was given by the dimensions shown in figure 6.6.

The simulated geometry consisted of the central region of the trap and the nanowire. It was modeled directly within Comsol and placed in a rectangular region of interest (ROI) of size 1 mm × 2 mm × 3.5 mm as shown in figure 8.1. The boundaries of the ROI were set to *infinite element domains*, i. e., the trap was approximated to be placed in free space and the simulated potentials satisfied $\Phi \to 0$ for distances $|\vec{r}| \to \infty$. This approximation was necessary in order to prevent numerical artifacts at the boundaries of the ROI. The approximation was justified, as the distances to other components contributing to the total potential Φ_{tot} (such as the walls of the vacuum chamber) were significantly larger than the trapping region covered by the ROI. Simulations including the entire vacuum chamber and other components of the setup would have required exceedingly large computation times for negligible effects on the total potential Φ_{tot}.

In the following chapters, the principal axes of the trap are denoted as x, y and z, while the horizontal and vertical axes of the laboratory frame are denoted as x', y' and z' (see figure 8.1). The longitudinal axis z of the trap coincides with the axis z' in the laboratory frame, i. e., $z = z'$.

8.1 Potential Basis Functions

For a given geometry consisting of a set of N electrodes, the potential Φ_i generated by each individual electrode i was simulated with an applied voltage of 1 V, while all other electrodes were grounded (0 V). This resulted in a set of potential *basis functions* Θ_i [80, 136, 137]. The values of the basis functions were exported on a three-dimensional grid with a mesh size of 5 µm × 5 µm × 5 µm.

The total potential Φ_{tot} generated by the entire geometry was then computed by the superposition of all basis functions with applied voltages V_i to each individual electrode i:

$$\Phi_{\text{tot}} = Q \sum_{i=1}^{N} V_i \Theta_i. \tag{8.1}$$

Here, Q is the charge of a particle in the total potential Φ_{tot}. Note that the basis functions Θ_i defined here are dimensionless.

In the case of the simulated geometry presented here, a total of $N = 16$ individual basis functions Θ_i were computed (fourteen DC electrodes, one pair of electrically connected RF electrodes and the nanowire).

It is important to note that a change in the simulated geometry, such as a change in the position of the nanowire, requires the computation of new potential basis functions Θ_i. Only basis functions computed with the same geometry can be combined to obtain the correct total potential Φ_{tot} given by equation 8.1.

Following chapter 2.7, the RF potential basis function Θ_{RF} can be used to compute a *pseudopotential* Φ_{pseudo}. The effective (static) total potential Φ_{tot} is then given by [80, 136]:

$$\begin{aligned} \Phi_{\text{tot}} &= \Phi_{\text{DC}} + \Phi_{\text{pseudo}} \\ &= Q \sum_{i=1}^{N} V_i \Theta_i + \frac{Q^2 V_{\text{RF}}^2}{4 m \Omega^2} |\vec{\nabla} \Theta_{\text{RF}}|^2, \end{aligned} \tag{8.2}$$

where $|\vec{\nabla}\Theta_{\text{RF}}|^2 = (\frac{\partial}{\partial x}\Theta_{\text{RF}})^2 + (\frac{\partial}{\partial y}\Theta_{\text{RF}})^2 + (\frac{\partial}{\partial z}\Theta_{\text{RF}})^2$. m is the mass of the trapped ion, V_{RF} is the voltage applied to the RF electrodes and Ω is the applied angular radiofrequency.

8.2 Trapping Potential without Nanowire

The potential Φ_{tot} generated by the linear radiofrequency trap was simulated with Comsol Multiphyscis [112] as discussed above. For the potentials shown in the following, the nanowire was not included in the simulated geometry, in order to study and characterize the fields generated by the trap alone.

Over the course of this project, a nanowire was accidentally crashed into the lower central electrode DC11 of the trap. This resulted in the destruction of the respective nanowire and the breaking of the electrode. The nanowire was replaced, but the electrode was removed from the trap. Due to this, ions were subsequently trapped in the edge region of the linear radiofrequency trap instead of in the center. In order to study the consequences and effects arising from the modified trap geometry, the generated potentials were simulated with Comsol and compared to the original trap.

Experimentally, the trapping of single ions and small ion crystals in the edge region of the modified trap was successful. However, we encountered high excess micromotion and the requirement for large detunings δ_0 of the 397 nm laser for the main cooling transition $4^2\mathrm{S}_{1/2} \leftrightarrow 4^2\mathrm{P}_{1/2}$. Attempts to compensate the excess micromotion with the DC and compensation electrodes were unsuccessful. Despite the inconveniences arising from the necessity of trapping the ions in the edge region of the trap, coupling of the ion-nanowire hybrid system was still successfully demonstrated (see chapter 11). The large excess micromotion at the radiofrequency Ω did not interfere with the measurements of the driven secular motion at frequency ω_z, due to the large mismatch between the frequencies ($\Omega \gg \omega_z$). The measurements performed with the photon-correlation method (see also chapter 7.3.2) were only sensitive to periodic motion at the secular frequency ω_z, correlated to the applied reference frequency $\omega_{\text{ref}} = \omega_z/3$. Contributions from the excess micromotion at frequency Ω were entirely uncorrelated to the reference frequency ω_{ref} and thus averaged out.

8.2.1 Original Trap Geometry

In the case of the original geometry, ions are ideally confined in the geometrical center $\vec{x} = (0, 0, 0)$ of the trap. It is instructive to study the total DC potential Φ_{DC} generated from the fourteen DC electrodes and the RF potential Φ_{RF} generated from the pair of RF electrodes individually.

Figure 8.2 shows the RF potential Φ_{RF} generated by the RF electrodes at a voltage of V_0 in the radial $(x', y', z' = 0)$ and axial $(x', y' = 0, z')$ plane. As can be seen in figure 8.2b and 8.2d, the RF potential exhibits no significant field gradient along the axial z-direction in the

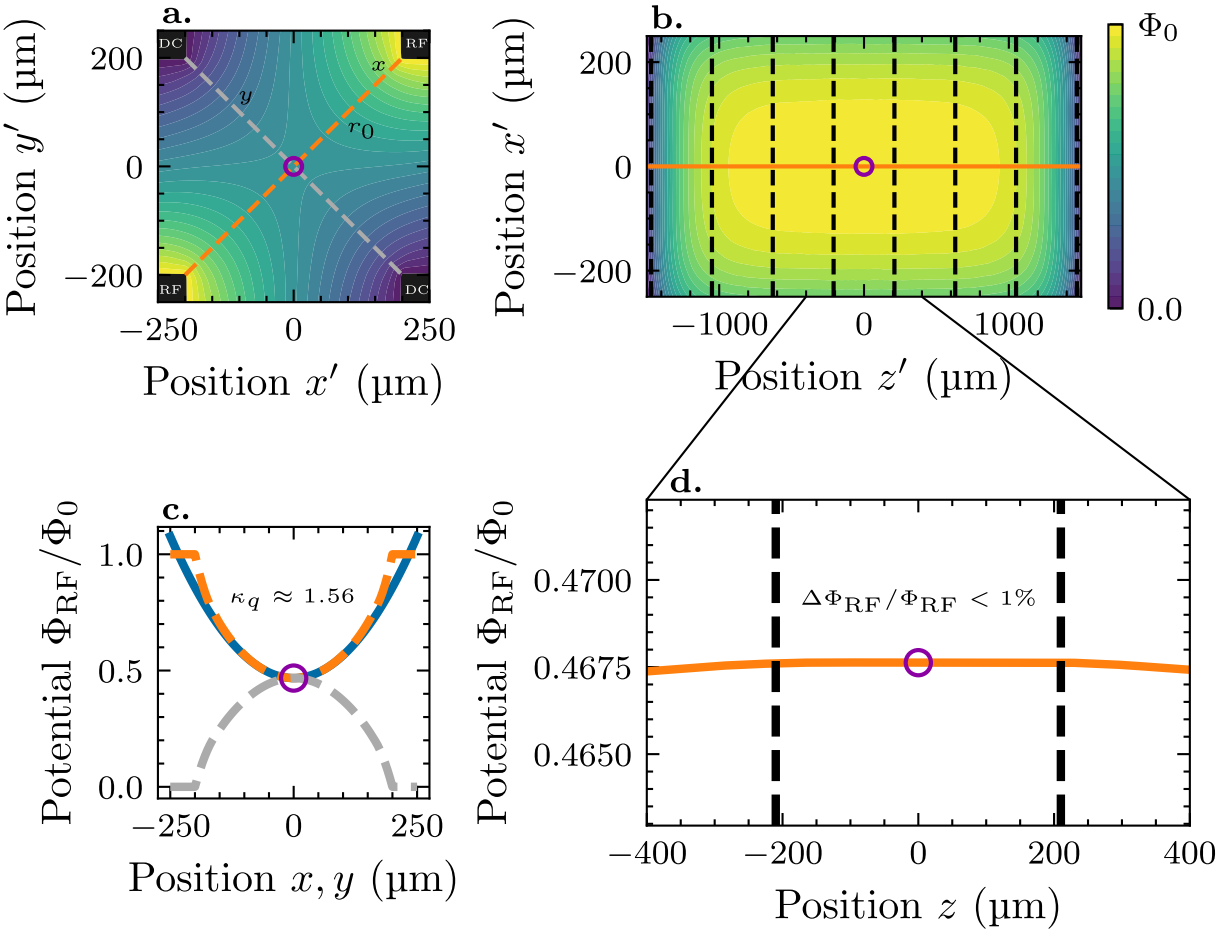

Figure 8.2: Radiofrequency potential Φ_{RF} generated by the linear ion trap. The RF electrodes were set to a potential $\Phi_0 = QV_0$. **a**, Radial plane of Φ_{RF} in the geometrical center of the trap ($z' = 0$). x and y denote the principal axes of the trap, while x' and y' denote the horizontal and vertical axes in the laboratory frame, respectively (with $z = z'$). **b**, Axial plane of Φ_{RF} at $y' = 0$. The dashed black lines indicate the regions spanned by the seven DC electrode segments on each side of the trap. **c**, Potential Φ_{RF} along the principal axes x and y (see **a**). The geometric correction factor was determined to be $\kappa_q \approx 1.56$. The blue curve shows the corresponding harmonic approximation of the potential. **d**, Potential Φ_{RF} along the longitudinal axis. In the center of the trap, the potential is nearly free of a gradient along z.

center of the trap. Gradients along z are only noticeable near the edge regions of the trap, far away from the trapping position of the ions. In conjunction with figure 8.2a and 8.2c, it can be seen that the generated RF potential in the center is well described by a quadrupolar potential (see also chapter 2.4):

$$\Phi_{RF} = \kappa_q \frac{\Phi_0}{2r_0^2}(x^2 - y^2) + \Phi_{offset}, \tag{8.3}$$

where $r_0 \approx 283$ µm is the radial distance from the electrodes to the center of the trap (see figure 8.2a), $\Phi_0 = QV_0$ is the potential applied to the RF electrodes and κ_q is a geometric correction factor [126–128]. κ_q was determined from a multidimensional generalization of the a- and q-parameters ($a \to A_{ij}$, $q \to Q_{ij}$) [189, 190], defined by the entries $H_{ij} = \frac{\partial^2}{\partial x_i \partial x_j}$ of the

Hessian matrix [80]:

$$\begin{aligned} A_{ij} &= \frac{4}{m\Omega^2}\frac{\partial^2\Phi_{\mathrm{DC}}}{\partial x_i \partial x_j}, \\ Q_{ij} &= \frac{2}{m\Omega^2}\frac{\partial^2\Phi_{\mathrm{RF}}}{\partial x_i \partial x_j}, \end{aligned} \tag{8.4}$$

where Ω is the applied radiofrequency and the derivatives are evaluated at the trapping position $\vec{x}_0$. κ_q shown in figure 8.2c was obtained from the second-order derivative of the simulated RF potential Φ_{RF} along the radial axis x of the trap:

$$\begin{aligned} \kappa_q &= \frac{1}{2}\frac{2r_0^2}{\Phi_0}\frac{\partial^2\Phi_{\mathrm{RF}}}{\partial x^2}, \\ \kappa_q &\approx 1.56. \end{aligned} \tag{8.5}$$

Figure 8.3 shows the DC potential Φ_{DC} generated by the original trap geometry for a symmetric supply of DC voltages $V_{\mathrm{DC},i}$. The central electrodes were grounded, i. e., $V_{\mathrm{DC},4} = V_{\mathrm{DC},11} = 0$. The remaining electrodes were set to $V_{\mathrm{DC},i} = U_0$, corresponding to a potential of $\Phi_0 = QU_0$. The resulting DC potential Φ_{DC} exhibits a saddle point in the center of the trap and is well approximated by:

$$\Phi_{\mathrm{DC}} = \kappa_a \frac{QU_0}{2z_0^2}(2z^2 - y^2 - x^2). \tag{8.6}$$

$z_0 = 220$ µm is the distance from the endcap electrodes to the center of the trap along z. κ_a is a geometric correction factor for the DC potential [126–128]. As for the RF potential, the generalized description of the a- and q-parameters yielded:

$$\kappa_a \approx 0.104. \tag{8.7}$$

Overall, the simulations of the original trap geometry have shown the generation of potentials well described by the ideal potential of a linear radiofrequency trap given by equation 2.11. The DC electrodes generate a harmonic potential along z with a saddle point in the center of the trap. The RF electrodes generate a quadrupolar potential with negligible gradient along the axial z-direction.

8.2.2 Modified Trap Geometry

Figures 8.4 and 8.5 show the RF and DC potentials of the modified trap geometry simulated with Comsol Multiphysics [112], respectively. The simulations of the potential basis functions Θ_i were performed as discussed in chapter 8.1. However, the lower central electrode DC11 (see

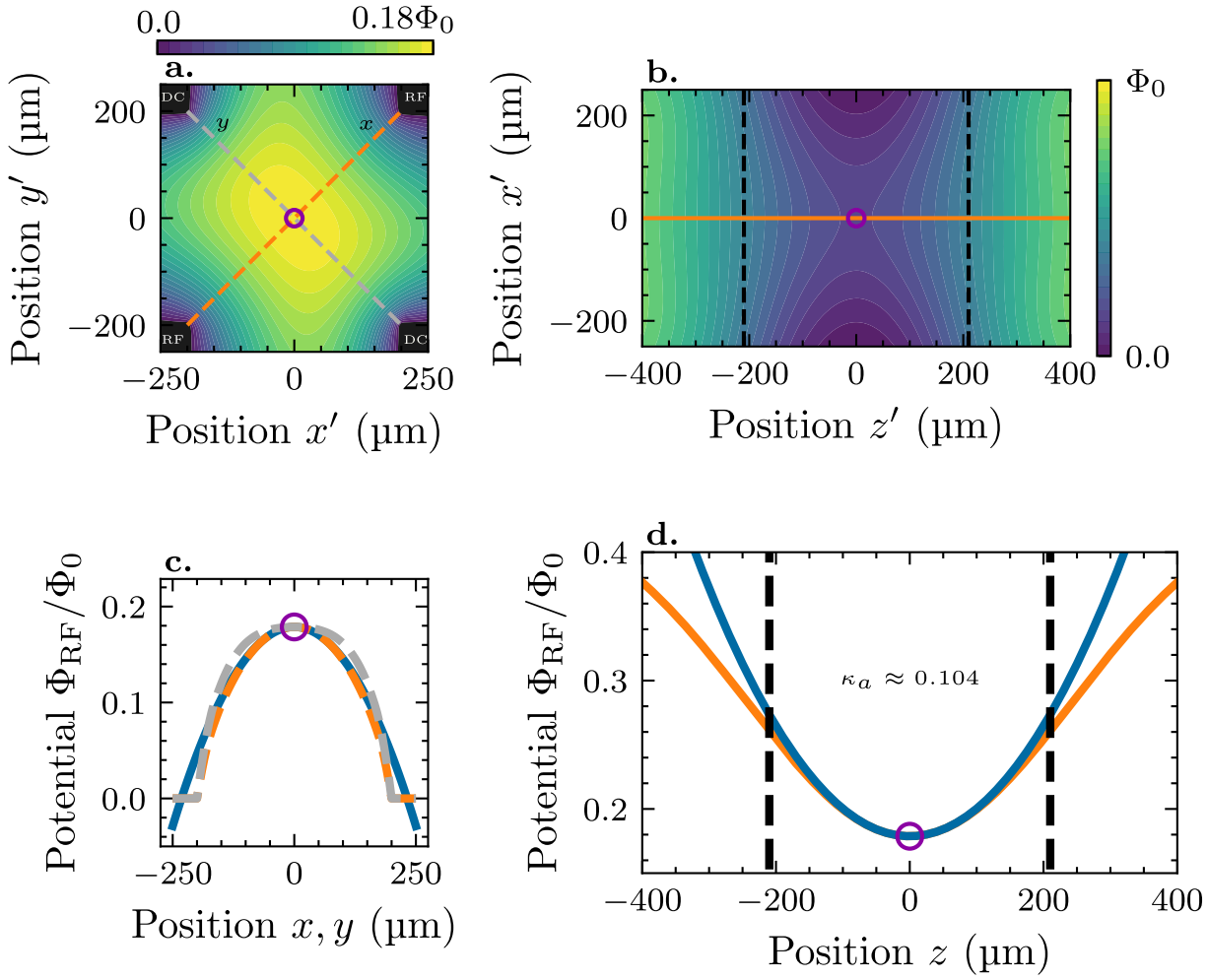

Figure 8.3: DC potential Φ_{DC} generated by the linear ion trap. The central electrode segments (DC4 and DC11) and the RF electrodes were grounded (0 V). All other DC electrodes were set to a potential $\Phi_0 = QU_0$. **a**, Radial plane of Φ_{DC} at $z' = 0$. **b**, Axial plane of Φ_{DC} at $y' = 0$. **c**, Potential Φ_{DC} along the principal axes x and y of the trap (see **a**). **d**, Potential Φ_{DC} along the longitudinal axis z. In conjunction with **c**, it can be seen that the potential exhibits a three-dimensional saddle point in the center of the trap. The geometric correction factor was determined to be $\kappa_a \approx 0.104$. The blue curves in **c** and **d** show the corresponding harmonic approximation of the potential.

figure 8.1) was removed from the geometry.

Due to the absence of the central DC electrode, the resulting RF potential deviated significantly from the desired quadrupolar potential with vanishing gradient along z in the trap center. Experimentally, we decided to continue by trapping ions in the edge region of the trap, in between the grounded electrodes DC6 and DC13 ($V_{\mathrm{DC},6} = V_{\mathrm{DC},13} = 0$). This corresponded to trapping at $\vec{x}_0 = (0, 0, -840\ \mu\mathrm{m})$.

As can be seen in figure 8.4a and 8.4c, the radial plane of the simulated RF potential Φ_{RF} at the new trapping position $\vec{x}_0$ was approximately quadrupolar with a geometric correction factor $\kappa_q \approx 1.56$, not significantly different from the central potential generated by the original trap geometry (compare to figure 8.2c). The RF electrodes were set to a potential $\Phi_0 = QV_0$.

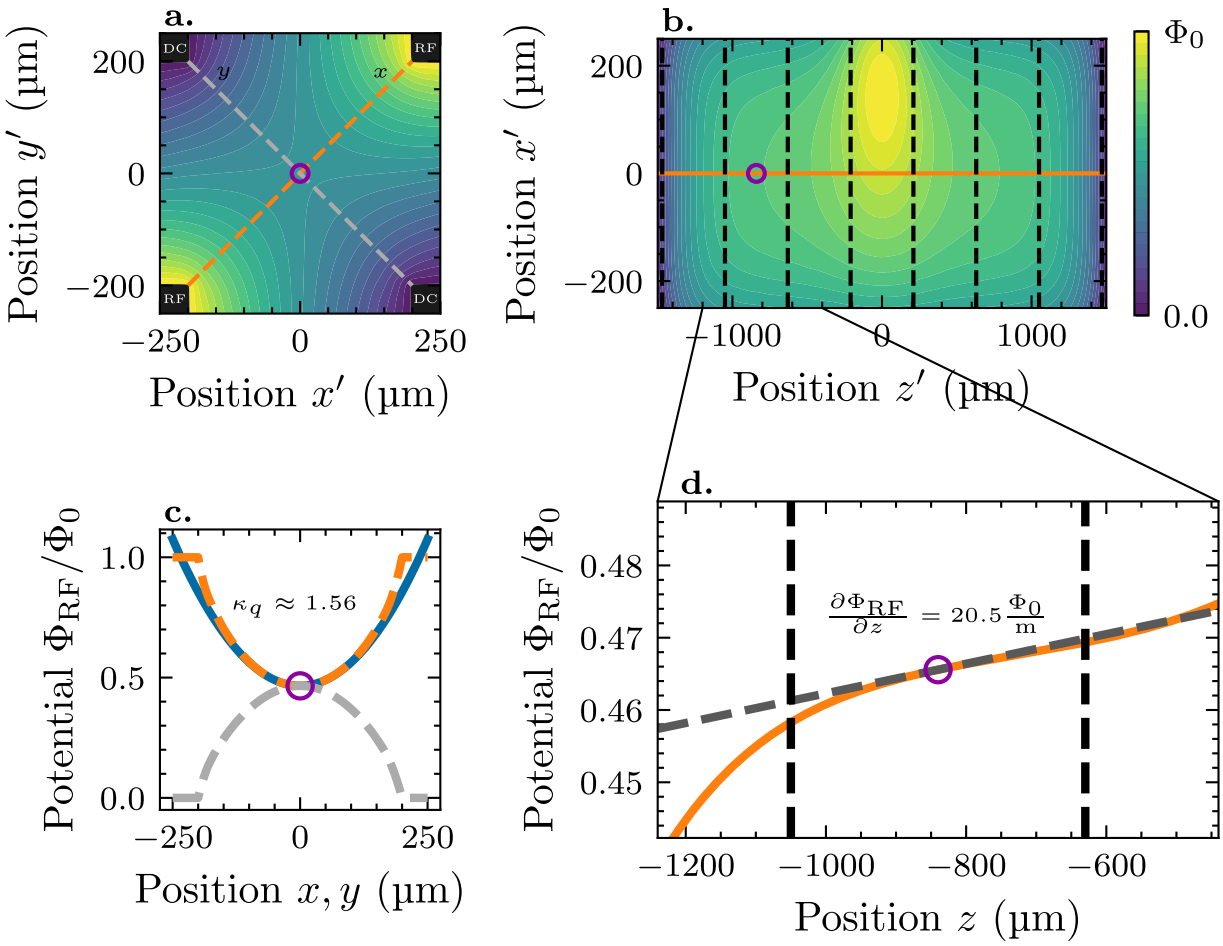

Figure 8.4: RF potential Φ_{RF} generated by the modified ion trap. The trapping position of the ions in the modified trap geometry was $\vec{x}_0 = (0, 0, -840)$ µm. **a**, Radial plane of Φ_{RF} at $z' = -840$ µm. **b**, Axial plane of Φ_{RF} at $y' = 0$. The missing DC electrode in the center leads to strong distortions of the RF potential and introduces field gradients. **c**, Potential Φ_{RF} along x and y (see **a**). The radial potential at the edge of the trap is not significantly distorted compared to the center of the original trap and the geometric correction factor was found to be $\kappa_q \approx 1.56$. The blue curve shows the corresponding harmonic approximation of the potential. **d**, The potential Φ_{RF} along z exhibits a gradient at the trapping position $\vec{x}_0$, introducing additional micromotion along z.

The potential Φ_{RF} along the axial z-direction, however, exhibited a clear gradient at the new trapping position near the edge of the trap. At $\vec{x}_0 = (0, 0, -840$ µm), the gradient to first order was determined to be:

$$\frac{\partial \Phi_{\mathrm{RF}}}{\partial z} \approx 20.5 \frac{\Phi_0}{\mathrm{m}}. \tag{8.8}$$

As can be seen in figure 8.5, the generated DC potential Φ_{DC} at the new $\vec{x}_0$ obtained from the simulations did not strongly deviate from the potential generated by the original trap in the center (compare to figure 8.3). Here, all DC electrodes (except for DC6 and DC13) were set to the same voltage $V_{\mathrm{DC},i} = U_0$ ($\Rightarrow \Phi_0 = QU_0$). The geometric correction factor was found to be $\kappa_a \approx 0.1$. Asymmetries and anharmonicities of the DC potential could experimentally

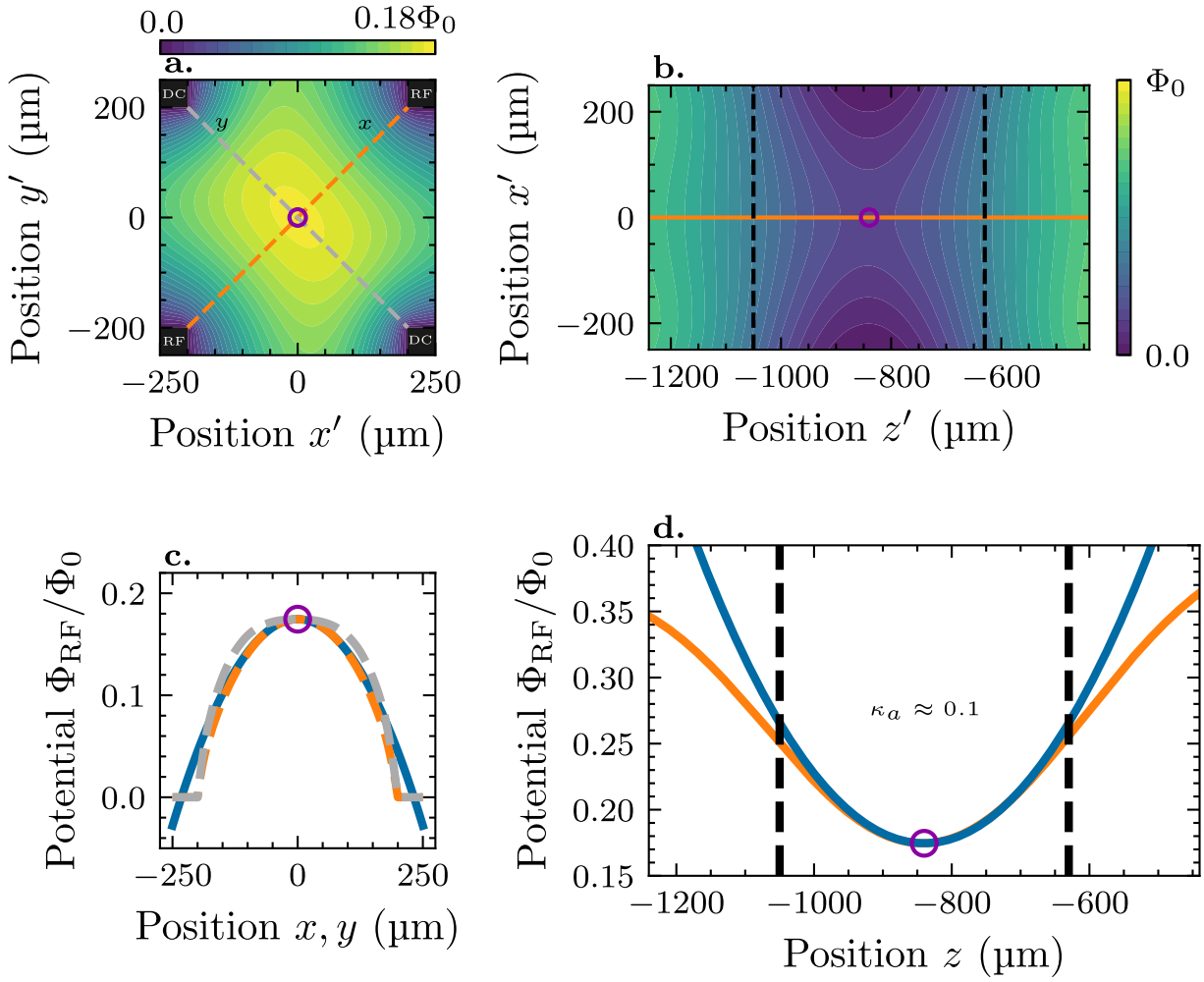

Figure 8.5: DC potential Φ_{DC} generated by the modified ion trap. The trapping position of the ions in the modified trap geometry was $\vec{x}_0 = (0, 0, -840)$ µm. All DC electrodes were set to $\Phi_0 = QU_0$, with the exception of the grounded electrodes DC6 and DC13 at the edge of the trap (0 V). **a**, Radial plane of Φ_{DC} at $z' = -840$ µm. **b**, Axial plane of Φ_{DC} at $y' = 0$ around the edge region of the trap. **c**, Potential Φ_{DC} along x and y (see **a**). **d**, The potential Φ_{DC} along z around the trapping position $\vec{x}_0$. In conjunction with **c**, it can be seen that the potential exhibits a three-dimensional saddle point at $\vec{x}_0$. The geometric correction factor was found to be $\kappa_a \approx 0.1$. The blue curves in **c** and **d** show the corresponding harmonic approximation of the potential.

be compensated by applying different voltages $V_{\mathrm{DC},i}$. The geometry of the trap with thirteen DC electrodes and one designated compensation electrode offered a large amount of degrees of freedom for this compensation.

Figure 8.6 shows the effective pseudopotential Φ_{tot} of the modified trap geometry computed with equation 8.2. The applied voltages for the DC potential basis functions were $V_i = 1$ V (with the exception of the grounded electrodes $V_6 = V_{13} = 0$ V) and the amplitude of the RF voltage was $V_{\mathrm{RF}} = 50$ V. As can be seen in figure 8.6, the effective potential at the new trapping position $\vec{x}_0 = (0, 0, -840$ µm) exhibits a confining potential along all principal axes of the trap. The resulting secular frequencies in this voltage configuration were $f_x \approx 1.2$ MHz, $f_y \approx 1.3$ MHz and $f_z \approx 502$ kHz. The experiments presented in this thesis were conducted

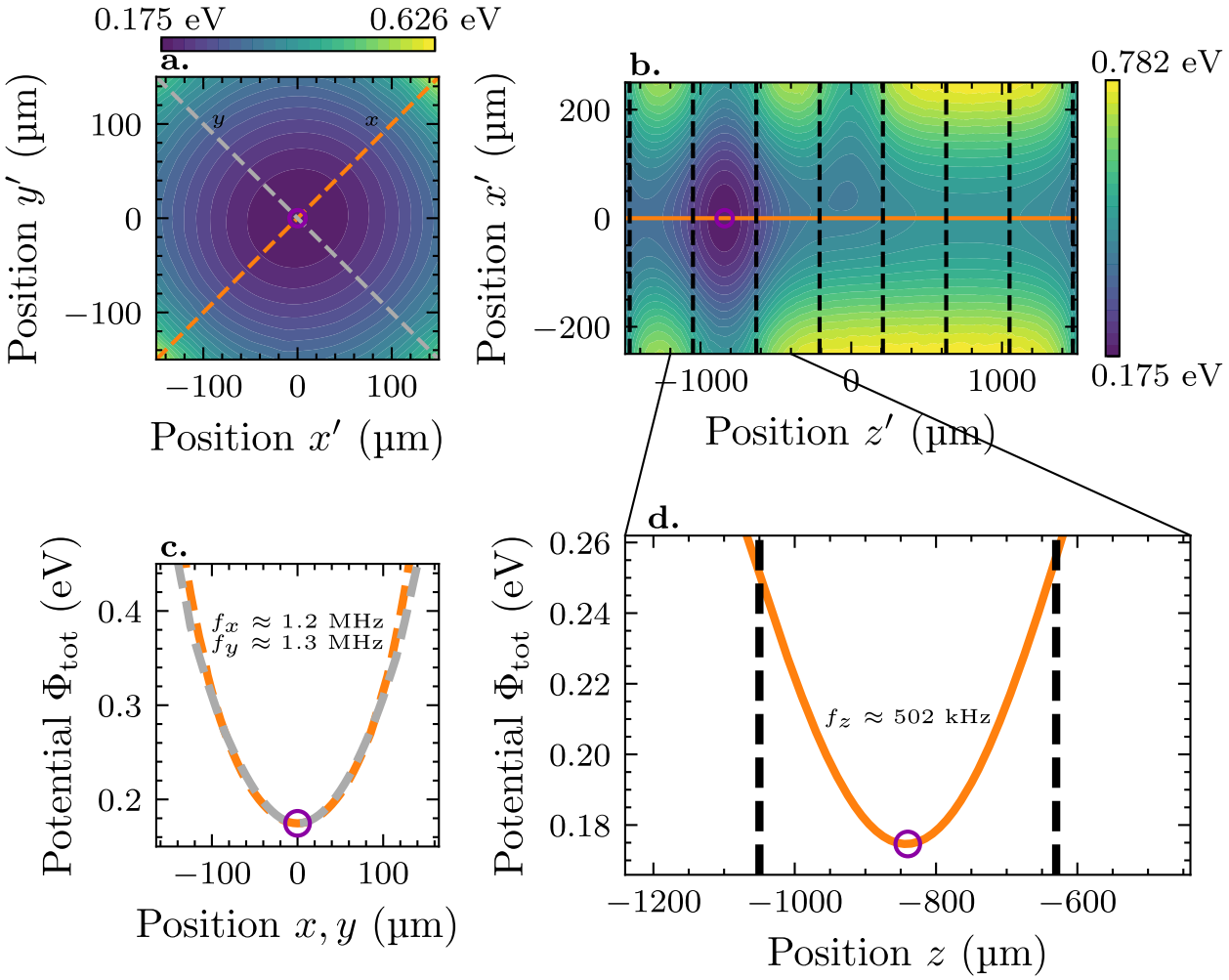

Figure 8.6: Effective potential Φ_{tot} in the modified trap geometry. The effective potential was computed following equation 8.2 with the RF and DC potentials shown in figures 8.4 and 8.5, respectively. The applied voltages were an endcap voltage of $U_0 = 1$ V and an RF amplitude of $V_0 = 50$ V. As can be seen in **c** and **d**, the effective potential exhibits minima, and thus confinement of positively charged ions, along all principal axes of the trap. At the given voltage configuration, the secular frequencies obtained from the simulations were $f_x \approx 1.2$ MHz, $f_y \approx 1.3$ MHz and $f_z \approx 502$ kHz, comparable to frequencies observed in the experiments for similar voltage configurations.

under similar voltage configurations and frequencies comparable to the values obtained from the simulations were observed.

Overall, the modified trap geometry introduced a gradient of the radiofrequency potential Φ_{RF} along the axial direction, leading to additional micromotion along z. This micromotion could be suppressed by the introduction of additional RF fields at frequency Ω, compensating for the gradient. For the work presented in this thesis, such a compensation was not implemented as it would have no effect on the validity of the presented results. Despite the introduction of the gradient of the RF potential along z, figure 8.6 shows that the effective pseudopotential Φ_{tot} generated by the modified trap geometry still enables the trapping of ions at the new trapping position $\vec{x}_0$.

8.3 Trapping Potential with Nanowire

The introduction of the nanowire to the trap geometry is an additional source of distortions to the trapping potential Φ_{tot} generated by the linear radiofrequency trap. The distortions increase the closer the nanowire is positioned to the center of the trap. With a diameter of $d = 250$ µm, the tungsten holder of the nanowire was of comparable size to the DC electrode segments. As such, the contributions of the holder to the total potential could be significant, even if the nanowire was grounded (0 V).

Not only did the introduction of the nanowire to the geometry lead to changes in the effective trap frequencies (see also chapters 9.3 and 11.2), it also shifted the effective RF and DC minima positions away from the center and increased the driven micromotion of the ions due to stronger gradients along all directions. In general, the nanowire introduced asymmetries and anharmonicities to the total potential Φ_{tot}. While position shifts of the DC potential Φ_{DC} may be adjusted by applying compensation voltages, the shift of the effective RF potential is dictated by the geometry of the trap, including the nanowire. Shifts of the RF potential can only be compensated by additional RF fields.

In the following, we discuss the effects of the nanowire on the effective trapping position of the ions observed experimentally and from simulations performed with Comsol Multiphysics [112].

8.3.1 Single-Phase Operation of the Radiofrequency

The quadrupolar radiofrequency potential Φ_{RF} of a linear ion trap is typically generated by one of two configurations for the applied RF voltages. Traps can be operated with a *single-phase* RF potential generated from a sinusoidal RF voltage $V_{\text{RF}}(t) = V_0 \sin(\Omega t)$ applied to one pair of diagonally opposed RF electrodes, as is the case for the trap presented in this thesis (see also figure 2.4a). On the other hand, the RF potential can be generated by two sinusoidal voltages of *opposite phase* $V_{\text{RF}}(t) = \pm V_0 \sin(\Omega t)$ applied to two pairs of diagonally opposed RF electrodes (see also figure 2.4b).

Figure 8.7 shows the radiofrequency potential Φ_{RF} simulated with Comsol with the nanowire tip positioned in the center of the trap. Here, the trap was simulated in single-phase RF operation and the RF electrodes were set to a potential of $\Phi_0 = QV_0$. All DC electrodes, as well as the nanowire, were grounded (0 V).

A distortion of the RF potential can be seen in figure 8.7a. The relatively large tungsten holder ($d = 250$ µm) of the nanowire acts as an intrusive grounded electrode positioned within the center of the trap. The symmetry of the resulting radiofrequency potential Φ_{RF} is broken (compare to figure 8.2a). The position of the saddle point of the RF potential (effective trapping position) is shifted toward the upper DC electrodes at $\vec{x}_0 = (-75, 40, 0)$ µm.

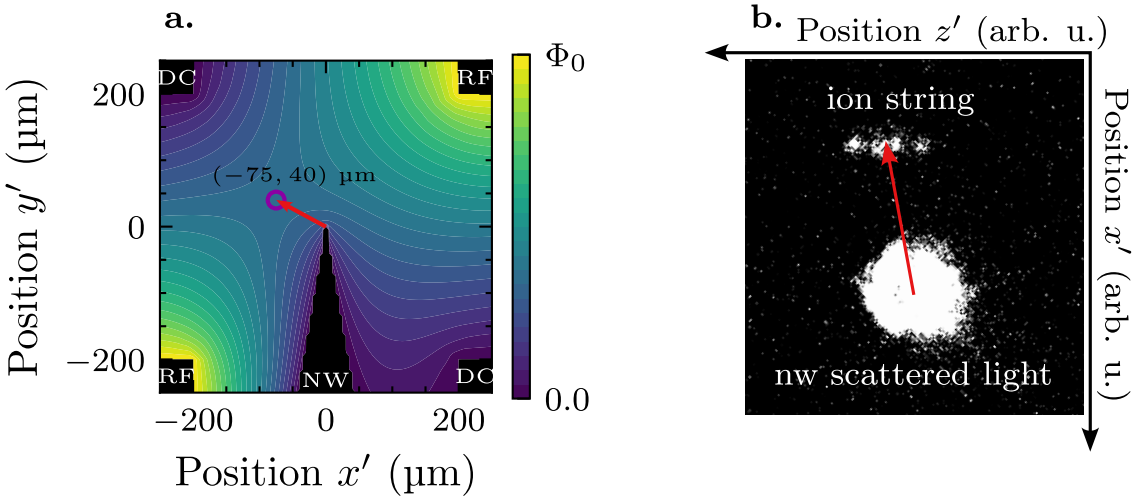

Figure 8.7: Shift of the position of trapped ions due to the introduction of the nanowire to the trap geometry. **a**, Radial plane of the simulated radiofrequency potential Φ_{RF} with the nanowire tip positioned in the center of the trapping region. The RF electrodes were set to $\Phi_0 = QV_0$. All DC electrodes and the nanowire were grounded (0 V). The introduction of the nanowire to the geometry leads to distortions of the RF potential (compare to figure 8.4). These distortions can be attributed to the electrically conductive tungsten holder, acting as a relatively large electrode. The symmetry of the radial RF potential is broken and the effective trapping position is shifted toward the upper DC electrodes at $(x', y') = (-75, 40)$ µm. **b**, EMCCD image of a string of four ions, shifted by the nanowire. The tip of the nanowire (visible due to the scattered light of the 397 nm cooling laser) was positioned near the center of the trap. The equilibrium position of the trapped ions was shifted along the red arrow. The direction of the shift occurred toward the upper DC electrodes, as predicted by the simulation shown in **a**. The final equilibrium position of the ions depends further on the applied DC potentials. Those can be compensated and adjusted to overlap the effective DC and RF trapping positions.

Figure 8.7b shows a qualitative confirmation of the position shift predicted by the simulations. It shows an EMCCD image of a linear string of four ions, shifted by the nanowire. The camera was positioned above the experimental chamber (see also chapter 6.5) and imaged the horizontal $x'z'$-plane. The nanowire was initially positioned below the trap and the ions were trapped exactly above the nanowire in the horizontal plane. By raising the nanowire to the center of the trap, the ions were shifted along the red arrow. The direction of the shift occurred toward the upper DC electrode segments, as predicted by the simulations. In the final position shown in figure 8.7b, the nanowire tip was positioned near the geometrical center of the trap and could be seen from scattered light of the 397 nm main cooling laser.

The shift of the effective trapping position of the ions is an indicator of distorted fields and an effect of the electrically conductive tungsten holder. Contributions of the nanowire on the tip are negligible. However, the effective trapping potential at the shifted position can still be approximated to that of a harmonic oscillator. Figure 8.8 shows the effective pseudopotential

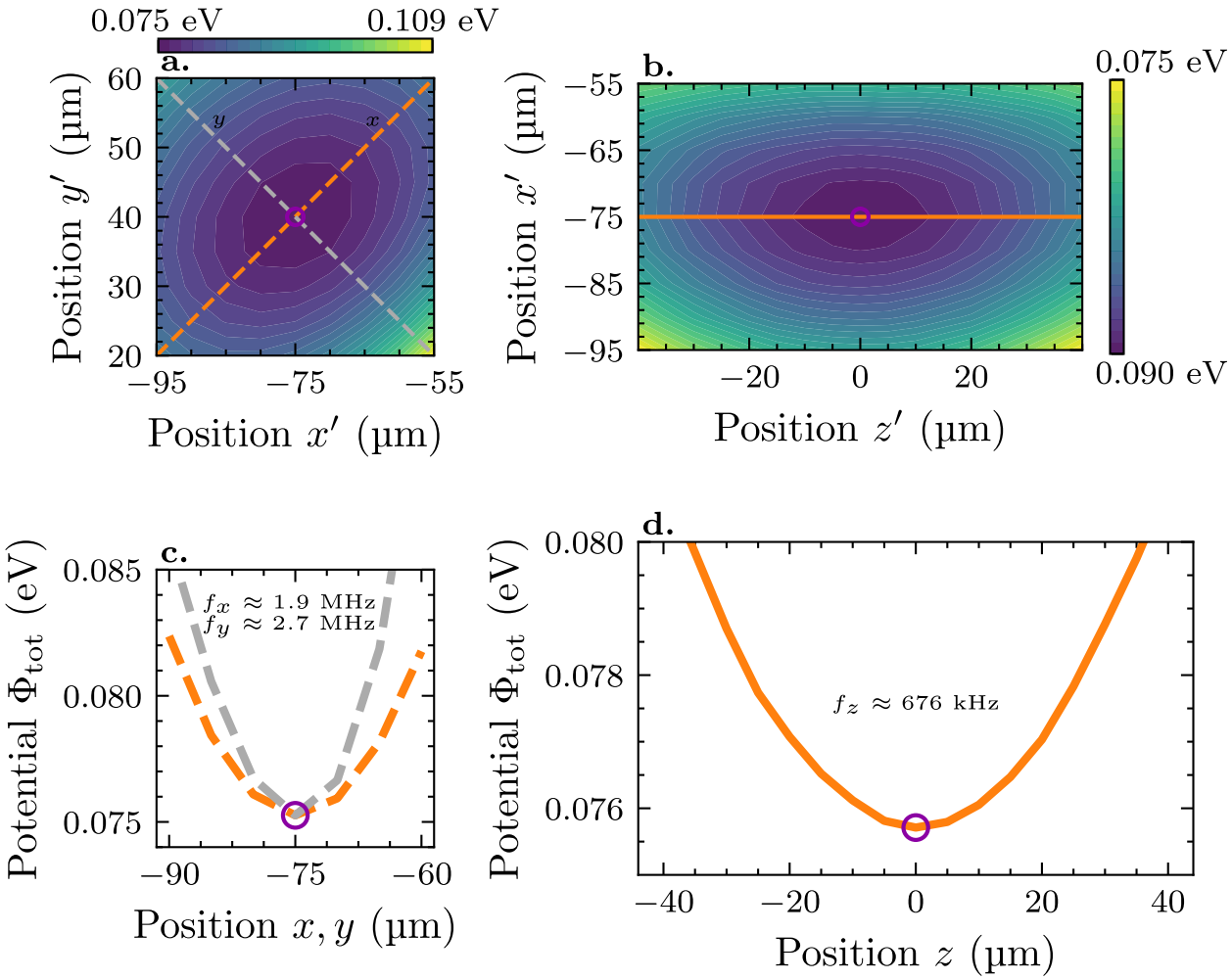

Figure 8.8: Effective potential Φ_{tot} in the presence of the nanowire. The nanowire was grounded ($V_{\text{nw}} = 0$ V) and its tip was positioned in the center of the trap at $\vec{x}_{\text{nw}} = (0, 0, 0)$. The effective potential Φ_{tot} is shown around the shifted equilibrium position $\vec{x}_0 = (-75, 40, 0)$ µm of trapped ions (purple marker, see also figure 8.7). The amplitude of the RF voltage was $V_{\text{RF}} = 50$ V and the RF potential was overlapped with a DC potential generated by an endcap voltage of $U_0 = 0.5$ V. The effective pseudopotential Φ_{tot} computed with equation 8.2 exhibits confinement with approximately harmonic potentials along all principal axes around $\vec{x}_0$ (see **c** and **d**). With the given configuration of applied voltages, the secular frequencies were simulated to be $f_x \approx 1.9$ MHz, $f_y \approx 2.7$ MHz and $f_z \approx 676$ kHz.

Φ_{tot} around the shifted position $\vec{x}_0 = (-75, 40, 0)$ µm, computed with equation 8.2. For the potential shown in figure 8.8, the amplitude of the RF voltage was set to $V_{\text{RF}} = 50$ V. The effective minimum of the RF potential was overlapped with the saddle point of the DC potential generated with an endcap voltage of $U_0 = 0.5$ V. The central DC electrodes and the nanowire were grounded ($V_4 = V_{11} = V_{\text{nw}} = 0$ V). The resulting effective potential Φ_{tot} exhibits approximately harmonic trapping potentials along all principal axes, enabling the trapping of ions at the shifted position $\vec{x}_0$. It is important to note that the overlapping of the effective minima of the DC and RF potentials in the presence of the nanowire is not trivial. Applying a static voltage to the nanowire shifts the effective minimum of the DC potential additionally. In general, asymmetric configurations for voltages applied to the DC electrodes are required in order to overlap the potentials.

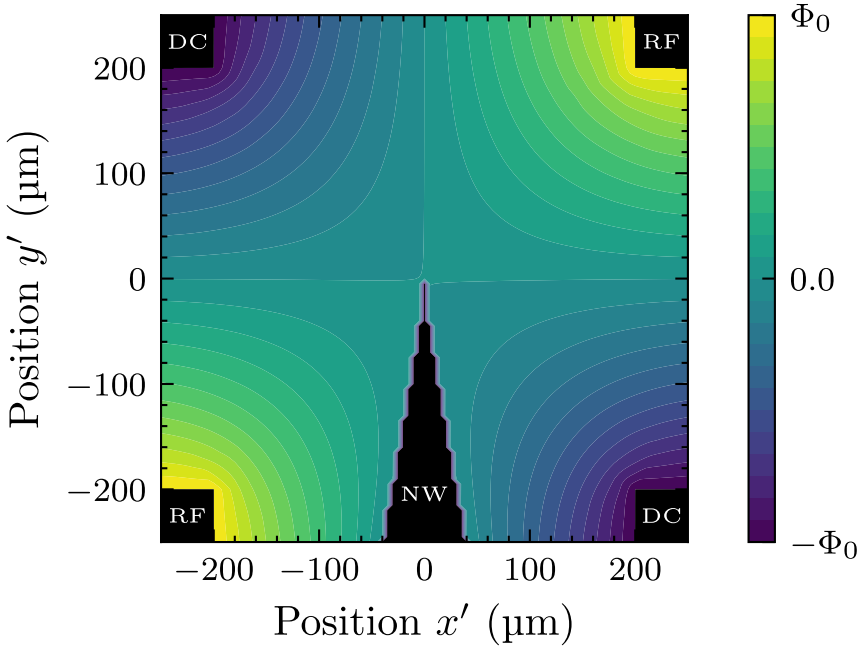

Figure 8.9: Simulated radiofrequency potential Φ_{RF} including the nanowire with an opposite-phase RF configuration. The tip of the nanowire was positioned in the center of the trapping region at $(x', y') = (0, 0)$. The simulated field corresponds to operation of the trap with an opposite-phase RF configuration. The RF electrodes were set to $\Phi_0 = QV_0$, while all DC electrodes were set to $-\Phi_0 = -QV_0$. The nanowire was grounded (0 V). The application of two RF components with opposite signs recovers the symmetry and leads to weaker distortions of the potential (compare to figures 8.7a and 8.4a).

However, the shift of the ion equilibrium position also offers an advantage for the experimental setup used during this project. As can be seen in figure 8.7b, the horizontal shift of the ions allowed a clear distinction of the ions from the 397 nm photons scattered from the nanowire. If the ions were not shifted, their detection would be increasingly difficult due to the high background of the light scattered from the nanowire.

In order to avoid the shift in the ion equilibrium position, a dielectric material with low reflectivity for the holder of the nanowire could be used. This, however, would require new design considerations and may come with additional issues such as the generation of patch potentials by accumulation of charges [191].

8.3.2 Double-Phase Operation of the Radiofrequency

Figure 8.9 shows the simulated radiofrequency potential Φ_{RF} obtained when operating the trap with two RF voltages of opposite phases. The nanowire was grounded (0 V) and its tip was positioned in the center of the trap. The RF electrodes of the trap were set to a potential of $+\Phi_0 = QV_0$, while the DC electrodes were additionally set to a potential of $-\Phi_0 = -QV_0$. Note that the simulated RF potential generated by the DC electrodes needs to be treated independently of the static DC potential basis functions. The DC electrodes can thus be used to

generate a static DC potential as well as an additional oscillating RF potential $\Phi_{\text{tot}} = \Phi_{\text{DC}} + \Phi_{\text{RF}}$.

As can be seen in figure 8.9, the symmetry of the RF potential is well recovered by the addition of an RF voltage with opposite sign applied to the DC electrodes and the saddle point of the potential remains close to the center of the trap. This enables the positioning of the nanowire close to the ions without a drastic shift of the ion position (compare to figure 8.7a). It is important to note, however, that the contributions from the DC potentials generated by the DC electrodes and the nanowire need to be considered for the total potential $\Phi_{\text{tot}} = \Phi_{\text{DC}} + \Phi_{\text{RF}}$. The large amount of degrees of freedom for the supply of static voltages allows the optimization of the ion position by compensation of the total DC potential Φ_{DC}.

Operation of the trap in a double-phase configuration appears to be the better choice for the given geometry of the trap and the nanowire presented here. This, however, was not experimentally implemented in the work presented in this thesis and the trap was operated with the single-phase configuration discussed in chapter 8.3.1. This decision was made due to the design of the trap, originally intended to be operated with a single RF voltage, evident by the *RC* low-pass filters added to the DC electrodes (see chapter 6.6). Furthermore, as discussed in chapter 8.3.1, the shift of the ion position in the horizontal plane proved useful for a clear distinction of the fluorescence of trapped ions from 397 nm photons scattered from the nanowire.

9 Ion-Nanowire Interaction Model

The coupling mechanism of the ion-nanowire hybrid system is the electrostatic Coulomb interaction between the two charges of the subsystems. We approximate the potential generated by the nanowire in the combined nanowire-trap geometry to that of a point charge close to the tip of the nanowire [80, 84]. Given the ion and nanowire tip positions $\vec{x}_{\mathrm{ion}}$ and $\vec{x}_{\mathrm{nw}}$, the static interaction potential Φ_{IA} is given by:

$$\Phi_{\mathrm{IA}} = k_{\mathrm{c}} \frac{q_{\mathrm{ion}} q_{\mathrm{nw}}}{|\vec{r}|}. \tag{9.1}$$

Here, $|\vec{r}| = |\vec{x}_{\mathrm{ion}} - \vec{x}_{\mathrm{nw}}| = \sqrt{(x_{\mathrm{ion}} - x_{\mathrm{nw}})^2 + (y_{\mathrm{ion}} - y_{\mathrm{nw}})^2 + (z_{\mathrm{ion}} - z_{\mathrm{nw}})^2}$ is the distance between the ion and the nanowire tip, $q_{\mathrm{ion}} = 1.602 \times 10^{-19}$ As is the charge of a single ion and $k_{\mathrm{c}} = \frac{1}{4\pi\varepsilon_0}$ is the Coulomb constant.

In the case of mechanically driven nanowire motion in the z-direction, the potential changes to [84]:

$$\Phi_{\mathrm{IA}} = k_{\mathrm{c}} \frac{q_{\mathrm{ion}} q_{\mathrm{nw}}}{\sqrt{(x_{\mathrm{ion}} - x_{\mathrm{nw}})^2 + (y_{\mathrm{ion}} - y_{\mathrm{nw}})^2 + (z_{\mathrm{ion}} - z_{\mathrm{nw}} - A\cos(\omega_{\mathrm{nw}} t))^2}}. \tag{9.2}$$

Here, A is the nanowire oscillation amplitude and ω_{nw} is the angular frequency of the driven nanowire vibrations.

9.1 Comsol Simulations of Combined Nanowire-Trap Geometry

In order to estimate the effective charge q_{nw} of the nanowire, finite-element-method (FEM) simulations have been performed with Comsol Multiphysics [112]. Figure 9.1 shows the simulated electric potential generated by the nanowire at a static voltage $V_{\mathrm{nw}} = 1$ V with its tip positioned in the geometrical center of the trap. This geometry corresponds closely to the conditions during the experimental demonstration of the ion-nanowire coupling discussed in chapter 11.

As can be seen in figure 9.1a, the electric potential Φ_{IA} generated by the nanowire is not spherically symmetric and thus not perfectly described by equation 9.1. Deviations from the ideal point-charge potential can mainly be attributed to the tungsten holder which acts as an electrode of comparable size to the overall dimensions of the trap (see also chapter 6). Due to this, the equipotential lines in the radial plane region $y < y_{\mathrm{nw}} = 0$ (below the nanowire tip) approach the edges of the conical holder tip. However, the potential for $y > y_{\mathrm{nw}}$ (above the nanowire tip) can still be approximately well described by the spherically symmetric point-charge potential. As shown in figure 9.1, this approximation is best given along the y-direction

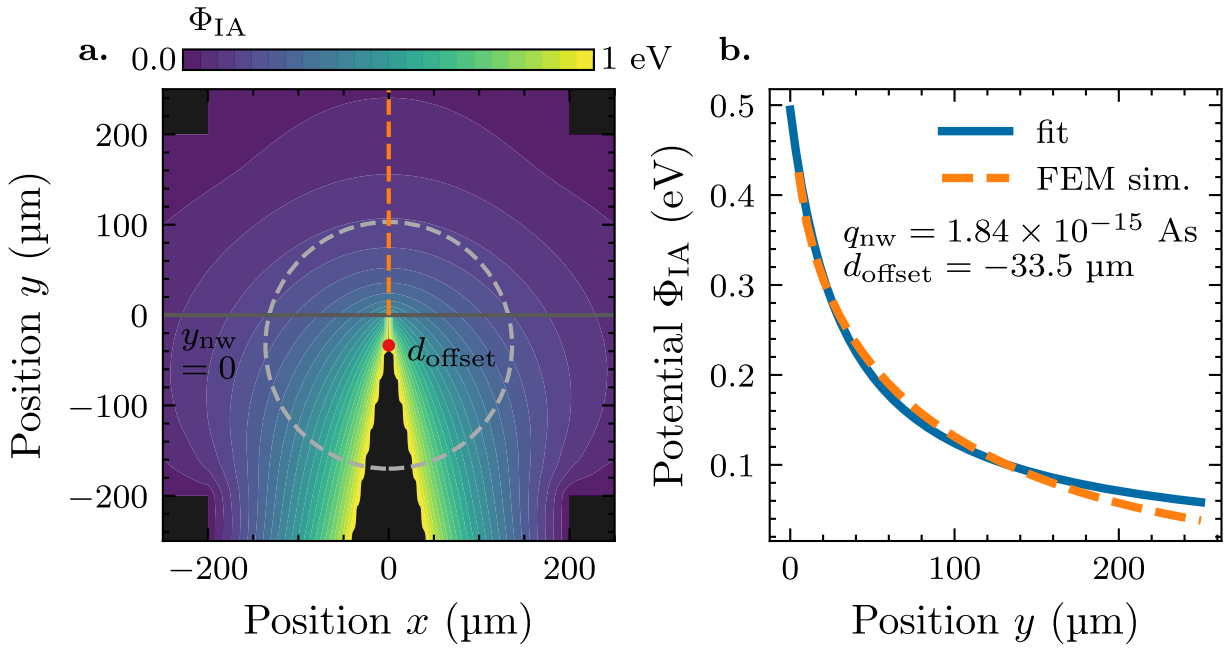

Figure 9.1: FEM simulations of the interaction potential Φ_{IA} generated by the nanowire at $V_{nw} = 1$ V in the center of the trap. **a**, xy-plane of the interaction potential at $z = 0$ with the nanowire and the four rectangular RF and DC electrodes (black). The equipotential lines of the simulated potential show deviations from a perfect point-charge potential with spherical symmetry (indicated by light gray circle). The strongest deviations are found in the region $y < y_{nw} = 0$ (dark gray line) due to the presence of the tungsten holder. The potential is closest to that of a point charge along the y-axis (orange line) with the charge located at $d_{offset} = -33.5$ µm (red dot). **b**, Simulated potential along the y-axis (orange curve) with the fit of a point-charge model $\Phi_{IA}(y) = k_c q_{ion} q_{nw}/(y - d_{offset})$ (blue curve). Deviations can be attributed to the charge distribution of the tungsten holder. The effective charge of the nanowire at $V_{nw} = 1$ V was found to be $q_{nw} = 1.84 \times 10^{-15}$ As.

which is least distorted from other trap electrodes and least affected by the conical holder tip.

Assuming the point-charge model given by equation 9.1, the charge of the nanowire was estimated from a least-square fit to the simulated potential along y as shown in figure 9.1b. The fit function was given by:

$$\Phi(y) = k_c \frac{q_{ion} q_{nw}}{y - d_{offset}}. \tag{9.3}$$

Here, q_{nw} and d_{offset} are the fit parameters. d_{offset} is an additional degree of freedom corresponding to an effective offset position of the point charge best describing the potential generated by the nanowire. The parameters were found to be:

$$\begin{aligned} q_{nw} &= 1.84 \times 10^{-15} \text{ As}, \\ d_{offset} &= -33.5 \text{ µm}. \end{aligned} \tag{9.4}$$

Thus, the potential Φ_{IA} generated by the charged nanowire at $V_{nw} = 1$ V shown in figure 9.1 is best approximated by a point charge of $q_{nw} = 1.84 \times 10^{-15}$ As located below the nanowire tip

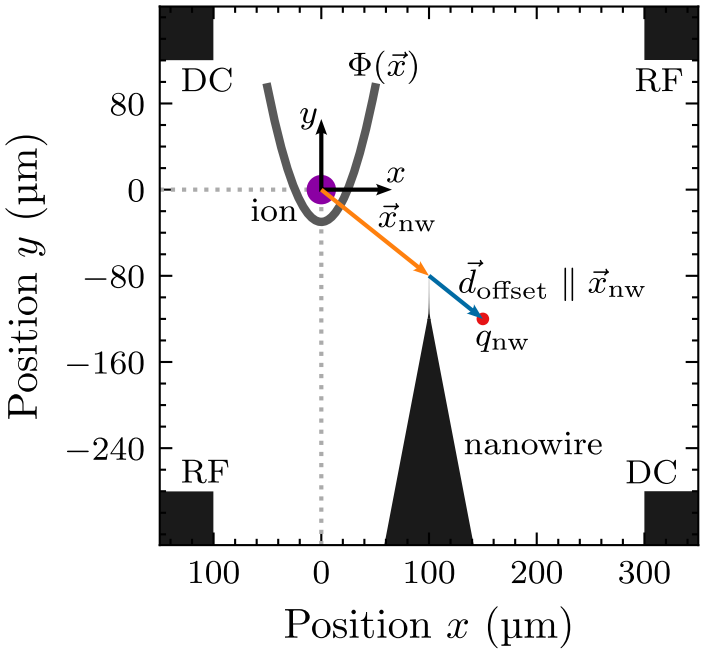

Figure 9.2: Choice of coordinate system for the ion-nanowire interaction model. The origin is set to the ion equilibrium position (purple dot) corresponding to a confining minimum of the total potential $\Phi(\vec{x})$ (indicated by the dark gray curve). The position of the effective nanowire point charge q_{nw} (red dot) is given by the extended nanowire position vector $\vec{x}_{\mathrm{nw}} + \vec{d}_{\mathrm{offset}}$ with $\vec{d}_{\mathrm{offset}} \parallel \vec{x}_{\mathrm{nw}}$ and $|\vec{d}_{\mathrm{offset}}| = 33.5$ µm (not to scale). This ensures that the interaction potential Φ_{IA} generated by the nanowire closely corresponds to the point-charge potential derived in chapter 9.1.

at an offset position of $d_{\mathrm{offset}} = -33.5$ µm. The effective charge is proportional to the applied voltage V_{nw} and can be computed directly for any other voltage by:

$$q_{\mathrm{nw}} = 1.84 \times 10^{-15} \frac{V_{\mathrm{nw}}}{1\ \mathrm{V}}\ \mathrm{As}. \tag{9.5}$$

While the theoretical model presented in this thesis only considers an effective point charge, the total charge distribution of the tungsten holder may be captured by including higher-order terms of a multipole expansion [113, 192].

9.2 Taylor Expansion of the Interaction Potential

It is instructive to analyze the classical dynamics of the ion motion under the influence of the static ion-nanowire interaction potential Φ_{IA} given by equation 9.1 with its Taylor expansion [94].

We set the origin of the coordinate system $\vec{x} = (0, 0, 0)$ to the ion equilibrium position as shown in figure 9.2. In general, the equilibrium position of the total potential Φ does not necessarily coincide with the geometrical center of the trap due to distortions from the nanowire and geometrical imperfections. The actual nanowire tip position vector $\vec{x}_{\mathrm{nw}}$ is extended by an offset

vector $\vec{d}_{\text{offset}}$ such that $\vec{x}_{\text{nw}} \to \vec{x}_{\text{nw}} + \vec{d}_{\text{offset}}$. The length of the offset vector is $|\vec{d}_{\text{offset}}| = 33.5$ µm and we demand $\vec{d}_{\text{offset}} \parallel \vec{x}_{\text{nw}}$. This way, the effective point charge q_{nw} is positioned opposite the ion with respect to the nanowire tip. The ion then experiences the point charge potential with parameters given in equation 9.4. The equilibrium distance d between the ion and the nanowire in the chosen coordinate system is given by:

$$d = |\vec{x}_{\text{nw}}| = \sqrt{x_{\text{nw}}^2 + y_{\text{nw}}^2 + z_{\text{nw}}^2}. \tag{9.6}$$

The interaction potential Φ_{IA} depends on a total of 6 variables: the ion and nanowire position coordinates $\vec{x} = (x, y, z)$ and $\vec{x}_{\text{nw}} = (x_{\text{nw}}, y_{\text{nw}}, z_{\text{nw}})$. It can thus be considered as a multivariate scalar function:

$$\Phi_{\text{IA}}(\vec{x}, \vec{x}_{\text{nw}}) : \mathbb{R}^6 \to \mathbb{R}. \tag{9.7}$$

The Taylor expansion for small variations $\delta\vec{x}$ around an expansion point $\vec{a}$ for N multivariate scalar functions $f(\vec{x}) : \mathbb{R}^N \to \mathbb{R}$ up to second order is given by [193, 194]:

$$f(\vec{x}) = f(\vec{a}) + \sum_{j=1}^{N} \frac{\partial f(\vec{a})}{\partial x_j} \delta x_j + \frac{1}{2} \sum_{j=1}^{N} \sum_{k=1}^{N} \frac{\partial^2 f(\vec{a})}{\partial x_j \partial x_k} \delta x_j \delta x_k. \tag{9.8}$$

The derivatives are evaluated at the specific point $\vec{a}$.

In order to study the effect of the interaction potential Φ_{IA} on the classical dynamics of trapped ions, we want to perform a Taylor expansion around the equilibrium point $\vec{a} = (0, 0, 0, x_{\text{nw}}, y_{\text{nw}}, z_{\text{nw}})$, where the first three and last three entries correspond to the ion and nanowire equilibrium positions, respectively. This can be interpreted as a Taylor expansion around two points in space.

It is convenient to begin with analyzing the force $\vec{F} = -\vec{\nabla}\Phi_{\text{IA}}$ instead of the potential Φ_{IA} as this requires only a Taylor expansion to first order without loss of information on the ion dynamics. The following calculations are performed for the force component $F_z = -\frac{\partial \Phi_{\text{IA}}}{\partial z}$ along the axial trap direction z. The same arguments hold true for all other spatial directions.

The analytical expression of the force component F_z due to the ion-nanowire interaction along the axial trap direction is given by:

$$F_z = -\frac{\partial \Phi_{\text{IA}}}{\partial z} = \frac{\varepsilon(z - z_{\text{nw}})}{\sqrt{(x - x_{\text{nw}})^2 + (y - y_{\text{nw}})^2 + (z - z_{\text{nw}})^2}^3}. \tag{9.9}$$

Here, we defined the parameter $\varepsilon = k_{\text{c}} q_{\text{ion}} q_{\text{nw}}$. Following equation 9.8, Taylor expansion of

equation 9.9 around $\vec{a} = (0, 0, 0, x_{\mathrm{nw}}, y_{\mathrm{nw}}, z_{\mathrm{nw}})$ to first order yields:

$$\begin{aligned} F_z(\vec{x}, \vec{x}_{\mathrm{nw}}) = &- \frac{\varepsilon z_{\mathrm{nw}}}{d^3} \\ &- \frac{3\varepsilon x_{\mathrm{nw}} z_{\mathrm{nw}}}{d^5}\delta x - \frac{3\varepsilon y_{\mathrm{nw}} z_{\mathrm{nw}}}{d^5}\delta y + \left(\frac{\varepsilon}{d^3} - \frac{3\varepsilon z_{\mathrm{nw}}^2}{d^5}\right)\delta z \\ &+ \frac{3\varepsilon x_{\mathrm{nw}} z_{\mathrm{nw}}}{d^5}\delta x_{\mathrm{nw}} + \frac{3\varepsilon y_{\mathrm{nw}} z_{\mathrm{nw}}}{d^5}\delta y_{\mathrm{nw}} - \left(\frac{\varepsilon}{d^3} - \frac{3\varepsilon z_{\mathrm{nw}}^2}{d^5}\right)\delta z_{\mathrm{nw}}. \end{aligned} \tag{9.10}$$

The trajectories δx and δy around the equilibrium position of a laser-cooled ion confined in an ion trap correspond to oscillations of very small amplitudes. For now, we assume those to be sufficiently decoupled from the dynamics in z-direction such that they can be neglected in equation 9.10. We substitute $\delta z \to z$ since we expanded around $z = 0$. Furthermore, we assume the driven motion of the nanowire to be forced along the axial z-direction, such that $\delta x_{\mathrm{nw}} = \delta y_{\mathrm{nw}} = 0$ and $\delta z_{\mathrm{nw}} = A\cos(\omega_{\mathrm{nw}} t)$, corresponding to the analytical expression 9.2.

The approximated force experienced by the ion is thus:

$$F_z = -\frac{\varepsilon z_{\mathrm{nw}}}{d^3} + \left(\frac{\varepsilon}{d^3} - \frac{3\varepsilon z_{\mathrm{nw}}^2}{d^5}\right) z - \left(\frac{\varepsilon}{d^3} - \frac{3\varepsilon z_{\mathrm{nw}}^2}{d^5}\right) A\cos(\omega_{\mathrm{nw}} t). \tag{9.11}$$

The first term corresponds to a constant force that shifts the equilibrium position of the ion. The second term introduces a restoring force that leads to a frequency shift of the harmonic trapping potential along the z-direction. The third term corresponds to a periodic driving force that couples the nanowire motion to the ion motion. The effects of the individual terms on the total potential of the trap-nanowire geometry will be described in more detail in chapters 9.3 and 9.4.

9.3 Static Ion-Nanowire Potential Dynamics

The total electric potential Φ experienced by the ions is given by the sum of the trapping potential Φ_{trap} generated by the trap electrodes and the interaction potential Φ_{IA} generated by the nanowire given by equation 9.1. As in chapter 9.2, we will discuss the ion dynamics in z-direction. The discussed arguments and calculations can be analogously applied to the x- and y-direction by using the pseudopotential approximation for the trapping potential Φ_{trap} [33, 135] (see also chapter 2.7).

The harmonic trapping potential of a trapped ion with mass m in z-direction is given by:

$$\Phi_{\mathrm{trap}} = \frac{1}{2} m\omega_{0,z}^2 (z - z_0)^2. \tag{9.12}$$

The respective force in z-direction is:

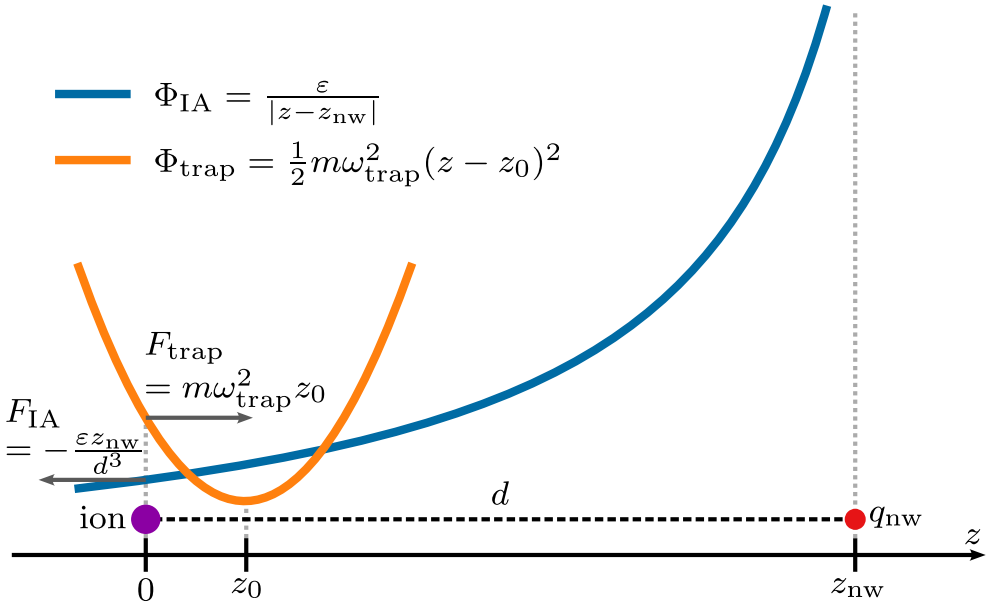

Figure 9.3: Equilibrium forces F and potentials Φ acting on a trapped ion in the presence of a charged nanowire. The repulsion due to the charge of the nanowire shifts the equilibrium position of the trapped ion (purple) from z_0 to $z = 0$ in the chosen coordinate system. Equilibrium is given by balance of the forces $F_{\mathrm{trap}} = -F_{\mathrm{IA}}$, corresponding to $z_0 = \varepsilon z_{\mathrm{nw}}/(m\omega_{0,z}^2 d^3)$. The nanowire tip with point charge q_{nw} (red) is positioned at $z_{\mathrm{nw}} = d$. Effects on the nanowire are neglected due to the high mass difference $M_{\mathrm{nw}} \gg m_{\mathrm{ion}}$. The potentials Φ_{trap} and Φ_{IA} indicated are schematics and not drawn to scale.

$$F_{\mathrm{trap}} = -m\omega_{0,z}^2 (z - z_0). \tag{9.13}$$

Here, $\omega_{0,z}$ is the angular trap frequency and z_0 is the position of the trapping potential minimum. The total force component F_z experienced by the ion can be approximated by the sum of equation 9.13 and the Taylor expanded force given by equation 9.11:

$$\begin{aligned} F_z &= -m\omega_{0,z}^2 (z - z_0) - \frac{\varepsilon z_{\mathrm{nw}}}{d^3} + \left(\frac{\varepsilon}{d^3} - \frac{3\varepsilon z_{\mathrm{nw}}^2}{d^5} \right) z \\ &= \left(m\omega_{0,z}^2 z_0 - \frac{\varepsilon z_{\mathrm{nw}}}{d^3} \right) + \left(\frac{\varepsilon}{d^3} - \frac{3\varepsilon z_{\mathrm{nw}}^2}{d^5} - m\omega_{0,z}^2 \right) z. \end{aligned} \tag{9.14}$$

Here, the second line was rearranged to show the constant force components and the restoring force components. Equation 9.14 corresponds to the static case in which the nanowire motion is not driven. The addition of the periodic driving force $(\frac{\varepsilon}{d^3} - \frac{3\varepsilon z_{\mathrm{nw}}^2}{d^5}) A \cos(\omega_{\mathrm{nw}} t)$ from equation 9.11 will be discussed in chapter 9.4. Figure 9.3 visualizes the acting constant forces for the special case of the nanowire tip positioned on the z-axis $\vec{x}_{\mathrm{nw}} = (0, 0, z_{\mathrm{nw}})$.

For the equilibrium position of the ion to be at the origin $\vec{x} = (0, 0, 0)$, the constant forces in equation 9.14 have to cancel each other out at $z = 0$, resulting in:

$$
\begin{aligned}
z_0 &= \frac{\varepsilon z_{\mathrm{nw}}}{m\omega_{0,z}^2 d^3}, \\
\Rightarrow F_z &= \left(\frac{\varepsilon}{d^3} - \frac{3\varepsilon z_{\mathrm{nw}}^2}{d^5} - m\omega_{0,z}^2\right) z \\
&= \left(\frac{\varepsilon}{d^3}\left(1 - \frac{3z_{\mathrm{nw}}^2}{d^2}\right) - m\omega_{0,z}^2\right) z.
\end{aligned}
\tag{9.15}
$$

We define the *coupling strength* of the ion-nanowire system as ε/d^3, as those parameters describe the fundamental strength of the ion-nanowire interaction shown in equation 9.15. It is convenient to report the coupling strength in units of $m\omega_{0,z}^2$ for a given trapping frequency $\omega_{0,z}$.

The restoring force part of equation 9.14 changes the trapping frequency from the applied $\omega_{0,z}$ to an effective trapping frequency ω_z given by:

$$
\begin{aligned}
\omega_z &= \sqrt{\omega_{0,z}^2 - \frac{\varepsilon}{md^3} + \frac{3\varepsilon z_{\mathrm{nw}}^2}{md^5}} \\
&= \sqrt{\omega_{0,z}^2 + \Delta\omega_z^2}.
\end{aligned}
\tag{9.16}
$$

Vice versa, for a desired ω_z (e. g. $\omega_z = \omega_{\mathrm{nw}}$ to obtain resonance with the nanowire) the initial trapping frequeny $\omega_{0,z}$ needs to be given by:

$$
\omega_{0,z} = \sqrt{\omega_z^2 + \frac{\varepsilon}{md^3} - \frac{3\varepsilon z_{\mathrm{nw}}^2}{md^5}}. \tag{9.17}
$$

From equation 9.16, it can be seen that the frequency shift $\Delta\omega_z^2 = -\frac{\varepsilon}{md^3} + \frac{3\varepsilon z_{\mathrm{nw}}^2}{md^5}$ does not only depend on the total ion-nanowire distance d, but also on the ratio $\frac{z_{\mathrm{nw}}}{d}$. Notably, $\Delta\omega_z^2$ vanishes for the conditons $z_{\mathrm{nw}} = \pm\frac{1}{\sqrt{3}}d$. Figure 9.4 shows the behaviour of $\Delta\omega_z^2$ for different ratios $\frac{z_{\mathrm{nw}}}{d}$.

It is important to note that the parameter $\Delta\omega_z^2$ defined here can be a negative or positive real number. Furthermore, the actual frequency shift is *not* given by $\sqrt{\Delta\omega_z^2}$, but by $\omega_z - \omega_{0,z} \neq \sqrt{\Delta\omega_z^2}$.

9.4 Driven Ion-Nanowire Potential Dynamics

In the case of a nanowire mechanically oscillating along the z-axis, equation 9.14 gets extended by the periodic driving force from equation 9.11, resulting in:

$$
F_z = -m\omega_z^2 z - \left(\frac{\varepsilon}{d^3} - \frac{3\varepsilon z_{\mathrm{nw}}^2}{d^5}\right) A\cos\left(\omega_{\mathrm{nw}} t\right). \tag{9.18}
$$

As discussed in chapter 9.3, equilibrium at $\vec{x} = (0,0,0)$ is already implied such that constant force terms add up to 0. Furthermore, $\omega_z^2 = \omega_{0,z}^2 + \Delta\omega_z^2$ as given by equation 9.16. ω_{nw} is the

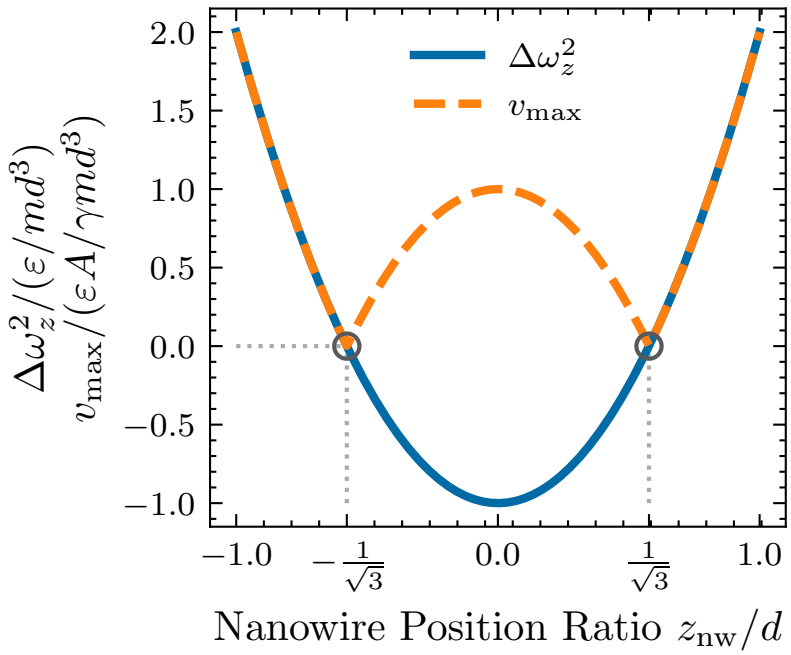

Figure 9.4: Frequency shift $\Delta\omega_z^2$ and driven velocity amplitude $v_{\max}$ for different ratios z_{nw}/d of the nanowire position. The conditions $z_{\mathrm{nw}} = \pm\frac{1}{\sqrt{3}}d$ lead to $\Delta\omega_z^2 = 0$ and $v_{\max} = 0$ (dark gray markers). The velocity amplitude and frequency shift in z-direction are maximized for $z_{\mathrm{nw}} = \pm d$.

angular frequency of the oscillating nanowire motion.

Deriving the underlying equation of motion to equation 9.18 yields:

$$\ddot{z} + \gamma\dot{z} + \omega_z^2 z = -\left(\frac{\varepsilon}{md^3} - \frac{3\varepsilon z_{\mathrm{nw}}^2}{md^5}\right) A\cos\left(\omega_{\mathrm{nw}}t\right). \tag{9.19}$$

Here, the damping constant γ was added to represent laser cooling of trapped ions as discussed in chapter 4.1.1.

Equation 9.19 is that of a periodically driven damped harmonic oscillator (see also chapter 5.6). The steady-state solutions of the ion trajectory $z(t)$ and velocity $v_z(t)$ for $t \to \infty$ are given by [121, 167]:

$$\begin{aligned} z(t) &= -\left(\frac{\varepsilon}{md^3} - \frac{3\varepsilon z_{\mathrm{nw}}^2}{md^5}\right)\frac{A}{\gamma\omega_{\mathrm{nw}}}\cos\left(\omega_{\mathrm{nw}}t - \varphi\right), \\ v_z(t) &= \left(\frac{\varepsilon}{md^3} - \frac{3\varepsilon z_{\mathrm{nw}}^2}{md^5}\right)\frac{A}{\gamma}\sin\left(\omega_{\mathrm{nw}}t - \varphi\right). \end{aligned} \tag{9.20}$$

Here, φ is the phase of the oscillations relative to the periodic driving force. Equation 9.20 assumes resonant drive of the motion, i. e., $\omega_{\mathrm{nw}} = \omega_z$. For off-resonant drive, γ needs to be adjusted to $\gamma \to \sqrt{\gamma^2 + \frac{1}{\omega_{\mathrm{nw}}^2}(\omega_z^2 - \omega_{\mathrm{nw}}^2)^2}$ [121].

The velocity amplitude of the driven ion motion is thus given by:

$$v_{\max} = \left| \left(\frac{\varepsilon}{md^3} - \frac{3\varepsilon z_{\mathrm{nw}}^2}{md^5} \right) \frac{A}{\gamma} \right|. \tag{9.21}$$

Figure 9.4 shows $v_{\max}$ for different ratios $\frac{z_{\mathrm{nw}}}{d}$. Just as in equation 9.16, $z_{\mathrm{nw}} = \pm\frac{1}{\sqrt{3}}d$ represent special cases in which the driving force vanishes. Furthermore, the sign of the oscillation amplitude flips at $z_{\mathrm{nw}} = \pm\frac{1}{\sqrt{3}}d$, corresponding to a phase shift of π.

The notion of the driven ion-nanowire coupling vanishing for some seemingly arbitrary values of $\frac{z_{\mathrm{nw}}}{d}$ may seem counter-intuitive at first. However, the drive strength amplitude is determined by the *gradient* of the interaction force acting on the ion, i. e., the *variation* of the force due to the periodic change in position $\delta z_{\mathrm{nw}} = A\cos(\omega_{\mathrm{nw}}t)$ of the oscillating nanowire. This can be understood by considering that the oscillating nanowire point charge moves the interaction potential Φ_{IA} along with its oscillatory motion at amplitude A. This leads to a periodic modulation of the potential and force experienced by the ion, proportional to the gradient (or slope) of the force. To first order, the amplitude of the driving force is given by $\Delta F_z = (\partial F_z/\partial z_{\mathrm{nw}})A$ at the equilibrium position of the ion $z = 0$. This is visualized in figure 9.5 by showing the acting potentials, forces and force gradients in z-direction for different values of $\frac{z_{\mathrm{nw}}}{d}$. The gradient vanishes for the special cases $z_{\mathrm{nw}} = \pm\frac{1}{\sqrt{3}}d$, following the analytical expression for Φ_{IA} given in equation 9.1.

From equation 9.21, the velocity amplitude $v_{\max}$ of a driven ion is predicted to be proportional to the oscillation amplitude A and the charge q_{nw} of the nanowire in the definition of $\varepsilon = k_{\mathrm{c}}q_{\mathrm{ion}}q_{\mathrm{nw}}$. The relation between $v_{\max}$ and the ion-nanowire distance d is more complex and also depends on the specific position coordinate z_{nw} of the nanowire. It is given by $v_{\max} \propto \frac{1}{d^3} - 3\frac{z_{\mathrm{nw}}^2}{d^5}$. In the case of $z_{\mathrm{nw}} = 0$, proportionality to $\frac{1}{d^3}$ is expected.

Numerical simulations of the static and driven ion-nanowire interaction were consistent with the predictions given in equations 9.16 and 9.21. The simulations were computed with the analytical expression for the interaction potential Φ_{IA} (equation 9.1) and the pseudopotential approximation [33] for the trapping potentials (see also chapter 2.7). The results are discussed in chapters 10.2 and 10.3.

9.5 Ion-Nanowire Potential Stability

Stable confinement of positively charged ions requires an electric potential minimum at the equilibrium position $\vec{x} = (0, 0, 0)$. Mathematically, this corresponds to a negative force gradient $\frac{\partial F_z}{\partial z} < 0$ at the equilibrium position. From the expression of the total force F_z given in equation 9.15 we can compute the condition [94]:

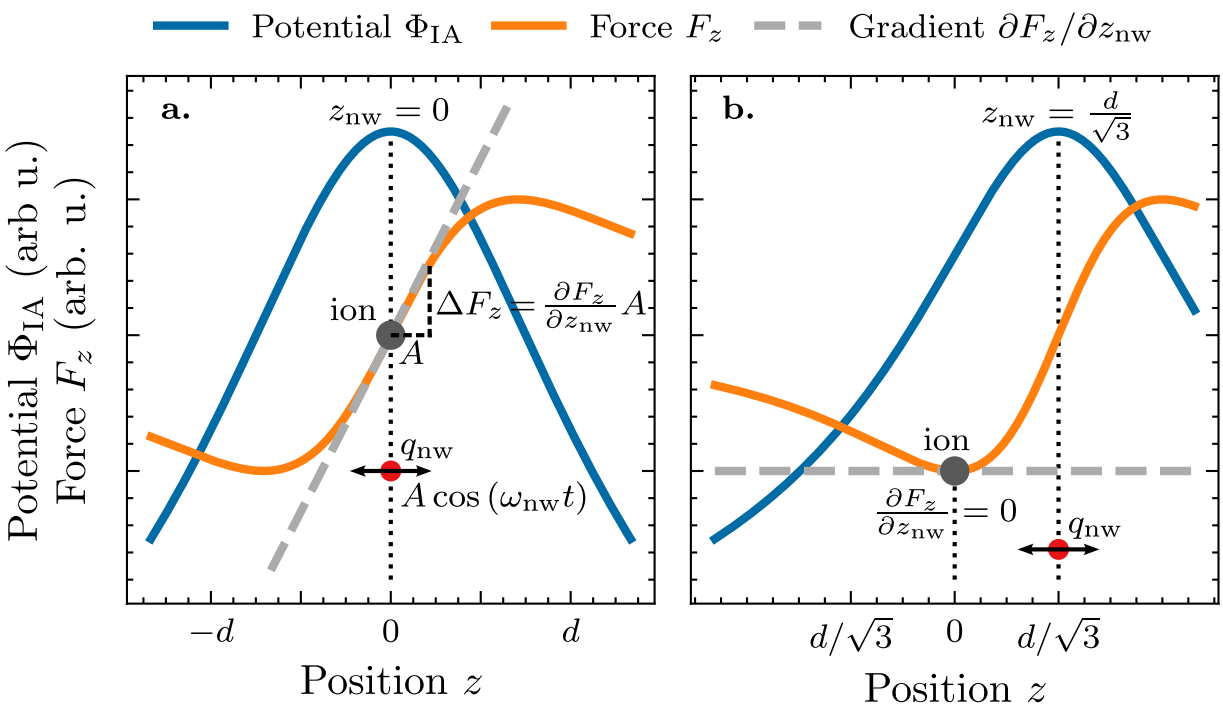

Figure 9.5: Potential Φ_{IA} and driving force amplitude ΔF_z experienced by a trapped ion due to the gradient of the interaction force. The interaction potentials, forces and force gradients are shown for nanowires positioned at $z_{nw} = 0$ (**a**) and $z_{nw} = \frac{d}{\sqrt{3}}$ (**b**). The point charge q_{nw} of an oscillating charged nanowire (red dot) exerts a periodic variation of the potential and force experienced by an ion at its equilibrium position (dark gray marker). The interaction potential moves along with the nanowire motion at amplitude A. To first order, this leads to a periodic change of the force acting on the ion with an amplitude given by $\Delta F_z = (\partial F_z/\partial z_{nw})A$. The gradient is non-zero except for the cases $z_{nw} = \pm d/\sqrt{3}$.

$$\kappa_{stab} = \frac{\varepsilon}{m\omega_{0,z}^2 d^3}\left(1 - \frac{3z_{nw}^2}{d^2}\right) < 1. \tag{9.22}$$

Here, we introduced the stability parameter κ_{stab}. The condition given in equation 9.22 is equivalent to the requirement that the effective trap frequency ω_z given by equation 9.16 needs to be a real and positive number:

$$\omega_z = \sqrt{\omega_{0,z}^2 + \Delta\omega_z^2} > 0. \tag{9.23}$$

Figure 9.6 shows the resulting total potentials $\Phi = \Phi_{trap} + \Phi_{IA}$ along z for different values of κ_{stab} and different nanowire positions z_{nw}/d. In the case of $\kappa_{stab} \geq 1$ the formation of plateaus and double well potentials is observed.

It is important to consider that κ_{stab} given in equation 9.22 refers only to the z-direction. The stability parameters of the trapping potentials along the other directions need to be computed individually.

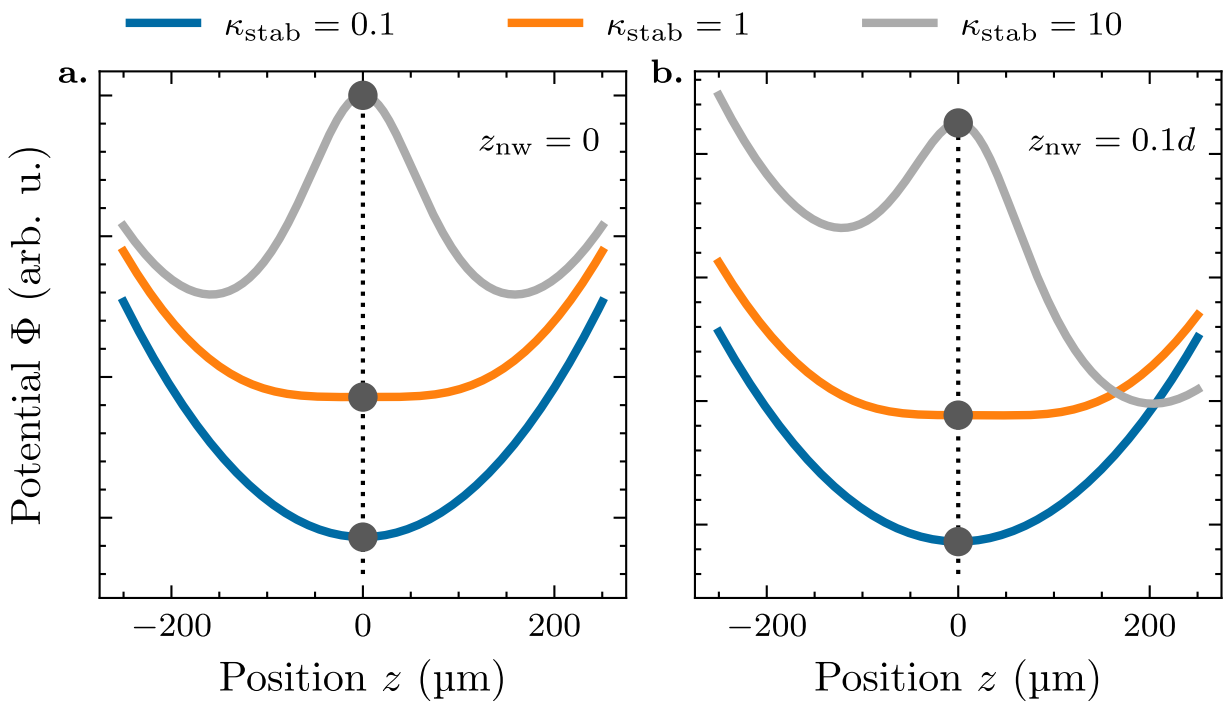

Figure 9.6: Total potentials Φ for different stability parameters κ_{stab}. The potentials $\Phi = \Phi_{\mathrm{trap}} + \Phi_{\mathrm{IA}}$ are shown along the z-direction for nanowire position components $z_{\mathrm{nw}} = 0$ (**a**) and $z_{\mathrm{nw}} = 0.1d$ (**b**). In order to obtain stable confinement at the imposed ion equilibrium position $z = 0$ (dark gray markers), a potential minimum is required. This corresponds to the condition $\kappa_{\mathrm{stab}} < 1$. For $\kappa_{\mathrm{stab}} \geq 1$, the formation of double-well potentials is observed. Depending on the position of the nanowire, the total potential Φ can be completely symmetric (**a**) or exhibit asymmetries (**b**).

9.6 Coupled Ion Motion in the Static Nanowire Potential

In equation 9.10, we assumed negligible coupling between the different motional directions x, y and z of a single trapped ion in the presence of the nanowire interaction potential Φ_{IA}. This assumption is valid for nanowire positions $\vec{x}_{\mathrm{nw}}$ with a single position component or low coupling strengths $\frac{\varepsilon}{d^3}$. However, the coupling between the directions of motion of the ion can be sufficiently large to have a noticeable effect on the resulting trap frequencies such that they are no longer accurately described by equation 9.16.

In matrix notation, the equations of motion for all directions are given by:

$$\begin{aligned}\begin{pmatrix}\ddot{x}\\ \ddot{y}\\ \ddot{z}\end{pmatrix} &= \begin{pmatrix}\left(\frac{\varepsilon}{md^3} - \frac{3\varepsilon x_{\mathrm{nw}}^2}{md^5} - \omega_{0,x}^2\right) & -\frac{3\varepsilon x_{\mathrm{nw}} y_{\mathrm{nw}}}{md^5} & -\frac{3\varepsilon x_{\mathrm{nw}} z_{\mathrm{nw}}}{md^5}\\ -\frac{3\varepsilon x_{\mathrm{nw}} y_{\mathrm{nw}}}{md^5} & \left(\frac{\varepsilon}{md^3} - \frac{3\varepsilon y_{\mathrm{nw}}^2}{md^5} - \omega_{0,y}^2\right) & -\frac{3\varepsilon y_{\mathrm{nw}} z_{\mathrm{nw}}}{md^5}\\ -\frac{3\varepsilon x_{\mathrm{nw}} z_{\mathrm{nw}}}{md^5} & -\frac{3\varepsilon y_{\mathrm{nw}} z_{\mathrm{nw}}}{md^5} & \left(\frac{\varepsilon}{md^3} - \frac{3\varepsilon z_{\mathrm{nw}}^2}{md^5} - \omega_{0,z}^2\right)\end{pmatrix}\begin{pmatrix}x\\ y\\ z\end{pmatrix}\\ &= \begin{pmatrix}k_{xx} & k_{xy} & k_{xz}\\ k_{xy} & k_{yy} & k_{yz}\\ k_{xz} & k_{yz} & k_{zz}\end{pmatrix}\begin{pmatrix}x\\ y\\ z\end{pmatrix} = K\begin{pmatrix}x\\ y\\ z\end{pmatrix},\end{aligned} \tag{9.24}$$

where the off-diagonal elements k_{ij} $(i \neq j)$ correspond to the coupling terms between the directions of motion of the ion, induced by the static interaction potential Φ_{IA} generated by the

nanowire.

The solutions $x(t)$, $y(t)$ and $z(t)$ to equation 9.24 can be found with the ansatz:

$$\begin{pmatrix} x \\ y \\ z \end{pmatrix} = Ae^{i\omega t} \ (A \in \mathbb{R}^3), \tag{9.25}$$

and finding the eigenfrequencies ω of the system by solving the resulting eigenvalue problem [193]:

$$\begin{aligned} KAe^{i\omega t} &= -\omega^2 Ae^{i\omega t}, \\ \Rightarrow \det\left(K + \omega^2 \mathbb{I}_3\right) &= 0. \end{aligned} \tag{9.26}$$

Here, $\mathbb{I}_3$ denotes the 3×3 identity matrix. The general solution to equation 9.26 in the presence of three non-vanishing coupling terms $k_{xy}, k_{xz}, k_{yz} \neq 0$ is a set of three eigenvalues ω^2 with lengthy expressions that will not be given in full here. It is recommended to compute the eigenfrequencies with mathematics tools such as Wolfram Mathematica [195].

However, the problem simplifies significantly if one direction of motion remains completely decoupled from the others (e. g. $k_{xy} = 0$ and $k_{xz} = 0$). This can be achieved by placing the nanowire at a position $\vec{x}_{\mathrm{nw}}$ with one vanishing component (here $x_{\mathrm{nw}} = 0$, see equation 9.24). In this case, the eigenvalues are given by the two expressions:

$$\begin{aligned} \omega_-^2 &= -\frac{1}{2}\left(k_{zz} + k_{yy} + \sqrt{(k_{zz} - k_{yy})^2 + 4k_{yz}^2}\right), \\ \omega_+^2 &= -\frac{1}{2}\left(k_{zz} + k_{yy} - \sqrt{(k_{zz} - k_{yy})^2 + 4k_{yz}^2}\right). \end{aligned} \tag{9.27}$$

The ion motions $y(t)$ and $z(t)$ are thus coupled and consist of superpositions of oscillations at frequencies ω_- and ω_+, while $x(t)$ remains uncoupled and oscillates at ω_x given by equation 9.16. Note how equation 9.27 reduces to equation 9.16 for small $k_{yz}^2 \ll (k_{yy} - k_{zz})^2$.

The general real solution for $z(t)$ (and analogously for $y(t)$) is given by:

$$z(t) = A_z \cos\left(\omega_+ t - \varphi_+\right) + B_z \cos\left(\omega_- t - \varphi_-\right), \tag{9.28}$$

with $A_z, B_z, \varphi_+, \varphi_- \in \mathbb{R}$ given by the boundary conditions of the system.

Figure 9.7 compares the frequencies obtained from equations 9.16 and 9.27 for different coupling strengths ε/d^3 and position ratios z_{nw}/d with frequencies $\omega_{0,z} = 2\pi \times 422$ kHz and $\omega_{0,y} = 2\pi \times 1.2$ MHz. $\omega_{0,z}$ and $\omega_{0,y}$ were chosen to correspond closely to frequencies applied

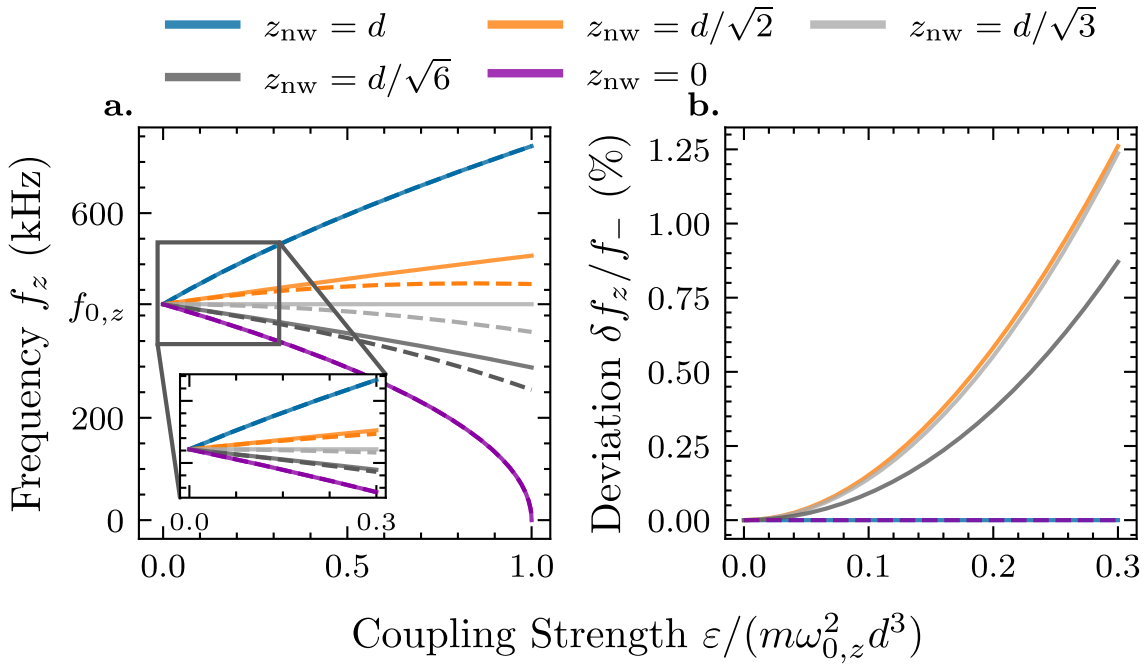

Figure 9.7: Comparison of frequency shifts in z-direction for the coupled and uncoupled description of the ion motion. The trap frequencies were set to $f_{0,z} = 422$ kHz and $f_{0,y} = 1.2$ MHz. **a**, The curves show the shifted frequency f_z as a function of the ion-nanowire coupling strength for different ratios z_{nw}/d ($\Rightarrow y_{\mathrm{nw}} = \sqrt{d^2 - z_{\mathrm{nw}}^2}$). The solid curves correspond to the uncoupled description of f_z given by equation 9.16, while the dashed curves correspond to the coupled frequency f_- given by equation 9.27. The behaviors are identical for $z_{\mathrm{nw}} = 0$ and $z_{\mathrm{nw}} = d$ due to the vanishing of the coupling term k_{yz}. Other ratios z_{nw}/d show a noticeable deviation $\delta f_z = f_z - f_-$ for high coupling strengths. The inset shows the region of low coupling strengths $\varepsilon/d^3 \leq 0.3 m\omega_{0,z}^2$ relevant for experiments presented in this thesis. **b**, Relative deviation $\delta f_z/f_-$ of the frequencies as described by the coupled and uncoupled motion. For coupling strengths $\leq 0.3 m\omega_{0,z}^2$ (inset of **a**), the relative deviation is $\lesssim 1.25\%$ and an uncoupled approximation of the ion motion is justified.

during experiments (see chapter 11). As can be seen in figure 9.7b, the deviation under experimental conditions presented in this thesis ($\varepsilon/d^3 \leq 0.3 m\omega_{0,z}^2$) is negligible ($\lesssim 1.25\%$). However, the coupling of the ion motion can become significant for high nanowire charges q_{nw} and low ion-nanowire distances d.

9.7 Coupled Ion Motion Driven by the Nanowire

The description of coupled motion in the static potential of a nanowire presented in chapter 9.6 can be extended to include the resonant drive by an oscillating nanowire.

Here, we only consider the coupling of two directions of oscillation (y and z). We further limit the discussion to resonant drive at the frequency component ω_-, corresponding to the shifted axial frequency of the ion given in equation 9.27.

In the case of a nanowire driven along the z-axis, the nanowire position in the Taylor expansion of the interaction force is given by $\delta z_{\mathrm{nw}} = A\cos(\omega_{\mathrm{nw}} t)$ (see equation 9.10). The equations of motion 9.24 for y and z including the resonant drive of the oscillating nanowire and adding a

damping factor γ are then found to be:

$$\begin{aligned}\ddot{y} + \gamma\dot{y} - k_{yy}y - k_{yz}z &= \frac{3\varepsilon y_{\mathrm{nw}} z_{\mathrm{nw}}}{md^5} A\cos(\omega_{\mathrm{nw}}t),\\ \ddot{z} + \gamma\dot{z} - k_{zz}z - k_{yz}y &= -\left(\frac{\varepsilon}{md^3} - \frac{3\varepsilon z_{\mathrm{nw}}^2}{md^5}\right) A\cos(\omega_{\mathrm{nw}}t).\end{aligned} \tag{9.29}$$

The right-hand sides of equation 9.29 are found by Taylor expansion of the interaction forces F_z and F_y analogous to equation 9.10. Resonant drive of the motion is given when $\omega_{\mathrm{nw}} = \omega_-$, i. e., when the nanowire oscillates at the shifted axial frequency ω_- given in equation 9.27. In the following, we always assume resonance and denote both ω_{nw} and ω_- as ω_z.

The steady-state solutions of damped and periodically driven harmonic oscillators are oscillations at the driven frequency ω_z. In order to find the steady-state solutions for the coupled case given by equation 9.29, we use the ansatz:

$$\begin{aligned}y(t) &= y_{\max} e^{i\omega_z t},\\ z(t) &= z_{\max} e^{i\omega_z t},\end{aligned} \tag{9.30}$$

where $y_{\max}$ and $z_{\max}$ are the driven oscillation amplitudes of the steady-state solutions to be determined. Inserting equation 9.30 into the equations of motion 9.29 yields the following system of equations:

$$\begin{aligned}\left(-\omega_z^2 + i\omega_z\gamma - k_{yy}\right) y_{\max} - k_{yz} z_{\max} &= A_y,\\ \left(-\omega_z^2 + i\omega_z\gamma - k_{zz}\right) z_{\max} - k_{yz} y_{\max} &= A_z,\end{aligned} \tag{9.31}$$

with $A_y = \frac{3\varepsilon y_{\mathrm{nw}} z\mathrm{nw}}{md^5} A$ and $A_z = -(\frac{\varepsilon}{md^3} - \frac{3\varepsilon z_{\mathrm{nw}}^2}{md^5})A$.

Equation 9.31 is a system of linear equations yielding complex solutions $y_{\max}, z_{\max} \in \mathbb{C}$ with lengthy expressions. To shorten the solutions, we define the following parameters:

$$\begin{aligned}k_{\mathrm{R}} &= k_{yz}^2 - k_{yy}k_{zz} - \omega_z^2\left(k_{yy} + k_{zz} - \gamma^2\omega_z^2\right),\\ k_{\mathrm{I}} &= \gamma\omega_z\left(k_{yy} + k_{zz} + 2\omega_z^2\right).\end{aligned} \tag{9.32}$$

We are ultimately interested in the driven motion along the axial z-direction. The solutions $z_{\max}$ and the corresponding velocity amplitude $v_{\max}$ in z-direction are found to be:

$$\begin{aligned}z_{\max} = \frac{1}{k_{\mathrm{R}}^2 + k_{\mathrm{I}}^2}\Big| &\left(k_{\mathrm{R}}\left(-A_z k_{yy} + A_y k_{yz} - A_z\omega_z^2\right) + k_{\mathrm{I}}\left(-A_z\gamma\omega_z\right)\right)\\ &+ i\left(k_{\mathrm{I}}\left(-A_z k_{yy} + A_y k_{yz} - A_z\omega_z^2\right) + k_{\mathrm{R}}\left(A_z\gamma\omega_z\right)\right)\Big|,\\ \Rightarrow v_{\max} = \omega_{\mathrm{z}} z_{\max},&\end{aligned} \tag{9.33}$$

where the absolute values yield the physically relevant *real* solutions of the amplitude response

of the nanowire [121, 168].

Equation 9.33 is a correction to equation 9.20 required if coupling between the directions of oscillation of a single trapped ion driven by the nanowire becomes significant. The validity of equation 9.33 is demonstrated in numerical simulations of the driven ion motion in chapter 10.3. However, the approximate expression 9.20 adequately describes the driven ion motion for the experimental results presented in chapter 11.

The theoretical description of the ion-nanowire interaction presented in this chapter used a model in which the nanowire was approximated by a perfect point charge. This approximation describes the interaction potential well if we view the nanowire as an isolated object. In reality, however, the nanowire used in this thesis was attached to the tip of a conical tungsten holder of relatively large size compared to the geometry of the trap. As was shown in figure 9.1a, the introduction of the holder to the trap geometry introduces deviations from the point-charge potential. An extended description of the interaction would thus account for these deviations in equation 9.2 by identifying a suitable expression for the interaction potential. This would introduce contributions from the holder to the Taylor expanded force given by equation 9.8.

.

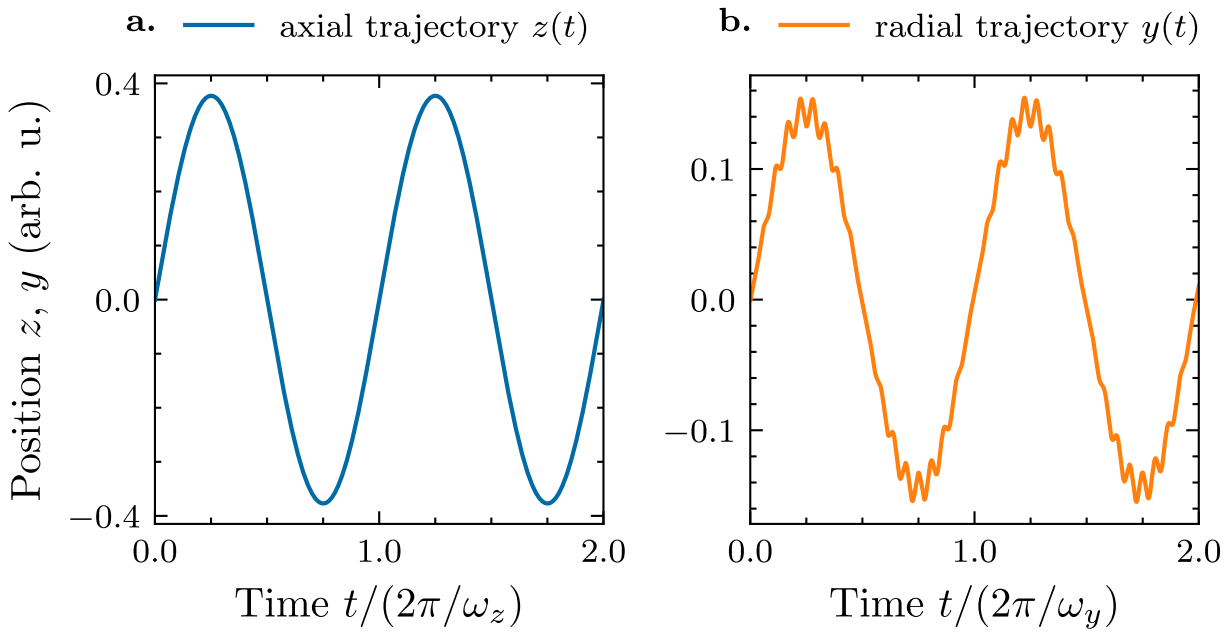

Figure 10.1: Velocity Verlet simulations of trajectories of a single ion in a linear radiofrequency trap. The shown trajectories are numerical solutions to the Mathieu equations 2.13 and do not include laser cooling or heating of the ion. **a**, The axial motion $z(t)$ with parameters $(a_z, q_z) = (1.52 \times 10^{-3}, 0.0)$ is completely free of micromotion. **b**, The radial motion $y(t)$ of the ion exhibits superimposed micromotion at trap parameters $(a_y, q_y) = (-0.76 \times 10^{-3}, -0.162)$. The secular motion frequencies of the trajectories are consistent with the expected behavior $\omega_i = \sqrt{a_i + \frac{q_i^2}{2}}\frac{\Omega}{2}$, where $i \in \{x, y, z\}$ (see chapter 2.3).

10 Numerical (MD) Simulations of Classical Ion-Nanowire Dynamics

10.1 Velocity Verlet Algorithm

The dynamics of trapped ions were simulated by numerically solving their equations of motion with the velocity Verlet algorithm [196, 197] commonly used in molecular dynamics (MD) simulations [198]. Figure 10.1 shows a simulated axial ($z(t)$) and radial ($y(t)$) trajectory of a single trapped ion in a linear radiofrequency trap. The shown trajectories correspond to solutions of the Mathieu equations of motion 2.13.

The velocity Verlet algorithm is closely related to Leapfrog integration [199], but evaluates particle positions $\vec{x}(t)$, velocities $\vec{v}(t)$ and accelerations $\vec{a}(t)$ at each time step Δt. The algorithm repeatedly follows three evaluation steps given by:

$$\begin{aligned} \vec{x}_{i+1} &= \vec{x}_i + \vec{v}_i \Delta t + \frac{1}{2}\vec{a}_i \Delta t^2, \\ \vec{a}_{i+1} &= \vec{a}(\vec{x}_{i+1}, t_{i+1}), \\ \vec{v}_{i+1} &= \vec{v}_i + \frac{1}{2}(\vec{a}_i + \vec{a}_{i+1})\Delta t. \end{aligned} \tag{10.1}$$

The initial parameters are given by the ion position $\vec{x}_0$ and velocity $\vec{v}_0$ at the starting time t_0. The initial acceleration $\vec{a}_0$ is calculated from the applied force at t_0:

$$\vec{a}_0 = \vec{a}(\vec{x}_0, t_0) = \frac{\vec{F}(\vec{x}_0, t_0)}{m}. \tag{10.2}$$

The time steps Δt were chosen to be smaller than any relevant dynamics of the simulated system. For the fastest relevant oscillations at the applied radiofrequency $\Omega = 2\pi \times 21.629$ MHz in the experiments presented in this thesis, the choice was $\Delta t = 1$ ns $< \frac{2\pi}{\Omega} \approx 46$ ns.

10.1.1 Simulation of Laser Cooling

Laser cooling of ions was implemented in the simulations by the addition of a continuous friction force as discussed in chapter 4.1.1. After each time step Δt of evaluations given by equation 10.1, the velocity was additionally adjusted by a damping factor γ:

$$\vec{v}_{i+1} \to \vec{v}_{i+1} - \gamma \Delta t \vec{v}_{i+1}. \tag{10.3}$$

In the case of an ion in a harmonic trapping potential of angular frequency ω_0, equation 10.3 corresponds to the addition of a damping term $\gamma\dot{\vec{x}}$ in the equations of motion:

$$\ddot{\vec{x}} + \gamma\dot{\vec{x}} + \omega_0^2\vec{x} = \frac{\vec{F}(\vec{x}, t)}{m}. \tag{10.4}$$

10.1.2 Simulation of Heating Mechanisms

To counteract the continuous laser cooling of the simulated ion motion (leading to $\vec{v}(t) \to 0$ for $t \to \infty$), heating mechanisms should be added to the algorithm. Heating processes can be implemented in the form of velocity kicks of amplitude Δv_k in random directions for each time step Δt [140, 200]. For a fixed velocity kick amplitude Δv_k, the *average* increase in temperature T (and thus kinetic energy E_kin) of a particle of mass m for each time step Δt is constant and given by the heating rate [200]:

$$k_\mathrm{heat} = \frac{\langle \Delta T \rangle}{\Delta t} = \frac{2\langle \Delta E_\mathrm{kin} \rangle}{3k_\mathrm{B}\Delta t} = \frac{m\Delta v_\mathrm{k}^2}{3k_\mathrm{B}\Delta t}. \tag{10.5}$$

k_heat can be determined experimentally [201] or by comparison of simulations to experimental results [202–204]. The velocity kick amplitude Δv_k per time step Δt is chosen to effectively take all relevant heating mechanisms such as background collisions [200] or RF/DC field noise [201]

into consideration. It is given by:

$$\Delta v_{\mathrm{k}} = \sqrt{k_{\mathrm{heat}} \frac{3k_{\mathrm{B}}}{m} \Delta t}, \tag{10.6}$$

in order to correspond to the heating rate given by equation 10.5.

The random direction of the velocity kick vector $\Delta\vec{v}_k$ is achieved by computing the spherical coordinate angles $\phi \in [0, 2\pi]$ and $\theta \in [0, \pi]$ with the generation of two random variables $u, v \in [0, 1]$ [155]:

$$\begin{aligned} & u, v \in [0,1], \\ \Rightarrow & \phi = 2\pi u, \\ & \theta = \arccos(1-2v), \\ \Rightarrow \Delta\vec{v}_{\mathrm{k}} = \Delta v_{\mathrm{k}} & \begin{pmatrix} \sin(\theta)\cos(\phi) \\ \sin(\theta)\sin(\phi) \\ \cos(\theta) \end{pmatrix}. \end{aligned} \tag{10.7}$$

Heating is then included by addition of $\Delta\vec{v}_{\mathrm{k}}$ to the velocity evaluation step given by equation 10.3. Figure 10.2a shows the simulated heating of a free particle initialized at $T = 0$ K for a single simulation as well as the average over $N = 100$ simulations. Figure 10.2b shows a typical trajectory for an oscillating trapped ion with the addition of laser cooling as a friction force and the discussed heating mechanism.

10.2 Ion Dynamics in a Static Nanowire Potential

The theoretical model for the description of the ion-nanowire hybrid system is given in detail in chapter 9. In the case of an undriven nanowire at a static bias voltage V_{nw}, the ion dynamics are affected by the introduction of a static interaction potential Φ_{IA}.

To summarize the relevant points here, the introduction of the charged nanowire to the trap leads to a shift in the effective angular trapping frequencies ω_i along all directions $i \in \{x, y, z\}$ as well as a shift in the ion equilibrium position within the trap. The interaction potential Φ_{IA} is described by two interacting point charges and the total potential $\Phi = \Phi_{\mathrm{trap}} + \Phi_{\mathrm{IA}}$ is given by:

$$\Phi = \frac{1}{2} m \left(\omega_{0,x}^2 x^2 + \omega_{0,y}^2 y^2 + \omega_{0,z}^2 z^2 \right) + k_{\mathrm{c}} \frac{q_{\mathrm{ion}} q_{\mathrm{nw}}}{|\vec{x}_{\mathrm{ion}} - \vec{x}_{\mathrm{nw}}|}. \tag{10.8}$$

The trapping potential Φ_{trap} in equation 10.8 used for the numerical simulations shown in the following chapters was described by the pseudopotential approximation (see chapter 2.7). $\omega_{0,i}$

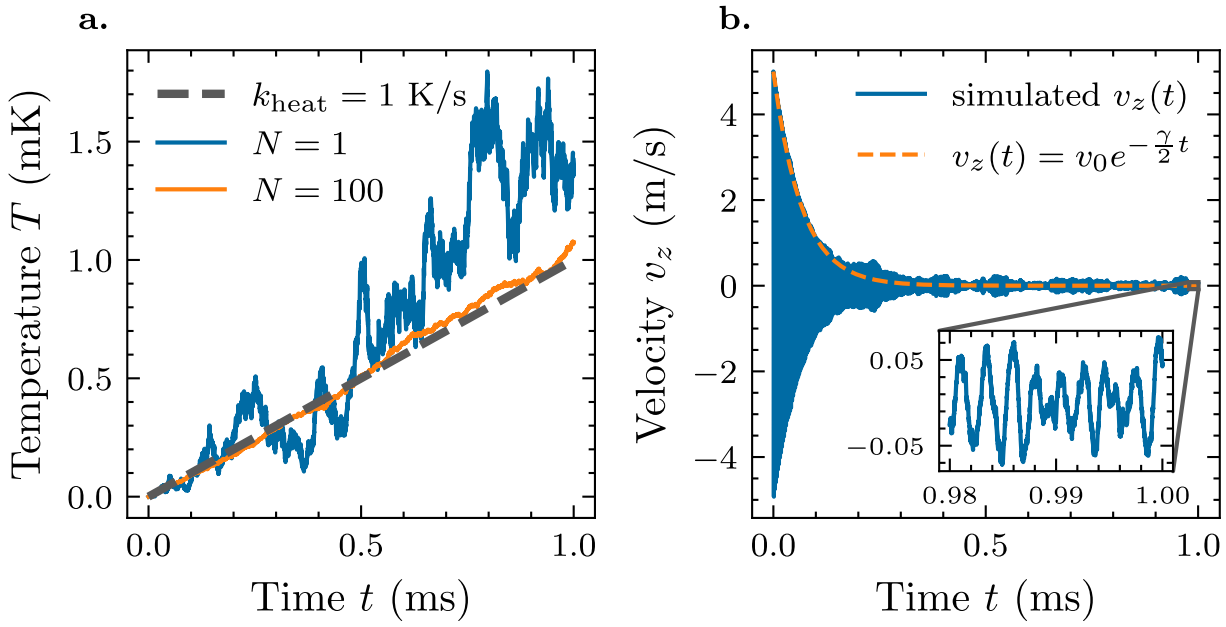

Figure 10.2: Numerical simulations including heating mechanisms. **a**, Temperature $T = \frac{2E_{\text{kin}}}{3k_{\text{B}}}$ of a free particle only subject to velocity kicks of random directions at fixed magnitude v_{k}, corresponding to a heating rate of $k_{\text{heat}} = 1$ K/s (dark gray line). The initial particle velocity for all simulations was $\vec{v}_0 = (0, 0, 0)$ ($\Rightarrow T = 0$) at simulation time steps $\Delta t = 10$ ns. A single simulation ($N = 1$, blue) follows the expected trend in temperature increase, but shows significant deviations due to the probabilistic nature of the simulated heating. Averaging over many simulations ($N = 100$, orange) shows that the *average* increase in temperature occurs indeed at the heating rate k_{heat}. **b**, Simulated axial velocity $v_z(t)$ (blue curve) of a single trapped ion at a trapping frequency $\omega_z = 2\pi \times 422$ kHz. The simulation included laser cooling at a damping factor of $\gamma = 30 \times 10^3$ s^{-1} and a heating rate of $k_{\text{heat}} = 2$ K/s with time steps $\Delta t = 1$ ns. The initial ion velocity in z-direction was $v_0 = 5$ m/s. The exponential decay from the laser cooling (orange curve) was counteracted by the probabilistic heating mechanisms, resulting in noisy ion oscillations at frequency ω_z (inset).

are the unperturbed angular frequencies of the trapping potential ($i \in \{x, y, z\}$).

The equations of motion obtained from equation 10.8 are given by:

$$\begin{aligned}
\ddot{x}_{\text{ion}} &= -\omega_{0,x}^2(x - x_0) + \frac{k_{\text{c}}}{m}\frac{q_{\text{ion}}q_{\text{nw}}}{|\vec{x}_{\text{ion}} - \vec{x}_{\text{nw}}|^3}(x_{\text{ion}} - x_{\text{nw}}), \\
\ddot{y}_{\text{ion}} &= -\omega_{0,y}^2(y - y_0) + \frac{k_{\text{c}}}{m}\frac{q_{\text{ion}}q_{\text{nw}}}{|\vec{x}_{\text{ion}} - \vec{x}_{\text{nw}}|^3}(y_{\text{ion}} - y_{\text{nw}}), \\
\ddot{z}_{\text{ion}} &= -\omega_{0,z}^2(z - z_0) + \frac{k_{\text{c}}}{m}\frac{q_{\text{ion}}q_{\text{nw}}}{|\vec{x}_{\text{ion}} - \vec{x}_{\text{nw}}|^3}(z_{\text{ion}} - z_{\text{nw}}),
\end{aligned} \tag{10.9}$$

where x_0, y_0 and z_0 were included in the simulations to shift the coordinate system such that the equilibrium position of a single trapped ion is at the origin $\vec{x} = (0, 0, 0)$. They are given by:

Parameter	Value
Ion Mass m	6.655×10^{-26} kg ≈ 40 u
Ion Charge q_{ion}	1.602×10^{-19} As $= 1e$
Nanowire Charge $q_{\mathrm{nw}}/V_{\mathrm{nw}}$	1.844×10^{-15} As/V $\approx 11.5 \times 10^{3} e$/V
Radiofrequency Ω	$2\pi \times 21.629$ MHz
Radial Frequencies $\omega_{0,x}$, $\omega_{0,y}$	$2\pi \times 1.2$ MHz
Number of Time Steps N	10^6
Time Step Δt	1 ns

Table 10.1: Parameters for the numerical simulations of ion trajectories $\vec{x}_i(t)$ and velocities $\vec{v}_i(t)$ peformed with the velocity Verlet algorithm. Parameters given in this table remained unchanged for all shown simulations. The choices and variations of further parameters are discussed in the respective chapters.

$$\begin{aligned} x_0 &= \frac{\varepsilon x_{\mathrm{nw}}}{m\omega_{0,x}^2 d^3}, \\ y_0 &= \frac{\varepsilon y_{\mathrm{nw}}}{m\omega_{0,y}^2 d^3}, \\ z_0 &= \frac{\varepsilon z_{\mathrm{nw}}}{m\omega_{0,z}^2 d^3}. \end{aligned} \tag{10.10}$$

Numerical solutions to the equations of motion 10.9 were obtained with the velocity Verlet algorithm described in chapter 10.1. Table 10.1 gives an overview of parameters used throughout all simulations shown in the following chapters. The simulations were performed over a total of $N = 10^6$ time steps at a step size of $\Delta t = 1$ ns, resulting in the simulation of the ion dynamics over a total time of 1 ms.

For all simulations shown in chapters 10.2.1 to 10.2.4, a single ion was initialized at position $\vec{x}_0 = (0, 0, 0)$ and initial velocity $\vec{v}_0 = (-0.5, -0.5, -0.5)$ m/s. Laser cooling and heating was omitted for the undriven ion-nanowire simulations in order to study the freely oscillating steady-state dynamics of the system. The absence of laser cooling and heating, as well as variations of the initial positions $\vec{x}_0$ and velocities $\vec{v}_0$ of the ion had no influence on the obtained frequency shifts.

The dynamics of a single ion experiencing a static perturbation from an undriven charged nanowire were studied for the variation of the following parameters:

- Variation of z_{nw} at a constant coupling strength ε/d^3.
- Variation of the ion-nanowire distance d.
- Variation of the effective nanowire charge q_{nw}.

In the following, we present the results and insights gained from these simulations of the ion dynamics in the static interaction potential Φ_{IA}. We focus on the dynamics along the axial z-direction, as we are ultimately interested in the resonant excitation of the axial ion motion

by the mechanically driven nanowire. We present the velocities $v_z(t)$ rather than $z(t)$, as those were experimentally determined with the photon-correlation method in chapter 11.

10.2.1 Variation of z_{nw} at a Constant Coupling Strength ε/d^3

For these simulations, the nanowire position was set to $\vec{x}_{\mathrm{nw}} = (0, y_{\mathrm{nw}}, z_{\mathrm{nw}})$ at a fixed ion-nanowire distance of $d = 250$ µm. The simulations were performed for different values of z_{nw} with $y_{\mathrm{nw}} = -\sqrt{d^2 - z_{\mathrm{nw}}^2}$ to ensure the fixed distance d. This corresponds to positioning the nanowire tip along a semicircle around the ion equilibrium position. The static nanowire voltage was set to $V_{\mathrm{nw}} = 1$ V and the unperturbed trapping frequencies of Φ_{trap} were set to $\omega_{0,z} = 2\pi \times 422$ kHz and $\omega_{0,x} = \omega_{0,y} = 2\pi \times 1.2$ MHz. This corresponds to a coupling strength of $\varepsilon/d^3 \approx 0.36 m\omega_{0,z}^2$.

The expected shifted frequencies ω_z and ω_y for coupled motion in y- and z-direction are given by:

$$\begin{aligned} \omega_z &= \sqrt{-\frac{1}{2}\left(k_{zz} + k_{yy} + \sqrt{(k_{zz} - k_{yy})^2 + 4k_{yz}^2}\right)}, \\ \omega_y &= \sqrt{-\frac{1}{2}\left(k_{zz} + k_{yy} - \sqrt{(k_{zz} - k_{yy})^2 + 4k_{yz}^2}\right)}, \end{aligned} \tag{10.11}$$

with parameters k_{yy}, k_{zz} and k_{yz} defined in equation 9.24. $k_{yz} = -3\varepsilon y_{\mathrm{nw}} z_{\mathrm{nw}}/(md^5)$ describes the coupling between y and z. Equation 10.11 corresponds to $\sqrt{\omega_-^2}$ and $\sqrt{\omega_+^2}$ from equation 9.27.

Figure 10.3 shows the ion velocities $v_z(t)$ and their FFT signals for $z_{\mathrm{nw}} \in \{0, d/\sqrt{3}, d\}$. As expected, the ion follows single-frequency oscillations for $z_{\mathrm{nw}} = 0$ and $z_{\mathrm{nw}} = d$, where the coupling term k_{yz} vanishes. For $z_{\mathrm{nw}} = d/\sqrt{3}$, the motion exhibits two superimposed oscillations with frequency components shifted from the unperturbed frequencies $\omega_{0,z}$ and $\omega_{0,y}$. The axial frequencies obtained from numerical simulations are consistent with the theoretical predictions given by equation 10.11 within the resolution of the FFT of 1 kHz. The results are summarized in table 10.2.

10.2.2 Variation of the Ion-Nanowire Distance d

The simulations for the variation of the ion-nanowire distance d were performed with the parameters given in table 10.1 at a static nanowire voltage of $V_{\mathrm{nw}} = 1$ V. The distance was varied from $d = 250$ µm to $d = 750$ µm in steps of 50 µm with the position vector of the nanowire given by $\vec{x}_{\mathrm{nw}} = (0, -\sqrt{d^2 - z_{\mathrm{nw}}^2}, z_{\mathrm{nw}})$. The lowest value for the distance $d = 250$ µm was chosen to be comparable to the ion-nanowire distances determined during the experimental demonstration of the ion-nanowire coupling (see chapter 11.3). The unperturbed axial trap frequency was set to $\omega_{0,z} = 2\pi \times 422$ kHz. The corresponding coupling strengths ranged from $\varepsilon/d^3 \approx 0.01 m\omega_{0,z}^2$

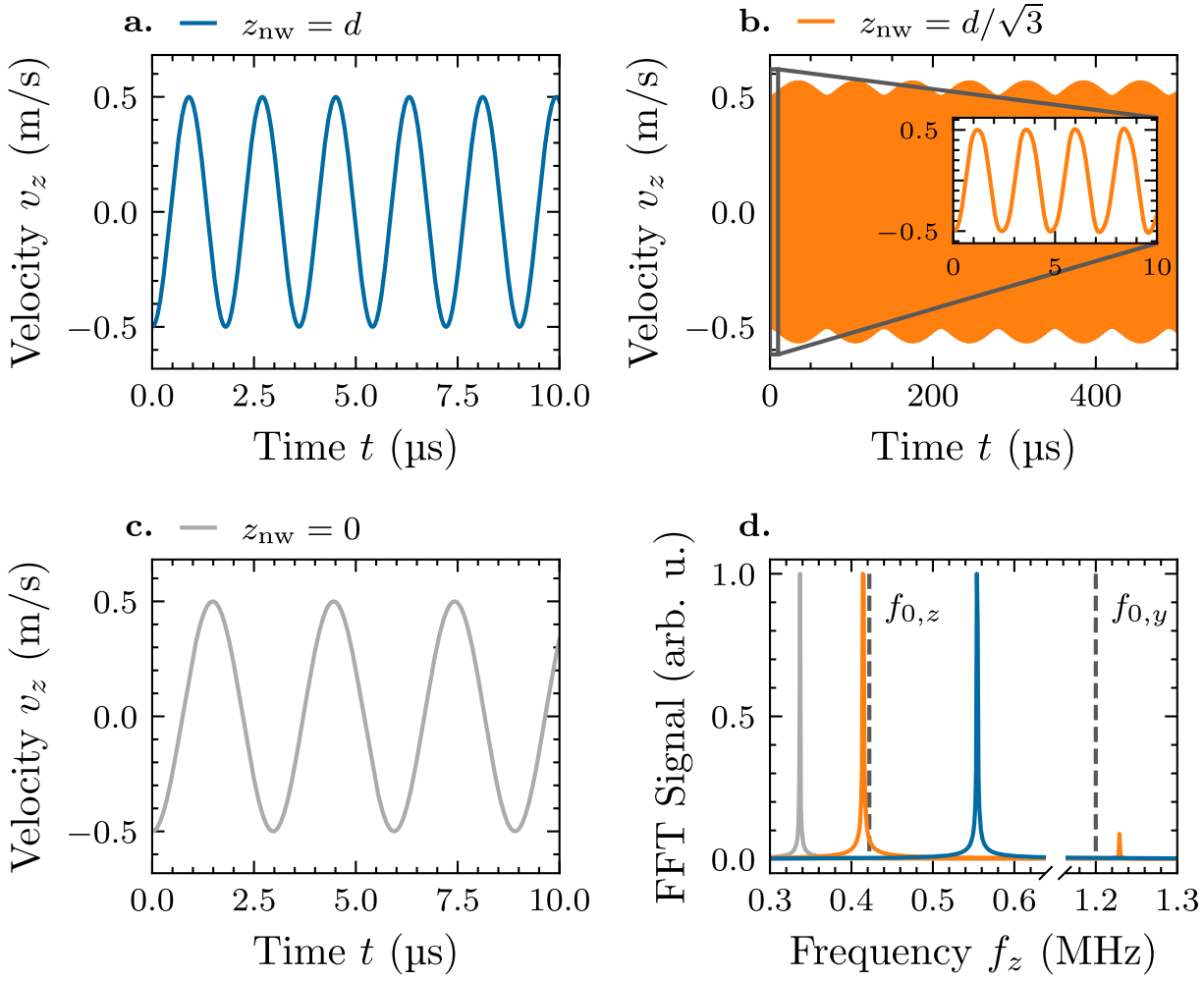

Figure 10.3: Simulated axial motion of a single ion in the static potential of an undriven charged nanowire. The nanowire was set to a voltage of $V_{\mathrm{nw}} = 1$ V and placed at an ion-nanowire distance $d = 250$ µm. The unperturbed axial frequency was $f_{0,z} = 422$ kHz. **a**, Harmonic ion motion at the shifted frequency $f_z = 554$ kHz. The nanowire was positioned at $\vec{x}_{\mathrm{nw}} = (0, 0, d)$. **b**, The ion motion exhibits two coupled oscillations for $\vec{x}_{\mathrm{nw}} = (0, -\sqrt{2/3}d, \sqrt{1/3}d)$. The oscillations correspond to the shifted axial and radial frequencies $f_z = 414$ kHz and $f_y = 1229$ kHz. **c**, For $\vec{x}_{\mathrm{nw}} = (0, -d, 0)$, the ion motion is harmonic at the positively shifted frequency $f_z = 337$ kHz. **d**, Normalized FFT signals of the ion motions shown in **a** − **c**. The frequencies are shifted from $f_{0,z}$ and $f_{0,y}$ (dark gray lines) and show the second frequency component for $z_{\mathrm{nw}} = d/\sqrt{3}$ (orange).

to $\varepsilon/d^3 \approx 0.36 m\omega_{0,z}^2$.

Figure 10.4a shows the axial frequencies f_z obtained from FFTs of the numerically simulated trajectories of a single trapped ion for the variation of d at different ratios z_{nw}/d. The frequencies are compared to the theoretical predictions given by the analytical expression for ω_z in equation 10.11. All of the data points obtained from the simulations are accurately described by the theory and the analytical values fall within the resolution of the FFT (1 kHz).

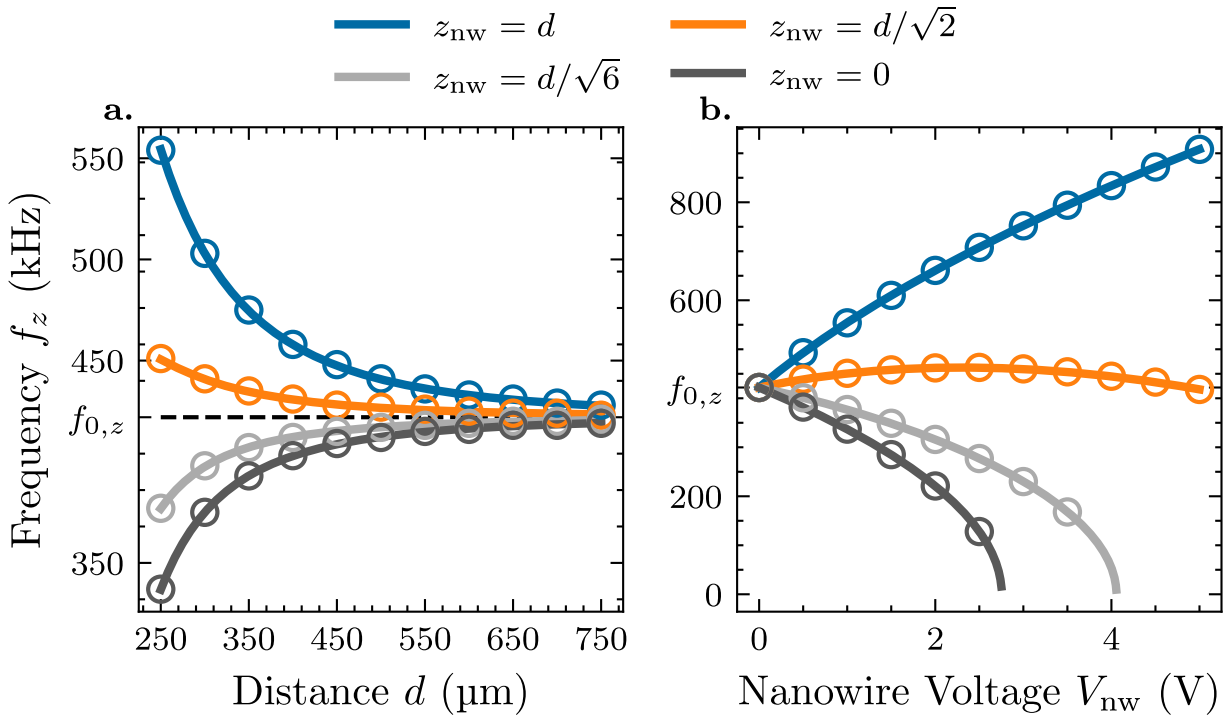

Figure 10.4: Shifted axial frequencies f_z in the static potential of an undriven charged nanowire for different nanowire positions z_{nw}. The unshifted frequency of the trapping potential Φ_{trap} was set to $f_{0,z} = 422$ kHz and the nanowire was positioned at $\vec{x}_{\mathrm{nw}} = (0, -\sqrt{d^2 - z_{\mathrm{nw}}^2}, z_{\mathrm{nw}})$. The data obtained from FFTs of numerical simulations (circles) is compared to the analytical expression given by equation 10.11 (solid curves). They are in agreement within the resolution of the FFT of 1 kHz. **a**, Low ion-nanowire distances d can lead to a significant shift in the effective trapping frequency f_z. The sign of the shift depends on the position of the nanowire relative to the ion equilibrium position. The shift vanishes for large distances d due to the reduced coupling between the ion and the nanowire. The voltage applied to the nanowire was set to $V_{\mathrm{nw}} = 1$ V. **b**, Variation of the static voltage V_{nw} leads to a shift of the effective trapping frequency f_z. This corresponds to a change of the charge of the nanowire q_{nw}. The sign and strength of the shift further depends on the position of the nanowire relative to the ion equilibrium position. The ion-nanowire distance was set to $d = 250$ µm.

10.2.3 Variation of the Effective Nanowire Charge q_{nw}

The parameter ε in the definition of the coupling strength ε/d^3 is given by:

$$\varepsilon = \frac{V_{\mathrm{nw}}}{1\ \mathrm{V}} \frac{q_{\mathrm{nw}} q_{\mathrm{ion}}}{4\pi\varepsilon_0}, \tag{10.12}$$

with $q_{\mathrm{nw}} = 1.844 \times 10^{-15}$ As at $V_{\mathrm{nw}} = 1$ V. V_{nw} is the static bias voltage applied to the nanowire. The effective charge of the nanowire q_{nw} (see also equation 9.5) is thus directly proportional to the applied voltage V_{nw}.

For the simulations of different effective nanowire charges q_{nw} presented here, the applied nanowire voltage was varied from $V_{\mathrm{nw}} = 0$ V up to $V_{\mathrm{nw}} = 5$ V in steps of 0.5 V at a constant ion-nanowire distance $d = 250$ µm. This corresponds to coupling strengths ranging from $\varepsilon/d^3 = 0$ to $\varepsilon/d^3 \approx 1.82 m\omega_{0,z}^2$. The simulations were performed with the parameters given in table 10.1 at an unperturbed axial frequency of $\omega_{0,z} = 2\pi \times 422$ kHz and a nanowire position

z_{nw}	$f_{z,\mathrm{theory}}$ (kHz)	$f_{z,\mathrm{FFT}}$ (kHz)
0	336.78	337
$d/\sqrt{3}$	$\{414.5, 1229.2\}$	$\{414, 1229\}$
d	554.45	554

Table 10.2: Theoretically predicted and simulated frequencies for different nanowire position components z_{nw}. The frequencies correspond to the simulations shown in figure 10.3 with the nanowire positioned at $\vec{x}_{\mathrm{nw}} = (0, -\sqrt{d^2 - z_{\mathrm{nw}}^2}, z_{\mathrm{nw}})$. The frequencies are accurately predicted within the resolution of the FFT of 1 kHz.

of $\vec{x}_{\mathrm{nw}} = (0, -\sqrt{d^2 - z_{\mathrm{nw}}^2}, z_{\mathrm{nw}})$

Figure 10.4b shows the frequencies f_z obtained from FFTs of numerical simulations at different ratios of the nanowire position z_{nw}/d. The frequencies are compared to the analytical expression for ω_z given by equation 10.11. The frequencies obtained from the simulations are in agreement with the analytical expression within the resolution of the FFT (1 kHz).

For $z_{\mathrm{nw}} = 0$ and $z_{\mathrm{nw}} = d/\sqrt{6}$, the resulting frequency shifts lead to instability ($f_z < 0$) before $V_{\mathrm{nw}} = 5$ V was reached. For $z_{\mathrm{nw}} = 0$, this corresponds exactly to the condition for the stability parameter κ_{stab} defined in equation 9.22.

10.2.4 Three-Dimensional Coupled Motion

For the sake of completeness, figure 10.5a shows the simulated and theoretical values of the shifted frequencies f_x, f_y and f_z for a nanowire position of $\vec{x}_{\mathrm{nw}} = (\sqrt{2/6}, -\sqrt{3/6}, \sqrt{1/6})d$. In this case, all three directions of motion of the ion are coupled due to the static interaction potential Φ_{IA} generated from the nanowire, with coupling terms $k_{xy}, k_{xz}, k_{yz} \neq 0$ (see equation 9.24). The ion motion then consists of three superimposed oscillations with frequencies corresponding to the shifted f_x, f_y and f_z (see figure 10.5b and 10.5c).

The simulations were performed for a variety of coupling strengths ε/d^3 and with initial trapping frequencies $(f_{0,x}, f_{0,y}, f_{0,z}) = (800, 1200, 422)$ kHz. Instead of evaluating the frequencies from the resulting lengthy analytical expressions, the theoretical values for f_z shown in figure 10.5a were computed directly by solving the eigenvalue problem (see equation 9.26) with Wolfram Mathematica [195].

10.3 Driven Ion-Nanowire Dynamics

In the following chapters 10.3.1 to 10.3.3, we discuss the results obtained from numerical simulations of a single ion mechanically driven by an oscillating nanowire. The simulations were performed with the exact analytical expression for the potential $\Phi = \Phi_{\mathrm{trap}} + \Phi_{\mathrm{IA}}$ and the re-

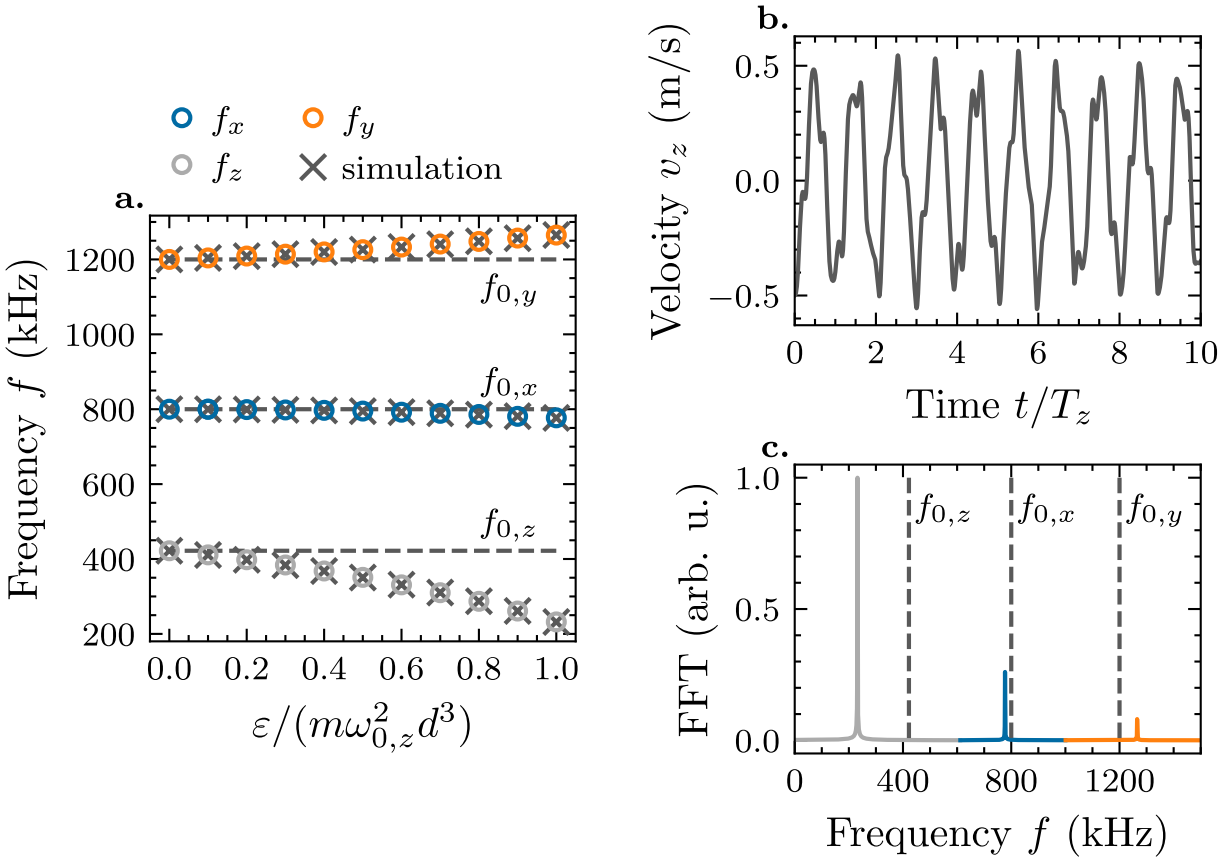

Figure 10.5: Shifted frequencies f_x, f_y and f_z for the coupling of all three directions of oscillation of a single trapped ion. The unshifted frequencies were set to $f_{0,x} = 800$ kHz, $f_{0,y} = 1.2$ MHz and $f_{0,z} = 422$ kHz (dashed gray lines). All directions of oscillation x, y and z are coupled due to the static potential generated by the nanowire positioned at $\vec{x}_{\mathrm{nw}} = (\sqrt{2/6}, -\sqrt{3/6}, \sqrt{1/6})d$. **a**, The effective trapping frequencies experience a stronger shift for higher coupling strengths. The coupling strengths ranged from $\varepsilon/d^3 = 0$ to $\varepsilon/d^3 = m\omega_{0,z}^2$. The frequencies obtained from FFTs of numerical simulations (crosses) are compared to the analytical values computed with Wolfram Mathematica [195] (circles). They are in agreement within the resolution of the FFT of 1 kHz. **b**, The velocity $v_z(t)$ of the motion of the ion in z-direction consists of three superimposed oscillations at the shifted frequencies f_x, f_y and f_z. The curve corresponds to $\varepsilon/(m\omega_{0,z}^2 d^3) = 1.0$ in **a**. **c**, FFT signal of $v_z(t)$ shown in **b**. The frequencies are clearly shifted from $f_{0,x}$, $f_{0,y}$ and $f_{0,z}$ and correspond to the shifts at $\varepsilon/(m\omega_{0,z}^2 d^3) = 1.0$ shown in **a** with the same color coding.

sulting equations of motion. The expressions Φ_{trap} and Φ_{IA} were given by:

$$\begin{aligned} \Phi_{\mathrm{trap}} &= \frac{1}{2} m \left(\omega_{0,x}^2 x^2 + \omega_{0,y}^2 y^2 + \omega_{0,z}^2 z^2\right), \\ \Phi_{\mathrm{IA}} &= k_{\mathrm{c}} \frac{q_{\mathrm{ion}} q_{\mathrm{nw}}}{\sqrt{(x - x_{\mathrm{nw}})^2 + (y - y_{\mathrm{nw}})^2 + (z - z_{\mathrm{nw}} - A\cos(\omega_{\mathrm{nw}} t))^2}}, \end{aligned} \tag{10.13}$$

where the driven nanowire position was $\vec{x}_{\mathrm{nw}} = (0, y_{\mathrm{nw}}, z_{\mathrm{nw}} + A\cos(\omega_{\mathrm{nw}} t))$. A is the amplitude of oscillation of the nanowire, ω_{nw} is the driven angular frequency of the nanowire and $\sqrt{y_{\mathrm{nw}}^2 + z_{\mathrm{nw}}^2} = d$ is the distance between the equilibrium positions of the ion and the nanowire.

The simulations were performed with the parameters given in table 10.1, with the exception of $\omega_{0,x}$ and $\omega_{0,y}$ which required adjustments to ensure a resonant drive. Additionally, a damping factor of $\gamma = 30 \times 10^3$ s^{-1} was added to the simulations to represent laser cooling as discussed

in chapter 10.1.1.

In the case of two non-vanishing position components $y_{\mathrm{nw}}, z_{\mathrm{nw}} \neq 0$ of the nanowire, coupling between the directions of motion y and z occurs. In order to ensure resonance of the oscillating nanowire to the axial motion of the trapped ion ($\omega_{\mathrm{nw}} = \omega_z$), the frequency shifts due to the static interaction potential shown in chapter 10.2 need to be counteracted. The shifted frequencies ω_z and ω_y correspond to ω_- and ω_+ given in equation 9.27. Resonance ($\omega_z = \omega_{\mathrm{nw}}$) in the numerical simulations was ensured by choosing the required values for the unshifted trapping frequencies $\omega_{0,i}$ ($i \in \{x, y, z\}$) of the trapping potential Φ_{trap}. The unshifted frequencies for $x_{\mathrm{nw}} = 0$ are found from equations 9.16 and 9.27:

$$\begin{aligned}
\omega_{0,x} &= \sqrt{\omega_x^2 + \frac{\varepsilon}{md^3}}, \\
\omega_{0,y} &= \sqrt{-\frac{1}{2}\left(-\omega_z^2 - \omega_y^2 - \sqrt{(\omega_y^2 - \omega_z^2)^2 - 4k_{yz}^2}\right) + \frac{\varepsilon}{md^3} - \frac{3\varepsilon y_{\mathrm{nw}}^2}{md^5}}, \\
\omega_{0,z} &= \sqrt{-\frac{1}{2}\left(-\omega_z^2 - \omega_y^2 + \sqrt{(\omega_y^2 - \omega_z^2)^2 - 4k_{yz}^2}\right) + \frac{\varepsilon}{md^3} - \frac{3\varepsilon z_{\mathrm{nw}}^2}{md^5}},
\end{aligned} \tag{10.14}$$

with $k_{yz} = -\frac{3\varepsilon y_{\mathrm{nw}} z_{\mathrm{nw}}}{md^5}$ respresenting the coupling strength between the y- and z-direction.

As discussed in detail in chapter 9.4, the driven ion motion is expected to depend on the position of the nanowire $\vec{x}_{\mathrm{nw}}$, the oscillation amplitude of the nanowire A, the ion-nanowire distance d and the effective charge of the nanowire q_{nw}. All simulations were compared to the analytical expressions derived from the Taylor expanded force in chapter 9.4.

10.3.1 Variation of the Nanowire Position z_{nw}

The equations of motion of a single ion mechanically driven by a nanowire were approximated to those of a periodically driven harmonic oscillator in chapter 9.4. They entail steady-state solutions of harmonic oscillations at the drive frequeny ω_{nw}. The periodic driving force experienced by the ion in z-direction was found to depend on the position component z_{nw} of the nanowire relative to the equilibrium position of the ion. For a nanowire oscillating along the z-direction, it is given by:

$$F_{\mathrm{drive},z} = -\left(\frac{\varepsilon}{d^3} - \frac{3\varepsilon z_{\mathrm{nw}}^2}{d^5}\right) A \cos(\omega_{\mathrm{nw}} t). \tag{10.15}$$

Equation 10.15 shows that the amplitude of the driving force depends on the absolute ion-nanowire distance d as well as on the nanowire position z_{nw} relative to the ion equilibrium position. The driving force in z-direction vanishes for $z_{\mathrm{nw}} = d/\sqrt{3}$.

On resonance ($\omega_{\mathrm{nw}} = \omega_z$), the amplitudes for the steady-state trajectory $z(t)$ and the ve-

locity $v_z(t)$ for coupled motions y and z are given by (see equation 9.33):

$$\begin{aligned} z_{\max} = \frac{1}{k_{\mathrm{R}}^2 + k_{\mathrm{I}}^2} \Big| & \left(k_{\mathrm{R}} \left(-A_z k_{yy} + A_y k_{yz} - A_z \omega_z^2\right) + k_{\mathrm{I}} \left(-A_z \gamma \omega_z\right)\right) \\ & + i \left(k_{\mathrm{I}} \left(-A_z k_{yy} + A_y k_{yz} - A_z \omega_z^2\right) + k_{\mathrm{R}} \left(A_z \gamma \omega_z\right)\right) \Big|, \\ \Rightarrow v_{\max} &= \omega_z z_{\max}, \end{aligned} \tag{10.16}$$

with parameters defined in chapters 9.6 and 9.7. Equation 10.16 simplifies to equation 9.21 if the coupling k_{yz} between y and z vanishes or becomes negligible.

Figure 10.6 shows the velocities $v_z(t)$ and velocity amplitudes $v_{\max}$ obtained from numerical simulations for different values of z_{nw}. For all simulations shown in figure 10.6, a single ion was initialized at position $\vec{x} = (0, 0, 0)$ and velocity $\vec{v}_z = (-5, -5, -5)$ m/s. The ion-nanowire distance was $d = 250$ µm and the static bias voltage on the nanowire was set to $V_{\mathrm{nw}} = 1$ V. The final oscillation frequencies were $\omega_z = 2\pi \times 422$ kHz and $\omega_x = \omega_y = 2\pi \times 1.2$ MHz, where $\omega_{0,x}$, $\omega_{0,y}$ and $\omega_{0,z}$ were determined according to equation 10.14.

The mechanical drive of the nanowire was initially turned off, leading to the exponential decay of the velocity amplitude until $t = t_0$. At $t_0 = 100$ µs, the oscillation amplitude of the nanowire was set to 200 nm at frequency $\omega_{\mathrm{nw}} = 2\pi \times 422$ kHz, leading to the resonant excitation and subsequent steady-state oscillation of the ion motion.

As shown in figure 10.6d, the velocity amplitudes $v_{\max}$ obtained from numerical simulations with different values z_{nw} are well described by the theoretical expression given by equation 10.16. The distribution shows the expected behavior (see also figure 9.4) with the velocity amplitude minimized close to $z_{\mathrm{nw}} = d/\sqrt{3}$. While the driving force along z vanishes for $z_{\mathrm{nw}} = d/\sqrt{3}$, the motion in y-direction remains driven at a periodic driving force $F_{\mathrm{drive},y} = -m k_{yz} A \cos(\omega_{\mathrm{nw}} t)$ (see equation 9.29). The steady-state velocity thus does not completely vanish at $z_{\mathrm{nw}} = d/\sqrt{3}$ due to the coupling between the oscillations in y- and z-direction.

10.3.2 Variation of Experimental Parameters A, d and q_{nw}

The simulations of driven ion motion presented in this chapter show the velocity amplitudes $v_{\max}$ of the steady-state solutions for the variation of the nanowire oscillation amplitude A, the ion-nanowire distance d and the effective charge of the nanowire q_{nw}.

A single ion was initialized at position $\vec{x} = (0, 0, 0)$ and velocity $\vec{v} = (-5, -5, -5)$ m/s. As in chapter 10.3.1, the nanowire drive was initially absent and activated at $t_0 = 100$ µs. The shifted trapping frequencies were set to $\omega_z = 2\pi \times 422$ kHz and $\omega_x = \omega_y = 2\pi \times 1.2$ MHz, with $\omega_{0,i}$ ($i \in \{x, y, z\}$) determined from equation 10.14 and the nanowire was driven at

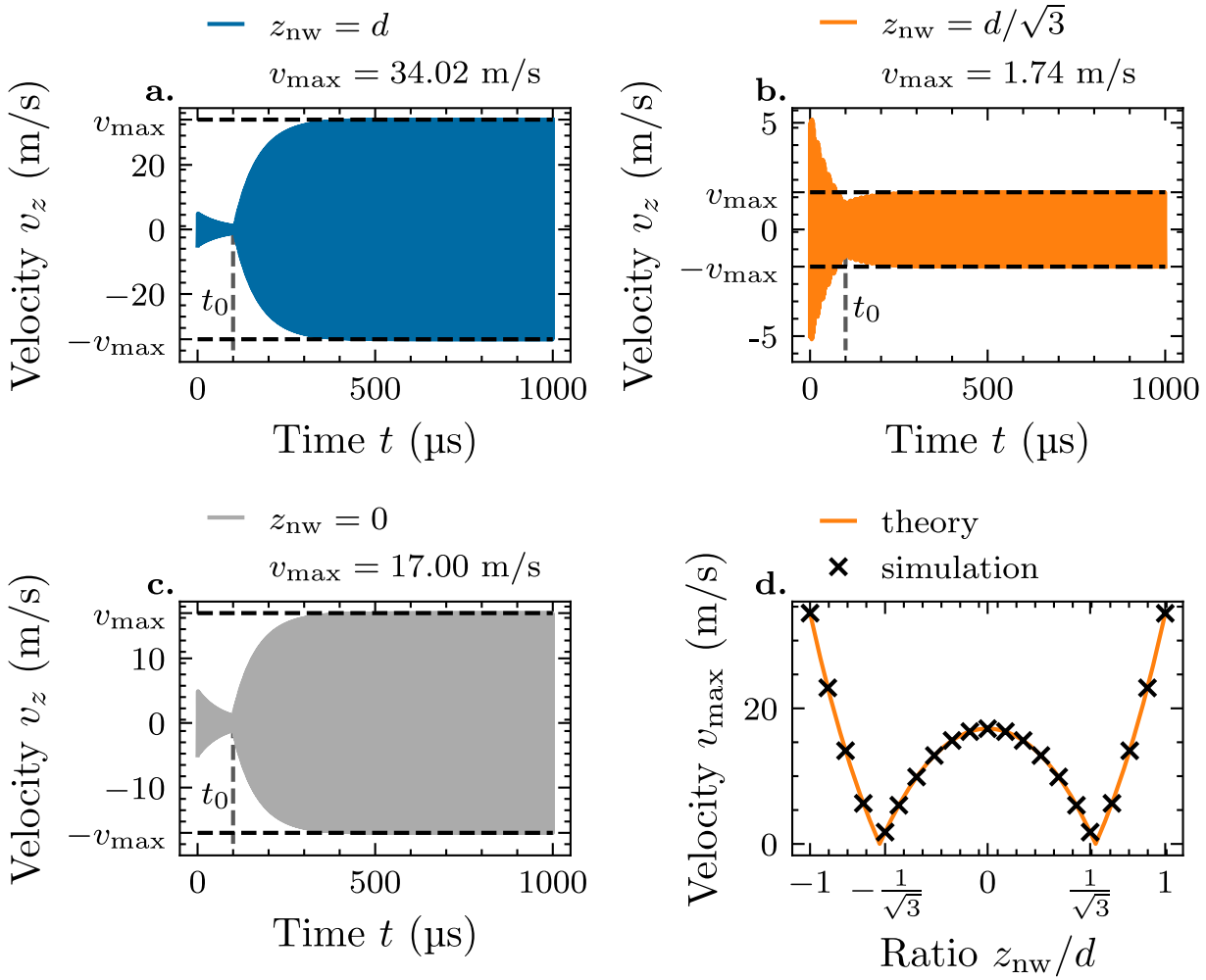

Figure 10.6: Simulations of the axial velocity $v_z(t)$ of a single ion resonantly driven by an oscillating nanowire for different z_{nw}. The nanowire oscillated along the z-direction with an amplitude of $A = 200$ nm at frequency $\omega_{nw} = \omega_z = 2\pi \times 422$ kHz. A damping factor of $\gamma = 30 \times 10^3$ s^{-1} was added to simulate laser cooling of the ion. The resonant drive was activated at $t_0 = 100$ µs. The ion-nanowire distance was $d = 250$ µm and the voltage applied to the nanowire was $V_{nw} = 1$ V. **a** – **c**, The simulated steady-state solutions of the driven motions at $z_{nw} \in \{d, d/\sqrt{3}, 0\}$ yielded velocity amplitudes of $v_{max} \in \{34.02, 1.74, 17.00\}$ m/s, respectively. **d**, The distribution of velocity amplitudes v_{max} obtained from simulations for a variety of z_{nw} (black crosses) is well described by equation 10.16 (orange curve).

$\omega_{nw} = 2\pi \times 422$ kHz, on resonance with ω_z. The charge of the nanowire was adjusted by changing the bias voltage V_{nw} applied to the nanowire.

The parameters A, d and V_{nw} for the different simulations were given as follows:

- The variation of A was performed for oscillation amplitudes ranging from $A = 0$ to $A = 500$ nm in steps of 50 nm at an ion-nanowire distance $d = 250$ µm and an applied nanowire voltage of $V_{nw} = 1$ V.
- The variation of the distance d was performed from $d = 250$ µm to $d = 750$ µm in steps of 50 µm at an oscillation amplitude $A = 200$ nm and an applied nanowire voltage $V_{nw} = 1$ V.

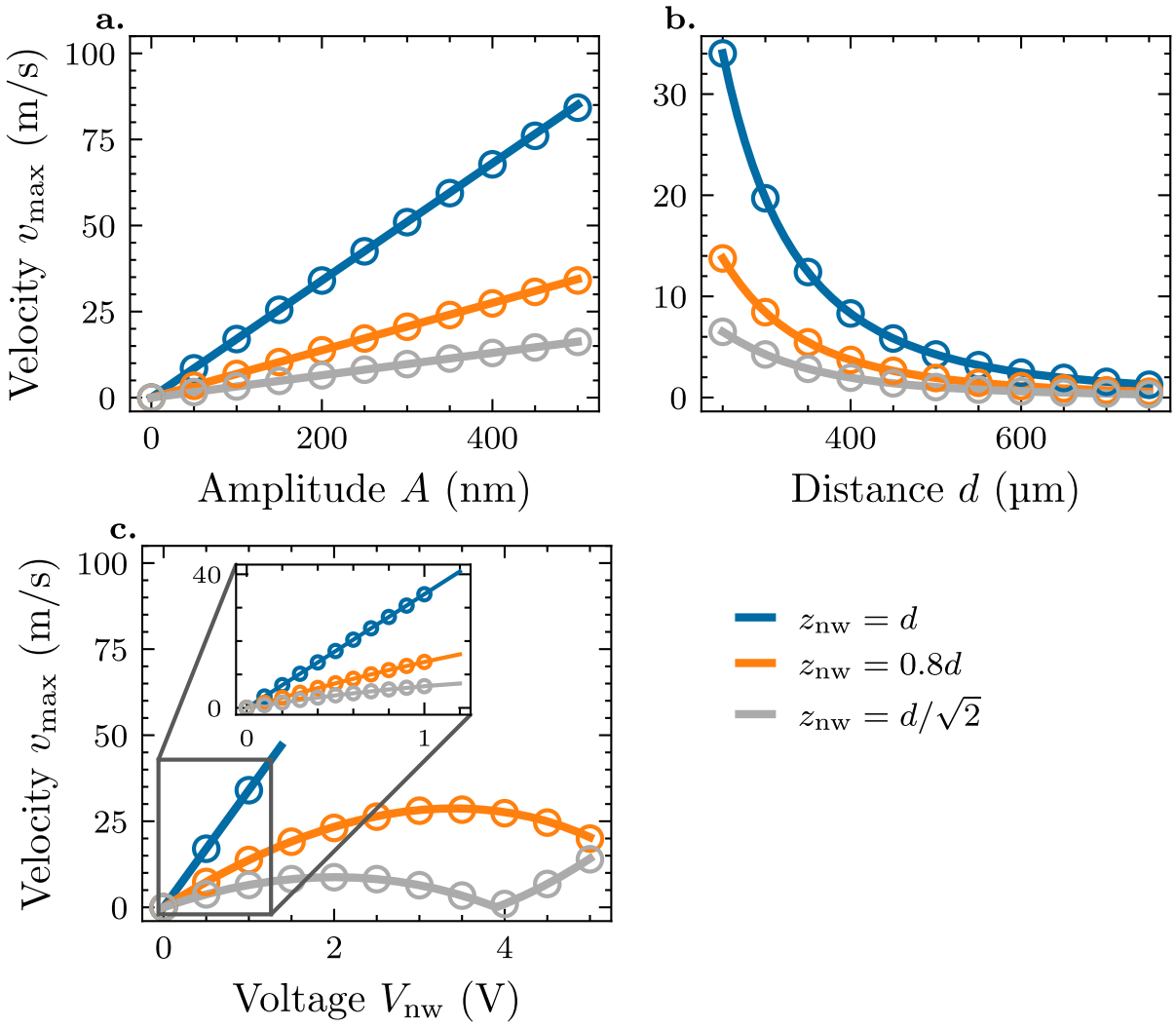

Figure 10.7: Simulated velocity amplitudes v_{max} of a resonantly driven ion for different parameters A, d and V_{nw}. The data obtained from simulations (circles) is well described by equation 10.16 (solid curves) and depends on the nanowire position z_{nw}. **a**, v_{max} is proportional to the oscillation amplitude A of the nanowire. **b**, The dependence of v_{max} on the ion-nanowire distance d follows equation 10.16. It is proportional to $1/d^3$ for negligible coupling between the directions of motion of the ion. **c**, v_{max} is approximately proportional to V_{nw} at low voltages (inset). At higher voltages and thus stronger coupling, the driven velocity amplitude shows non-linear behavior for $k_{yz} \neq 0$. For $z_{nw} = d$ (with $d = 250$ µm, blue line), the total potential Φ became anti-confining for $V_{nw} \gtrsim 1.5$ V.

- The variation of q_{nw} was performed by changing the voltage applied to the nanowire from $V_{nw} = 0$ to $V_{nw} = 5$ V in steps of 0.5 V. The ion-nanowire distance was set to $d = 250$ µm and the oscillation amplitude of the nanowire was set to $A = 200$ nm. Additionally, simulations with V_{nw} ranging from 0 V to 1 V in smaller steps of 0.1 V were performed to show the behavior at low coupling strengths.

Figure 10.7 shows the velocity amplitudes v_{max} obtained from numerical simulations of the driven motion of the ion compared to the theoretical expression given by equation 10.16 for the variation of A, d and V_{nw}. The values obtained from the simulations are well described by the theoretical predictions. The theory of the ion-nanowire interaction discussed in chapter 9 is thus well suited to describe the classical ion-nanowire dynamics if the nanowire can be approximated as a point charge. Experimentally, deviations from the simulations can be expected due

to the presence of the conductive tungsten holder of the nanowire. The interaction potential generated by the holder introduces deviations from the point-charge potential assumed in our model (see also chapter 9.1).

The results shown in this chapter can be generalized to the coupling of all three directions of motion x, y and z, occurring for nanowire positions with three non-vanishing components $x_{\mathrm{nw}}, y_{\mathrm{nw}}, z_{\mathrm{nw}} \neq 0$. Due to the lengthy analytical expression for v_{max} in this case, it is recommended to compute the velocity amplitudes with the help of a program such as Wolfram Mathematica [195].

10.3.3 Off-Resonant Drive

We have confirmed with numerical simulations that the dynamics of a single ion driven by an oscillating charged nanowire are well described by the approximations derived in chapter 9. For low coupling strengths $\varepsilon/(m\omega_{0,z}^2 d^3) \ll 1$ and thus negligible coupling between the directions of oscillation of a driven ion, the approximated amplitude response is identical to a driven harmonic oscillator with a damping factor γ. It is given by the Lorentz function [121, 168]:

$$v_{\mathrm{max}} = \left| \left(\frac{\varepsilon}{md^3} - \frac{3\varepsilon z_{\mathrm{nw}}^2}{md^5} \right) \frac{A}{\sqrt{\gamma^2 + \frac{1}{\omega_{\mathrm{nw}}^2} \left(\omega_z^2 - \omega_{\mathrm{nw}}^2\right)^2}} \right|, \tag{10.17}$$

where ω_z is the effective frequency of the total potential $\Phi = \Phi_{\mathrm{trap}} + \Phi_{\mathrm{IA}}$ and ω_{nw} is the frequency of oscillation of the nanowire, corresponding to the drive frequency of the ion.

Figure 10.8 shows the velocity amplitude v_{max} obtained from numerical simulations for different detunings $\delta = \omega_{\mathrm{nw}} - \omega_z$ at $\omega_z = 2\pi \times 422$ kHz. The nanowire voltage was set to $V_{\mathrm{nw}} = 1$ V. The nanowire was positioned at $\vec{x}_{\mathrm{nw}} = (0, 0, d)$ with an ion-nanowire distance of $d = 250$ µm. The damping factor was $\gamma = 30 \times 10^3$ and the amplitude of oscillation of the nanowire was $A = 200$ nm. The simulations were performed for detunings ranging from $\delta = -2\pi \times 10$ kHz to $\delta = 2\pi \times 10$ kHz in steps of $2\pi \times 1$ kHz. The off-resonant drive is accurately described by equation 10.17.

While the oscillation amplitude of the nanowire was kept at $A = 200$ nm in figure 10.8, it is important to note that the amplitude response of a nanowire to an experimentally implemented driving mechanism is also described by a driven harmonic oscillator (see chapter 5.6). The amplitude A thus generally decreases for increasing detunings $|\delta|$ from the resonance frequency ω_{r} of the nanowire, unless the drive strength is increased accordingly.

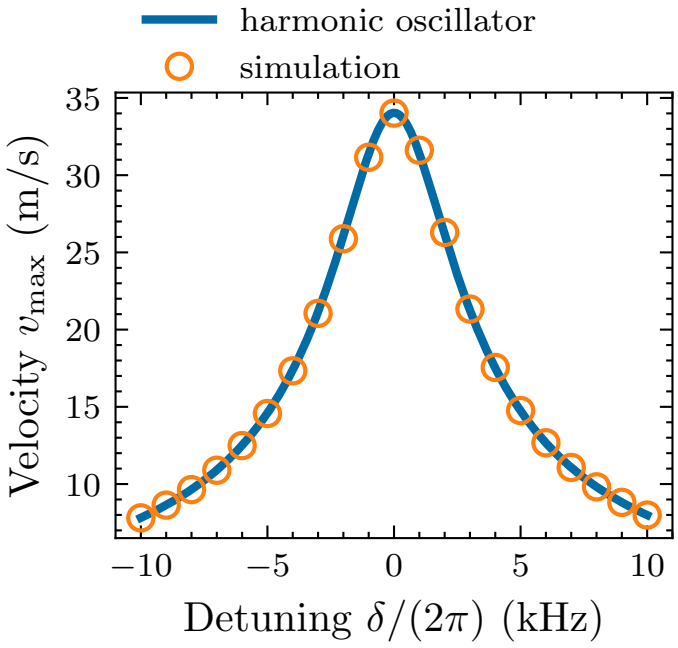

Figure 10.8: Velocity amplitude response $v_{\max}(\delta)$ of a single ion driven by an oscillating nanowire at different drive frequencies ω_{nw}. The oscillation amplitude of the nanowire was $A = 200$ nm and the nanowire position was $\vec{x}_{\mathrm{nw}} = (0, 0, 250)$ µm with a static voltage $V_{\mathrm{nw}} = 1$ V applied to the nanowire. The detuning was given by $\delta = \omega_{\mathrm{nw}} - \omega_z$ with $\omega_z = 2\pi \times 422$ kHz. The response of the velocity amplitude $v_{\max}(\delta)$ follows the spectrum of a driven harmonic oscillator given by equation 10.17.

10.4 Two-Ion Strings

Two positively charged ions simultaneously confined in a linear radiofrequency trap experience mutual repulsion due to their Coulomb interaction potential Φ_{c}. For typical experimental parameters in ion trapping experiments, this leads to a string arrangement of the ion positions along the longitudinal symmetry axis z of the trap.

The axial trapping potential Φ_z and the electrostatic repulsion potential Φ_{c} are given by:

$$\begin{aligned} \Phi_z &= \frac{1}{2} m \omega_z^2 z^2, \\ \Phi_{\mathrm{c}} &= k_{\mathrm{c}} \frac{e^2}{|\vec{r}|}. \end{aligned} \tag{10.18}$$

e and m are the charges and masses of the trapped ions, respectively. k_{c} is the Coulomb constant and ω_z is the angular trapping frequency along the z-direction. Here, we only consider same-species ions of identical mass and charge. We further limit the Coulomb repulsion to occur solely along z such that $|\vec{r}| = |z_1 - z_2|$, where z_i are the positions of the ions ($i \in \{1, 2\}$) on the z-axis.

The equilibrium distance $2r_0$ of the ions along z is given by [205, 206]:

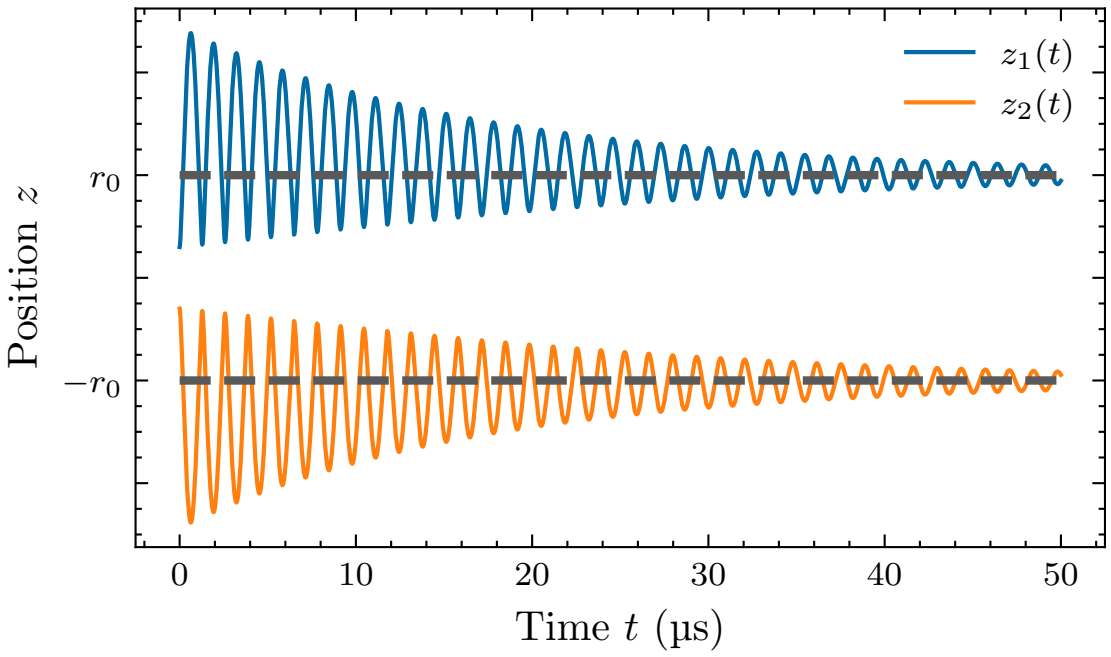

Figure 10.9: Axial trajectories $z_i(t)$ of two simultaneously laser-cooled trapped ions. The same-species ions $i \in \{1, 2\}$ repulse each other due to their positive charges $q = e$. The initial positions of the ions were $\vec{x}_{\text{init},i} = (0, 0, \pm 0.3 r_0)$ with initial velocities $\vec{v}_{\text{init},1} = -\vec{v}_{\text{init},2} = (1, 1, 1)$ m/s. A damping factor of $\gamma = 100 \times 10^3$ s^{-1} was added to simulate laser cooling. The trajectories show sharp repulsions in their oscillations whenever the ions get close to each other. They quickly reach their equilibrium positions at $\vec{x}_{\text{eq},i} = (0, 0, \pm r_0)$ (dark gray lines).

$$2r_0 = \sqrt[3]{\frac{2k_c e^2}{m\omega_z^2}}. \tag{10.19}$$

Figure 10.9 shows the numerically simulated trajectories of two laser-cooled trapped ions quickly reaching their equilibrium positions at $z_{\text{eq},i} = \pm r_0$. The dynamics were computed with the velocity Verlet algorithm by adding the repulsion force $\vec{F}_c = -\vec{\nabla}\Phi_c$ to the equations of motion.

10.4.1 Resonant Excitation of the Breathing Mode of a Two-Ion String

Two-ion strings can be regarded as harmonic oscillators coupled by Φ_c given in equation 10.18. In addition to their in-phase center-of-mass (COM) motion at angular frequency $\omega_{\text{COM}} = \omega_z$, they exhibit an opposite-phase *breathing mode* motion [207] with applications for quantum computing [205] and quantum information processing [161, 208]. The COM and breathing mode motions are shown in figure 10.10. The breathing mode frequency ω_{breath} and respective period T_{breath} for two ions of identical mass m and identical charge q is given by[209][208]:

$$\begin{aligned} \omega_{\text{breath}} &= \sqrt{3}\omega_{\text{COM}}, \\ T_{\text{breath}} &= \frac{1}{\sqrt{3}} T_{\text{COM}}. \end{aligned} \tag{10.20}$$

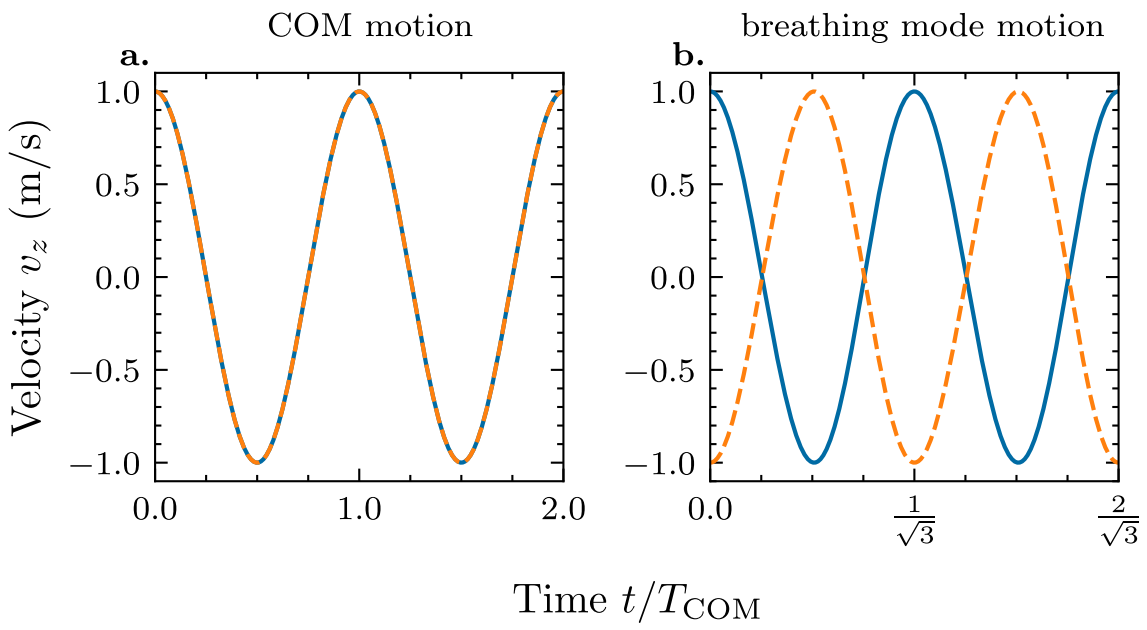

Figure 10.10: Numerical simulations of the center-of-mass (COM) and breathing mode motion of two simultaneously trapped ions. The ions $i \in \{1, 2\}$ oscillate freely according to the Mathieu equations 2.13 with the addition of their mutual repulsion force. The ions were initialized at their equilibrium positions $\vec{x}_{\mathrm{init},i} = (0, 0, \pm r_0)$ with initial velocities $v_{\mathrm{init},i}$. **a**, For in-phase motion ($v_{\mathrm{init},1} = v_{\mathrm{init},2} = (1, 1, 1)$ m/s) the ions oscillate at the angular trap frequency $\omega_z = \omega_{\mathrm{COM}}$. **b**, Opposite-phase motion ($v_{\mathrm{init},1} = -v_{\mathrm{init},2} = (1, 1, 1)$ m/s) occurs at the breathing mode angular frequency $\omega_{\mathrm{breath}} = \sqrt{3}\omega_{\mathrm{COM}}$.

The opposite-phase nature of the breathing mode motion makes it more challenging to be driven on resonance compared to the center-of-mass motion. It requires periodic driving forces with field gradients and cannot be driven by uniform electric fields [207, 210]. The mechanically driven motion of a charged nanowire may offer a way to implement such driving forces.

Resonant drive of the breathing mode could in principle be achieved in two ways: applying a periodic voltage to the undriven nanowire or mechanically driving oscillations of the charged nanowire. The former corresponds to a periodic change of the effective nanowire charge $q_{\mathrm{nw}}(t) = q_0 + q_{\mathrm{amp}} \cos(\omega_{\mathrm{breath}} t)$. One issue of this approach is the resulting change in the generated potential Φ_{IA}, which will in turn periodically alter the effective trapping frequency ω_z. The mechanical approach corresponds to the excitation of the ion motion discussed in chapters 9.4 and 10.3. In the following, we focus only on the *mechanical* excitation of the ion motion along z by a nanowire oscillating at $A \cos(\omega_{\mathrm{breath}} t)$.

In order to drive the breathing mode of a two-ion string with an oscillating nanowire, the oscillation frequency of the nanowire ω_{nw} needs to coincide with the frequency of the breathing mode ω_{breath}. Following equation 10.20, the effective trapping frequency of the total potential (corresponding to the center-of-mass motion) thus needs to be:

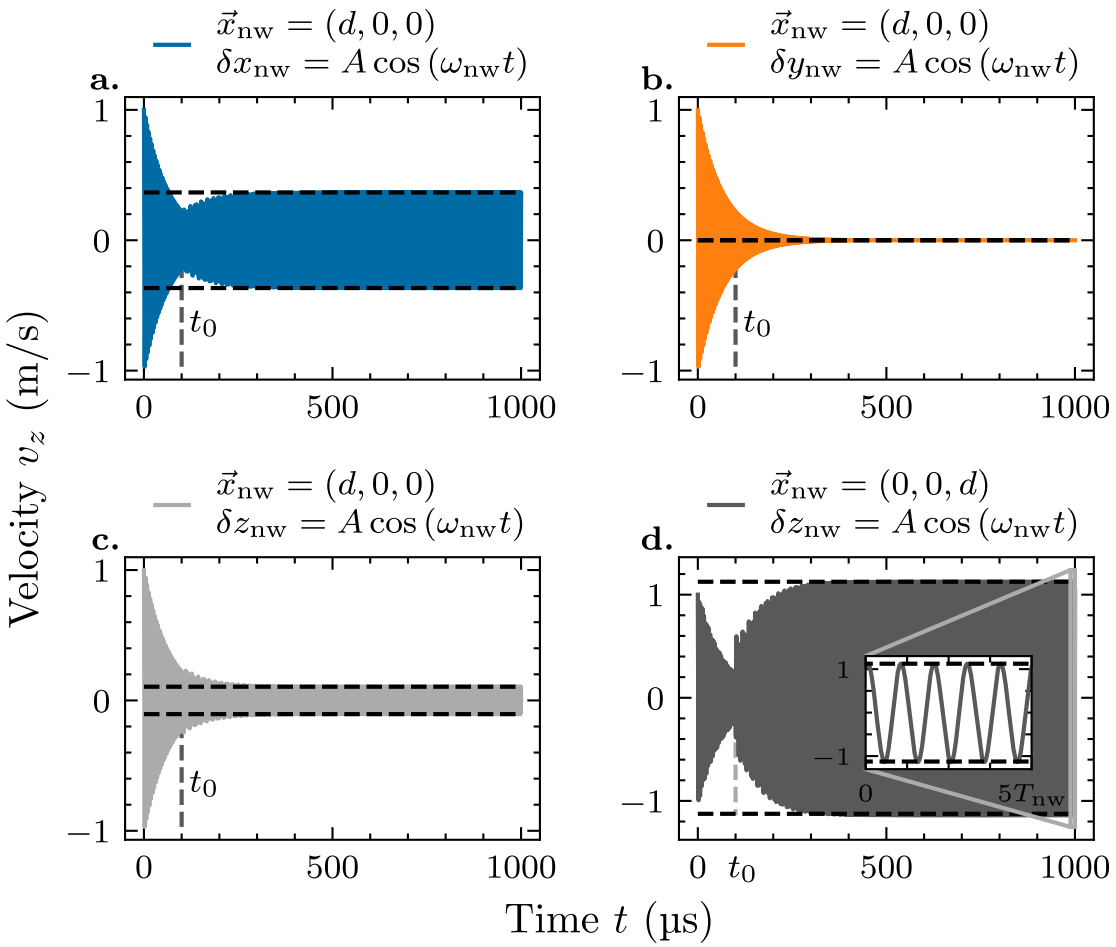

Figure 10.11: Resonant excitation of the breathing mode motion of a two-ion string with a mechanically driven charged nanowire. The nanowire tip was positioned along the x-axis (**a** – **c**) and the symmetry axis z (**d**) of the trap. The ion string was aligned along z. Both ions reached identical velocity amplitudes (black lines). **a**, The nanowire oscillated along x, resulting in a breathing mode excitation with final velocity amplitude of $v_{\mathrm{max}} = 0.37$ m/s. **b** The nanowire oscillated along y. No resonant drive was observed due to the absence of coupling for $y_{\mathrm{nw}} = 0$ (see equation 10.25). **c**, The nanowire oscillated in z-direction, resulting in a velocity amplitude of $v_{\mathrm{max}} = 0.11$ m/s. **d**, The nanowire oscillated in z-direction while positioned along the z-axis, yielding the strongest drive with velocity amplitude $v_{\mathrm{max}} = 1.13$ m/s at $\omega_{\mathrm{nw}} = \omega_{\mathrm{breath}}$ (inset).

$$\begin{aligned} \omega_z &= \omega_{\mathrm{nw}}/\sqrt{3}, \\ \Rightarrow \omega_{\mathrm{nw}} &= \omega_{\mathrm{breath}}. \end{aligned} \tag{10.21}$$

Figure 10.11 shows the axial velocities $v_z(t)$ obtained from numerical simulations of a two-ion string driven by the charged nanowire oscillating along different directions x, y and z. The nanowire oscillated at $\omega_{\mathrm{nw}} = 2\pi \times 422$ kHz with an amplitude of $A = 200$ nm. The axial trapping frequency was set to $\omega_z = 2\pi \times 422/\sqrt{3}$ kHz $\approx 2\pi \times 243.64$ kHz, such that $\omega_{\mathrm{breath}} = 2\pi \times 422$ kHz. The resulting equilibrium positions of the ions were $z_{\mathrm{eq},i} = \pm r_0 \approx \pm 7.18$ µm. The nanowire tip was positioned on the radial x-axis perpendicular to the longitudinal axis z at $\vec{x} = (d, 0, 0)$ in figure 10.11a – c and along the longitudinal axis at $\vec{x}_{\mathrm{nw}} = (0, 0, d)$ in figure 10.11d. The distance

of the nanowire tip to the center of the trapping potential was $d = 350$ µm and a static voltage of $V_{\mathrm{nw}} = 1$ V was applied to the nanowire. Further simulation parameters are given in table 10.1, with the exception of $\omega_{0,x}$ and $\omega_{0,y}$ which were chosen to yield $\omega_x = \omega_y = 2\pi \times 1.2$ MHz. The ions $i \in \{1, 2\}$ were initialized at positions $\vec{x}_{\mathrm{init},1} = (0, 0, r_0)$ and $\vec{x}_{\mathrm{init},2} = (0, 0, -r_0)$ with an in-phase motion $\vec{v}_{\mathrm{init},1} = \vec{v}_{\mathrm{init},2} = (1, 1, 1)$ m/s. The damping factor for laser cooling was set to $\gamma = 30 \times 10^3$ s^{-1}.

As can be seen in figure 10.11, the resonant excitation of the breathing mode of a two-ion string along z can be achieved with nanowire oscillations perpendicular (figure 10.11a) and parallel (figure 10.11c – d) to the z-axis. The strongest drive for the given parameters was achieved for parallel oscillations of the nanowire along z with the nanowire positioned along the longitudinal axis at $\vec{x}_{\mathrm{nw}} = (0, 0, d)$.

This can also be shown by looking at the forces exerted on the ions (see also chapter 9). As shown in equation 9.10, the force components along z acting on a single trapped ion due to oscillations of the nanowire can be approximated as:

$$F_z = \frac{3\varepsilon x_{\mathrm{nw}} z_{\mathrm{nw}}}{d^5}\delta x_{\mathrm{nw}} + \frac{3\varepsilon y_{\mathrm{nw}} z_{\mathrm{nw}}}{d^5}\delta y_{\mathrm{nw}} - \left(\frac{\varepsilon}{d^3} - \frac{3\varepsilon z_{\mathrm{nw}}^2}{d^5}\right)\delta z_{\mathrm{nw}}, \tag{10.22}$$

where oscillations of the nanowire along x, y and z correspond to setting δx_{nw}, δy_{nw} or δz_{nw} to $A\cos(\omega_{\mathrm{nw}} t)$, respectively, while the other terms remain at zero.

The position components x_{nw}, y_{nw} and z_{nw} of the nanowire in equation 10.22 are defined relative to the equilibrium positions of the ions at $\vec{x}_{\mathrm{eq}} = (0, 0, \pm r_0)$. Setting the origin of the coordinate system to either of the ion equilibrium positions yields:

$$\begin{aligned} &\vec{x}_{\mathrm{nw}} \to (x_{\mathrm{nw}}, y_{\mathrm{nw}}, z_{\mathrm{nw}} \pm r_0), \\ &d \to \sqrt{x_{\mathrm{nw}}^2 + y_{\mathrm{nw}}^2 + (z_{\mathrm{nw}} \pm r_0)^2}. \end{aligned} \tag{10.23}$$

Inserting equation 10.23 into equation 10.22, the strength of the driving forces along z for all possible directions of oscillation of the nanowire can be found:

- For nanowire oscillations along x:

$$\begin{aligned} &\delta x_{\mathrm{nw}} = A\cos(\omega_{\mathrm{nw}} t), \\ \Rightarrow\ &F_z = \frac{3\varepsilon x_{\mathrm{nw}}(z_{\mathrm{nw}} \pm r_0)}{d^5} A\cos(\omega_{\mathrm{nw}} t). \end{aligned} \tag{10.24}$$

  Both ions experience periodic driving forces exhibiting a gradient, as required for the excitation of the breathing mode motion. For $z_{\mathrm{nw}} = 0$ (figure 10.11a), the ions experience driving forces of opposing signs at all times. The forces vanish for $x_{\mathrm{nw}} = 0$.

- For nanowire oscillations along y:

$$\begin{aligned} \delta y_{\mathrm{nw}} &= A\cos\left(\omega_{\mathrm{nw}}t\right), \\ \Rightarrow F_z &= \frac{3\varepsilon y_{\mathrm{nw}}(z_{\mathrm{nw}} \pm r_0)}{d^5} A\cos\left(\omega_{\mathrm{nw}}t\right). \end{aligned} \tag{10.25}$$

  This case is identical to the nanowire oscillations along x. However, the driving forces vanish for the nanowire positions discussed here due to $y_{\mathrm{nw}} = 0$ (figure 10.11b).

- For nanowire oscillations along z:

$$\begin{aligned} \delta z_{\mathrm{nw}} &= A\cos\left(\omega_{\mathrm{nw}}t\right), \\ \Rightarrow F_z &= -\left(\frac{\varepsilon}{d^3} - \frac{3\varepsilon(z_{\mathrm{nw}} \pm r_0)^2}{d^5}\right) A\cos\left(\omega_{\mathrm{nw}}t\right). \end{aligned} \tag{10.26}$$

  The ions experience driving forces from an electric field with a gradient, enabling the resonant excitation of the breathing mode motion (figure 10.11c – d). For the parameters shown here, the gradient and the resulting driving forces are higher for the nanowire position $\vec{x}_{\mathrm{nw}} = (0, 0, d)$ along the symmetry axis of the trap.

The resonant excitation of the breathing mode for the different cases shown in figure 10.11 was compared to the resonant excitation of the COM mode under the same conditions and initial parameters, with the exception of the drive frequency of the nanowire ω_{nw}. It was set to the COM mode frequency, i. e., $\omega_{\mathrm{nw}} = 2\pi \times 422/\sqrt{3}$ kHz. The resonant drive of the center-of-mass motion obtained from these simulations was generally stronger and exhibited higher velocity amplitudes. For the discussed cases of $x_{\mathrm{nw}} = d$ and $z_{\mathrm{nw}} = d$, resonant drive only occurred for nanowire oscillations along the axial direction z and yielded velocity amplitudes $v_{\mathrm{max}} = 6.19$ m/s and $v_{\mathrm{max}} = 11.83$ m/s, respectively.

The insights gained from the discussions presented in this chapter can be generalized to arbitrary positions and directions of oscillation of the nanowire. The numerical simulations have shown the possibility of driving the breathing mode motion of a two-ion string resonantly with a mechanically oscillating charged nanowire. The nanowire was modeled as an effective point charge localized at its tip, resulting in an inhomogeneous interaction potential exhibiting sufficiently high field gradients over the extension $2r_0$ of the two-ion string required for the breathing mode excitation.

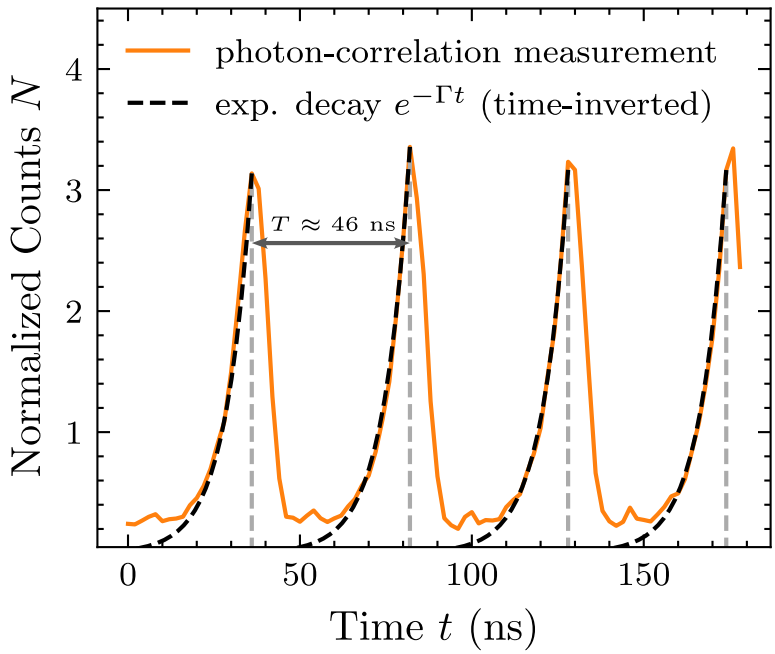

Figure 11.1: Measurement of micromotion with the photon-correlation method. The measurement was performed in the modified trap geometry (lower central electrode DC11 missing) and the ions were trapped in the edge region of the trap. A high detuning of $\delta_0 = -3061$ MHz was required for the 397 nm main cooling laser. High levels of excess micromotion were observed with the photon-correlation method (orange curve). The periodic distribution at frequency $\Omega = 2\pi \times 21.629$ MHz ($\Rightarrow T \approx 46$ ns) exhibits sharp peaks and shallow valleys, characteristic for high velocity amplitudes $v_{\max}$ of the oscillatory ion motion in combination with high detunings δ_0 (compare to figure 7.5). The natural linewidth Γ of the $4^2S_{1/2} \leftrightarrow 4^2P_{1/2}$ cooling transition was close to Ω, i. e., $\Gamma \approx \Omega$. Due to this, the exponential decay of the excited $4^2P_{1/2}$ state was resolved in the fluorescence (black dashed curves). The shown distribution was background-corrected with a background of 20% and normalized as discussed in chapter 7.3.4.

11 Experimental Results

11.1 Micromotion Measurements

The photon-correlation method discussed in chapter 7.3.2 was tested by measuring the micromotion of trapped $^{40}Ca^+$ ions. For the micromotion measurements presented here, the grounded nanowire ($V_{\text{nw}} = 0$ V) was positioned below the trap and had no effect on the trapping potential Φ experienced by the ions. Micromotion is driven oscillatory motion at the angular radiofrequency Ω applied to the RF electrodes of the trap [119]. In order to resolve four full periods of the micromotion measured with the photon-correlation method, the reference frequency was set to $\omega_{\text{ref}} = \frac{1}{4}\Omega$. Figure 11.1 shows a typical histogram obtained from the measurements. The radiofrequency was set to $\Omega = 2\pi \times 21.629$ MHz ($\Rightarrow T \approx 46$ ns) and the bin size in figure 11.1 was $\Delta t = 2$ ns.

The experimental setup for the photon-correlation method was implemented after the lower central electrode DC11 was broken and removed from the trap (see also chapter 8.2.2). In the present measurements, the ions were confined in the edge region of the modified trap geometry with strong RF fields (see also figure 8.4). This lead to the requirement of high detunings

$\delta_0 \approx -3000$ MHz of the 397 nm laser used for the main cooling transition $4^2S_{1/2} \leftrightarrow 4^2P_{1/2}$ due to strong excess micromotion, evident by the shape of the histogram shown in figure 11.1. The histograms exhibited high amplitudes of the periodic fluorescence distributions of the ions, as well as sharp peaks and shallow valleys, characteristic for high detunings (see also figure 7.5).

For typical experimental conditions in linear ion traps, excess micromotion yields approximately sinusoidal distributions of small amplitudes at frequency Ω for the fluorescence of trapped ions [120, 162]. It can be compensated by overlapping of the effective DC and RF trapping positions in order to exhibit a nearly constant signal obtained from the photon-correlation method [120, 162]. Attempts at compensating the excess micromotion shown in figure 11.1 were unsuccessful for the ions confined in the modified trap geometry. This limited the attainable cooling efficiency for the ions, but did not prevent the successful demonstration of the ion-nanowire coupling and the resonant drive of the secular ion motion by the mechanical vibrations of the nanowire shown in chapter 11.3. This is because the frequency of the micromotion was substantially larger than the frequency of the driven secular motion ($\Omega \gg \omega_z$) and the photon-correlation method is only sensitive to motion which is correlated to the applied reference frequency ω_{ref}. Contributions from the micromotion at frequency $\Omega \gg \omega_z$ were uncorrelated to ω_{ref} and thus averaged out (see also chapter 7.3.2).

In contrast to equation 7.1, the observed periodic distribution of the fluorescence of the ions shown in figure 11.1 was not symmetric around the peaks. A slower rise on the left flank of the peaks was visible, compared to the faster decrease in fluorescence on the right flank. This behavior is explained by the applied angular radiofrequency $\Omega = 2\pi \times 21.629$ MHz ≈ 136 MHz. It was of comparable size to the natural linewidth $\Gamma \approx 132$ MHz [140] of the $4^2S_{1/2} \leftrightarrow 4^2P_{1/2}$ main cooling transition. As a result, the spontaneous decay $4^2P_{1/2} \rightarrow 4^2S_{1/2}$ of the ions was resolved in the measured fluorescence distributions.

Since the histograms obtained with the photon-correlation method bin the time *differences* $\Delta t = t_{\text{stop}} - t_{\text{start}}$ between a start signal and a stop signal, lower values of Δt correspond to events that occurred at later times t_{start} within one period of the reference signal $T_{\text{ref}} = 1/f_{\text{ref}}$. The distribution in figure 11.1 thus shows the *time-inverted* trace of the fluorescence. Due to this, the exponential decay $R(t) = R_0 e^{-\Gamma t}$ of the excited state $4^2P_{1/2}$ was visible on the left flank of the peaks of the distribution.

11.1.1 Simulation of Micromotion Measurements

As discussed in chapter 11.1, the observed distributions of the ion fluorescence for the excess micromotion at angular frequency Ω were not well described by equation 7.1 (see figure 11.1). Fitting of equation 7.1 yielded no satisfactory results for the extraction of parameters such as the velocity amplitude v_{max} of the observed micromotion. Instead, we simulated the experi-

mental procedure of the photon-correlation method by applying the state-to-state laser cooling discussed in chapter 4.1.2. This allowed a confirmation of the observed behavior.

A state-tracking variable $|n\rangle$ was assigned to a single ion, either found in the ground state or in the excited state of the $4^2S_{1/2} \leftrightarrow 4^2P_{1/2}$ cooling transition ($|n\rangle \in \{|g\rangle, |e\rangle\}$). For each time step $\Delta t = 0.5$ ns of the simulation, the probability of absorption, stimulated emission and spontaneous emission were computed as discussed in chapter 4.1.2 and the state $|n\rangle$ was adjusted accordingly. Here, the total detuning of the cooling laser to the resonance of the transition was time-dependent and given by $\delta(\vec{v}) = \delta_0 - kv_{\max} \cos(\Omega t)$.

The reference signals used for the photon-correlation method were sinusoidal voltages $V_{\text{ref}}(t)$ at frequency $\omega_{\text{ref}} = \frac{1}{4}\Omega$:

$$V_{\text{ref}}(t) = \sin(\omega_{\text{ref}} t - \varphi). \tag{11.1}$$

The possible times t_{stop} defining the stop of a time measurement for the photon-correlation method were thus given by:

$$t_{\text{stop}} = n\frac{2\pi}{\omega_{\text{ref}}}, \tag{11.2}$$

where $n \in \mathbb{N}$ and the phase φ in equation 11.1 can be chosen arbitrarily for the simulations discussed here.

Photons triggering the start of a time measurement for the photon-correlation method needed to have been scattered by *spontaneous* emission, as photons emitted by stimulated emission were coherent with the cooling lasers and thus did not reach the detector (photon-multiplier tube) in the presented setup (see chapters 6.5 and 7.3.2).

As such, whenever an event of spontaneous emission occurred within the simulation, a variable t_{start} for the starting time was created. The time difference between t_{start} and the following t_{stop} given by equation 11.2 simulated the time difference measured by the photon-correlation method. Note that the values of t_{start} were generated with a certain probability, while the values of t_{stop} were predetermined by equation 11.2. Figure 11.2 shows a trace obtained from the simulation procedure described here, compared to the experimentally obtained distribution shown in figure 11.1. The parameters of the simulation are given in table 11.1. The simulation was stopped when the number of simulated counts was equal to the experimental number of counts. The simulated and experimentally obtained histograms were normalized as discussed in chapter 7.3.4.

As can be seen in figure 11.2, the simulations confirmed the observed features of the experimen-

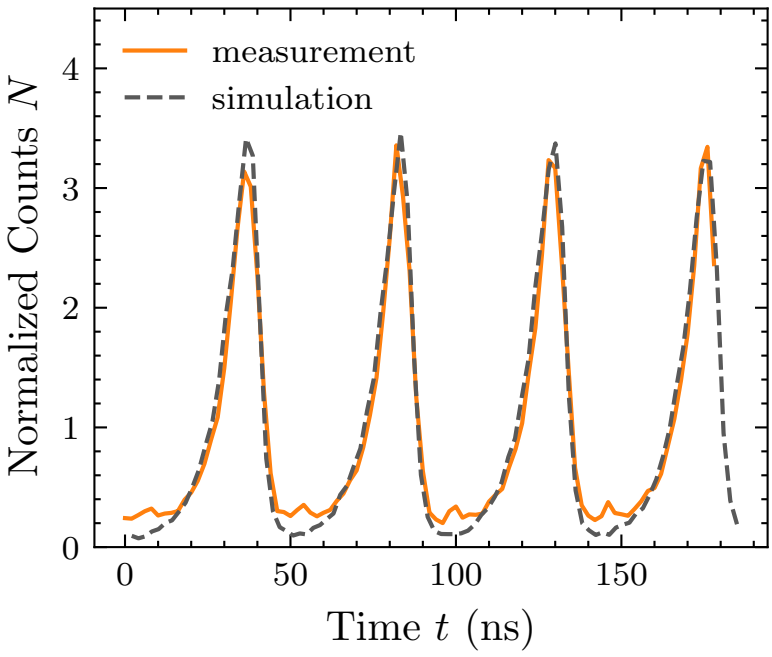

Figure 11.2: Simulation of photon-correlation measurements for the determination of excess micromotion. The orange curve corresponds to the experimentally obtained measurement of excess micromotion with the photon-correlation method shown in figure 11.1. In order to investigate the features of the distribution, the implementation of the photon-correlation method was simulated as described in chapter 11.1.1. The parameters for the simulation are given in table 11.1. The results of the simulation (dashed gray curve) confirmed the features observed in the experiment for large detunings and high velocity amplitudes v_{max}. They exhibit the sharp peaks, shallow valleys and the superimposed exponential decay of the excited $4^2\mathrm{P}_{1/2}$ state with natural linewidth Γ. Both curves were normalized as discussed in chapter 7.3.4.

tally obtained distributions. They were a consequence of high micromotion velocity amplitudes v_{max}, high detunings δ_0 and the spontaneous emission of the excited state with natural linewidth $\Gamma \approx \Omega$.

11.2 Motional Frequency Shifts

The matching of the axial frequency $f_z = \frac{\omega_z}{2\pi}$ of trapped ions to one of the resonance frequencies f_{nw} of the nanowire assembly (see figure 7.2) is crucial for an efficient transfer of energy between the two systems. However, variations of coupling parameters such as the ion-nanowire distance d and the effective nanowire charge q_{nw} result in shifts of the effective trapping frequency f_z. Those shifts occur due to the resulting changes in the total potential Φ experienced by the ions (see chapter 9.3). This requires the adjustment of the trapping potential using the static voltages applied to the DC electrodes in order to preserve resonance, i. e., $f_z = f_{\mathrm{nw}}$. In the limit of low coupling strengths $\varepsilon/d^3 \lesssim 0.3 m\omega_{0,z}^2$, the frequency shift was approximated by a Taylor expansion of the interaction potential Φ_{IA} in chapter 9.3. For a nanowire positioned at $\vec{x}_{\mathrm{nw}} = (x_{\mathrm{nw}}, y_{\mathrm{nw}}, z_{\mathrm{nw}})$, the shifted frequency f_z was given by:

$$f_z = \frac{1}{2\pi}\sqrt{f_{0,z}^2 - \frac{\varepsilon}{md^3} + \frac{3\varepsilon z_{\mathrm{nw}}^2}{md^5}}, \tag{11.3}$$

Parameter	Value
Wave Number k	$2\pi/397$ nm^{-1}
Detuning δ_0	-3061 MHz
Velocity Amplitude $v_{\max}$	$0.9 \times \delta_0/k$
Time Step Δt	0.5 ns
Radiofrequency Ω	21.629 MHz
Reference Frequency ω_{ref}	$\Omega/4$
Relative Intensity s_0	10
Phase φ	$0.7 \times \pi$

Table 11.1: Simulation parameters for the simulated photon-correlation measurement shown in figure 11.2. The phase φ was chosen to obtain overlapping peaks for the measurement and simulation.

where $f_{0,z}$ is the axial trap frequency in the absence of the ion-nanowire interaction potential Φ_{IA} and $\varepsilon = k_{\text{c}} q_{\text{ion}} q_{\text{nw}}$.

The shifts of the axial frequency f_z were experimentally observed for a variety of ion-nanowire distances d and applied nanowire voltages V_{nw}. These experiments were performed within the original trap geometry, before the central lower electrode DC11 was broken. Small ion crystals were loaded into the center of the trap and the nanowire was positioned at distances d below the ions, i. e., $\vec{x}_{\text{nw}} = (0, -d, 0)$. The term $3\varepsilon z_{\text{nw}}^2/(md^5)$ in equation 11.3 was thus negligible and the model for the frequency shift here was given by:

$$f_z = \frac{1}{2\pi}\sqrt{f_{0,z}^2 - \frac{\varepsilon}{md^3}}. \tag{11.4}$$

The position of the nanowire was changed by raising it with the nanopositioners (see chapter 6.2). However, the exact step size and position was not known and later estimated by a fit of equation 11.4. With the nanowire initially set to the lowest possible position below the trap, the applied steps for seven different positions were $n_{\text{steps}} \in \{2500, 3000, 3500, 4000, 4500, 5000, 6000\}$. For each position, six different voltages $V_{\text{nw}} \in \{0.0, 0.4, 0.8, 1.2, 1.6, 2.0\}$ V were applied to the nanowire and the resulting axial frequencies f_z were determined by parametric excitation [187] with uncertainties of ± 0.2 kHz.

Figure 11.3 shows the frequencies f_z measured for the variation of d at the applied voltages $V_{\text{nw}} \in \{0.0, 1.2, 2.0\}$ V. The distances d were determined from fits of equation 11.4 to the experimental data and were found to be $d \in \{0.87, 1.20, 1.36, 1.53, 1.70, 1.86, 2.02\}$ mm with a corresponding step size of $\Delta d \approx 330$ nm for a single vertical step of the nanopositioners.

As can be seen in figure 11.3, the measured frequency f_z changed as a function of the ion-nanowire distance d, even in the case of $V_{\text{nw}} = 0$ (blue curve). This was expected, as the nanowire assembly acts as an additional electrode to the overall geometry of the trap and thus

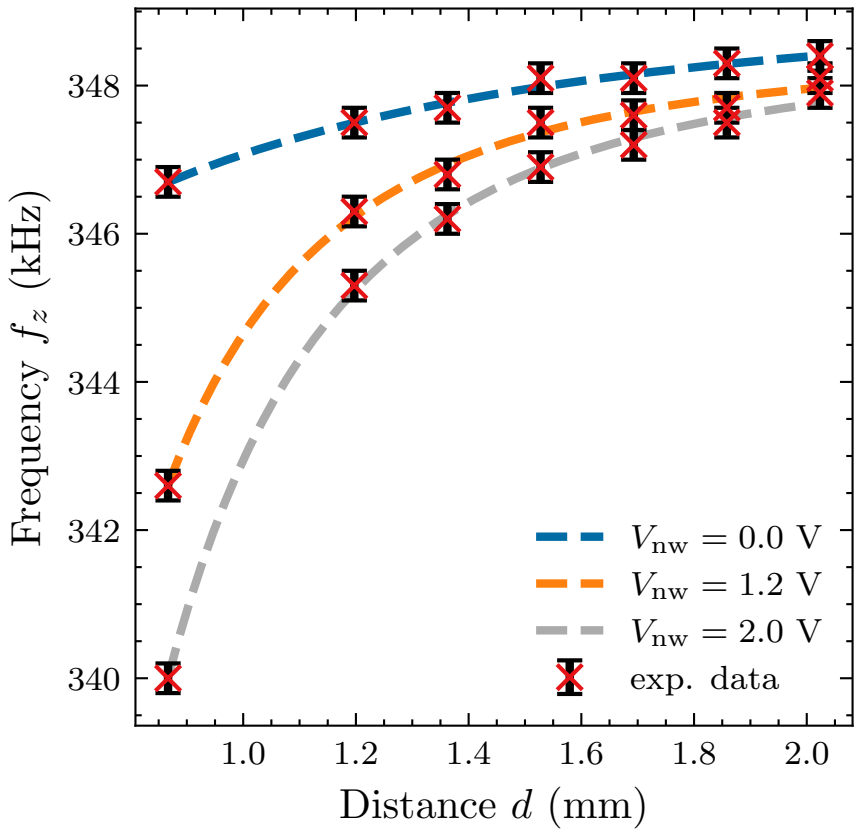

Figure 11.3: Measured frequency shifts of the axial frequency f_z of trapped ions for the variation of the ion-nanowire distance d and the nanowire voltage V_{nw}. The nanowire was positioned below the ions at $\vec{x}_{\mathrm{nw}} = (0, -d, 0)$, at distances reaching from $d \approx 0.87$ mm to $d \approx 2.02$ mm. At those distances, no shifts of the ion equilibrium position $\vec{x}_0$ were observed. Variations of d and V_{nw} lead to changes in the axial frequency f_z of trapped ions, determined by parametric excitation [187]. These shifts were also observed when the nanowire was grounded ($V_{\mathrm{nw}} = 0$, blue curve), because the nanowire acted as an additional electrode to the overall geometry of the trap and thus affected the total potential Φ. A constant parameter $\kappa = (1.41 \pm 0.02)$ Hz^{2}m^3 was added to the model in order to capture this behavior (see equation 11.5). Higher nanowire voltages V_{nw} lead to higher shifts of f_z over the same range of nanowire positions, due to the increased coupling strength ε/d^3. The shown experimental data points are well described by fits of equation 11.5 and follow the predicted behavior.

introduces changes to the total potential Φ, even when grounded ($V_{\mathrm{nw}} = 0$ V). This behavior, however, is not captured by equation 11.4 because $\varepsilon \to 0$ if $q_{\mathrm{nw}} \to 0$. We thus substituted $f_{0,z}^2 \to f_{0,z}^2(d)$ in equation 11.4 and assumed an additional dependence of $1/d^3$ for $f_{0,z}^2(d)$ in order to represent the effect on the frequency for the grounded nanowire:

$$f_z = \frac{1}{2\pi}\sqrt{f_0^2 - \frac{\kappa}{d^3} - \frac{\varepsilon}{md^3}}, \tag{11.5}$$

where f_0 is the trapping frequency without the nanowire and κ represents the effect of the grounded nanowire. By fitting of equation 11.5 to the experimental data, κ was found to be given by:

$$\kappa = (1.41 \pm 0.02)\ \mathrm{Hz}^2\mathrm{m}^3. \tag{11.6}$$

κ was also included in the curves for $V_{\mathrm{nw}} = 1.2$ V and $V_{\mathrm{nw}} = 2.0$ V shown in figure 11.3. The reported uncertainty of κ in equation 11.6 is given by the error of the fit.

Overall, the observed behavior of f_z for different ion-nanowire distances d and nanowire voltages V_{nw} were well described by equation 11.5 (see figure 11.3). Smaller distances d and larger voltages V_{nw} lead to lower frequencies f_z, as reflected by the term $-\varepsilon/(md^3) < 0$ in equation 11.5. Furthermore, lower voltages V_{nw} lead to weaker ion-nanowire coupling and thus smaller changes of f_z for the variation of the ion-nanowire distance d.

11.3 Experimental Demonstration of Ion-Nanowire Coupling

In the following, we report and discuss the central experimental results of the work presented in this thesis. As theoretically discussed in chapter 9 and simulated in chapter 10, single trapped $^{40}Ca^{+}$ ions were successfully coupled to the charged Ag_2Ga nanowire assembly. The motion of the trapped ions was resonantly driven along the axial direction by mechanical vibrations of the nanomechanical oscillator in the z-direction. In order to achieve strong coupling between the ions and the nanowire, the tip of the nanowire was positioned in close proximity to the center of the trapping region. This resulted in shifts of the trapping frequency f_z as well as the equilibrium position $\vec{x}_0$ of the ions.

The results presented in the following chapters were obtained with the modified trap geometry, in which the lower central electrode DC11 was removed from the trap. As a consequence, the $^{40}Ca^{+}$ ions were trapped near the edge region of the trap (see chapter 8.2.2). As previously discussed in chapter 11.1, we encountered strong excess micromotion and required high detunings δ_0 of the 397 nm laser for the trapping and cooling of the ions.

The calculations for the reported uncertainties of v_{max} shown in figure 11.4 and 11.6 are discussed in appendix A.3. All data points shown in figure 11.4 and 11.6 correspond to the mean value of v_{max} for sets of measurements taken on three different days.

11.3.1 Mechanical Drive of Trapped Ion Motion

In order to demonstrate the *mechanical* nature of the observed resonant drive of the ion motion, the amplitude response v_{max} of the driven ions was measured over a range of frequencies around the 422 kHz resonance peak of the nanowire assembly. Figure 11.4 shows the driven ion velocity amplitudes v_{max} obtained with the photon-correlation method discussed in chapter 7.3.2. An overview of the applied experimental parameters is given in table 11.2.

For each data point, a string of two ions was loaded into the trap and the axial trap fre-

Parameter	Value
Number of Trapped Ions N	2
Nanowire Voltage V_{nw}	1.2 V
Piezo Drive Voltage V_{piezo}	7 V
Ion-Nanowire Distance d	307 µm
Detuning δ_0	-3479 MHz

Table 11.2: Experimental parameters for the correlation of resonantly driven ion motion to the mechanical response spectrum of the nanowire (see figure 11.4).

quency f_z was adjusted to the desired value by changing the applied DC electrode voltages. f_z was determined with an uncertainty of ± 0.2 kHz by measuring it with the parametric excitation discussed in chapter 7.2 [187]. The nanowire was then mechanically driven along the z-direction with the attached piezo actuator at frequency $f_{\mathrm{drive}} = f_z$. This ensured frequency-matching to the ions and thus resonant drive of the ion motion by the nanowire.

The amplitude of oscillation A of the nanowire assembly driven by the piezo actuator is a function of the applied drive frequency ω_{drive}. For an ideal nanowire described by the Euler-Bernoulli beam theory (see chapter 5), the response is given by a Lorentzian function [121, 168]:

$$A(f_{\mathrm{drive}}) = A_0 \frac{\omega_0^2/Q}{\sqrt{(\omega_0^2 - \omega_{\mathrm{drive}}^2)^2 + \omega_0^2 \omega_{\mathrm{drive}}^2/Q^2}}, \tag{11.7}$$

with some amplitude response A_0 when driven on resonance, i. e., $\omega_{\mathrm{drive}} = \omega_0 = 2\pi \times 422$ kHz. Q is the quality factor of the resonator. As can be seen in figure 11.4, the experimentally determined spectrum of the mechanical oscillator assembly is more complex than the one described by equation 11.7. It exhibited an asymmetric shape of the resonance peak at 422 kHz. We tentatively attribute this asymmetry to overlapping mechanical modes arising from other components of the mechanically driven assembly, such as the nanopositioners.

The response of the driven ion motion was expected to be directly correlated to the amplitude A of the oscillating nanowire and thus to exhibit the strongest drive at the resonance $f_{\mathrm{drive}} = 422$ kHz. Figure 11.5a shows EMCCD images of ions driven near the resonance of the nanowire as well as far off the resonance. Figure 11.5b shows the corresponding histograms obtained from the photon-correlation method. A clear periodic drive of the ion motion was visible when driven near the resonance frequency of the nanowire, while no significant drive could be seen when the nanowire was driven off-resonantly. v_{max} was determined by least-square fitting of equation 7.1 to the data in the histograms shown in figure 11.5b.

Figure 11.4 shows a clear correlation of the frequency spectrum of the nanowire to the experimentally obtained velocity amplitudes v_{max}. More specifically, the results indicated proportionality of the squared velocity amplitudes $v_{\mathrm{max}}^2 \propto E_{\mathrm{kin}}$ to the spectrum of the nanowire

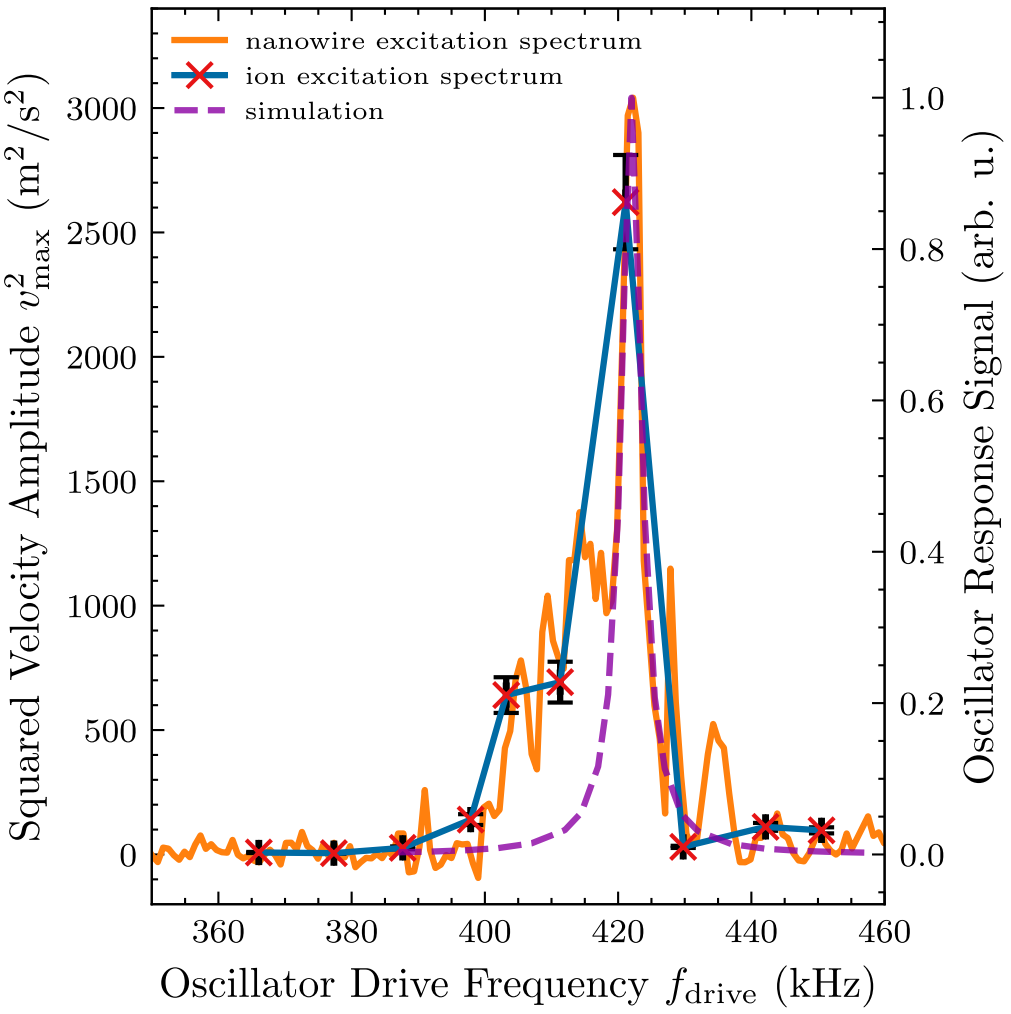

Figure 11.4: Mechanical excitation of trapped ions by the nanowire. The orange trace corresponds to the excitation spectrum of the nanowire assembly around the resonance at $f_0 = 422$ kHz (see also figure 7.2). We attribute the asymmetry of the excitation feature to contributions from other mechanically driven components, such as the nanopositioners. The velocity amplitudes v_{max} of resonantly driven ions were determined with the photon-correlation method for a variety of drive frequencies f_{drive}. The corresponding squared velocity amplitudes v^2_{max} (red crosses) showed a direct correlation to the motional spectrum of the mechanical assembly. Classical dynamics simulations (purple dashed line) assuming a Lorentzian line shape (equation 11.7) reproduced the behavior.

obtained from the optomechanical readout (see also chapter 7.1).

Assuming a Lorentzian behavior (equation 11.7) of the amplitude response of the mechanical oscillator, the squared velocity amplitudes v^2_{max} of driven ions were simulated with the velocity Verlet algorithm discussed in chapter 10.1. Neglecting the asymmetry of the optomechanically determined nanowire spectrum, the quality factor of the Lorentzian was estimated to be $Q \approx 117$ from the FWHM $\Delta f \approx 3.6$ kHz of the central peak at the resonance $f_0 = 422$ kHz in figure 11.4 (see also equation 5.27). The v^2_{max} determined from the simulations correlated well to the resonance peak in the measured spectrum of the oscillator shown in figure 11.4.

The observed correlation of the experimentally determined squared velocity amplitudes v^2_{max} of

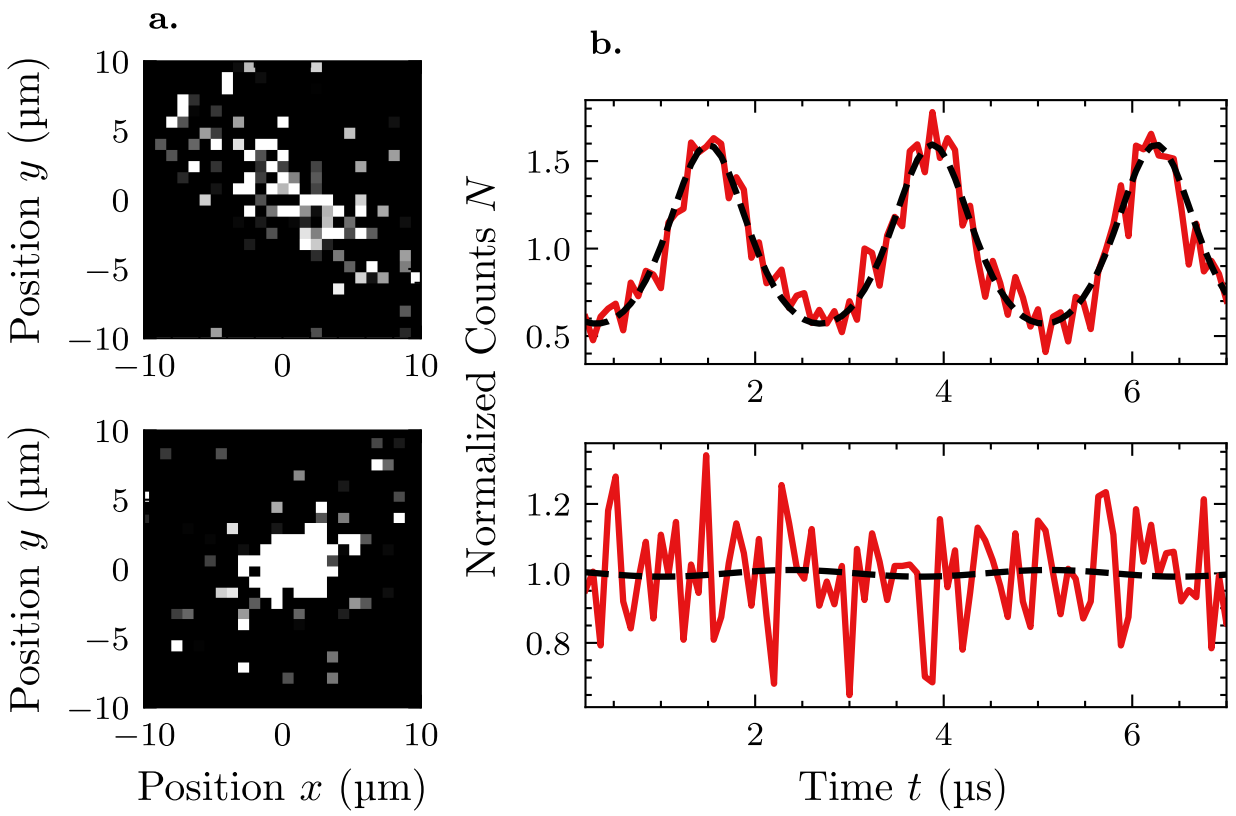

Figure 11.5: Imaging of the mechanical excitation of trapped ions near and far off the nanowire resonance at $f_0 = 422$ kHz. **a**, EMCCD images of a single trapped ion mechanically driven at frequencies $f_{\text{drive}} = 421.0$ kHz (top) and $f_{\text{drive}} = 366.2$ kHz (bottom). The axial trap frequency was adjusted such that $f_z = f_{\text{drive}}$. Near the nanowire resonance at $f_0 = 422$ kHz (top), a strong excitation of the ion motion along the axial direction was visible, while far-off resonant drive (bottom) yielded no observable excitation of the ion motion on the image of the EMCCD camera. **b**, Fluorescence distributions obtained with the photon-correlation method, corresponding to the EMCCD images shown in **a**. A strong resonant excitation of the ion motion yielded clear periodic distributions for the measured ion fluorescence (top) due to the high velocity amplitudes v_{max} of driven motion at frequency ω_{drive}. Far-off resonant drive showed no observable excitation by photon correlation (bottom). The velocity amplitudes obtained from fits of equation 7.1 to the histograms were $v_{\text{max}} = 55.3 \pm 2.0$ m/s (top) and $v_{\text{max}} = 1.1 \pm 2.2$ m/s (bottom).

the driven ions to the spectrum of the mechanical oscillator showed the mechanical nature of the drive. It further showed that the ions were successfully coupled to the nanowire assembly in the classical regime and offered a proof-of-principle for the realization of a hybrid system consisting of trapped ions and a nanomechanical oscillator.

11.3.2 Resonantly Driven Ion Motion for the Variation of Experimental Parameters

The strength of the ion-nanowire coupling and the resulting velocity amplitudes v_{max} of the resonantly driven ion motion mainly depend on the following experimental parameters (see also chapters 9 and 10):

- The amplitude A of the oscillating nanowire.
- The ion-nanowire distance d.

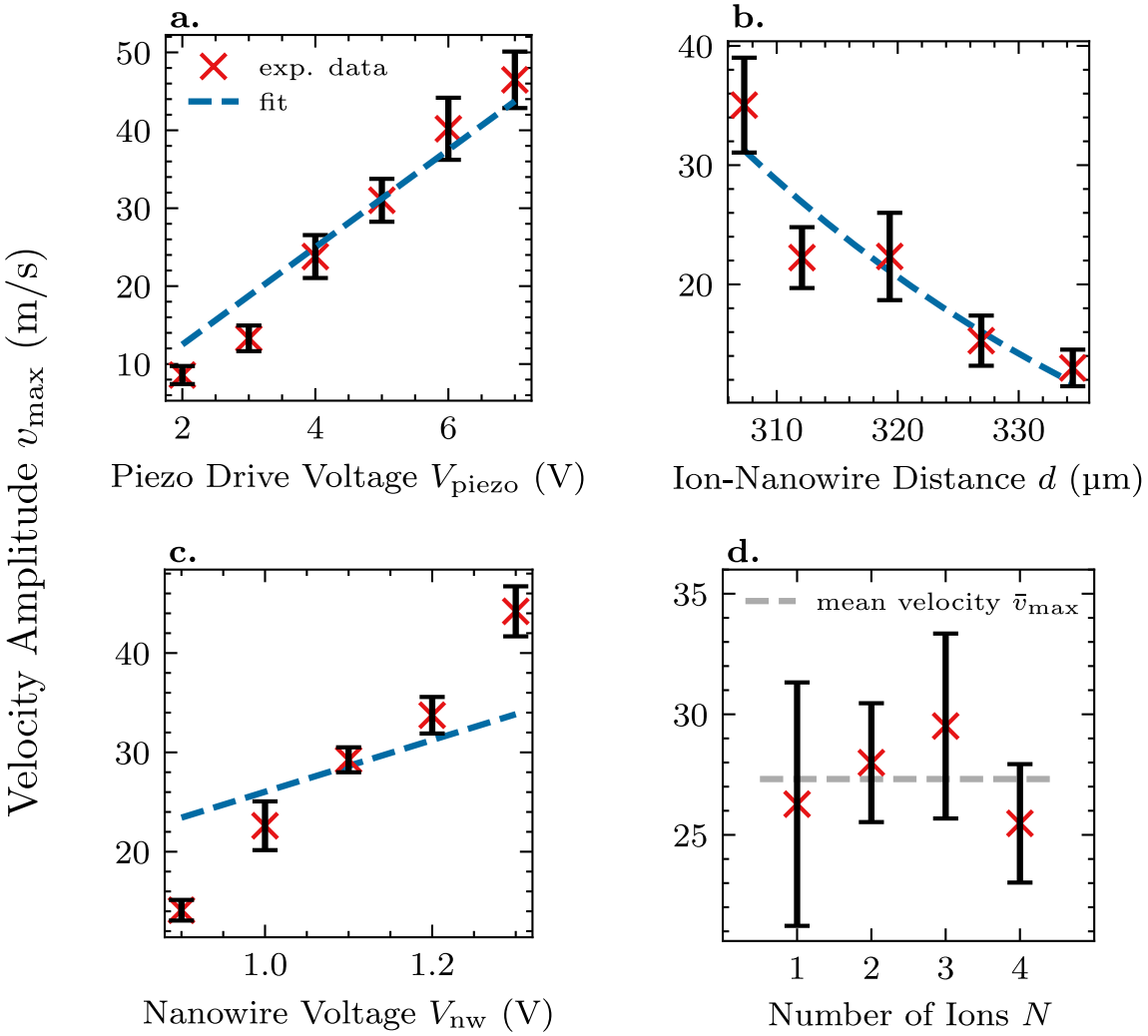

Figure 11.6: Resonantly driven ion motion for the variation of coupling parameters. A multivariable fit of equation 11.11 (blue curves) was in good agreement with the data shown in **a** and **b**, but the model failed to describe the data shown in **c** (more details in text). **a**, Variation of the drive voltage V_{piezo} applied to the piezo actuator. The ion excitation increased with higher drive voltages. **b**, Variation of the ion-nanowire distance d. Increased distances lead to weaker excitation of the ion motion. This behavior was consistent with the corresponding decrease of the coupling strength ε/d^3. **c**, Variation of the nanowire voltage V_{nw}. Higher nanowire voltages (and thus higher coupling strengths ε/d^3) lead to stronger excitation of the ions. **d**, Variation of the number of trapped ions N up to $N = 4$. No significant effect was observed ($\bar{v}_{\mathrm{max}} \approx 27.3$ m/s).

- The effective point charge q_{nw} of the nanowire.

We defined the *coupling strength* of the ion-nanowire interaction in chapter 9 as:

$$\frac{\varepsilon}{d^3} = k_{\mathrm{c}} \frac{q_{\mathrm{ion}} q_{\mathrm{nw}}}{d^3}, \tag{11.8}$$

where k_{c} is the Coulomb constant and $q_{\mathrm{ion}} = e$ is the charge of a single trapped $^{40}\mathrm{Ca}^{+}$ ion.

Figure 11.6a – c shows the velocity amplitudes v_{max} of resonantly driven ions, obtained for the variation of the applied drive voltage on the piezo actuator V_{piezo}, the ion-nanowire distance d and the applied static nanowire voltage V_{nw}. Additionally, figure 11.6d shows v_{max} for dif-

ferent amounts of trapped ions up to $N = 4$. In the following, we report on the experimental parameters and methods used here and discuss the results shown in figure 11.6.

As in chapter 11.3.1, the velocity amplitudes $v_{\max}$ were determined with the photon-correlation method (see also chapter 7.3.2). With the exception of the data shown in figure 11.6d, all experiments shown here were performed with strings consisting of two trapped ions. The axial trapping frequency of the ions was set to the resonance of the mechanical oscillator at $f_z = 422$ kHz and confirmed with an uncertainty of ± 0.2 kHz by parametric excitation [187]. The oscillator was driven at the same frequency $f_{\text{drive}} = 422$ kHz with the piezo actuator, leading to resonant excitation of the ion motion ($f_{\text{drive}} = f_z$) along the z-direction. The nanowire was raised until the tip was positioned close to the center of the trapping region. The nanowire position $\vec{x}_{\text{nw}} = (x_{\text{nw}}, y_{\text{nw}}, z_{\text{nw}})$ exhibited three non-zero components x_{nw}, y_{nw} and z_{nw} with respect to the shifted ion equilibrium position $\vec{x}_0 = (0, 0, 0)$. For variations of the ion-nanowire distance d (figure 11.6b), the nanowire was only moved along the axial z-direction. This allowed a controlled positioning of the nanowire in the horizontal plane with the EMCCD camera. Moving the nanowire along the vertical direction was avoided, as it prevented a reliable control over the position (see below).

As discussed in chapter 9.1 and shown in figure 9.1, the effective charge q_{nw} was determined from the applied voltage V_{nw} as:

$$q_{\text{nw}} = 1.84 \times 10^{-15} \frac{V_{\text{nw}}}{1\ \text{V}} As. \tag{11.9}$$

With a maximum applied voltage of $V_{\text{nw}} = 1.3$ V and a minimum ion-nanowire distance of $d \approx 307$ µm, the highest coupling strength for the experiments presented here was:

$$\frac{\varepsilon}{d^3} \approx 0.15 m \omega_{0,z}^2, \tag{11.10}$$

with $m = 6.66 \times 10^{-26}$ kg and $\omega_{0,z} = 2\pi \times 452.7$ kHz. $\omega_{0,z}$ was determined from equation 9.17, such that $\omega_z = 2\pi \times 422$ kHz. Here, the nanowire position was given by $\vec{x}_{\text{nw}} \approx (81, 288, -69)$ µm ($\Rightarrow d \approx 307$ µm). The effective position $\vec{x}_{\text{nw}}$ of the nanowire tip in the interaction model was further extended by an offset $\vec{d}_{\text{offset}}$ of length $|\vec{d}_{\text{offset}}| = 33.5$ µm as described in chapter 9.2 and shown in figure 9.2.

As discussed in chapter 9, $\varepsilon/d^3 \lesssim 0.3 m \omega_{0,z}^2$ justifies a description of the ion-nanowire interaction in which the directions of motion of the ions remain decoupled.

Determination of the ion-nanowire distance *d*:

The total ion-nanowire distance d for each data point shown in figure 11.6 was experimen-

tally determined with the image captured by the EMCCD camera in combination with a fit of the ion-nanowire interaction model.

The distance $d_{\mathrm{hori}} = \sqrt{x_{\mathrm{nw}}^2 + z_{\mathrm{nw}}^2}$ and the corresponding position components $(x_{\mathrm{nw}}, z_{\mathrm{nw}})$ of the nanowire in the horizontal plane of the trap were directly determined with the image of the EMCCD camera. The vertical distance $d_{\mathrm{vert}} = y_{\mathrm{nw}}$ was determined in a first step by moving the camera vertically and measuring the distance between the points at which the image of the camera was focused on the ions and the tip of the nanowire. This method provided a rough estimate for y_{nw}, but could not provide very accurate results. The vertical distance was found to be $y_{\mathrm{nw}} \approx (250 \pm 50)$ µm. To obtain a more accurate estimate for y_{nw}, it was added as an additional fitting parameter to the model describing the ion-nanowire interaction (see also equation 11.11).

Fitting of the ion-nanowire interaction model:

In chapter 9.4, we have derived an analytical expression for the velocity amplitude v_{max} of the steady-state oscillations of a single trapped ion resonantly driven by a vibrating nanowire along the z-direction. It was given by:

$$\begin{aligned} v_{\mathrm{max}} &= \left| \left(\frac{\varepsilon}{d^3} - \frac{3\varepsilon z_{\mathrm{nw}}^2}{d^5} \right) \frac{A}{m\gamma} \right| \\ &= \left| \left(\frac{\varepsilon}{\sqrt{d_{\mathrm{hori}}^2 + y_{\mathrm{nw}}^2}^3} - \frac{3\varepsilon z_{\mathrm{nw}}^2}{\sqrt{d_{\mathrm{hori}}^2 + y_{\mathrm{nw}}^2}^5} \right) \kappa_A V_{\mathrm{piezo}} \right| . \end{aligned} \tag{11.11}$$

Equation 11.11 assumed a description of the nanowire as an effective point charge, as well as decoupled oscillations of the trapped ion motion along x, y and z (justified by equation 11.10). The second line of equation 11.11 shows the fitting parameters y_{nw} and κ_A. y_{nw} corresponds to the vertical ion-nanowire distance and κ_A describes the linear response of the system to the applied drive voltage V_{piezo}. $\kappa_A = A/V_{\mathrm{piezo}} \times (m\gamma)^{-1}$ incorporates the amplitude A of the nanowire per applied piezo voltage V_{piezo}, as well as the mass m and the damping factor γ of the laser-cooled ion.

Initially, a multivariable fit of equation 11.11 to all data points shown in figure 11.6a – c was performed. However, the model given by equation 11.11 assumes proportionality of v_{max} to the applied voltage V_{nw}. This proportionality was not reflected by the data points obtained from the variation of V_{nw} shown in figure 11.6c and the fit failed to yield proper results.

Instead, we limited the multivariable fit of equation 11.11 to the data points shown in figure 11.6a and 11.6b. The curves obtained from the fits were in good agreement with the data points and the fitting parameters were found to be:

$$
\begin{aligned}
y_{\mathrm{nw}} =& (288 \pm 26)\ \mu\mathrm{m}, \\
\kappa_A =& (2.9 \pm 0.5) \times 10^{-10}\ \frac{\mathrm{ms}}{\mathrm{kgV}},
\end{aligned}
\tag{11.12}
$$

where the reported uncertainties are given by the errors of the fit.

In the following, we discuss the variations of the different experimental parameters individually.

Variation of the piezo drive voltage V_{piezo}:

The velocity amplitudes v_{max} obtained for the variation of the piezo drive voltage V_{piezo} are shown in figure 11.6a. Here, the nanowire voltage was set to $V_{\mathrm{nw}} = 1.2$ V and the total ion-nanowire distance was $d \approx 307$ µm. The piezo drive voltage was varied from $V_{\mathrm{piezo}} = 2$ V to $V_{\mathrm{piezo}} = 7$ V in steps of $\Delta V_{\mathrm{piezo}} = 1$ V. As expected, the resonantly driven velocity amplitudes v_{max} increased with higher piezo drive voltages V_{piezo}. The fit of equation 11.11 was in good agreement with the data and the amplitude A of the nanomechanical oscillator was assumed to be directly proportional to the applied piezo voltage V_{piezo}.

Variation of the total ion-nanowire distance d:

The velocity amplitudes v_{max} obtained for the variation of the ion-nanowire distance d are shown in figure 11.6b. Here, the nanowire voltage was set to $V_{\mathrm{nw}} = 1.2$ V and the piezo actuator was driven with a voltage of $V_{\mathrm{piezo}} = 5$ V. The total ion-nanowire distance $d = \sqrt{x_{\mathrm{nw}}^2 + y_{\mathrm{nw}}^2 + z_{\mathrm{nw}}^2}$ was varied by moving the nanowire along the axial z-direction. The position components x_{nw} and y_{nw} remained approximately unchanged. The distances d of the data points shown in figure 11.6b are $d \in \{307, 312, 319, 327, 334\}$ µm. The resonantly driven velocity amplitudes v_{max} decreased with increasing ion-nanowire distances d, due to the reduced coupling strength ε/d^3 of the system. The fit of equation 11.11 was in good agreement with the data.

Variation of the nanowire voltage V_{nw}:

The velocity amplitudes v_{max} obtained for the variation of the applied static nanowire voltage V_{nw} are shown in figure 11.6c. Here, the piezo actuator was driven with a voltage of $V_{\mathrm{piezo}} = 5$ V and the ion-nanowire distance was $d \approx 307$ µm. The nanowire voltage was varied from $V_{\mathrm{nw}} = 0.9$ V to $V_{\mathrm{nw}} = 1.3$ V in steps of $\Delta V_{\mathrm{piezo}} = 0.1$ V. Qualitatively, the driven velocity amplitudes v_{max} increased with increasing nanowire voltage V_{nw}. This behavior was expected due to the corresponding increase in the effective charge q_{nw} of the nanowire, leading to a higher coupling strength ε/d^3. However, the model given by equation 11.11 assumed proportionality of v_{max} to V_{nw}, represented by the blue line of the fit shown in figure 11.6c. The data points exhibited a higher slope compared to the prediction provided by the model and were not well

described by a fit of equation 11.11.

A few possible reasons for the discrepancy of the data shown in figure 11.6c to the model given by equation 11.11 can be identified. As discussed in chapter 9, the model assumed the description of the nanowire as an effective point charge. However, the relatively large and electrically conductive tungsten holder of the nanowire assembly introduces distortions and contributions to the total potential Φ within the trapping region, as was discussed in chapter 8. Those contributions were found to increase the closer the tip of the nanowire was positioned near the center of the trap. The addition of higher-order terms of a multipole expansion [113, 192] may yield a more accurate description of the total charge distribution of the tungsten holder and thus capture the effects on v_{max} observed in figure 11.6c. Furthermore, the model given by equation 11.11 and derived in chapter 9 assumed a total absence of any ion-nanowire interaction potential Φ_{IA} if the nanowire is grounded ($V_{\mathrm{nw}} = 0$ V). In reality, however, the grounded nanowire assembly still acts as an additional electrode within the geometry of the trap and effectively changes the total potential Φ experienced by the ions. Mechanically driving the grounded nanowire would still introduce periodic variations to Φ and allow the drive of the ions, albeit to a weaker extent. This argument is also connected to the presence of the tungsten holder, which increases this effect due to its relatively large size. An extension of the data shown in figure 11.6c over a higher range of voltages V_{nw} may yield a more complete picture of the dynamics. The range presented here was chosen due to encountered limitations with respect to the stability of the trapped ions. Lastly, changes in V_{nw} lead to changes of the interaction potential Φ_{IA} generated by the nanowire assembly. This in turn lead to shifts in the equilibrium position of the ions. While the observed shifts in the ion position for the experiments presented here were negligible, it is still important to note the codependence of the nanowire voltage V_{nw} and the resulting ion-nanowire distance d. The final ion-nanowire distance d was further affected by adjustments of the DC electrode voltages to obtain resonance ($f_z = f_{\mathrm{drive}}$). Instead of observing the dynamics of v_{max} in dependence of V_{nw} and d individually, determination of the dependence on the coupling strength ε/d^3 may be an alternative approach.

Variation of the number of trapped ions N:

Figure 11.6d shows the velocity amplitudes v_{max} obtained for different amounts of trapped ions N, up to $N = 4$. The ions were trapped as linear ion chains. The piezo drive voltage was set to $V_{\mathrm{piezo}} = 5$ V, a static voltage $V_{\mathrm{nw}} = 1.2$ V was applied to the nanowire and the ion-nanowire distance was set to $d \approx 307$ µm. For the small ion strings investigated here, no significant change in v_{max} was observed. The mean velocity amplitude was found to be $\bar{v}_{\mathrm{max}} \approx 27.3$ m/s.

12 Conclusion & Outlook

The work presented in this thesis aimed at the experimental demonstration and characterization of the coupling of a charged Ag_2Ga nanowire to trapped $^{40}Ca^+$ ions in a novel ion-nanowire hybrid system [80]. In this work, the coupling of the systems by their electrostatic interaction was experimentally demonstrated and the motion of the trapped $^{40}Ca^+$ ions was resonantly excited by driven mechanical vibrations of the nanowire in the classical regime. The results show the mechanical manipulation of the motion of trapped ions with a nanomechanical oscillator. In future experiments, this may be extended to the manipulation and preparation of the motional states of single ions in the quantum regime [80, 84]. In addition to the experimental demonstration of the ion-nanowire coupling, the theoretical model in the classical regime [80, 93] was extended and studied for arbitrary positions $\vec{x}_{\mathrm{nw}}$ of the nanowire, as well as for the inclusion of coupled motion along different directions of oscillation of the ions. The findings were compared to and confirmed by numerical simulations.

The experimental setup presented here was assembled and specifically designed for the realization of an ion-nanowire hybrid system by Panagiotis Fountas [80]. In this work, we have shown the practical feasibility of the design by the successful coupling of $^{40}Ca^+$ ions to the Ag_2Ga nanowire. Over the course of this project, the linear ion trap [80] was successfully taken into operation and the experimental setup was gradually improved over several iterations. These improvements included quality-of-life changes such as the implementation of reliable connectors to the trap electrodes, as well as crucial additions to the setup such as the shielding of the piezo actuator and the implementation of the photon-correlation method. Most of the practical issues encountered over the course of the project were addressed. However, a selection of possible improvements of the setup that deserve further consideration and investigation are the application of radiofrequency voltages at different phases, the addition of more compensation electrodes, the use of a dielectric material for the holder of the nanomechanical oscillator and the implementation of nanopositioners with integrated resistive encoders [211, 212] for a reliable positioning of the nanowire in all spatial directions. Driving the mechanical modes of the nanowire optically [69] with a dedicated laser focused on its tip may provide a better approach than the mechanical drive by the piezo actuator located at the base of the holder. This approach would entirely prevent electrical excitation of the ions and may enable the localized excitation of isolated nanowire modes, without additional vibrations from the holder. Furthermore, the design of the ion-nanowire hybrid system was not optimized for the characterization and readout of the resonances of the nanowire. As such, it is recommended to perform a complete characterization of the nanomechanical oscillator prior to introducing it to the assembly.

The results presented in this thesis lay the foundation for future experiments with the presented ion-nanowire hybrid system in the classical regime and in the quantum regime. One such prospect is the resonant excitation of the breathing mode motion of two-ion strings by

the mechanically driven nanowire. Furthermore, the nanowire acts as an additional electrode to the geometry of the trap and offers additional degrees of freedom for the shaping of the trapping potential by varying parameters such as its position and the applied static voltage. This may allow the controlled introduction of anharmonicities to the potential and the generation of double-well potentials [84, 109]. These may be used for the transmission of quantum information [109], the cooling of trapped ions in quantum charge-coupled device (QCCD) architectures [213] or the simultaneous trapping of positively and negatively charged ions. The nanowire may act as a mediator and narrow band-pass filter between the trapped particles. Another interesting prospect is the study of the ion-nanowire interaction for different phases of the nanowire oscillations. Controlling the phase and the duration of the mechanically driven vibrations of the nanowire relative to the oscillations of the trapped ions may offer a way of mechanically cooling the ions due to the delayed amplitude response of the coupled mechanical oscillators. Moreover, the well-controllable motional states of trapped ions may be transferred onto the nanowire and thus create non-classical states of motion of the nanooscillator [84]. While the experimental excitation of trapped ions in the classical regime for the variation of the amplitude of the nanowire A, the applied nanowire voltage V_{nw} and the ion-nanowire distance d was presented in this thesis, the theoretically predicted dependencies on the nanowire position $\vec{x}_{\mathrm{nw}}$ and the directions of oscillation of the nanowire are yet to be confirmed experimentally. The addition of resolved sideband cooling to the setup may allow the preparation of single trapped ions in their motional ground state in order to study the driven ion-nanowire dynamics in the quantum regime. The possibility of engineering a variety of motional state distributions, such as coherent states and Schrödinger cat states [50], with the mechanical excitation offered by the presented hybrid system has been shown theoretically in previous works [80, 84]. Challenges to overcome in future experiments are the strong excess micromotion and the resulting low cooling efficiencies and high detunings δ_0 encountered over the course of this project. Furthermore, the experiments presented in this thesis were performed at room temperature $T \approx 300$ K. This prevented any observations of quantum effects on the nanowire due to its estimated high phonon number of $\langle N \rangle \approx 15 \times 10^6$ and thermal decoherence rate of $\gamma_{\mathrm{th}} \approx 335$ GHz.

13 Acknowledgments

I would like to express my acknowledgments and gratitude to all the people who supported me throughout this project. First and foremost, I would like to thank **Prof. Stefan Willitsch** for giving me the opportunity to pursue my PhD at the University of Basel in the beautiful country of Switzerland. I want to thank him for his continuous mentorship, support and guidance throughout this project. I would also like to thank **Prof. Martino Poggio** for the close collaboration. As my second supervisor, he would always offer any resources he could to support my work. I want to thank **Prof. Dr. Martina Knoop** for acting as the external referee for this thesis. Furthermore, I want to express special thanks to **Dr. Panagiotis Fountas**, my predecessor on this project. He lay the foundation for my scientific findings by designing and manufacturing the experimental setup and he guided me through my first year of the project.

I would also like to thank all of my other colleagues and peers that I had throughout the years. They truly made my time in Basel a wonderful experience and became dear friends. I would like to start by thanking all the PhD students and postdocs of the group. We all shared the same experiences of struggles and successes and could always relate to each other. I want to especially thank everybody whom I shared an office with: **Miko**, **Aleks**, **Richard**, **Mudit**, **Kaveh**, **Misha**, **Nanditha**, **Adrien**, **Prerna**, **Meïssa** and **Ziv**. Their positive attitudes, humour and knowledge gave the office a great atmosphere and it was always fun being around them. We could always discuss scientific and non-scientific topics and support each other with our struggles. I want to express special thanks to **Miko**, **Aleks** and **Richard** for all the fun times in the laboratory. They truly made the work so much more enjoyable and I am happy about all the music that we shared. I also want to especially thank my successor **Adrien** for his support during the final months of my project and wish him all the best and a lot of success for future endeavors with the experiment. I further want to thank all other members of the group: **Tomislav**, **Christian**, **Pietro**, **Claudio**, **Ludger**, **Patrik**, **Amit**, **Lei**, **Uxia**, **Ardita**, **Aswin**, **Jutta**, **Thomas**, **Chao** and **Yanning**. I want to especially thank **Tomislav** for all of our chess-related discussions, chess puzzles we solved together and for introducing me to SG Trümmerfeld. I want to thank everybody again for all the support and friendship they offered during my time at the University of Basel and beyond.

I would like to thank all the technical staff members of the group, as well as the members of the workshop: **Georg**, **Anatoly**, **Philipp** and **Grischa**. Without them and their support, everything would come to a halt and the scientific efforts and successes of the group would not be possible. I also want to thank all members of the secretary's office who were always there to help and support us with all administrative questions: **Maya**, **Mariella** and **Tatsiana**.

I would also like to thank the **Swiss Nanoscience Institute (SNI)** for funding this PhD project (P1808). I want to thank **all the staff members** and **all other PhD students** of the SNI for all the support and the fun times at extracurricular events.

Lastly, I would like to thank **all of my friends** and **everybody that I love**. My deepest gratitude goes to **all members of my family**, and especially to **my parents** whom I love dearly and who gave me their unconditional support throughout this project and my entire life.

A Appendix

A.1 Symbols, Units & Constants

Here, we provide an overview of symbols, units and constants used throughout the thesis.

Physical Quantity	Symbol	Unit
Position	x, y, z	1 m
Time	t, T	1 s
Velocity	v	1 m s^{-1}
Acceleration	a	1 m s^{-2}
Frequency	f	1 Hz = 1 s^{-1}
Angular Frequency	$\omega, \Omega = 2\pi f$	1 Hz = 1 s^{-1}
Mass	m, M	1 kg
Atomic Mass	m, M	1 u = 1.661×10^{-27} kg
Force	F	1 N = 1 kg m s^{-2}
Energy	E	1 J = 1 N m = 1 kg m^2 s^{-2}
Power	P	1 W = 1 J s^{-1} = 1 kg m^2 s^{-3}
Intensity	I	1 W m^{-2} = 1 kg s^{-3}
Temperature	T	1 K
Charge	q, Q	1 C = 1 A s
Voltage	V, U	1 V = 1 kg m^2 A^{-1} s^{-3}
Potential	Φ	1 J = 1 V A s = 1 kg m^2 s^{-2}
Electric Field	E	1 V m^{-1} = 1 kg m s^{-3} A^{-1}
Area Moment of Inertia	I	1 m^4
Density	ρ	1 kg m^{-3}
Young's Modulus	E_Y	1 Pa = 1 N m^{-2} = 1 kg m^{-1} s^{-2}
Wavelength	λ	1 m
Angular Wavenumber	$k = 2\pi/\lambda$	1 m^{-1}
Detuning	δ	1 Hz = 1 s^{-1}
Linewidth	Γ	1 Hz = 1 s^{-1}

Table A.1: Selection of physical quantities and their symbols used throughout this thesis. In the last column, we show useful unit conversions and the conversion to fundamental SI units.

Constant	Symbol	Value
Elementary Charge	e	1.602×10^{-19} As
Reduced Planck Constant	$\hbar$	1.055×10^{-34} Js
Vacuum Electric Permittivity	ε_0	8.854×10^{-12} $\frac{\mathrm{As}}{\mathrm{Vm}}$
Coulomb Constant	k_c	8.988×10^{9} $\frac{\mathrm{Nm}^2}{\mathrm{A}^2\mathrm{s}^2}$
Boltzmann Constant	k_B	1.381×10^{-23} $\frac{\mathrm{J}}{\mathrm{K}}$

Table A.2: Fundamental physical constants used throughout this thesis.

A.2 Quantum Harmonic Oscillator

Here, we give a brief overview over the most important concepts and equations regarding the quantum harmonic oscillator. More details on quantum harmonic oscillators can be found in many standard text books [158, 214, 215].

The classical potential Φ of a harmonic oscillator is given by:

$$\Phi(z) = \frac{1}{2} m\omega^2 \vec{x}^2. \tag{A.1}$$

By replacing $\vec{x}$ with the position operator $\hat{x}$, the Schrödinger equation for the harmonic oscillator is given by:

$$\begin{aligned} i\hbar \frac{\partial}{\partial t}\Psi &= \left(\frac{\hat{p}^2}{2m} + \frac{1}{2} m\omega^2 \hat{x}^2 \right) \Psi \\ &= \hbar\omega \left(\hat{a}^\dagger \hat{a} + \frac{1}{2} \right) \Psi, \end{aligned} \tag{A.2}$$

where $\hat{a}^\dagger$ and $\hat{a}$ are the *creation* and *annihilation* operator, respectively. They are defined by $\hat{p}$ and $\hat{z}$ as:

$$\begin{aligned} \hat{a}^\dagger &= \sqrt{\frac{m\omega}{2\hbar}} \left(\hat{x} - \frac{i\hat{p}}{m\omega} \right), \\ \hat{a} &= \sqrt{\frac{m\omega}{2\hbar}} \left(\hat{x} + \frac{i\hat{p}}{m\omega} \right). \end{aligned} \tag{A.3}$$

Vice versa, the position and momentum operator can be written in terms of the creation and annihilation operators:

$$\begin{aligned} \hat{x} &= \sqrt{\frac{\hbar}{2m\omega}} (\hat{a}^\dagger + \hat{a}), \\ \hat{p} &= i\sqrt{\frac{m\hbar\omega}{2}} (\hat{a}^\dagger - \hat{a}). \end{aligned} \tag{A.4}$$

Quantum harmonic oscillators exhibit eigenstates $|n\rangle$ with energy $E_n = (n + \frac{1}{2})\hbar\omega$ and occupation number n. The relations of $|n\rangle$ to the creation and annihilation operators are:

$$\begin{aligned} \hat{a}^\dagger |n\rangle &= \sqrt{n+1}|n+1\rangle, \\ \hat{a}|n\rangle &= \sqrt{n}|n-1\rangle, \\ \langle n|\hat{a}^\dagger \hat{a}|n\rangle &= n. \end{aligned} \tag{A.5}$$

The extension x_n of the wavefunction of a state $|n\rangle$ is defined as $\sqrt{\langle n|\hat{x}^2|n\rangle}$. Using equations A.4 and A.5, we can see that:

$$x_n = \sqrt{\frac{\hbar}{2m\omega}(2n+1)}. \tag{A.6}$$

A.3 Error Calculation

The reported observable is the velocity amplitude $v_{\max}$ of the driven ion oscillations. The individual velocity amplitudes for single measurements are extracted from the fitting of function 7.1 to the data as described in chapter 7.3.2. The total error reported here consists of the *fit error* and the *statistical error*.

A.3.1 Fit Error

The fits of equation 7.1 to the individual histograms are performed with the `curve_fit` function of the `scipy.optimize` Python library. Each fit yields a $v_{\max,i}$ value as well as the corresponding covariance σ_i^2. The corresponding standard deviation $\sigma_i = \sqrt{\sigma_i^2}$ is taken to represent the fit error of an individual measurement. The reported $v_{\max}$ is the mean of a set of N individual $v_{\max,i}$:

$$v_{\max} = \frac{1}{N}\sum_{i=1}^{N} v_{\max,i} \tag{A.7}$$

Following Gaussian error propagation, the total fit error of one data point $v_{\max}$ is given by:

$$\sigma_{\text{fit},v} = \frac{1}{N}\sqrt{\sum_{i=1}^{N}\sigma_i^2} \tag{A.8}$$

A.3.2 Statistical Error

The statistical error of a data point $v_{\max}$ (see equation A.7) is given by the standard deviation for the distribution of the individual values $v_{\max,i}$:

$$\sigma_{\text{stat},v} = \sqrt{\frac{1}{N-1}\sum_{i=1}^{N}(v_{\max} - v_{\max,i})^2} \tag{A.9}$$

A.3.3 Total Error

The total error for the measured $v_{\max}$ is given by a combination of the fit error and statistical error:

$$\sigma_{\text{tot},v} = \sqrt{\sigma_{\text{fit}}^2 + \sigma_{\text{stat}}^2} \tag{A.10}$$

In figure 11.4 we report the squared values $v_{\max}^2$. Here, the total reported error is given by the Gaussian error propagation:

$$\sigma_{\text{tot},v^2} = 2v_{\max}\sigma_{\text{tot},v} \tag{A.11}$$

.

References

[1] J. P. Dowling and G. J. Milburn. "Quantum technology: the second quantum revolution". In: *Phil. Trans. R. Soc. Lond. A* 361 (2003), p. 1655.

[2] C. Monroe. "Quantum information processing with atoms and photons". In: *Nature* 416 (2002), p. 238.

[3] N. Gisin and R. Thew. "Quantum Communication". In: *Nature Photon.* 1 (2007), p. 165.

[4] S. Pirandola et al. "Advances in quantum cryptography". In: *Adv. Opt. Photon.* 12 (2020), p. 1012.

[5] A. J. Daley et al. "Practical quantum advantage in quantum simulation". In: *Nature* 607 (2022), p. 667.

[6] C. W. Bauer et al. "Quantum simulation of fundamental particles and forces". In: *Nat. Rev. Phys.* 5 (2023), p. 420.

[7] A. W. Elshaari et al. "Hybrid integrated quantum photonic circuits". In: *Nature Photon.* 14 (2020), p. 285.

[8] V. Giovannetti, S. Lloyd, and L. Maccone. "Advances in quantum metrology". In: *Nature Photon.* 5 (2011), p. 222.

[9] C. L. Degen, F. Reinhard, and P. Cappellaro. "Quantum sensing". In: *Rev. Mod. Phys.* 89 (2017), p. 035002.

[10] R. P. Feynman. "Simulating physics with computers". In: *Int. J. Theor. Phys.* 21 (1982), p. 467.

[11] P. W. Shor. "Polynomial-Time Algorithms for Primce Factorization and Discrete Logarithms on a Quantum Computer". In: *SIAM J. Comput.* 26 (1997), p. 1484.

[12] A. Miessen et al. "Quantum algorithms for quantum dynamics". In: *Nat. Comput. Sci.* 3 (2022), p. 25.

[13] M. Motta and J. E. Rice. "Emerging quantum computing algorithms for quantum chemistry". In: *WIREs Comput. Mol. Sci.* 12 (2022), e1580.

[14] B. Bauer et al. "Quantum Algorithms for Quantum Chemistry and Quantum Materials Science". In: *Chem. Rev.* 120 (2020), p. 12685.

[15] V. Hassija et al. "Present landscape of quantum computing". In: *IET Quantum. Commun.* 1 (2020), p. 42.

[16] B. Fauseweh. "Quantum many-body simulations on digital quantum computers: State-of-the-art and future challenges". In: *Nature Comm.* 15 (2024), p. 2123.

[17] M. Kjaergaard et al. "Superconducting Qubits: Current State of Play". In: *Annu. Rev. Condens. Matter Phys.* 11 (2020), p. 369.

[18] C. Wang et al. "Probing resonating valence bonds on a programmable germanium quantum simulator". In: *npj Quantum Inf.* 9 (2023).

[19] C. E. Bradley et al. “A Ten-Qubit Solid-State Spin Register with Quantum Memory up to One Minute”. In: *Phys. Rev. X* 9 (2019), p. 031045.

[20] J. I. Cirac and P. Zoller. “Quantum Computations with Cold Trapped Ions”. In: *Phys. Rev. Lett.* 74 (1995), p. 4091.

[21] H. Häffner, C. F. Roos, and R. Blatt. “Quantum computing with trapped ions”. In: *Phys. Rep.* 469 (2008), p. 155.

[22] T. M. Graham et al. “Multi-qubit entanglement and algorithms on a neutral-atom quantum computer”. In: *Nature* 604 (2022), p. 457.

[23] T. P. Harty et al. “High-Fidelity Preparation, Gates, Memory, and Readout of a Trapped-Ion Quantum Bit”. In: *Phys. Rev. Lett.* 113 (2014), p. 220501.

[24] P. Wang et al. “Single ion qubit with estimated coherence time exceeding one hour”. In: *Nat. Comm.* 12 (2021), p. 233.

[25] C. Langer et al. “Long-Lived Qubit Memory Using Atomic Ions”. In: *Phys. Rev. Lett.* 95 (2005), p. 060502.

[26] S. Kotler et al. “Hybrid quantum systems with trapped charged particles”. In: *Phys. Rev. A* 95 (2017), p. 022327.

[27] B. P. Lanyon et al. “Universal Digital Quantum Simulation with Trapped Ions”. In: *Science* 334 (2011), p. 57.

[28] R. Blatt and C. F. Roos. “Quantum simulations with trapped ions”. In: *Nat. Phys.* 8 (2012), p. 277.

[29] Jacob Whitlow et al. “Quantum simulation of conical intersections using trapped ions”. In: *Nature Chemistry* 15 (2023), p. 1509.

[30] S. D. Bartlett, H. de Guise, and B. C. Sanders. “Quantum encodings in spin systems and harmonic oscillators”. In: *Phys. Rev. A* 65 (2002), p. 052316.

[31] C. Flühmann et al. “Encoding a qubit in a trapped-ion mechanical oscillator”. In: *Nature* 566 (2019), p. 513.

[32] D Leibfried et al. “Quantum dynamics of single trapped ions”. In: *Rev. Mod. Phys.* 75 (2003), p. 281.

[33] F. G. Major, V. N. Gheorghe, and G. Werth. *Charged Particle Traps*. Springer, 2005.

[34] D. J. Wineland and Wayne M. Itano. “Laser cooling of atoms”. In: *Phys. Rev. A* 20 (1979), p. 1521.

[35] H. J. Metcalf and P. van der Straten. *Laser Cooling and Trapping*. Springer, 1999.

[36] R. J. Hendricks et al. “Doppler cooling of calcium ions using a dipole-forbidden transition”. In: *Phys. Rev. A* 77 (2008), p. 021401.

[37] D. J. Wineland et al. “Atomic-Ion Coulomb Clusters in an Ion Trap”. In: *Phys. Rev. Lett.* 59 (1987), p. 2935.

[38] Y. Wan et al. “Precision spectroscopy by photon-recoil signal amplification”. In: *Nat. Commun.* 5 (2014), p. 3096.

[39] C. Champenois et al. “Ion ring in a linear multipole trap for optical frequency metrology”. In: *Phys. Rev. A* 81 (2010), p. 043410.

[40] A. D. Ludlow et al. “Optical Atomic Clocks”. In: *Rev. Mod. Phys.* 87 (2015), p. 637.

[41] C. D. Bruzewicz et al. “Trapped-ion quantum computing: Progress and challenges”. In: *Appl. Phys. Rev.* 6 (2019), p. 021314.

[42] S. Willitsch. “Coulomb-crystallised molecular ions in traps: methods, applications, prospects”. In: *Int. Rev. Phys. Chem.* 31 (2012), p. 175.

[43] Ziv Meir et al. “Dynamics of a Ground-State Cooled Ion Colliding with Ultracold Atoms”. In: *Phys. Rev. Lett.* 117 (2016), p. 243401.

[44] S. Willitsch. “Chemistry With Controlled Ions”. In: *Adv. Chem. Phys.* 162 (2017), p. 307.

[45] M. Sinhal et al. “Quantum-nondemolition state detection and spectroscopy of single trapped molecules”. In: *Science* 367 (2020), p. 1213.

[46] S. Willitsch. “Ion-atom hybrid systems”. In: *Proc. Int. Sch. Phys. Enrico Fermi* 189 (2015), p. 255.

[47] Michał Tomza et al. “Cold hybrid ion-atom systems”. In: *Rev. Mod. Phys.* 91 (2019), p. 035001.

[48] C. Mangeng et al. “Experimental implementation of laser cooling of trapped ions in strongly inhomogeneous magnetic fields”. In: *Phys. Rev. Res.* 5 (2023), p. 043180.

[49] D. M. Meekhof et al. “Generation of nonclassical motional states of a trapped atom”. In: *Phys. Rev. Lett.* 76 (1996), p. 1796.

[50] D. J. Wineland et al. “Experimental Issues in Coherent Quantum-Sate Manipulation of Trapped Atomic Ions”. In: *J. Res. Natl. Inst. Stan.* 103 (1998), p. 259.

[51] K. C. McCormick et al. “Quantum-enhanced sensing of a single-ion mechanical oscillator”. In: *Nature* 572 (2019), p. 86.

[52] R. Srinivas et al. “Coherent Control of Trapped-Ion Qubits with Localized Electric Fields”. In: *Phys. Rev. Lett.* 131 (2023), p. 020601.

[53] M. J. Biercuk et al. “Ultrasensitive detection of force and displacement using trapped ions”. In: *Nat. Nanotechnol.* 5 (2010), p. 646.

[54] P. A. Ivanov, N. V. Vitanov, and K. Singer. “High-precision force sensing using a single trapped ion”. In: *Sci. Rep.* 6 (2016), p. 28078.

[55] A. Levy et al. “Single-atom heat engine as a sensitive thermal probe”. In: *New. J. Phys.* 2 (2020), p. 093020.

[56] M. D. Hughes et al. “Microfabricated ion traps”. In: *Contemp. Phys.* 52 (2011), p. 505.

[57] C. Monroe and J. Kim. "Scaling the Ion Trap Quantum Processor". In: *Science* 339 (2013), p. 1164.

[58] C. Decaroli et al. "Design, fabrication and characterization of a micro-fabricated stacked-wafer segmented ion trap with two X-junctions". In: *Quantum Sci. Technol.* 6 (2021), p. 044001.

[59] J. M. Pino et al. "Demonstration of the trapped-ion quantum CCD computer architecture". In: *Nature* 592 (2021), p. 209.

[60] Z. et al. Yang. "Single-nanowire spectrometers". In: *Science* 365 (2019), p. 1017.

[61] F. J. Giessibl. "Advances in atomic force microscopy". In: *Rev. Mod. Phys.* 75 (2003), p. 949.

[62] M. Poggio et al. "Feedback Cooling of a Cantilever's Fundamental Mode below 5 mK". In: *Phys. Rev. A.* 99 (2007), p. 017201.

[63] J. Chan et al. "Laser cooling of a nanomechanical oscillator into its quantum ground state". In: *Nature* 10 (2011), p. 1038.

[64] E. Verhagen et al. "Quantum-coherent coupling of a mechanical oscillator to an optical cavity mode". In: *Nature* 482 (2012), pp. 63–67.

[65] A. Jöckel et al. "Sympathetic cooling of a membrane oscillator in a hybrid mechanical-atomic system". In: *Nat. Nanotech.* 10 (2015), p. 1038.

[66] G. Schmid et al. "Coherent Feedback Cooling of a Nanomechanical Membrane with Atomic Spins". In: *Phys. Rev. X* 12 (2022), p. 011020.

[67] F. R. Braakman and M. Poggio. "Force sensing with nanowire cantilevers". In: *Nanotechnology* 30 (2019), p. 18.

[68] M. Poggio et al. "Nuclear magnetic resonance force microscopy with a microwire rf source". In: *Appl. Phys. Lett.* 90 (2007), p. 263111.

[69] A. Gloppe et al. "Bidimensional nano-optomechanics and topological backaction in a non-conservative radiation force field". In: *Nat. Nanotech.* 9 (2014), p. 920.

[70] D. H. Slichter et al. "UV-sensitive superconducting nanowire single photon detectors for integration in an ion trap". In: *Opt. Express* 25 (2017), p. 8705.

[71] B. Hampel et al. "Trap-integrated superconducting nanowire single-photon detectors with improved rf tolerance for trapped-ion qubit state readout". In: *Appl. Phys. Lett* 122 (2023), p. 174001.

[72] K. K. Mehta et al. "Integrated optical addressing of an ion qubit". In: *Nat. Nanotech.* 11 (2016), p. 1066.

[73] J. Stuart et al. "Chip-Integrated Voltage Sources for Control of Trapped Ions". In: *Phys. Rev. Appl.* 11 (2019), p. 024010.

[74] Z. D. Romaszko et al. “Engineering of microfabricated ion traps and integration of advanced on-chip features”. In: *Nat. Rev.* 2 (2020), p. 285.

[75] S. L. Todaro et al. “State Readout of a Trapped Ion Qubit Using a Trap-Integrated Superconducting Photon Detector”. In: *Phys. Rev. Lett.* 126 (2021), p. 010501.

[76] M. Wallquist et al. “Hybrid quantum devices and quantum engineering”. In: *Phys. Script.* T137 (2009), p. 014001.

[77] N. Daniilidis and H. Häffner. “Quantum Interfaces Between Atomic and Solid-Sate Systems”. In: *Annu. Rev. Condens. Matter Phys.* 4 (2013), p. 83.

[78] P. Treutlein et al. *Hybrid Mechanical Systems. In: Cavity Optomechanics*. Ed. by M. Aspelmeyer, T. J. Kippenberg, and F. Marquardt. Springer, 2014.

[79] A. A. Clerk et al. “Hybrid quantum systems with circuit quantum electrodynamics”. In: *Nat. Phys.* 16 (2020), p. 257.

[80] P. N. Fountas. “Theoretical Study and Experimental Implementation of an Ion-Nanowire Hybrid System”. PhD thesis. University of Basel, 2020.

[81] G. Kurizki et al. “Quantum technologies with hybrid systems”. In: *PNAs* (2015), p. 3866.

[82] S. C. Burd et al. “Quantum amplification of mechanical oscillator motion”. In: *Science* 364 (2019), p. 1163.

[83] D. S. Bykov et al. “3D sympathetic cooling and detection of levitated nanoparticles”. In: *Optica* 10 (2023), p. 438.

[84] P. N. Fountas, M. Poggio, and S. Willitsch. “Classical and quantum dynamics of a trapped ion coupled to a charged nanowire”. In: *New J. Phys* 21 (2019), p. 013030.

[85] D. Hunger et al. “Resonant Coupling of a Bose-Einstein Condensate to a Micromechanical Oscillator”. In: *Phys. Rev. Lett.* 104 (2010), p. 143002.

[86] S. Camerer et al. “Realization of an Optomechanical Interface Between Ultracold Atoms and a Membrane”. In: *Phys. Rev. Lett.* 107 (2011), p. 223001.

[87] A. J. Shields. “Semiconductor quantum light sources”. In: *Nat. Photonics* 1 (2007), p. 215.

[88] R. Hanson and D. D. Awschalom. “Coherent manipulation of single spins in semiconductors”. In: *Nature* 453 (2008), p. 1043.

[89] J. Clarke and F. K. Wilhem. “Superconducting quantum bits”. In: *Nature* 453 (2008), p. 1031.

[90] Z. Xiang et al. “Hybrid quantum circuits: Superconducting circuits interacting with other quantum systems”. In: *Rev. Mod. Phys.* 85 (2013), p. 623.

[91] A. A. Geraci and J. Kitching. “Ultracold mechanical resonators coupled to atoms in an optical lattice”. In: *Phys. Rev. A.* 80 (2009), p. 014001.

[92] H. Wang and I. Lekavicius. “Coupling spins to nanomechanical resonators: Toward quantum spin-mechanics”. In: *Appl. Phys. Lett* 117 (2020), p. 230501.

[93] L. Tian and P. Zoller. “Coupled Ion-Nanomechanical Systems”. In: *Phys. Rev. Lett.* 93 (2004), p. 266403.

[94] D. Hunger et al. “Coupling ultracold atoms to mechanical oscillators”. In: *C. R. Phys.* 12 (2011), p. 871.

[95] A. Bachtold, J. Moser, and M. I. Dykman. “Mesoscopic physics of nanomechanical systems”. In: *Rev. Mod. Phys.* 94 (2022), p. 045005.

[96] D. S. Bykov et al. “Hybrid electro-optical trap for experiments with levitated particles in vacuum”. In: *Rev. Sci. Instrum.* 93 (2022), p. 073201.

[97] W. K. Hensinger et al. “Ion trap transducers for quantum electromechanical oscillators”. In: *Phys. Rev. A* 72 (2005), p. 041405.

[98] S. Singh et al. “Coupling Nanomechanical Cantilevers to Dipolar Molecus”. In: *Phys. Rev. Lett.* 101 (2008), p. 263603.

[99] P. Treutlein et al. “Bose-Einstein Condensate Coupled to a Nanomechanical Resonator on an Atom Chip”. In: *Phys. Rev. Lett.* 99 (2007), p. 140403.

[100] A. Tretiakov and L. J. LeBlanc. “Magnetic-field-mediated coupling and control in hybrid atomic-nanomechanical systems”. In: *Phys. Rev. A* 94 (2016), p. 043802.

[101] S. Gröblacher et al. “Observation of strong coupling between a micromechanical resonator and an optical cavity field”. In: *Nature* 460 (2009), p. 724.

[102] J. D. Thompson et al. “Strong dispersive coupling of a high-finesse cavity to a micromechanical membrane”. In: *Nature* 452 (2008), p. 72.

[103] K. Hammerer et al. “Strong Coupling of a Mechanical Oscillator and a Single Atom”. In: *Phys. Rev. Lett.* 103 (2009), p. 063005.

[104] A. Vochezer et al. “Light-Mediated Collective Atomic Motion in an Optical Lattice Coupled to a Membrane”. In: *Phys. Rev. Lett.* 120 (2018), p. 073602.

[105] S. Chu. “Cold atoms and quantum control”. In: *Nature* 416 (2002), p. 206.

[106] M. A. Kasevich. “Coherence with Atoms”. In: *Science* 298 (2002), p. 1363.

[107] D. J. Wineland. “Quantum information processing and quantum control with trapped atomic ions”. In: *Phys. Scr.* 2009 (2009), p. 014007.

[108] K R Brown et al. “Coupled quantized mechanical oscillators”. In: *Nature* 471 (2011), p. 196.

[109] M. Harlander et al. “Trapped-ion antennae for the transmission of quantum information”. In: *Nature* 471 (2011), p. 200.

[110] D. An et al. “Coupling Two Laser-Cooled Ions via a Room-Temperature Conductor”. In: *Phys. Rev. Lett.* 128 (2022), p. 063201.

[111] M. Gierling et al. “Cold-atom scanning probe microscopy”. In: *Nat. Nanotech.* 6 (2011), p. 446.

[112] COMSOL AB. *COMSOL Multiphysics® v. 6.2.* Stockholm, Sweden, 2024. URL: `https://www.comsol.com`.

[113] J. D. Jackson. *Classical Electrodynamics*. Wiley, 1998.

[114] N. W. McLachlan. *Theory and Application of Mathieu Functions*. Oxford University press, 1947.

[115] M. Abramowitz and I. A. Stegun. *Handbook of Mathematical Functions with Formulas, Graphs, and Mathematical Tables*. NBS, 1964.

[116] A. Drakoudis, M. Söllner, and G. Werth. “Instabilities of ion motion in a linear Paul trap”. In: *Int. J. Mass Spectrom.* 252 (2006), p. 61.

[117] M. Knoop. *Radiofrequency Traps. In: Trapped Charged Particles*. Ed. by M. Knoop, N. Madsen, and R. C. Thompson. World Scientific, 2016.

[118] G. Werth, V. N. Gheorghe, and F. G. Major. *Charged Tarticle Traps II*. Springer, 2009.

[119] L. A. Zhukas et al. “Direct observation of ion micromotion in a linear Paul trap”. In: *Phys. Rev. A* 103 (2021), p. 023105.

[120] D. J. Berkeland et al. “Minimization of ion micromotion in a Paul trap”. In: *J. Appl. Phys.* 83 (1998), p. 5025.

[121] L. N. Hand and J. D. Finch. *Analytical Mechanics*. Cambridge University Press, 1998.

[122] R. C. Thompson. “Ion Coulomb crystals”. In: *Contemp. Phys.* 56 (2015), p. 63.

[123] A. Walther et al. “Controlling Fast Transport of Cold Trapped Ions”. In: *Phys. Rev. Lett.* 109 (2012), p. 080501.

[124] V. Kaushal et al. “Shuttling-based trapped-ion quantum information processing”. In: *AVS Quantum Sci.* 2 (2020), p. 014101.

[125] H. C. Nägerl et al. *Linear Ion Traps for Quantum Computation. In: The Physics of Quantum Information*. Ed. by D. Bouwmeester, A. Ekert, and A. Zeilinger. Springer, 2000.

[126] M. G. Raizen et al. “Ionic crystals in a linear Paul trap”. In: *Phys. Rev. A* 45 (1992), p. 6493.

[127] C. A. Schrama et al. “Novel miniature ion traps”. In: *Opt. Commun.* 101 (1993), p. 32.

[128] J. Pedregosa et al. “Anharmonic contributions in real RF linear quadrupole traps”. In: *Int. J. Mass Spectrom.* 290 (2010), p. 100.

[129] H. C. Nägerl et al. “Laser addressing of individual ions in a linear ion trap”. In: *Phys. Rev. A.* 60 (1999), p. 145.

[130] E. I. Butikov. “Analytical expressions for stability regions in the Ince-Strutt diagram of Mathieu equation”. In: *Am. J. Phys.* (2018), p. 257.

[131] R. Blümel. "Nonlinear dynamics of trapped ions". In: *Phys. Scr.* T59 (1995), p. 369.

[132] M. Drewsen and A. Brøner. "Harmonic linear Paul trap: Stability diagram and effective potentials". In: *Phys. Rev. A* 62 (2000), p. 045401.

[133] C. Champenois. "About the dynamics and thermodynamics of trapped ions". In: *J. Phys. B* 42 (2009), p. 154002.

[134] D. Gerlich. *State-Selected and State-to-State Ion-Molecule Reaction Dynamics*. Wiley, 1992.

[135] H. G. Dehmelt. "Radiofrequency Spectroscopy of Stored Ions I: Storage". In: *Adv. At. Mol. Phys.* 3 (1967), p. 53.

[136] A. Mokhberi. "Scalable Microchip Ion Traps and Guides for Cold Molecular Ions". PhD thesis. Universiy of Basel, 2016.

[137] D. Hucul et al. "On the transport of atomic ions in linear and multidimensional ion trap arrays". In: *Quantum Inf. Comput.* 8 (2008), p. 501.

[138] A. Mokhberi, R. Schmied, and S. Willitsch. "Optimised surface-electrode ion-trap junctions for experiments with cold molecular ions". In: *New. J. Phys.* 19 (2017), p. 043023.

[139] C. F. Foot. *Atomic Physics*. Oxford University Press, 2005.

[140] I. Rouse. "A hybrid ion-atom chip trap and the non-equilibrium statistical mechanics of trapped ions". PhD thesis. University of Basel, 2018.

[141] H. C. Nägerl et al. *Cavity QED-Experiments: Atoms in Cavities and Trapped Ions. In: The Physics of Quantum Information*. Ed. by D. Bouwmeester, A. Ekert, and A. Zeilinger. Springer, 2000.

[142] C. Champenois. *Laser Cooling Techniques Applicable to Trapped Ions. In: Trapped Charged Particles*. Ed. by M. Knoop, N. Madsen, and R. C. Thompson. World Scientific, 2016.

[143] P. Gould. "Laser cooling of atoms to the Doppler limit". In: *Am. J. Phys.* 65 (1997), p. 1120.

[144] P. D. Lett et al. "Optical Molasses". In: *J. Opt. Soc. Am. B* 6 (1989), p. 2084.

[145] M. Marciante et al. "Ion dynamics in a linear radio-frequency trap with a single cooling laser". In: *Phys. Rev. A* 82 (2010), p. 033406.

[146] P. A. Barton et al. "Measurement of the lifetime of the $3d^2D_{5/2}$ state in $^{40}Ca^{+}$". In: *Phys. Rev. A* 62 (2000), p. 032503.

[147] D. McCarron. "Laser cooling and trapping molecules". In: *J. Phys. B: At. Mol. Opt. Phys.* 51 (2018), p. 212001.

[148] K. Mølhave and M. Drewsen. "Formation of translationally cold MgH^+ and MgD^+ molecules in an ion trap". In: *Phys. Rev. A* 62 (2000), p. 011401.

[149] A. Shlykov, M. Roguski, and S. Willitsch. "Optimized Strategies for the Quantum-State Preparation of Single Trapped Nitrogen Molecular Ions". In: *Adv. Quantum Technol.* 0 (2023), p. 2300268.

[150] M. D. Di Rosa. "Laser-cooling molecules". In: *Eur. Phys. J. D* 31 (2004), p. 395.

[151] E. S. Shuman, J. F. Barry, and D. DeMille. "Laser cooling of a diatomic molecule". In: *Nature* 467 (2010), p. 820.

[152] L. Anderegg et al. "Laser cooling of optically trapped molecules". In: *Nat. Phys.* 14 (2018), p. 890.

[153] B. L. Augenbraun et al. "Laser-cooled polyatomic molecules for improved electron electric dipole moment searches". In: *New J. Phys.* 22 (2020), p. 022003.

[154] D. Mitra et al. "Direct laser cooling of a symmetric top molecule". In: *Science* 369 (2020), p. 1366.

[155] N. Sillitoe and L. Hilico. *Numerical Simulations of Ion Cloud Dynamics. In: Trapped Charged Particles*. Ed. by M. Knoop, N. Madsen, and R. C. Thompson. World Scientific, 2016.

[156] R. Karl, Y. Yin, and S. Willitsch. "Laser cooling of trapped ions in strongly inhomogeneous magnetic fields". In: *Mol. Phys.* 0 (2023), p. 2199099.

[157] I. Rouse and S. Willitsch. "Superstatistical velocity distributions of cold trapped ions in molecular-dynamics simulations". In: *Phys. Rev. A* 92 (2015), p. 053420.

[158] D. J. Griffiths. *Introduction to Quantum Mechanics*. Pearson Education, 1995.

[159] R. H. Dicke. "The Effect of Collisions upon the Doppler Width of Spectral Lines". In: *Phys. Rev.* 89 (1953), p. 472.

[160] F. Diedrich et al. "Laser Cooling to the Zero-Point Energy of Motion". In: *Phys. Rev. Lett.* 62 (1989), p. 403.

[161] M. Šašura and V. Bužek. "Cold trapped ions as quantum information processors". In: *J. Mod. Opt.* 49 (2002), p. 1593.

[162] J. Keller et al. "Precise determination of micromotion for trapped-ion optical clocks". In: *J. Appl. Phys.* 118 (2015), p. 104501.

[163] E. Peik et al. "Sideband cooling of ions in radio-frequency traps". In: *Phys. Rev. A* 60 (1999), p. 439.

[164] A. Öchsner. *Classical Beam Theories of Structural Mechanics*. Springer, 2021.

[165] A. N. Cleland. *Foundations of Nanomechanics*. Springer, 2003.

[166] W. J. Bottega. *Engineering Vibrations*. CRC Press, 2013.

[167] S. Schmid, L. G. Villanueva, and M. L. Roukes. *Fundamentals of Nanomechanical Resonators*. Springer, 2016.

[168] N. Rossi. "Force sensing with nanowires". PhD thesis. University of Basel, 2019.

[169] M. Imboden and P. Mohanty. "Dissipation in nanoelectromechanical systems". In: *Phys. Rep.* 534 (2014), p. 89.

[170] E. J. Salumbides et al. "High-precision frequency measurement of the 423-nm Ca I line". In: *Phys. Rev. A* 83 (2011), p. 012502.

[171] S. Gulde et al. "Simple and efficient photo-ionization loading of ions for precision ion-trapping experiments". In: *Appl. Phys. B* 73 (2001), p. 861.

[172] H. Shao et al. "Laser ablation and two-step photo-ionization for the generation of $^{40}Ca^{+}$". In: *J. Phys. Commun.* 2 (2018), p. 095019.

[173] L. B. Biedermann et al. "Characterization of silver-gallium nanowires for force and mass sensing applications". In: *Nanotechnology* 21 (2010), p. 305701.

[174] D. Heinrich et al. "Ultrafast coherent excitation of a $^{40}Ca^{+}$ ion". In: *New J. Phys.* 21 (2019), p. 073017.

[175] F. Gebert et al. "Precision Isotope Shift Measurements in Calcium Ions Using Quantum Logic Detection Schemes". In: *Phys. Rev. Lett.* 115 (2015), p. 053003.

[176] M. Hettrich et al. "Measurement of Dipole Matrix Elements with a Single Trapped Ion". In: *Phys. Rev. Lett.* 115 (2015), p. 143003.

[177] Alexander Franzen. *ComponentLibrary*. URL: `https://www.gwoptics.org/ComponentLibrary`.

[178] NI. *LabView*. URL: `https://www.ni.com`.

[179] P. Eberle. "Increased Control over Reaction Conditions in a Hybrid Trap". PhD thesis. University of Basel, 2020.

[180] PyQt. *Qt for Python*. URL: `https://doc.qt.io`.

[181] J. D. Siverns et al. "On the application of radio frequency voltages to ion traps via helical resonators". In: *Appl. Phys. B* 107 (2012), p. 921.

[182] N. Batra et al. "Design and Construction of a Helical Resonator for Delivering Radio Frequency to an Ion Trap". In: *MAPAN* 32 (2017), p. 193.

[183] K. Deng et al. "A modified model of helical resonator with predictable loaded resonant frequency and Q-factor". In: *Rev. Sci. Instrum.* 85 (2014), p. 104706.

[184] L. Pedrosa-Rodriguez et al. "Design, development and testing of a helical resonator for trapping Sr^{+} ions for frequency standards and sensing applications". In: *Measurement* 125 (2018), p. 156.

[185] D. J. Harra. "Predicting and Evaluating Titanium Sublimation Pump Performance". In: *Japan J. Appl. Phys.* 13 (1974), p. 41.

[186] B. Sanii and P. D. Ashby. "High Sensitivity Deflection Detection of Nanowires". In: *Phys. Rev. Lett* 104 (2010), p. 147203.

[187] X. Zhao, V. L. Ryjkov, and H. A. Schuessler. "Parametric excitations of trapped ions in a linear rf ion trap". In: *Phys. Rev. A* 66 (2002), p. 063414.

[188] B. Wang et al. “Direct measurement of micromotion speed in a linear quadrupole trap”. In: *J. Appl. Phys.* 108 (2010), p. 013108.

[189] M. G. House. “Analytic model for electrostatic fields in surface-electrode ion traps”. In: *Phys. Rev. A* 78 (2008), p. 033402.

[190] F. A. Shaikh and A. Ozakin. “Stability analysis of ion motion in asymmetric planar ion traps”. In: *J. Appl. Phys.* 112 (2012), p. 074904.

[191] A. Härter et al. “Long-term drifts of stray electric fields in a Paul trap”. In: *Appl. Phys. B* 114 (2014), pp. 275–281.

[192] R. Anandakrishnan et al. “Point Charges Optimally Placed to Represent the Multipole Expansion of Charge Distributions”. In: *PLoS ONE* 8 (2013), e67715.

[193] K. F. Riley, M. P. Hobson, and S. J. Bence. *Mathematical Methods For Physics and Engineering*. Cambridge University Press, 1998.

[194] P. Mikusiński and M. D. Taylor. *An Introduction to Multivariable Analysis from Vector to Manifold*. Springer, 2002.

[195] Wolfram Research Inc. *Mathematica, Version 14.0*. Champaign, Illinois, 2024. URL: `https://www.wolfram.com/mathematica`.

[196] L. Verlet. “Computer "Experiments" on Classical Fluids. I. Thermodynamical Properties of Lennard-Jones Molecules”. In: *Phys. Rev.* 159 (1967), p. 98.

[197] Q. Spreiter and M. Walter. “Classical Molecular Dynamics Simulation with the Velocity Verlet Algorithm at Strong External Magnetic Fields”. In: *J. Comp. Phys.* 152 (1999), p. 102.

[198] B. J. Alder and T. E. Wainwright. “Studies in Molecular Dynamics. I. General Method”. In: *J. Chem. Phys.* 31 (1959), p. 459.

[199] R. I. McLachlan. “Perspectives on geometric numerical integration”. In: *J. R. Soc. N. Z.* 49 (2019), p. 114.

[200] C. B. Zhang et al. “Molecular-dynamics simulations of cold single-species and multi-species ion ensembles in a linear Paul trap”. In: *Phys. Rev. A* 76 (2007), p. 012719.

[201] E. Brama et al. “Heating rates in a thin ion trap for microcavity experiments”. In: *Appl. Phys. B* 107 (2012), p. 945.

[202] R. J. Epstein et al. “Simplified motional heating rate measurements of trapped ions”. In: *Phys. Rev. A* 76 (2007), p. 033411.

[203] J. H. Wesenberg et al. “Fluorescence during Doppler cooling of a single trapped atom”. In: *Phys. Rev. A* 76 (2007), p. 053416.

[204] A. Mokhberi and S. Willitsch. “Structural and energetic properties of molecular Coulomb crystals in a surface-electrode ion trap”. In: *New J. Phys.* 17 (2015), p. 045008.

[205] D. F. V. James. "Quantum dynamics of cold trapped ions with application to quantum computation". In: *Appl. Phys. B* 66 (1998), p. 181.

[206] M. Germann. "Dipole-Forbidden Vibrational Transitions in Molecular Ions". PhD thesis. University of Basel, 2016.

[207] H. C. Nägerl et al. "Coherent excitation of normal modes in a string of Ca^+ ions". In: *Opt. Express* 3 (1998), p. 89.

[208] G. Morigi and H. Walther. "Two-species Coulomb chains for quantum information". In: *Eur. Phys. J. D* 13 (2001), p. 261.

[209] M. Drewsen et al. "Nondestructive identification of cold and extremely localized single molecular ions". In: *Phys. Rev. Lett.* 93 (2004), p. 243201.

[210] B. E. King et al. "Cooling the Collective Motion of Trapped Ions to Initialize a Quantum Register". In: *Phys. Rev. Lett.* 81 (1998), p. 1525.

[211] attocube. *attocube nanopositioners*. URL: `https://attocube.com`.

[212] W. Kundhikanjana et al. "Cryogenic microwave imaging of metal-insulator transition in doped silicon". In: *Rev. Sci. Instrum.* 82 (2011), p. 033705.

[213] S. D. Fallek et al. "Rapid exchange cooling with trapped ions". In: *Nat. Comm.* 15 (2024), p. 1089.

[214] C. Cohen-Tannoudji, B. Diu, and F. Laloë. *Quantum Mechanics*. Wiley, 1977.

[215] J. J. Sakurai and J. Napolitano. *Modern Quantum Mechanics*. Addison-Wesley, 1994.